REPORT DOCUMENTATION PAGE

AFRL-SR-BL-TR-01-
0198

[illegible]

1. AGENCY USE ONLY (Leave blank)

2. REPORT DATE
2/26/01

3. REPORT TYPE AND DATES COVERED
FINAL TECHNICAL REPORT

4. TITLE AND SUBTITLE
ENERGY TRANSFER PROCESSES IN THE PRODUCTION OF EXCITED STATES IN REACTING ROCKET FLOWS

5. FUNDING NUMBERS
F49620-96-1-0184

6. AUTHOR(S)
J. WILLIAM RICH
IGOR ADAMOVICH
VISH V. SUBRAMANIAM

7. PERFORMING ORGANIZATION NAME(S) AND ADDRESS(ES)

DEPARTMENT OF MECHANICAL ENGINEERING
THE OHIO STATE UNIVERSITY
COLUMBUS, OH 43210-1154

8. PERFORMING ORGANIZATION REPORT NUMBER

9. SPONSORING/MONITORING AGENCY NAME(S) AND ADDRESS(ES)
SPACE PROPULSION AND POWER
DIRECTORATE OF AEROSPACE AND MATERIAL SCIENCES
AIR FORCE OFFICE OF SCIENTIFIC RESEARCH
801 N. RANDOLF ST.
ARLINGTON, VA 22203-1977

10. SPONSORING/MONITORING AGENCY REPORT NUMBER

11. SUPPLEMENTARY NOTES

12a. DISTRIBUTION/AVAILABILITY STATEMENT

APPROVED FOR PUBLIC RELEASE;
DISTRIBUTION IS UNLIMITED

12b. DISTRIBUTION CODE

AIR FORCE OFFICE OF SCIENTIFIC RESEARCH (AFOSR)
NOTICE OF TRANSMITTAL DTIC. THIS TECHNICAL REPORT
HAS BEEN REVIEWED AND IS APPROVED FOR PUBLIC RELEASE
LAW AFR 190-12. DISTRIBUTION IS UNLIMITED.

13. ABSTRACT (*Maximum 200 words*)

The present report incorporates the results of experimental and analytical research into kinetic mechanisms and rates of collisional and radiative energy transfer processes in nonequilibrium gas and plasma flows, such as exist in high-altitude rocket plumes, supersonic nozzles, and behind shock waves. The kinetic processes under consideration include vibrational relaxation and molecular dissociation of air species (N_2 and O_2), as well as of key combustion products (such as CO and NO), which are primarily responsible for persistent visible and ultraviolet radiation in low-density plumes. Associative ionization in collisions of vibrationally excited molecules, as well as strong coupling between plasma electrons and vibrationally excited species are also studied in detail. Finally, the report incorporates the results of kinetic modeling of nonequilibrium, reacting, ionized flows in supersonic nozzles, MHD channels, and behind the shock waves.

14. SUBJECT TERMS
ROCKET PLUME RADIATION, ENERGY TRANSFER PROCESSES, NONEQUILIBRIUM REACTING FLOWS

15. NUMBER OF PAGES
269

16. PRICE CODE

17. SECURITY CLASSIFICATION OF REPORT

18. SECURITY CLASSIFICATION OF THIS PAGE

19. SECURITY CLASSIFICATION OF ABSTRACT

20. LIMITATION OF ABSTRACT

EXECUTIVE SUMMARY

The present report incorporates the results of experimental and analytical research into kinetic mechanisms and rates of collisional and radiative energy transfer processes in nonequilibrium gas and plasma flows, such as exist in high-altitude rocket plumes, supersonic nozzles, and behind shock waves. The kinetic processes under consideration include vibrational relaxation and molecular dissociation of air species (N_2 and O_2), as well as of key combustion products (such as CO and NO), which are primarily responsible for persistent visible and ultraviolet radiation in low-density plumes. Associative ionization in collisions of vibrationally excited molecules, as well as strong coupling between plasma electrons and vibrationally excited species are also studied in detail. Finally, the report incorporates the results of kinetic modeling of nonequilibrium, reacting, ionized flows in supersonic nozzles, MHD channels, and behind the shock waves. The rates of kinetic processes developed during this research, including vibration-to-translation (V-T), vibration-to-vibration (V-V), and vibration-to-electronic (V-E) rates for air species, and nonequilibrium chemical reaction rates for air species have been incorporated into existing Navier-Stokes and DSMC nonequilibrium flow codes developed at University of Minnesota (Prof. Graham Candler), University of Michigan (Prof. Iain Boyd), and Pennsylvania State University (Prof. Deborah Levin). The results of these studies are also being provided to the Plumes Initiative Group at Air Force Research Laboratories (Dr. Ingrid Wysong).

Thus, the main objectives of the research, which include (i) development of analytical models of V-T, V-V, and V-E energy transfer and nonequilibrium chemical reaction rates for N_2, O_2, CO, and NO, (ii) experimental studies of kinetic mechanisms of energy transfer among these species and measurements of their rates, and (iii) development of nonequilibrium flow codes for kinetic modeling of high-enthalpy, strongly nonequilibrium gas and plasma flows have been accomplished.

The results of this research are published in 12 journal papers and presented as both invited and contributed papers at more than 40 national and international meetings, including AIAA Thermophysics and Plasmadynamics and Lasers Conferences, Gaseous Electronics Conferences, International Symposia on Molecular Spectroscopy, International Conferences on Phenomena in Ionized Gases, and at IEEE International Conferences on Plasma Science. These results provide new insight into kinetics of nonequilibrium flows, as well as new valuable data on the rates of the key energy transfer processes.

20010329 029

TABLE OF CONTENTS

CHAPTER I. THREE-DIMENSIONAL NONPERTURBATIVE ANALYTIC MODEL OF VIBRATIONAL ENERGY TRANSFER IN ATOM-MOLECULE COLLISIONS **3**

CHAPTER II. THREE-DIMENSIONAL NONPERTURBATIVE ANALYTIC MODEL OF VIBRATIONAL ENERGY TRANSFER IN MOLECULE-MOLECULE COLLISIONS **41**

CHAPTER III. SEMICLASSICAL MODELING OF STATE-SPECIFIC DISSOCIATION RATES IN DIATOMIC GASES **69**

CHAPTER IV. TIME-RESOLVED FOURIER TRANSFORM INFRARED SPECTROSCOPY OF OPTICALLY PUMPED CARBON MONOXIDE **94**

CHAPTER V. VIBRATIONAL ENERGY TRANSFER AMONG HIGH VIBRATIONAL LEVELS OF NITRIC OXIDE **132**

CHAPTER VI. VIBRATIONAL ENERGY STORAGE IN HIGH-PRESSURE MIXTURES OF DIATOMIC MOLECULES **150**

CHAPTER VII. THE EFFECT OF SUPERELASTIC ELECTRON-MOLECULE COLLISIONS ON THE VIBRATIONAL ENERGY DISTRIBUTION FUNCTION **174**

CHAPTER VIII. IONIZATION MEASUREMENTS IN OPTICALLY PUMPED DISCHARGES **185**

CHAPTER IX. THE EXISTENCE OF THE “BOTTLENECK” IN VIBRATIONAL RELAXATION OF DIATOMIC MOLECULES **201**

CHAPTER X. KINETICS OF NO FORMATION BEHIND STRONG SHOCK WAVES **214**

CHAPTER XI. FEASIBILITY STUDY OF MHD ACCELERATION OF UNSEEDED AND SEEDED AIR FLOWS **236**

CHAPTER I.

THREE-DIMENSIONAL NONPERTURBATIVE ANALYTIC MODEL OF VIBRATIONAL ENERGY TRANSFER IN ATOM-MOLECULE COLLISIONS

1. Introduction

Vibrational energy transfer processes in collisions of diatomic molecules play an extremely important role in gas discharges, molecular lasers, plasma chemical reactors, high enthalpy gas dynamic flows, and in the physics of the upper atmosphere. In these nonequilibrium environments, the energy loading per molecule may be as high as 0.1-5.0 eV, while disequipartition among translational, vibrational, and electronic energy modes of heavy species, and with the free electron energy, may be very strong. This often results in development and maintaining of strongly nonequilibrium molecular vibrational energy distributions, which induce a variety of energy transfer processes among different energy modes and species, chemical reactions, and ionization [1-4]. The rates of these processes are determined by the populations of high vibrational levels of molecules, which are often controlled by vibration-translation (V-T) processes

$$AB(i) + M \rightarrow AB(f) + M \tag{1}$$

and vibration-vibration (V-V-T) processes

$$AB(i_1) + CD(i_2) \rightarrow AB(f_1) + CD(f_2) \tag{2}$$

In Eqs. (1) and (2), AB, CD, and M represent diatomic molecules and an atom, respectively, and i_1, i_2, f_1, and f_2 are vibrational quantum numbers.

Quantitative data on the mechanisms and kinetic rates of these processes are needed for numerous practical applications, including novel chemical technologies, environmental pollution control, and radiation prediction in aerospace propulsion flows, in high altitude rocket plumes and behind shock waves. There exists an extensive literature on the experimental study of V-T and V-V-T energy transfer, including recent state-specific rate measurements for highly vibrationally excited molecules, such as NO, O_2, and CO [5-9]. However, for many high-temperature and high vibrational quantum number energy transfer processes, the experimental rate data are still unavailable. As a result, most such rates used in applied kinetic modeling are based on theoretical scattering calculations. Among numerous theoretical rate models available, one can separate the following major approaches: (i) fully quantum calculations, (ii) classical, quasiclassical, and semiclassical numerical trajectory calculations, and (iii) analytic methods.

Since the exact quantum calculations are rather computationally laborious, they have been usually made for a simplified model of collinear collisions of harmonic oscillators and used as tests for more approximate approaches [10-12]. However, some three-dimensional calculations of the state-specific vibrational energy transfer rates for O_2-O_2 using vibrational close-coupling infinite-order sudden approximation (VCC-IOSA) have been recently published [13].

Classical and quasiclassical trajectory methods, such as used for calculations of vibrational relaxation rates for O_2-Ar [14], N_2-N, and O_2-O [15,16], are applicable only for calculation of rather large transition probabilities. For accurate predictions of small transition probabilities $P<<1$, a large number of collision trajectories, $N \sim 1/P$, have to be averaged.

Among semiclassical calculations, one can mention the close-coupled method developed by Billing and validated by comparison with the exact quantum calculations, as well as with experimental data [17]. Trajectory calculations by this method have been made for a number of species such as H_2, N_2, O_2, and CO [18-23] in a wide range of collision energies and vibrational quantum numbers. These results comprise perhaps the most extensive and consistent vibrational energy transfer rate database.

In addition to some fundamental problems encountered in calculations by these advanced methods (such as the choice of the three-dimensional potential energy surface), their results are often difficult to interpret and use in kinetic modeling calculations. First, it is not always possible to identify the key energy transfer mechanisms that control the cross-sections obtained. Second, the number of the state-specific rates used as entries in modern master equation kinetic models for studies of strongly nonequilibrium gases and plasmas may reach 10^4-10^5. Even if some of these rate data are available from three-dimensional computer calculations, one has to rely on curve fitting, unreliable extrapolation, or inaccurate analytic parametrization to incorporate the rates into the model. As a result, such kinetic models do not provide new insight into kinetics, have limited applicability, and lack predictive capability.

Approximate analytic rate expressions are also widely used in kinetic modeling, mostly because of their simplicity. However, available analytic models have serious inherent flaws that make them much less reliable and accurate compared to numerical scattering calculations. First, most of these models, such as the Schwartz, Slawsky, Herzfeld (SSH) theory, Rapp-Englander-Golden model, Sharma-Brau theory etc. [24-27] are based on first-order perturbation theory (FOPT), and therefore cannot be applied at high collision energies, high quantum numbers, and for multi-quantum processes ($|i-f|>1$ in Eqs. (1,2)). An exception is the nonperturbative Forced Harmonic Oscillator (FHO) model [28-31], which takes into account the coupling of many vibrational states during a collision, and is therefore applicable for such conditions. Second, analytic models are typically developed only for collinear collisions of non-rotating molecules. A procedure commonly used to account for the effects of realistic three-dimensional collisions and molecular rotation is the introduction of adjustable correction parameters ("steric factors") into the resultant rate expression [32]. These coefficients, which are assumed to be temperature-independent, have very little or no theoretical basis and are found from comparison of a simple model with experiments or three-dimensional calculations.

There have been various attempts to develop non-empirical expressions for the steric factors and also to incorporate the effect of rotation into analytic models [32-35]. In most of them, the simplifying assumptions made, such as analyzing of collisions of arbitraryly oriented, but non-rotating, molecules [32], or, on the contrary, considering only collisions of rapidly rotating "breathing spheres" (i.e. isotropic three-dimensional oscillators) [33-35], were unrealistic. In addition, the coupled effects of orientation of colliding partners, molecular rotation, and non-zero impact parameter collisions have been analyzed separately. Finally, the procedure of comparison between the experimental relaxation rates and the analytic rates corrected for non-collinear orientation and rotation, used by some authors to validate theoretically obtained values of the steric factors, is hardly conclusive. It such cases, the agreement obtained might well be due to the formal adjustment of the intermolecular potential parameters used, i.e. to a curve fitting. The only credible procedure for analytic model validation would be comparing its predictions with the results of three-dimensional numerical calculations made for the same potential energy surface.

The present work addresses development of a semiclassical analytic vibrational relaxation model that incorporates the effects of three-dimensional collisions and molecular rotation. As a first step, we analyze energy transfer in collisions between a diatomic molecule and an atom. The two main goals of this study are (i) analytic transition probabilities that must be in agreement with trajectory calculations and (ii) expressions for transition probabilities that can be easily incorporated in nonequilibrium kinetic models. Such a model gives new insight into mechanisms of vibrational relaxation, as well as bridging the gap between state-of-the-art theoretical scattering techniques and their use for practical applications.

2. Collision trajectories and transition probabilities

The method used in the present work is somewhat similar to the approach developed by Skrebkov and Smirnov [36], which is perhaps the most advanced of available analytic models. They calculated the trajectory of a rotating diatomic molecule colliding with an atom when all three atoms are moving in the same plane, and used classical mechanics perturbation theory to evaluate the average vibrational energy transmitted in a collision. They also assumed a local exponential dependence of the intermolecular potential on all collision coordinates q_i, $U(q_i) \sim \exp[-\alpha(q_i - q_{0i})]$, in the vicinity of the turning point. This constraint forces both the translational motion and the rotation to stop at the turning point, which makes the motion equations tractable but does not allow incorporation of molecular rotation in three dimensions. In the present work, we uncouple the translational motion and the three-dimensional rotation, assuming the latter to be unaffected by the collision, i.e. free. Then the only effect of rotation on the collision trajectory is the periodic modulation of the interaction potential. Note that the assumption of free rotation is quite similar to the basic assumption made in all semiclassical theories, which evaluate the translational-rotational trajectory uncoupled from the vibrational motion of the oscillator. Also, instead of relying on perturbation theory, we will use the exact semiclassical solution of the Schrodinger equation (the FHO theory [28-31]) to evaluate the vibrational transition probabilities. This will expand the applicability of the model to high collision energies and allow prediction of multi-quantum vibrational transition rates.

Let us analyze the dynamics of collisions between a rotating symmetric diatomic molecule and an atom. First consider a head-on (zero impact parameter) collision (see Fig. 1). For the pairwise atom-to-atom interaction described by a repulsive exponential function, $U_i(R_i) = A\exp(-\alpha R_i)$, where R_i is the distance between the atoms, the atom-molecule interaction potential can be written as follows:

$$U(R,r,\vartheta,\varphi) = 2Ae^{-\alpha R}\cosh\left[\frac{\alpha r}{2}\cos\vartheta\cos\varphi\right] \tag{3}$$

In Eq. (3), R is the center-of-mass distance, r is the separation of atoms in a molecule, ϑ is the rotation angle, and φ is the angle between the plane of rotation and the radius vector R (see Fig. 3). To derive Eq. (3), we used the approximation $(R^2 + r^2/4 + Rr\cos\vartheta)^{1/2} \approx R + r\cos\vartheta/2$. Let us assume that the rotation is free, that is, neither the magnitude nor the direction of the angular momentum vector change in a collision. That gives $\vartheta(t) = \vartheta_0 + \Omega t$, $\varphi(t) = \varphi_0$, where Ω is the constant angular velocity of molecular rotation, and the subscript "0" means "at the point of maximum interaction", where U is maximum. To calculate the semiclassical trajectory R(t), we assume $r(t)=r_e$, where r_e is the equilibrium atom separation, so that

$$\begin{aligned} U(R,r_e,t) &= 2Ae^{-\alpha R(t)}\cosh[d\cos(\vartheta_0 + \Omega t)\cos\varphi_0] \\ &= Be^{-\alpha\tilde{R}(t)}\frac{\cosh[d\cos(\vartheta_0 + \Omega t)\cos\varphi_0]}{\cosh[d\cos\vartheta_0\cos\varphi_0]}, \end{aligned} \tag{4}$$

where $d = \alpha r_e/2 \gtrsim 1$, $\tilde{R}(t) = R(t) - R_0$ and $B = 2A\exp(-\alpha R_0)\cdot\cosh[d\cos\vartheta_0\cos\varphi_0]$. One can see that the potential (4) consists of the exponential translational part modulated by the periodic rotational factor. If the rotation is not very rapid, the modulation can substantially change the shape of the time-dependent perturbation, $U(\tilde{R},t)$. The classical equation of motion for this potential, $m\ddot{\tilde{R}}(t) = -\frac{\partial U(\tilde{R},t)}{\partial\tilde{R}}$, can be easily solved if the rotation is slow, so that the potential $U(R,r_e,t) = U(\tilde{R},t)$ can be expanded near the point of maximum interaction, R_0,

$$\begin{aligned} m\ddot{\tilde{R}}(t) &\approx \alpha Be^{-\alpha\tilde{R}(t)}[1 - \tanh(d\cos\vartheta_0\cos\varphi_0)d\sin\vartheta_0\cos\varphi_0\cdot\Omega t] \\ &\approx \alpha Be^{-\alpha\tilde{R}(t)}[1 - g(\vartheta_0,\varphi_0)d\Omega t] \end{aligned} \tag{5}$$

where $g(\vartheta_0, \varphi_0) = \tanh(d\cos\vartheta_0\cos\varphi_0)d\sin\vartheta_0\cos\varphi_0 \approx \frac{\sqrt{2}}{2}\sin 2\vartheta_0\cos\varphi_0$, and m is the collision reduced mass. Solving Eq. (5), one obtains

$$e^{-\alpha\tilde{R}(t)} \approx \frac{1+g(\vartheta_0,\varphi_0)d\Omega t}{\cosh^2\left[\alpha t\sqrt{\frac{B}{2m}}\right]} \approx \frac{1}{\cosh^2\left[\alpha t\sqrt{\frac{B}{2m}}\right]}\frac{\cosh[d\cos\vartheta_0\cos\varphi_0]}{\cosh[d\cos(\vartheta_0+\Omega t)\cos\varphi_0]} \tag{6}$$

and

$$U(t) = \frac{B}{\cosh^2\left[\alpha t\sqrt{\frac{B}{2m}}\right]}; \quad B = U(0) \tag{7}$$

Note that the trajectory of Eq. (7) is identical to the well-known result of one-dimensional theory [37] if one takes parameter B (the maximum interaction energy) equal to the translational kinetic energy at infinity, $B=E_{tr}=mv_\infty{}^2/2$. In our case, however, B depends on the molecular orientation and its rotational energy and is not necessarily equal to E_{tr}. Indeed, the full derivative of the interaction energy given by Eq. (4) is

$$\frac{DU(\tilde{R}(t),t)}{Dt} = \frac{\partial U}{\partial\tilde{R}}\dot{\tilde{R}} + \frac{\partial U}{\partial t}; \quad B = \int_{-\infty}^{0}\frac{DU}{Dt}dt \tag{8}$$

In Eq. (8), the first term in the right-hand-side is the work of the potential force and the second is the interaction energy change due to the free rotation, which depends only on time. Using Eqs. (4,6,8), one can obtain an implicit expression for B,

$$B = E - E_{rot} - \frac{\xi}{2}g(\vartheta_0,\varphi_0)^2 E_{rot} + \sqrt{\xi}\cdot g(\vartheta_0,\varphi_0)\sqrt{2E_{rot}B}, \tag{9}$$

where $E=E_{tr}+E_{rot}$ is the total energy of a molecule at infinity, $E_{rot}=m_o\Omega^2r_e^2/2$ is its rotational energy, m_o is the oscillator reduced mass, and $2\xi=m/m_o$ is the ratio of the collision and oscillator reduced masses.

For non-zero impact parameter collisions, the trajectory can be found by taking into account only radial relative motion of the colliding partners, R(t), in the vicinity of the maximum interaction point, as shown in Fig. 2. Then the problem is reduced to the case considered above by replacing the kinetic energy $E-E_{rot}$ by the energy of the radial motion, $E_{rad}=(E-E_{rot})[1-b^2/R(t)^2]\cong(E-E_{rot})(1-b^2/R_0^2)$ (the so-called modified wavenumber approximation [34]). Here b is the impact parameter and R_0 is the "collision diameter" (the distance at the maximum interaction point). This approach is justifiable for short-range repulsive interactions when the energy transfer is determined by a small portion of the trajectory near the maximum interaction point [38]. Therefore Eq. (7) for the trajectory remains unchanged while parameter B becomes

$$B=(E-E_{rot})\left(1-\frac{b^2}{R_0^2}\right)-\frac{\xi}{2}g(\vartheta_0,\varphi_0)^2E_{rot}+\sqrt{\xi}\cdot g(\vartheta_0,\varphi_0)\sqrt{2E_{rot}B} \qquad (9a)$$

Introducing dimensionless parameters $\beta=B/E$, $\varepsilon=E_{rot}/E$, and $y=b^2/R_0^2$, and solving Eq. (9a) for $\gamma=\sqrt{\beta}$, one has

$$U(t)=\frac{E\gamma^2}{\cosh^2\left[\gamma\alpha t\sqrt{\frac{E}{2m}}\right]} \qquad (7a)$$

$$\gamma(\varepsilon,y,\vartheta_0,\varphi_0)=\sqrt{\beta}\approx\max\left[0,-\frac{\sin 2\vartheta_0\cos\varphi_0}{2}\sqrt{\xi\varepsilon}+\sqrt{(1-\varepsilon)(1-y)}\right] \qquad (10)$$

Eq. (7a) describes a parametric set of three-dimensional trajectories with the same total collision energy E and various values of rotational energy, impact parameter, and orientation of collision partners, characterized by a single factor $\gamma=(\varepsilon,y,\vartheta_0,\varphi_0)$, which is given by Eq. (10). The factor $E\gamma^2$ in Eq. (7a) can be interpreted as the effective collision energy. One can see that at

$\varepsilon=y=\vartheta_0=\varphi_0=0$, one has $\gamma=1$, $E=E_{tr}$, and the trajectory coincides with the one-dimensional result for a head-on collinear collision of a non-rotating molecule with an atom [37].

The applicability of Eqs. (7a,10) is limited to relatively slow molecular rotation by an approximation made in Eqs. (3,4), $g(\vartheta_0,\varphi_0)d\Omega\tau \lesssim 1$, where $\tau\sim 2/\alpha v_\infty$ is the time scale for the interaction energy change. Therefore the described approach is valid only if

$$\varepsilon = E_{rot}/E \lesssim \frac{1}{2}\frac{\left(1-y^2\right)}{\left(1-y^2/2\right)}, \tag{11}$$

so that the collision trajectory of a rapidly rotating molecule cannot be accurately predicted, especially at large impact parameters. However, the contribution of such collisions to the overall transition probability as a function of the total collision energy E is expected to be small. Indeed, for such collisions (i) the available translational energy of radial motion is small, $E_{tr}=E(1-b^2/R_0^2)-E_{rot}<<E$, and (ii) the potential energy surface of Eq. (4) becomes nearly isotropic due to the rapid rotation so that the "breathing sphere" model [34] become applicable. As is well known [39], the vibrational transition probabilities in slow repulsive collisions of "breathing spheres" (i.e. isotropic three-dimensional oscillators) drop exponentially as the collision energy E_{tr} decreases. Therefore, in the present work we disregard such collisions. Later we will show that this assumption is consistent with the results of the three-dimensional trajectory calculations.

Having calculated the free rotation collision trajectory (7a,10), now we can evaluate the semiclassical vibrational energy transfer probabilities P_{if}, where i and f are initial and final vibrational quantum numbers, respectively. For this we will use the FHO theory [28-31], a nonperturbative analytic model, originally developed for collinear collisions of a nonrotating diatomic molecule and an atom. This model is based on the exact solution of the Schrodinger equation for the intermolecular potential $U(R,r,\vartheta,\varphi)$ linearized in r and therefore takes into account the coupling of all vibrational quantum states during a collision. It is applicable up to high collision energies and vibrational quantum numbers, as well as for multiquantum transitions. The scaling law predicted by this model, i.e. the probability dependence on the vibrational quantum numbers, is independent of the potential and is given by the following relation [38,40,41]:

$$P_{if} \approx J_s^2\left(2\sqrt{n_s Q}\right) \approx \frac{(n_s)^s}{(s!)^2} Q^s \exp\left[-\frac{2n_s}{s+1} Q - \frac{n_s^2}{(s+1)^2 (s+2)} Q^2\right] \quad ,$$

$$s = |i-f| \quad , \quad n_s = \left[\frac{\max(i,f)!}{\min(i,f)!}\right]^{1/s} \tag{12}$$

In Eq. (12), J_s is the Bessel function of the sth order, and the potential-dependent parameter $Q=\Delta E/\hbar\omega$ is the average dimensionless energy (i.e. the average number of quanta) transferred to the initially nonvibrating classical oscillator in a collision [28,29]:

$$Q = \frac{\langle 1|\tilde{r}|0\rangle^2}{\hbar^2} \left| \int_{-\infty}^{\infty} \left(\frac{\partial U(\tilde{R},\tilde{r},t)}{\partial \tilde{r}} \right)_{\tilde{r}=0} e^{i\omega t} dt \right|^2 \tag{13}$$

In Eq. (13), $\tilde{r} = r - r_e$, and $\langle 1|\tilde{r}|0\rangle^2 = \dfrac{\hbar}{2m_0\omega}$ is the squared matrix element of the transition 0→1. Using Eqs. (4,7a), one obtains

$$\begin{aligned} Q(E,\varepsilon,y,\vartheta_0,\varphi_0) &= \frac{\langle 1|\tilde{r}|0\rangle^2}{\hbar^2} \frac{q(\vartheta_0,\varphi_0)^2 \alpha^2}{4} \left| \int_{-\infty}^{\infty} U(t) e^{i\omega t} dt \right|^2 \\ &\approx \frac{\theta' \xi}{4\theta} \frac{\cos^2\vartheta_0 \cos^2\varphi_0}{\sinh^2\left[\dfrac{\pi\omega}{\alpha u \gamma(\varepsilon,y,\vartheta_0,\varphi_0)}\right]} \end{aligned} \tag{14}$$

In Eq. (14), $q(\vartheta_0,\varphi_0) = \tanh(d\cos\vartheta_0\cos\varphi_0)\cos\vartheta_0\cos\varphi_0 \approx \cos\vartheta_0\cos\varphi_0$, $\omega=|E_f-E_f|/s\hbar$ is the average vibrational quantum for the transition i→f, $\theta' = \dfrac{4\pi^2\omega^2 m}{\alpha^2 k}$, $\theta = \dfrac{\hbar\omega}{k}$, and $u = \sqrt{2E/m}$. Note that two different symbols, i.e. ϑ and θ, are being used throughout the work for the rotation angle and the characteristic vibrational temperature, respectively. The product $u\gamma$ can be interpreted as an effective collision velocity. One can see that at $\varepsilon=y=\vartheta_0=\varphi_0=0$, one has $\gamma=1$, $E=E_{tr}$, $q(\vartheta_0.\varphi_0)\cong 1$, and Eq. (14) coincides with the one-dimensional probability of the single-quantum transition 0→1, predicted by the SSH theory [24]. The difference between the present Forced Harmonic Oscillator - Free Rotator (FHO-FR) model and the one-dimensional SSH theory result is that Eqs. (10,12,14) incorporate three-dimensional trajectories of rotating molecules as well as the coupling of vibrational states during a collision.

3. Comparison with trajectory calculations

To verify the accuracy of the present model, it has to be compared with three-dimensional semiclassical trajectory calculations for the atom-diatom collisions, for the potential energy surface given by Eq. (3). For this purpose, we have used the computer code ADIAV developed by Billing [42]. The code calculates classical translational-rotational collision trajectories and evaluates vibrational transition probabilities by solving a set of coupled equations for the time-dependent expansion coefficients of the vibrational wavefunction over a basis of stationary states of a molecule. In this section, calculations were made for collisions of an N_2 molecule and an atom of the same mass of $m_C=28$ amu, so that $\xi=m/2m_o=1$. The coupling matrix elements $\langle i|\tilde{r}|i\pm 1\rangle$ used by ADIAV were calculated for the frequency corrected harmonic oscillator (i.e. with harmonic wavefunctions but anharmonic energy spectrum), with up to 30 states used for the vibrational wavefunction expansion. The frequency corrected harmonic oscillator approximation also implies that parameter ω in the FHO-FR model is evaluated as the average vibrational quantum of a transition, i.e. $\omega=|E_i-E_f|/\hbar$. The N_2 vibrational quantum, the anharmonicity, and the equilibrium atom separation were taken to be $\omega_e=2359.6\ \mathrm{cm}^{-1}$, $\omega_e x_e=14.456\ \mathrm{cm}^{-1}$, and $r_e=1.094$ A. The intermolecular repulsive potential parameters used were $A=1730$ eV, and $\alpha=4.0\ A^{-1}$ [19].

The calculation results are summarized in Figs. 3-9. We emphasize that in the present work we will always compare the absolute values of the analytic FHO-FR probability and numerical ADIAV probability, respectively, evaluated for two identical potential energy surfaces. We will also use the one-dimensional, collinear-collision SSH probability $P_{10}^{SSH}(E)=\frac{\theta'\xi}{4\theta}\sinh^{-2}\left(-\frac{\pi\omega}{\alpha u}\right)$ only as a convenient scale factor. This procedure is more challenging than comparison of the two relative probabilities (i.e. analytic vs. numerical), both normalized on their respective values at some reference point, which is commonly used for validation of analytic rate models. For brevity, let us omit the subscript "0" remembering, however, that from now on the angles ϑ and φ are always evaluated at the maximum interaction point. Figure 3 shows the ratio of the three-dimensional FHO-FR transition probability $P_{10}(E,\varepsilon,y,\vartheta,\varphi)$ given by Eqs. (10,12,14) to the SSH probability $P_{10}^{SSH}(E)$, as a function of the rotation angle ϑ. All other collision parameters were held constant at $E=10^3$ cm^{-1}, $\varepsilon=E_{rot}/E=0.2$, $y=b^2/R_0^2=0$, $\varphi=0$. Also shown in Fig. 3 is the ratio of the ADIAV transition probability, evaluated for the same collision parameters, to the same factor $P_{10}^{SSH}(E)$. One can see that the FHO-FR probability peaks at somewhat different value of the rotation angle ($\theta=0.76\pi$ instead of 0.67π for the ADIAV probability). However, the maximum probability, which exceeds P_{10}^{SSH} by more than two orders of magnitude, is predicted quite accurately. Figure 4 shows the ratio of $P_{10}(E,\varepsilon,y,\varphi)/P_{10}^{SSH}$, averaged over the rotation angle ϑ in the range $[0,\pi]$, as a function of the angular momentum angle φ. In Fig. 4, again, $E=10^3$ cm^{-1}, $\varepsilon=0.2$, $y=0$. This time both the predicted optimum value of $\varphi=0$ and the maximum value of probability, which is about a factor of 20 greater than P_{10}^{SSH}, are in good agreement (within 30%) with the ADIAV probability, evaluated for the same collision parameters. The effect of rotational energy of a molecule is demonstrated in Fig. 5. One can see that the ratio $P_{10}(E,\varepsilon,y,\varphi)/P_{10}^{SSH}$, averaged over ϑ at $E=10^3$ cm^{-1}, $y=0$, $\varphi=0$ and shown as a function of $\varepsilon=E_{rot}/E$, peaks at $\varepsilon=0.2$, which is also consistent with predictions of ADIAV. Note that (i) the most efficient value of rotational energy is within the limits of applicability of the FHO-FR model, $\varepsilon \lesssim 1/2$, given by Eq. (11), and (ii) the ADIAV transition probability sharply drops at $\varepsilon \rightarrow 1$, as has been discussed in Section 2. The last result justifies neglecting rapidly rotating molecule collisions (see Section 2). Note that the observed decrease of the analytic FHO-FR probability at $\varepsilon \sim 1$ is merely an artifact since the assumption of the slow rotation is no longer valid at these conditions. However, this behavior simplifies the formal analytic integration over the rotational energies, when necessary. Finally, in Fig. 6, the ratio $P_{10}(E,\varepsilon,y,\varphi)/P_{10}^{SSH}$, averaged over ϑ at $E=10^3$ cm^{-1}, $\varepsilon=0.2$, $\varphi=0$ is plotted versus the impact parameter b. In this case, again, the optimum value of the impact parameter, b=0, and the maximum value of the probability agree well with numerical calculations using ADIAV. The fact that the ratio $P_{10}(E,\varepsilon,y,\varphi)/P_{10}^{SSH}$ greatly exceeds unity near its maximum at the "optimum configuration" point $\varepsilon=0.2$, $b=0$, $\vartheta=3\pi/4$, $\varphi=0$ demonstrates that collisions with these values of parameters are much more efficient for vibrational energy transfer than head-on collinear collisions of a non-rotating molecule. This occurs because for the optimum configuration the force perturbing the vibrational motion of the oscillator, $\left(\frac{\partial U(\tilde{R},\tilde{r},t)}{\partial\tilde{r}}\right)_{\tilde{r}=0}$, drops the most steeply near the maximum interaction point at t=0, due to its modulation by rotation. This makes the perturbation more "abrupt" and increases the high-frequency components of its Fourier integral, given by Eq. (13). The optimum configuration is realized when $\frac{D^2}{Dt^2}\left\{\left(\frac{\partial U(\tilde{R},\tilde{r},t)}{\partial\tilde{r}}\right)_{\tilde{r}=0}\right\}_{t=0}$ is maximum. Obviously, to accurately predict the transition probability, it is enough to predict its behavior in the vicinity of the optimum configuration point.

Calculations made at the higher collision energy of $E=10^4$ cm^{-1} also showed very good agreement between the FHO-FR and the ADIAV probabilities P_{10} and provided results similar to shown in Figs. 3-6, the only difference being that the maximum at the optimum configuration point becomes less pronounced. Finally, comparison of the two-quantum transition probabilities P_{20} demonstrated the same kind of agreement (i.e. within a few tens of percent).

To compare the FHO-FR and ADIAV transition probabilities as functions of only the total collision energy E, we numerically averaged the probabilities $P_{if}(E,\varepsilon,y,\vartheta,\varphi)$, given by Eqs. (10,12,14), over the values of rotational energy, impact parameter, and orientation angles, using 10^5 points randomly chosen in phase space:

$$P_{if}(E)=\int_0^1 d\varepsilon\int_0^1 dy\int_0^\pi d\vartheta\int_0^\pi d\varphi\cdot P_{if}(E,\varepsilon,y,\vartheta,\varphi) \tag{15}$$

The respective ADIAV transition probabilities in a collision energy range $E=10^3$-10^6 cm^{-1} were obtained by Monte Carlo averaging over 1000 randomly chosen trajectories with the same value of E, which provided 10-20% accuracy. The initial separation between a molecule and an atom was 15 A, and the maximum impact parameter was 2.5 A.

First, we compared the Monte Carlo averaged ADIAV probabilities with two analytic models, both based on one-dimensional collinear-collision trajectories, i.e. the SSH theory [24] and the FHO model [28,29]. Figure 7 shows that the predictions of both these models significantly disagree with the trajectory calculations by ADIAV. At the low collision energies, the agreement might be somewhat improved by introducing a constant corrective steric factor, which is a rather commonly used procedure. However, one can see from Fig. 7 that at high collision energies, both these models completely break down. It is not surprising that the SSH theory fails because it is based on first-order perturbation theory and cannot be used for calculations of large transition probabilities. The only reason for the breakdown of the nonperturbative FHO model, however, is that it does not consider realistic three-dimensional collision trajectories. Indeed, the FHO model predicts a sharp decrease of the probabilities at high energies. However, even if the collision energy is large, there are always some configurations of the collision parameters, ε, y, ϑ, and φ, for which the parameter γ in Eqs. (10,14) is small (e.g. for ε~0 and y~1, γ~0). For these configurations, the effective collision velocity in Eq. (14), $u\gamma$, is much smaller and therefore the transition probability is much greater. For this reason the incorporation of three-dimensional trajectories into the FHO model, carried out in Section 2, is expected to diminish or even completely remove the probability drop at high collision energies, thereby improving the agreement with the trajectory calculations.

This qualitative conclusion is confirmed by Fig. 8 which compares the three-dimensional FHO-FR transition probabilities P_{i0}, using the same FHO scaling law of Eq. (12), with the trajectory calculations by ADIAV. One can see the remarkable agreement in the entire collision energy range considered, both for single-quantum and multi-quantum processes, up to s=5. Further calculations showed that the FHO-FR model accurately predicts the probabilities of the processes where as many as 10 quanta are transmitted. Beyond this point running ADIAV for a large number of trajectories ($N \sim 10^3$) becomes fairly time consuming because of the increasing number of coupled equations involved (50 to 60 for s=10). Figure 9 also demonstrates that the agreement is also very good even for high vibrational quantum numbers, i~40. In particular, this proves that the FHO scaling law of Eq. (12), developed for harmonic oscillator, is also quite accurate for the frequency corrected oscillator used in the present calculations by ADIAV.

Note that the approximation $(R^2 + r^2/4 + Rr\cos\vartheta)^{1/2} \approx R + r\cos\vartheta/2$, used to derive Eq. (3) becomes rather crude for collision energies $E \sim 10^5$ cm^{-1}. On the other hand, trajectory calculations by ADIAV without using this approximation still show very little difference from the approximate analytic model even at $E\sim10^6$ cm^{-1}. In addition, collisions with energies $E>10^5$ cm^{-1} affect the thermally averaged relaxation rates only at extremely high temperatures, $T>10^5$ K.

The results of the model validation calculations discussed above demonstrate that the analytic FHO-FR formulae given by Eqs. (10,12,14) accurately predict the transition probability dependence on all collision parameters such as total energy, molecular orientation during the collision, rotational energy, and impact parameter. The model is applicable in a very wide range of collision energies and vibrational quantum numbers, as well as for processes of transfer of many vibrational quanta. The last result also allows using the FHO-FR model for the accurate prediction of the rates of molecular dissociation from low vibrational levels by a single collision. Thus, taking into account (i) modulation of the interaction potential by the molecular rotation which is assumed to be free, (ii) non-zero impact parameters collisions using the modified wavenumber approximation, and (iii) many-state coupling using the FHO model, permits capturing the principal mechanism of molecule-to-atom vibrational energy transfer and gives an accurate three-dimensional analytic rate model.

4. Averaging the probabilities and discussion

To make the FHO-FR model useful for practical calculations, we have to find the transition probabilities as functions of only total collision energy E, that is to analytically evaluate the integral of Eq. (15). This integral can be calculated by the steepest descent method. First, let us rewrite Eq. (14) as follows:

$$\begin{aligned} Q^s(E,\varepsilon,y,\vartheta,\varphi) &= \frac{\theta'\xi}{\theta}\exp\left[2s\cdot\ln(\cos\vartheta\cos\varphi)-\frac{2\pi\omega s}{\alpha u\gamma(\varepsilon,y,\vartheta,\varphi)}\right] \\ &= \frac{\theta'\xi}{\theta}\exp[G(\varepsilon,y,\vartheta,\varphi)] \end{aligned} \qquad (16)$$

The approximation $\sinh(x)\cong e^x/2$ made in Eq. (16) is very accurate except for very high collision energies such that $x=\pi\omega/\alpha u\gamma\geq1$. Second, from Eqs. (10,12,16) we have to determine the optimum configuration of parameters ε, y, ϑ, φ, for which the probability P_{if} of Eq. (12) reaches maximum at a given total energy E. One can see that if $Q \le s^{th}$, such as

$$s^{th} = \frac{(s+1)(s+2)}{2n_s}\left(\sqrt{\frac{3s+2}{s+2}} - 1\right) \quad , \tag{17}$$

this occurs when both Q in Eq. (12) and $G \sim s \cdot \ln Q$ in Eq. (16) are maximum. If Q can exceed s^{th}, P_{if} always reaches maximum at some Q^* such as $Q^* = s^{th}$. The superscript "*" will denote the optimum configuration parameters through the remainder of this chapter.

If $Q \le s^{th}$, the unique optimum configuration is

$$\cos^2 \vartheta^* = \begin{cases} \dfrac{1+\sqrt{1+8/a}}{4}, \; a = \dfrac{\pi\omega}{\alpha u}\xi \ge 1 \\ 1, \; a < 1 \end{cases} ; \varphi^* = 0 ; y^* = 0 ; \varepsilon^* = \frac{\xi \sin^2 2\vartheta^*}{4 + \xi \sin^2 2\vartheta^*} ;$$

$$\gamma^* = \sqrt{1 + \xi \sin^2 2\vartheta^* / 4} \tag{18}$$

To avoid cumbersome calculations, from now on we will concentrate on a separate analysis of the two specific cases of Eq. (18), first corresponding to the collisions of a molecule with a heavy atom ($\xi = m/2m_o \sim 1$), such as N_2-Ar,

$$\vartheta^* = \frac{3\pi}{4}; \quad \varphi^* = 0; \quad y^* = 0; \quad \varepsilon^* = \frac{\xi}{4+\xi}; \quad \gamma^* = \sqrt{1+\xi/4}$$
$$\text{if} \quad a = \frac{\pi\omega}{\alpha u}\xi >> 1 \quad , \tag{18a}$$

and second that applies to the collisions of a molecule with a light atom ($\xi = m/2m_o << 1$), such as N_2-He,

$$\vartheta^* = 0; \quad \varphi^* = 0; \quad y^* = 0; \quad \varepsilon^* = 0; \quad \gamma^* = 1$$
$$\text{if} \quad a = \frac{\pi\omega}{\alpha u}\xi \lesssim 1 \tag{18b}$$

At the same collision energy, the values of parameter $a=\pi\omega\xi/\alpha u$ for these two cases differ by about a factor of 10, being a=33.6 and a=3.3 at $E=10^3$ cm^{-1}, respectively. One can see both the similarities and the qualitative difference between these two cases. In both cases, zero impact parameter collisions ($y^*=0$) are most efficient for the vibrational energy transfer. However, in the first case the probability reaches maximum for a non-collinear collision ($\vartheta^*=3\pi/4$) of a rotating diatomic molecule ($\varepsilon^*=E_{rot}/E=0.2$ for $\xi=1$) with an atom, when the angular momentum vector is perpendicular to the radius vector **R** near the point of maximum interaction ($\varphi^*=0$, see Fig. 1). On the other hand, in the second case the most efficient configuration is a head-on collision of a non-rotating molecule. The maximum probability for these two optimum configurations, P_{if}^*, is given by Eq. (12), where now

$$Q^* = \frac{1}{2}\frac{\theta'\xi}{\theta}\exp\left[-\frac{2\pi\omega}{\alpha u\sqrt{1+\xi/4}}\right] \tag{19a}$$

and

$$Q^* = \frac{\theta'\xi}{\theta}\exp\left[-\frac{2\pi\omega}{\alpha u}\right] \quad , \tag{19b}$$

respectively.

Expanding the probability of Eq. (12) in a series near the optimum configuration point ε^*, y^*, ϑ^*, φ^*, for the two cases described by Eqs. (18a,18b), and formally extending the integration limits to infinity, one obtains for $Q \ll s^{th}$

$$\begin{aligned} P_{if}(E, Q \ll s^{th}) &\approx P^*_{if} \int_{-\infty}^{\infty} e^{\frac{G''^*_{\varepsilon}\tilde{\varepsilon}^2}{2}} d\tilde{\varepsilon} \int_{0}^{\infty} e^{G'^*_{y}\tilde{y}} d\tilde{y} \int_{-\infty}^{\infty} \frac{e^{\frac{G''^*_{\vartheta}\tilde{\vartheta}^2}{2}}}{\pi} d\tilde{\vartheta} \int_{-\infty}^{\infty} \frac{e^{\frac{G''^*_{\varphi}\tilde{\varphi}^2}{2}}}{\pi} d\tilde{\varphi} \\ &= P^*_{if} \underbrace{\sqrt{\frac{\alpha u \xi}{\omega s \gamma^{*3}}}}_{\varepsilon} \underbrace{\frac{\alpha u \gamma^{*3}}{\pi \omega s}}_{y} \underbrace{\frac{1}{\pi}\sqrt{\frac{\alpha u \gamma^{*3}}{\pi \omega s \xi}}}_{\theta} \underbrace{\frac{1}{\pi}\sqrt{\frac{4\alpha u \gamma^{*3}}{\pi \omega s \xi}}}_{\varphi} \\ &= P^*_{if} \frac{2 \quad (1+\xi/4)^{9/4}}{\sqrt{\pi} \quad \sqrt{\xi}} \frac{1}{s^{5/2}} \left(\frac{\alpha u}{\pi \omega}\right)^{5/2} \approx 2P^*_{if} \frac{1}{s^{5/2}} \left(\frac{\alpha u}{\pi \omega}\right)^{5/2} \end{aligned} \tag{20a}$$

and

$$\begin{aligned} P_{if}(E, Q \ll s^{th}) &\approx P^*_{if} \int_{0}^{\infty} e^{G'^*_{\varepsilon}\tilde{\varepsilon}} d\tilde{\varepsilon} \int_{0}^{\infty} e^{G'^*_{y}\tilde{y}} d\tilde{y} \int_{-\infty}^{\infty} \frac{e^{\frac{G''^*_{\vartheta}\tilde{\vartheta}^2}{2}}}{\pi} d\tilde{\vartheta} \int_{-\infty}^{\infty} \frac{e^{\frac{G''^*_{\varphi}\tilde{\varphi}^2}{2}}}{\pi} d\tilde{\varphi} \\ &= P^*_{if} \underbrace{\frac{\alpha u}{\pi \omega s}}_{\varepsilon} \underbrace{\frac{\alpha u}{\pi \omega s}}_{y} \underbrace{\frac{1}{\pi}\sqrt{\frac{\pi}{s}}}_{\theta} \underbrace{\frac{1}{\pi}\sqrt{\frac{\pi}{s}}}_{\varphi} \\ &= P^*_{if} \frac{1}{\pi} \frac{1}{s^3} \left(\frac{\alpha u}{\pi \omega}\right)^2 \end{aligned} \tag{20b}$$

In Eqs. (20a,20b), $\tilde{\varepsilon} = \varepsilon - \varepsilon^*, \tilde{y} = y - y^*, \tilde{\vartheta} = \vartheta - \vartheta^*, \tilde{\varphi} = \varphi - \varphi^*$.

For Q=s^{th}, the maximum value of the probability at the optimum configuration point given by Eqs. (18a,18b) is the same both for relaxation by a heavy and by a light atom,

$$P_{if}{}^* \approx \frac{s^s}{s!} \exp(-s) \quad , \tag{21}$$

and expression for the transition probability modifies:

$$
\begin{aligned}
P_{if}(E,Q=s^{th}) &\approx P_{if}^{*}\int_{0}^{\infty} e^{\frac{s\left(\ln Q-Q/s^{th}\right)_{y}^{''*}\tilde{y}^{2}}{2}}\,d\tilde{y}\,\frac{1}{\pi^{2}}\prod_{\tilde{z}=\tilde{\varepsilon},\tilde{\vartheta},\tilde{\varphi}}\int_{-\infty}^{\infty} e^{\frac{s\left(\ln Q-Q/s^{th}\right)_{z}^{IV*}\tilde{z}^{4}}{24}}\,d\tilde{z}\\
&= P_{if}^{*}\underbrace{\left(\frac{\alpha u}{\pi\omega\sqrt{s}}\right)\gamma^{*3}\sqrt{\frac{\pi}{2}}}_{y}\underbrace{\left(\frac{\alpha u}{\pi\omega\sqrt{s}}\right)^{1/2}\frac{\left(\frac{2\xi^{2}}{\gamma^{*6}}\right)^{1/4}\Gamma\left(\frac{1}{4}\right)}{2}}_{\varepsilon}\\
&\quad\times\underbrace{\left(\frac{\alpha u}{\pi\omega\sqrt{s}}\right)^{1/2}\frac{\left(\frac{2\gamma^{*6}}{\xi^{2}}\right)^{1/4}\Gamma\left(\frac{1}{4}\right)}{2\pi}}_{\theta}\underbrace{\left(\frac{\alpha u}{\pi\omega\sqrt{s}}\right)^{1/2}\frac{\left(\frac{32\gamma^{*6}}{\xi^{2}}\right)^{1/4}\Gamma\left(\frac{1}{4}\right)}{2\pi}}_{\varphi}\\
&= P_{if}^{*}\,\frac{\Gamma^{3}\left(\frac{1}{4}\right)}{2^{7/4}\pi^{3/2}}\,\frac{(1+\xi/4)^{9/4}}{\sqrt{\xi}}\,\frac{1}{s^{5/4}}\left(\frac{\alpha u}{\pi\omega}\right)^{5/2}\approx 4P_{if}^{*}\,\frac{1}{s^{5/4}}\left(\frac{\alpha u}{\pi\omega}\right)^{5/2}
\end{aligned}
\tag{22a}
$$

and

$$
\begin{aligned}
P_{if}(E,Q=s^{th}) &\approx P_{if}^{*}\prod_{\tilde{z}=\tilde{y},\tilde{\varepsilon}}\int_{0}^{\infty} e^{\frac{s\left(\ln Q-Q/s^{th}\right)_{z}^{''*}\tilde{z}^{2}}{2}}\,d\tilde{z}\,\frac{1}{\pi^{2}}\prod_{\tilde{z}=\tilde{\vartheta},\tilde{\varphi}}\int_{-\infty}^{\infty} e^{\frac{s\left(\ln Q-Q/s^{th}\right)_{z}^{IV*}\tilde{z}^{4}}{24}}\,d\tilde{z}\\
&= P_{if}^{*}\underbrace{\left(\frac{\alpha u}{\pi\omega}\right)\sqrt{\frac{\pi}{2s}}}_{y}\underbrace{\left(\frac{\alpha u}{\pi\omega}\right)\sqrt{\frac{\pi}{2s}}}_{\varepsilon}\underbrace{\left(\frac{2}{s}\right)^{1/4}\frac{\Gamma\left(\frac{1}{4}\right)}{2\pi}}_{\vartheta}\underbrace{\left(\frac{2}{s}\right)^{1/4}\frac{\Gamma\left(\frac{1}{4}\right)}{2\pi}}_{\varphi}\\
&= P_{if}^{*}\,\frac{\Gamma^{2}\left(\frac{1}{4}\right)}{4\sqrt{2}\pi}\,\frac{1}{s^{3/2}}\left(\frac{\alpha u}{\pi\omega}\right)^{2}\cong 2P_{if}^{*}\,\frac{1}{\pi}\,\frac{1}{s^{3/2}}\left(\frac{\alpha u}{\pi\omega}\right)^{2}
\end{aligned}
\tag{22b}
$$

One can see that the expressions for the transition probabilities $P_{if}(E)$ in Eqs. (20,22) each contain a product of four factors due to integration over the collision parameters, y, ε, ϑ, and φ. For modeling of flows with rotational disequilibrium one can also obtain the probabilities as functions of both total collision energy and rotational energy, $P_{if}(E,\varepsilon)$, by skipping the integration over ε. The accuracy of the approximate integration in Eqs. (20,22) is 50%-100% compared with numerical integration in Eq. (15). Spreading of the probability maximum near the optimum configuration point is the main reason causing the accuracy to become somewhat worse as the collision energy increases.

If $Q>s^{th}$, the optimum configuration of collision parameters is no longer unique and cannot be found in closed analytic form. However, the asymptotic behavior of the probability at $Q>>s^{th}$ can be roughly estimated using the following simple argument. At high collision energies, the multiple optimum configurations are realized at $Q^{*}=s^{th}<<Q$, and therefore at $\gamma^{*}<<1$. Assuming the values of $\gamma\in[0,\sqrt{1+\xi/4}]$ to be approximately equiprobable, one can write

$$\begin{aligned} P_{if}(E, Q \gg s^{th}) &\approx P_{if}^{*}\int_{0}^{\infty} e^{\frac{s\left(\ln Q - Q/s^{th}\right)''^{*}_{\gamma}\tilde{\gamma}^{2}}{2}}\, d\tilde{\gamma} \\ &\approx P_{if}^{*}\,\frac{1}{\sqrt{s}}\left(\frac{\alpha u \gamma}{\pi\omega}\right)^{*} = \text{const} \end{aligned} \tag{23}$$

In Eq. (23), $\tilde{\gamma}=\gamma-\gamma^{*}$, $(\alpha u\gamma/\pi\omega)^{*}$ denote the multiple points where $Q=Q^{*}=s^{th}$, and P_{if}^{*} is given by Eq. (21).

Finally, the following two interpolation formulae bridge the gap between the three specific cases covered by Eqs. (20,22,23) and provide fairly accurate expressions for the transition probabilities in the entire range of collision energies considered, $E=10^{2}$-10^{6} cm^{-1}.

$$P_{if}(E) \approx \begin{cases} 2\,s^{-\frac{5}{2}+\frac{5\lambda}{4}} \left(\dfrac{\alpha u}{\pi\omega}\right)^{5/2} \\ \qquad \times \dfrac{(n_s)^s}{(s!)^2} Q^{*s} \exp\left[-\dfrac{2n_s}{s+1} Q^* - \dfrac{n_s^2}{(s+1)^2 (s+2)} Q^{*2}\right] \;, \quad \lambda = \dfrac{Q^*}{s^{th}} \le 1 \\ 2^{\frac{1}{\lambda}} s^{-\frac{1}{2}-\frac{3}{4\lambda}} \left[\dfrac{1}{2}\ln\left(\dfrac{\theta'\xi}{2s^{th}\theta}\right)\right]^{-1-\frac{3}{2\lambda}} \\ \qquad \times \dfrac{s^s}{s!} \exp(-s) \;, \quad \lambda = \dfrac{Q^*}{s^{th}} > 1 \end{cases} \tag{24a}$$

$$P_{if}(E) \approx \begin{cases} \dfrac{1}{\pi} s^{-3+\frac{3\lambda}{2}} \left(\dfrac{\alpha u}{\pi\omega}\right)^{2} \\ \qquad \times \dfrac{(n_s)^s}{(s!)^2} Q^{*s} \exp\left[-\dfrac{2n_s}{s+1} Q^* - \dfrac{n_s^2}{(s+1)^2 (s+2)} Q^{*2}\right] \;, \quad \lambda = \dfrac{Q^*}{s^{th}} \le 1 \\ \dfrac{1}{\pi^{\frac{1}{\lambda}}} s^{-\frac{1}{2}-\frac{1}{\lambda}} \left[\dfrac{1}{2}\ln\left(\dfrac{\theta'}{s^{th}\theta}\right)\right]^{-1-\frac{1}{\lambda}} \\ \qquad \times \dfrac{s^s}{s!} \exp(-s) \;, \quad \lambda = \dfrac{Q^*}{s^{th}} > 1 \end{cases} \tag{24b}$$

In Eqs. (24a,24b), factors s^{th} and Q^* are given by Eqs. (17,19a,19b). Figs. (10,11) compare the probabilities of Eqs. (24a,24b) with the trajectory calculations by ADIAV for collisions of N_2 molecule with a heavy atom (Ar) and a light atom (He), respectively. The potential used is the same as in Section 2. One can see that the accuracy of the analytic probabilities is typically within a factor of 2. Eqs. (24a,24b) can be used in the direct Monte Carlo modeling of strongly nonequilibrium flows of rarefied gases, for example, behind strong bow shocks [43].

Thermally averaged relaxation rate coefficients $k_{if}(T)$ can be determined by averaging of the transition cross-sections over the Boltzmann distribution [42]:

$$k_{if}(T) = \langle u \rangle \int_0^{\infty} \sigma_{if}(\overline{E}) \exp\left(-\frac{\overline{E}}{T}\right) d\left(\frac{\overline{E}}{T}\right) = \pi R_0^2 \langle u \rangle \int_0^{\infty} \left(\frac{\overline{E}}{T}\right)^2 P_{if}(\overline{E}) \exp\left(-\frac{\overline{E}}{T}\right) d\left(\frac{\overline{E}}{T}\right) \qquad (25)$$

In Eq. (25), $\langle u \rangle = \left(\frac{8kT}{\pi m}\right)^{1/2}$, $\overline{E} = E + (E_f - E_i)/2 + (E_f - E_i)^2/16E$ is the symmetrized collision energy [42], $\sigma_{if}(\overline{E})$ is the cross-section, and $P_{if}(\overline{E})$ is the transition probability given by Eq. (15). The factor $\pi R_0^2 \cdot (\overline{E}/T)^2$ in the expression for the cross-section appears due to integration over the values of orbital kinetic energy (or orbital angular momentum) and rotational energy (or rotational angular momentum) [42]. The maximum interaction distance R_0 is found as $U(R_0)=kT$, $R_0 \cong 2.5$ A at $T \sim 10^4$ K. Then the effective cross section for elastic collisions is $\langle\langle \sigma_{el} \rangle\rangle = \frac{k_{el}(T)}{\langle u \rangle} = 2\pi R_0^2 \approx 40A$, and the gas kinetic collision frequency is $Z = 2\pi R_0^2 \langle u \rangle$.

Evaluation of the integral in Eq. (25) at $Q \leq s^{th}$ yields

$$\begin{aligned} k_{if}(T) = \pi R_0^2 \langle u \rangle \frac{(n_s)^s}{(s!)^2} \frac{4(1+\xi/4)}{\sqrt{3\xi}} \left(\frac{\theta'\xi}{2\theta}\right)^s C_{VT}^{15/2} s^{\frac{5\lambda}{4}} \\ \times \exp\left[-\left(\frac{1}{C_{VT}} + \frac{C_{VT}^2}{2}\right)\left(\frac{\theta' s^2}{(1+\xi/4)T}\right)^{1/3} - s\left(1 - C_{VT}^3\right)\right] \\ \times \exp\left\{\frac{\theta s}{2T}\left(1 - \frac{\theta}{4T}\left(\frac{(1+\xi/4)T}{\theta' s^2}\right)^{1/3}\right)\right\}, \end{aligned} \qquad (26a)$$

$$\lambda = \frac{1}{s^{th}} \frac{\theta'\xi}{2\theta} \exp\left[-\frac{1}{C_{VT}}\left(\frac{\theta'}{(1+\xi/4)sT}\right)^{1/3}\right]$$

and

$$k_{if}(T) = \pi R_0^2 \langle u \rangle \frac{(n_s)^s}{(s!)^2} \frac{1}{\pi s} \sqrt{\frac{2\pi}{3}} \left(\frac{\theta'}{\theta} \right)^s \left(\frac{\theta' s^2}{T} \right)^{1/6} C_{VT}^7 s^{\frac{3\lambda}{2}}$$

$$\times \exp\left[-\left(\frac{1}{C_{VT}} + \frac{C_{VT}^2}{2} \right) \left(\frac{\theta' s^2}{T} \right)^{1/3} - s\left(1 - C_{VT}^3\right) \right]$$

$$\times \exp\left\{ \frac{\theta s}{2T} \left(1 - \frac{\theta}{4T} \left(\frac{T}{\theta' s^2} \right)^{1/3} \right) \right\}, \qquad (26b)$$

$$\lambda = \frac{1}{s^{th}} \frac{\theta'}{\theta} \exp\left[-\frac{1}{C_{VT}} \left(\frac{\theta'}{sT} \right)^{1/3} \right]$$

for the collisions with a heavy and a light atom, respectively. The last exponential factor in Eqs. (26a,26b) originates from the symmetrization of collision energy in Eq. (25). Following the procedure suggested in [42], we evaluate the rates of exothermic processes. The endothermic rates can be found simply as $k_{endo} = k_{exo} \cdot \exp(-\theta s / T)$. Eqs. (26a,26b) are valid only if $T \leq T^{th}$, where T^{th} is the threshold temperature that corresponds to the "switching" from the unique to the multiple optimum configuration regime,

$$T^{th} = \frac{\theta'}{\frac{15}{2}(1 + \xi/4) \ln^2 \left[\frac{\theta' \xi}{2 s^{th} \theta (1 + \xi/4)} \right]} \qquad (27a)$$

and

$$T^{th} = \frac{\theta'}{7 \ln^2 \left[\frac{\theta'}{s^{th} \theta} \right]} \qquad (27b)$$

Factor C_{VT} in Eqs. (26a,26b) determines the collision energy at which the integrand in Eq. (25) reaches maximum, and can be found by solving transcendental equations,

$$C_{VT} = \left\{ 1 - \frac{1}{s^{th}} \frac{\theta'\xi}{2\theta} \exp\left[-\frac{1}{C_{VT}} \left(\frac{\theta'}{(1+\xi/4)sT} \right)^{1/3} \right] + \frac{15 C_{VT}}{2} \left(\frac{(1+\xi/4)T}{\theta' s^2} \right)^{1/3} \right\}^{1/3} \tag{28a}$$

and

$$C_{VT} = \left\{ 1 - \frac{1}{s^{th}} \frac{\theta'}{\theta} \exp\left[-\frac{1}{C_{VT}} \left(\frac{\theta'}{sT} \right)^{1/3} \right] + 7 C_{VT} \left(\frac{T}{\theta' s^2} \right)^{1/3} \right\}^{1/3} , \tag{28b}$$

respectively. The deviation of C_{VT} from unity characterizes the influence of multi-state coupling effects. At small values of C_{VT}, we are far from the first-order perturbation limit. Eqs. (28a,28b) both have a single root and in practical calculations can be easily solved by the Newton method. From Eq. (28b), one can see that the most efficient dimensionless collision energy decreases with temperature from $\frac{\overline{E}^*}{kT} = \frac{1}{2}\left(\frac{\theta' s^2}{T}\right)^{1/3} \gg 1$ at $T << T^{th}$ to $\frac{\overline{E}^*}{kT} = \frac{7}{2}$ at $T = T^{th}$ (a similar relation can be obtained from Eq. (28a)). In other words, at the high temperatures such as $T > T^{th}$, vibrational energy transfer mainly occurs in collisions at nearly thermal energies.

At $Q > s^{th}$ (i.e. at $T > T^{th}$), the result of integration is

$$k_{if}(T) = 2\pi R_0^2 \langle u \rangle \frac{s^s}{s!} \exp(-s) \frac{1}{s^{\frac{1}{2}+\frac{3}{4\lambda}}} \left[\frac{1}{2} \ln\left(\frac{\theta'\xi}{2 s^{th} \theta} \right) \right]^{-1-\frac{3}{2\lambda}}$$

$$\times \exp\left\{ \frac{\theta s}{2T} \left(1 - \frac{\theta}{30T} \right) \right\} , \tag{29a}$$

$$\lambda^2 = \frac{1}{s^{th}} \frac{\theta'\xi}{2\theta} \exp\left[-\left(\frac{2\theta'}{15(1+\xi/4)T} \right)^{1/2} \right]$$

and

$$k_{if}(T) = 2\pi R_0^2 \langle u \rangle \frac{s^s}{s!} \exp(-s) \frac{1}{s^{\frac{1}{2}+\frac{1}{\lambda}}} \left[\frac{1}{2} \ln\left(\frac{\theta'}{s^{th}\theta} \right) \right]^{-1-\frac{1}{\lambda}}$$

$$\times \exp\left\{ \frac{\theta s}{2T} \left(1 - \frac{\theta}{28T} \right) \right\} \quad , \tag{29b}$$

$$\lambda^2 = \frac{1}{s^{th}} \frac{\theta'}{\theta} \exp\left[-\left(\frac{\theta'}{7T} \right)^{1/2} \right]$$

From Eqs. (29a,29b), one can see that the asymptotic behavior of the rate coefficients at $T >> T^{th}$ is $k_{if}(T) \sim const \cdot Z$. This again shows that the use of steric factors with the available one-dimensional rate models at high temperatures is completely erroneous (see also Fig. 7).

At low temperatures, such as $T << T^{th}$, one has $C_{VT} \cong 1$, and the expressions for the relaxation rates simplify:

$$k_{if}(T) = 2\pi R_0^2 \langle u \rangle \frac{(n_s)^s}{(s!)^2} \frac{4(1+\xi/4)}{\sqrt{3\xi}} \left(\frac{\theta'\xi}{2\theta} \right)^s \exp\left[-\frac{3}{2} \left(\frac{\theta' s^2}{(1+\xi/4)T} \right)^{1/3} \right]$$

$$\times \exp\left\{ \frac{\theta s}{2T} \left(1 - \frac{\theta}{4T} \left(\frac{(1+\xi/4)T}{\theta' s^2} \right)^{1/3} \right) \right\} \tag{30a}$$

and

$$k_{if}(T) = 2\pi R_0^2 \langle u \rangle \frac{(n_s)^s}{(s!)^2} \frac{1}{\pi s} \sqrt{\frac{2\pi}{3}} \left(\frac{\theta'}{\theta} \right)^s \left(\frac{\theta' s^2}{T} \right)^{1/6} \exp\left[-\frac{3}{2} \left(\frac{\theta' s^2}{T} \right)^{1/3} \right]$$

$$\times \exp\left\{ \frac{\theta s}{2T} \left(1 - \frac{\theta}{4T} \left(\frac{T}{\theta' s^2} \right)^{1/3} \right) \right\} \tag{30b}$$

One can see that at s=1 (for single-quantum processes) the latter equation exactly coincides with the one-dimensional SSH formula with a steric factor of $1/\pi$. This is not surprising since we have already seen that for relaxation by a light atom, the head-on collisions of a non-rotating molecule are the most efficient. In this case the only difference from the one-dimensional theory originates from the non-collinear orientation of a molecule. As is well known, this results in appearance of a 1/3 steric factor in the SSH formula [24]. However, for the relaxation by a heavy atom, the incorporation of rotation and non-zero impact parameter collisions change both the pre-exponential factor and the exponential dependence of the rate (see Eq. (30a)). In this case, the one-dimensional SSH formula cannot match either the FHO-FR model or the results of trajectory calculations by using a single temperature-independent steric factor. It is still possible to enforce the agreement between the SSH theory and the three-dimensional models, within a relatively narrow temperature range, by introducing a steric factor and varying the repulsive potential parameter α at the same time. This procedure, however, should be regarded as nothing more than a curve fitting to available three-dimensional data.

The values of the threshold temperature for O_2-Ar collisions, given by Eqs. (27), change from $T^{th}=9200$ K for the transition $1\to0$ to $T^{th}=1400$ K for the transition $30\to29$. This shows that both Eq. (26) and Eq. (29) must be used for the high-temperature vibrational relaxation rate calculations. Figs. 12, 13 compare the rates of Eqs. (26,29), calculated for O_2-Ar at s=1 and s=5, with the trajectory calculations by ADIAV in the temperature range of $200\leq T\leq 50000$ K and vibrational quantum number range $0\leq i\leq 30$, showing satisfactory agreement. In these calculations, $\omega_e=1580.3$ cm^{-1}, $\omega_e x_e=12.072$ cm^{-1}, $r_e=1.207$ A, and the potential parameters are the same as before, A=1730 eV, and $\alpha=4.0$ A^{-1}.

Up to this point, both analytic and numerical calculations have been made for the frequency corrected harmonic oscillator (HO), i.e. assuming coupling only between the adjacent quantum states, i and $i\pm1$, and the simple purely repulsive potential of Eq. (3). To evaluate the effect of anharmonic non-adjacent state coupling on the relaxation rates, an additional series of calculations by ADIAV was made, using the Morse oscillator (MO) coupling matrix elements, $\langle i|\tilde{r}^s|i\pm s\rangle$ $(s\leq 3)$. It was found that the anharmonic coupling affects the rate $k_{10}(T)$ fairly weakly, the ratio $k_{10,MO}/k_{10,HO}$ being less than a factor of 2 even at $T\sim10^4$ K. Finally, we compared the FHO-FR model predictions for N_2-He relaxation rates with the numerical calculations by ADIAV using *ab initio* coupled electron pair approximation (CEPA) potential energy surface [44], rather than the simplified atom-to-atom potential of Eq. (3). In the present work, we simply extended the N_2-He ADIAV-CEPA calculations [45] toward the high collision energies. Analytic FHO-FR relaxation rates have been evaluated using the value of α=4.0 A^{-1}, obtained by the least squares fit of Eq. (3) to the CEPA potential. The results, shown in Fig. 14, again demonstrate very good agreement between the trajectory calculations and the analytic model. Note that the long-range attractive part of the CEPA potential (with the maximum well depth of 17 K) significantly affects the rates only below room temperature (see Fig. 14). At 300 K, the difference between the ADIAV-CEPA and the FHO-FR rates does not exceed a factor of 2, and even at T=100 the difference is about a factor of 3. Also shown in Fig. 14 are the low-temperature experimental measurements of k_{10} [46].

Both results demonstrate that the approximation of a purely repulsive interaction of a frequency corrected harmonic oscillator and an atom is reasonably accurate within a wide temperature range. Therefore the state-specific rate coefficients of Eqs. (26,29) can be used in kinetic modeling calculations both at near room temperature (such as in gas discharges) and at very high temperatures (e.g. behind shock waves). Note that the repulsive potential parameter α in each case should be chosen from the best fit of the analytic potential to available experimental and *ab initio* data rather than arbitrarily adjusted.

5. Summary

Analysis of classical trajectories of a free-rotating symmetric diatomic molecule acted upon by a repulsive potential allow developing a three-dimensional semiclassical nonperturbative analytic model of vibrational energy transfer in atom-molecule collisions (FHO-FR model). The model takes into account the following coupled effects: (i) interaction potential modulation by free rotation of an arbitrarily oriented molecule during a collision, (ii) reduction of the effective collision velocity in non-zero impact parameter collisions of a rotating molecule, and (iii) multi-state coupling in a collision.

The FHO-FR model predictions have been compared with close-coupled semiclassical trajectory calculations using the same potential energy surface. The comparison demonstrates not only very good agreement between the analytic and numerical probabilities across a wide range of collision energies, but also shows that the analytic model correctly reproduces the probability dependence on other collision parameters such as rotation angle, angular momentum angle, rotational energy, impact parameter, and collision reduced mass. The model equally well predicts the cross-sections of single-quantum and multi-quantum transitions and is applicable up to very high collision energies and quantum numbers. The resultant analytic expressions for the probabilities do not contain any arbitrary adjustable parameters commonly referred to as "steric factors". Additional calculations showed that the effect of anharmonic state coupling is weak, while the influence of attractive forces become substantial only at temperatures $T \leq 300$ K. Therefore the predictions of the model are also applicable at near room temperature. The results obtained in the present work can be used for calculations of the state-specific relaxation rates of symmetric or nearly symmetric molecules such as N_2, O_2, and CO, on inert gas atoms such as Ar and He. It remains an open question, however, whether the approach used here is applicable for calculations of vibrational energy transfer rates in molecule-molecule collisions, in particular for processes induced by long-range multipole-multipole attraction.

The FHO-FR model provides new insight into kinetics of vibrational energy transfer. Analytic expressions for state-specific transitions probabilities and rate coefficients, obtained in this work, are available from the authors upon request as concise FORTRAN subroutines, which allow their incorporation in existing kinetic models and their use in modeling calculations.

References

1. Gordiets, B.F., Osipov, V.A., and Shelepin, L.A., Kinetic Processes in Gases and Molecular Lasers, Gordon and Breach, London, 1988, Chaps. 3,4
2. Rusanov, V.D., and Fridman, A.A., Physics of Chemically Active Plasmas, Nauka, Moscow, 1984, Chap. 1
3. Cacciatore, M., Capitelli, M., DeBenedictis, S., Dilonardo, M., and Gorse, C., "Vibrational Kinetics, Dissociation and Ionization of Diatomic Molecules under Nonequilibrium Conditions", Nonequilibrium Vibrational Kinetics, Springer-Verlag, Berlin, 1986, Chap. 2, pp. 5-46
4. Park, C., Nonequilibrium Hypersonic Aerodynamics, Wiley, New York, 1990, Chap. 3
5. Yang, X., Kim, E.H., and Wodtke, A.M., "Vibrational Energy Transfer of Very Highly Vibrationally Excited NO", Journal of Chemical Physics, Vol. 96, No. 7, 1992, pp. 5111-5122

6. Price, J.M., Mack, J.A., Rogaski, C.A., and Wodtke, A.M., "Vibrational-State-Specific Self-Relaxation Rate Constant Measurements of Highly Excited O_2(v=19-28)", Chemical Physics, Vol. 175, No. 1, 1993, pp. 83-98
7. Park, H., and Slanger, T.G., "O (X, v=8-22) 300 K Quenching Rate Coefficients for O_2 and N_2, and O_2(X) Vibrational Distribution from 248 nm O_3 Photo-dissociation", Journal of Chemical Physics, Vol. 100, No. 1, 1994, pp. 287-300
8. Klatt, M., Smith, I.W.M., Tuckett, R.P., and Ward, G.N., "State-Specific Rate Constants for the Relaxation of $O_2(X^3\Sigma_g^-)$ from Vibrational Levels v=8 to 11 by Collisions with NO and O ", Chemical Physics Letters, Vol. 224, Nos. 3,4, 1994, pp. 253-257
9. Deleon, R., and Rich, J.W., "Vibrational Energy Exchange Rates in Carbon Monoxide", Chemical Physics, Vol. 107, No. 2, 1986, pp. 283-292
10. Secrest, D., and Johnson, B.R., "Exact Quantum Mechanical Calculations of a Collinear Collision of a Particle with a Harmonic Oscillator", Journal of Chemical Physics, Vol. 45, No. 12, 1966, pp. 4556-4570
11. Chapuisat, X., Bergeron, G., and Launay, J.-M., "A Quantum-Mechanical Collinear Model Study of the Collision N_2-O_2", Chemical Physics, Vol. 20, No. 2, 1977, pp. 285-298
12. Chapuisat, X., and Bergeron, G., "Anharmonicity Effects in the Collinear Collision of Two Diatomic Molecules", Chemical Physics, Vol. 36, No. 3, 1979, pp. 397-405
13. R. Hernandez, R.Toumi, and D.C. Clary, "State-Selected Vibrational Relaxation Rates for Highly Vibrationally Excited Oxygen Molecules", Journal of Chemical Physics, Vol. 102, No. 24, 1995, pp. 9544-9558
14. Kuksenko, B.V., and Losev, S.A., "On the Theory of Vibrational Relaxation of Diatomic Molecules", High Temperature, Vol. 6, No. 5, 1968, pp. 794-799
15. Lagana, A., Garcia, E., and Ciccarelli, L., "Deactivation of Vibrationally Excited Nitrogen Molecules by Collision with Nitrogen Atoms", Journal of Physical Chemistry, Vol. 91, 1987, pp. 312-314
16. Lagana, A., and Garcia, E., "Temperature Dependence of N+N_2 Rate Coefficients", Journal of Physical Chemistry, Vol. 98, 1994, pp. 502-507
17. Billing, G.D., "Vibration-Vibration and Vibration-Translation Energy Transfer, Including Multiquantum Transitions in Atom-Diatom and Diatom-Diatom Collisions", Nonequilibrium Vibrational Kinetics, Springer-Verlag, Berlin, 1986, Chap. 4, pp. 85-111

18. R.E. Kolesnick, and Billing, G.D., "Rate Constants for Vibrational Transitions in Hydrogen and Isotopes", Chemical Physics, Vol. 170, No. 1, 1993, pp. 201-207

19. Billing, G.D., and Fisher, E.R., "VV and VT Rate Coefficients in N_2 by a Quantum-Classical Model", Chemical Physics, Vol. 43, No.3, 1979, pp. 395-401

20. Billing, G.D., and Kolesnick, R.E., "Vibrational Relaxation of Oxygen. State to State Rate Constants", Chemical Physics Letters, Vol. 200, No. 4, 1992, pp. 382-386

21. Cacciatore, M., and Billing, G.D., "Semiclassical Calculations of VV and VT Rate Coefficients in CO", Chemical Physics, Vol. 58, No. 3, 1981, pp. 395-407

22. Billing, G.D., "VV and VT Rates in N_2-O_2 Collisions", Chemical Physics, Vol. 179, No. 3, 1994, pp. 463-467

23. Cacciatore, M., Capitelli, M., and Billing, G.D., "Theoretical Semiclassical Investigation of the Vibrational Relaxation of CO Colliding with $^{14}N_2$", Chemical Physics, Vol. 89, No. 1, 1984, pp. 17-31

24. Herzfeld, K.F., and Litovitz, T.A., Absorption and Dispersion of Ultrasonic Waves, Academic, New York, 1959, Chap. 3

25. Rapp, D., and Sharp, T.E., "Vibrational Energy Transfer in Molecular Collisions Involving Large Transition Probabilities", Journal of Chemical Physics, Vol. 38, No. 11, 1963, pp. 2641-2648

26. Rapp, D., and Englander-Golden, P., "Resonant and Near-Resonant Vibrational-Vibrational Energy Transfer between Molecules in Collisions", Journal of Chemical Physics, Vol. 40, No.2, 1964, pp. 573-575;

Rapp, D., and Englander-Golden, P., "Erratum: Resonant and Near-Resonant Vibrational-Vibrational Energy Transfer between Molecules in Collisions", Journal of Chemical Physics, Vol. 40, No.10, 1964, pp. 3120-3121;

Rapp, D., "Interchange of Vibrational Energy between Molecules in collisions", Journal of Chemical Physics, Vol. 43, No.1, 1965, pp. 316-317

27. Sharma, R.D., and Brau, C.A., "Energy Transfer in Near-Resonant Molecular Collisions Due to Long-Range Forces with Application to Transfer of Vibrational Energy from ν_3 Mode of CO_2 to N_2", Journal of Chemical Physics, Vol. 50, No. 2, 1969, pp. 924-930

28. Kerner, E.H., "Note of the Forced and Damped Oscillations in Quantum Mechanics", Canadian Journal of Physics, Vol. 36, No.3, 1958, pp. 371-377

29. Treanor, C.E., "Vibrational Energy Transfer in High Energy Collisions", Journal of Chemical Physics, Vol. 43, No.2, 1965, pp. 532-538

30. Zelechow, A., Rapp, D., and Sharp, T.E., "Vibrational-Vibrational-Translational Energy Transfer between Two Diatomic Molecules", Journal of Chemical Physics, Vol. 49, No. 1, 1968, pp. 286-299

31. Kelley, J.D., "Vibrational Energy Transfer Processes in Collision between Diatomic Molecules", Journal of Chemical Physics, Vol. 56, No. 12, 1972, pp. 6108-6117

32. Shin, H.K., "Vibrational Energy Transfer", Dynamics of Molecular Collisions, Plenum, New York, 1976, Part A, Chap. 4, pp. 131-210

33. Schwartz, R.N., and K.F. Herzfeld, Journal of Chemical Physics, Vol. 22, No. 2, 1954, pp. 767-

34. Takayanagi, K., Progress in Theoretical Physics (Kyoto), Vol. 8, 1952, pp. 8-

35. Mies, F.H., and Shuler, K., Journal of Chemical Physics, Vol. 37, No. 1, 1962, pp. 177-

36. Skrebkov, O.V., and Smirnov, A.L., "Effect of Rotation on the Process of Energy Transfer between a Diatomic Molecule (Anharmonic Oscillator) and an Atom", Soviet Chemical Physics, Vol. 10, No. 8, 1991, pp. 1036-1046

37. Landau, L., and Teller, E., Physik. Z. Sowjetunion, Vol. 10, 1936, pp. 34-

38. Nikitin, E.E., and Osipov, A.I., "Vibrational Relaxation in Gases", Kinetics and Catalysis, Vol. 4, VINITI, All-Union Institute of Scientific and Technical Information, Moscow, 1977, Chap. 2

39. Rapp, D., and Kassal, T., "The Theory of Vibrational Energy Transfer between Simple Molecules in Nonreactive Collisions", Chemical Reviews, Vol. 69, No. 1, 1969, pp. 61-102

40. Adamovich, I.V., Macheret, S.O., Rich, J.W., and Treanor. C.E., "Vibrational Relaxation and Dissociation Behind Shock Waves Part 1: Kinetic Rate Models", AIAA Journal, Vol. 33, No. 6, 1995, pp. 1064-1069

41. Adamovich, I.V., Macheret, S.O., Treanor, C.E., and Rich, J.W., "Vibrational Energy Transfer Rates Using a Forced Harmonic Oscillator Model", Journal of Thermophysics and Heat Transfer, Vol. 12, No. 1, 1997, pp. 57-

42. Billing, G.D., "Rate Constants and Cross Sections for Vibrational Transitions in Atom-Diatom and Diatom-Diatom Collisions", Computer Physics Communications, Vol. 32, No. 1, 1984, pp. 45-62

43. Boyd, I.D., Candler, G.V., and Levin, D.A., "Dissociation Modeling in Low Density Hypersonic Flows of Air", Physics of Fluids, Vol.7, No. 7, 1995, pp. 1757-1763.
44. A.J. Banks, D.C. Clary, and H.-J. Werner, "Vibrational Relaxation of N_2 by Collision with He Atoms", Journal of Chemical Physics, Vol. 84, No. 7, 1986, pp. 3788-3797
45. G.D. Billing, "Comparison of Quantum Mechanical and Semiclassical Cross Sections and Rate Constants for Vibrational relaxation of N_2 and CO Colliding with ^4He", Chemical Physics, Vol. 107, 1986, pp. 39-46
46. M.M. Maricq, E.A. Gregory, C.T. Wickham-Jones, D.J. Cartwright, and C.J.S.M. Simpson, Chemical Physics, Vol. 75, 1983, pp. 347-

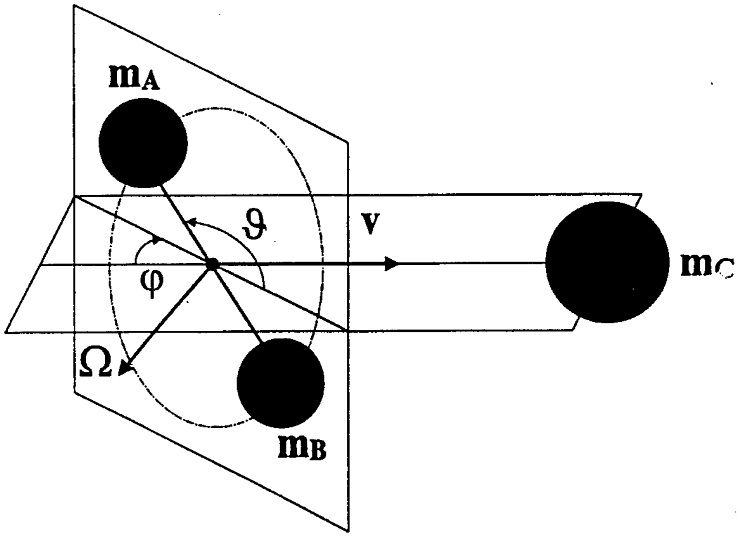

Figure 1. Schematic of a head-on collision between a rotating diatomic molecule and an atom.

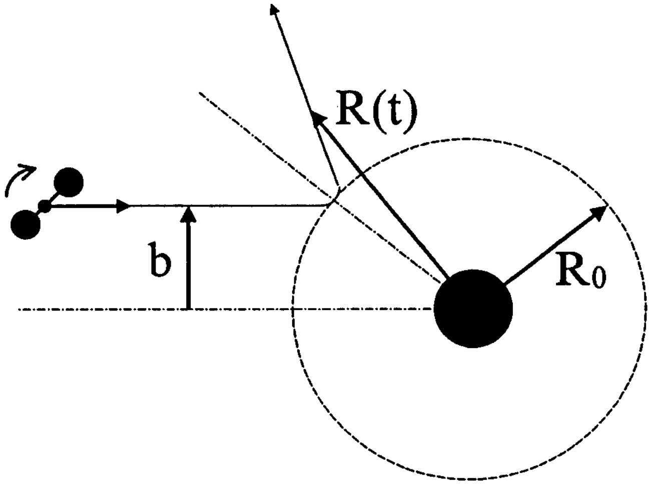

Figure 2. Schematic of a non-zero impact parameter atom-molecule collision.

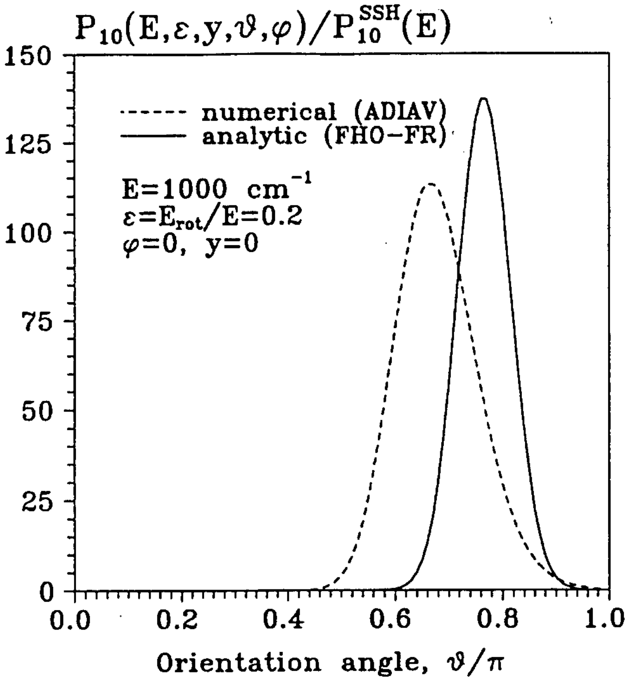

Figure 3. Comparison of the analytic FHO-FR probability and the numerical ADIAV probability of the vibrational transition 1→0 as a function of the rotation angle ϑ. In Figures 3-9, calculations are made for N_2 colliding with an atom with a mass $m_C=28$ at the total collision energy of $E=1000\ cm^{-1}$. The exponential repulsive potential parameter $\alpha=4.0\ A^{-1}$.

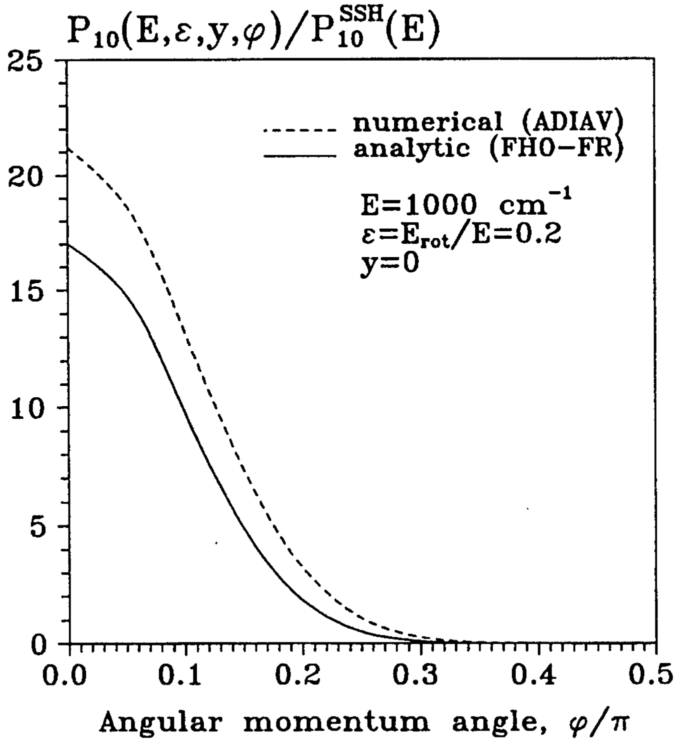

Figure 4. Comparison of the analytic FHO-FR probability and the numerical ADIAV probability (both averaged over ϑ) of the vibrational transition 1→0 as a function of the angular momentum angle φ.

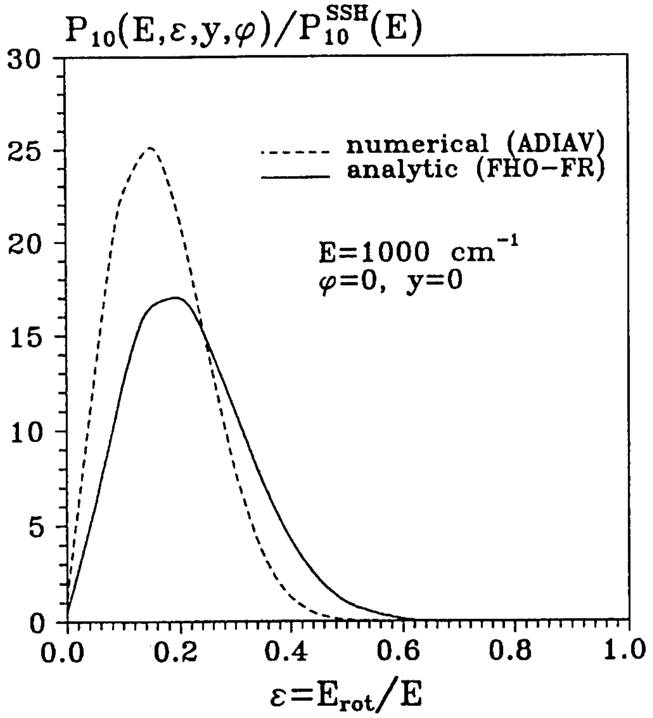

Figure 5. Comparison of the analytic FHO-FR probability and the numerical ADIAV probability (both averaged over ϑ) of the vibrational transition 1→0 as a function of the rotational energy of a molecule.

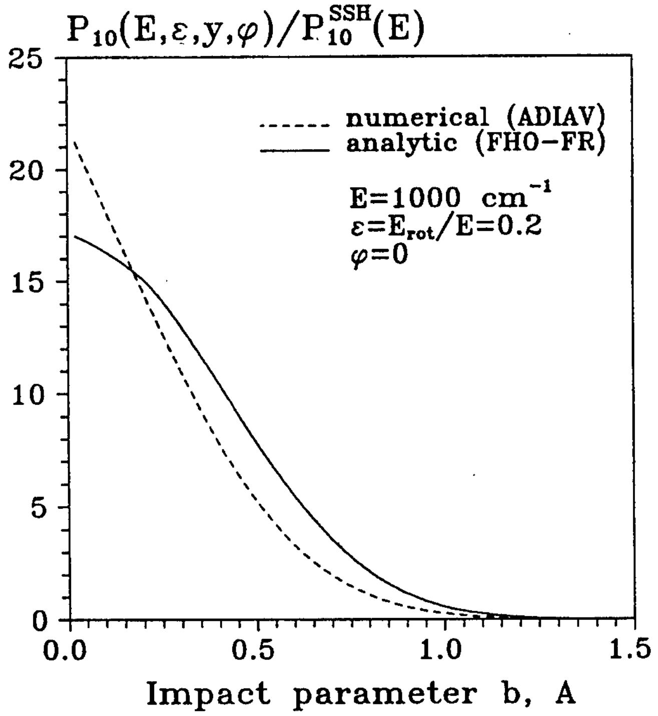

Figure 6. Comparison of the analytic FHO-FR probability and the numerical ADIAV probability (both averaged over ϑ) of the vibrational transition 1→0 as a function of the impact parameter.

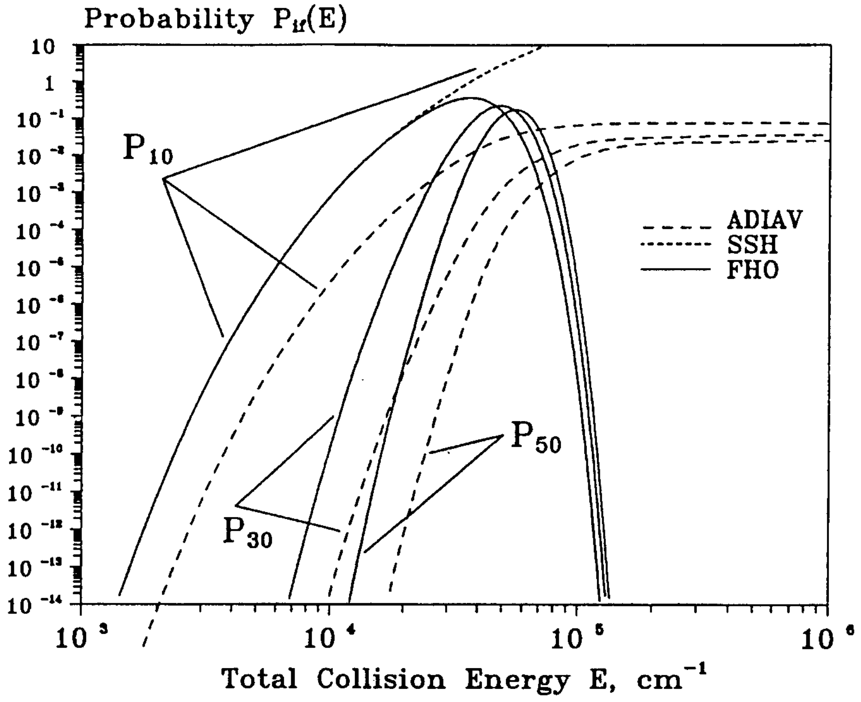

Figure 7. Comparison of the one-dimensional analytic models (SSH theory and FHO model) with the trajectory calculations by ADIAV.

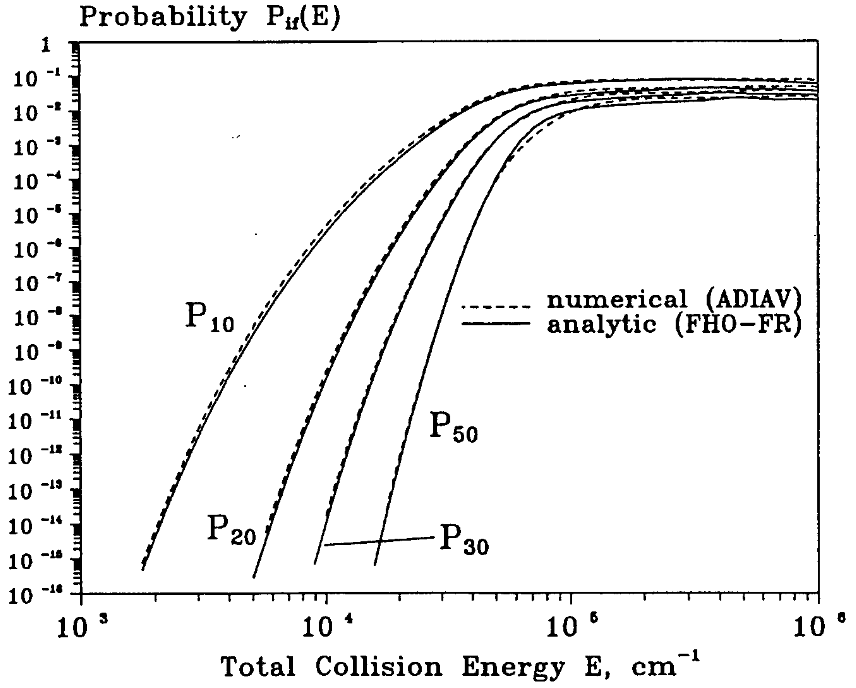

Figure 8. Comparison of the three-dimensional FHO-FR transition probabilities with the trajectory calculations by ADIAV for the low vibrational quantum numbers. The FHO-FR probability of Eqs. (10,12,14) is numerically averaged over the collision parameters ϑ, φ, ε, and y (see Eq. (15)).

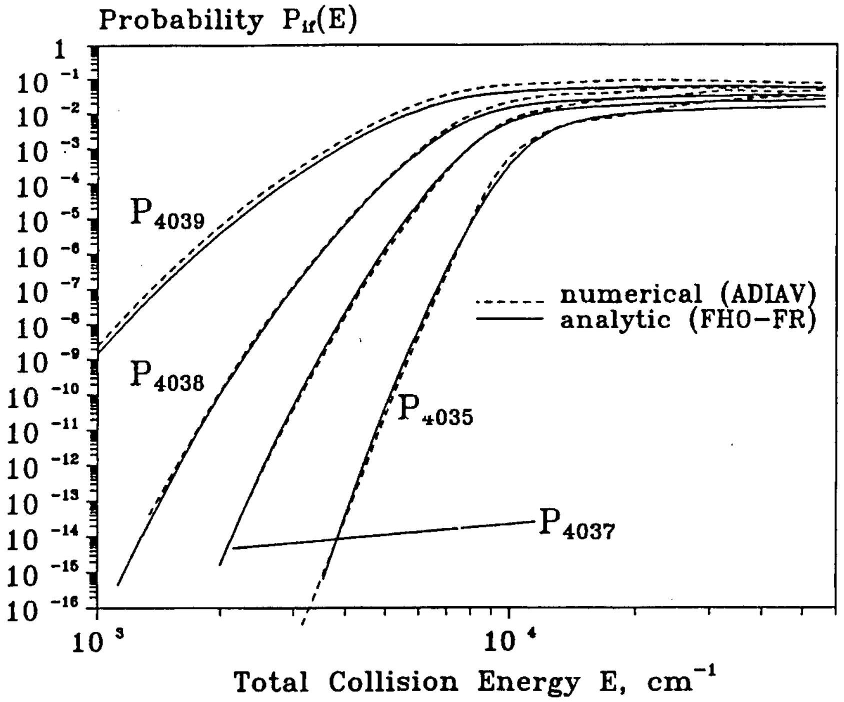

Figure 9. Comparison of the three-dimensional FHO-FR transition probabilities with the trajectory calculations by ADIAV for the high vibrational quantum numbers. FHO-FR probability of Eqs. (10,12,14) is numerically averaged over the collision parameters ϑ, φ, ε, and y (see Eq. (15)).

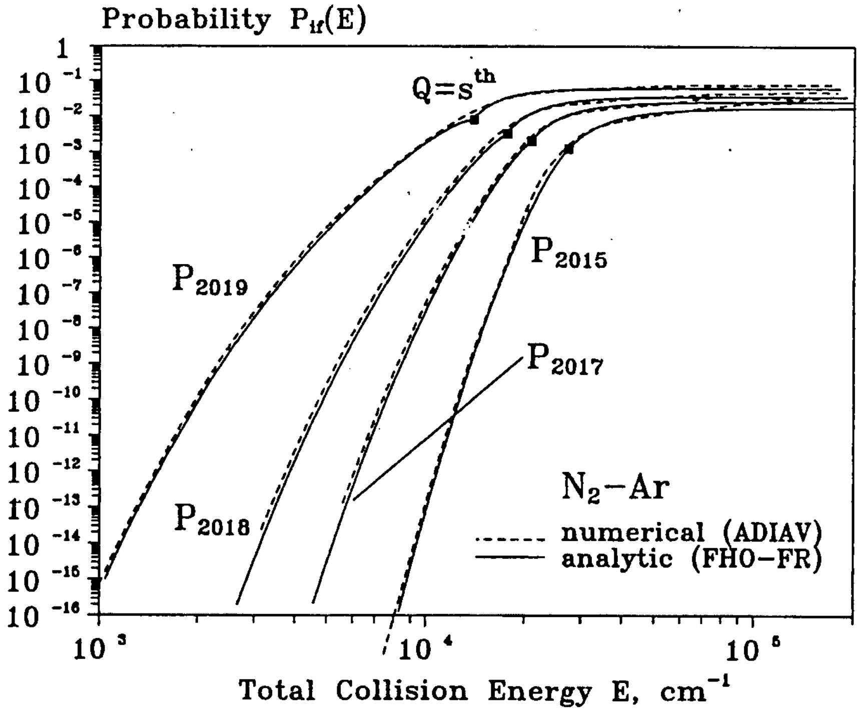

Figure 10. Comparison of the fully analytic FHO-FR probability of Eq. (24a) with the trajectory calculations by ADIAV for N_2-Ar.

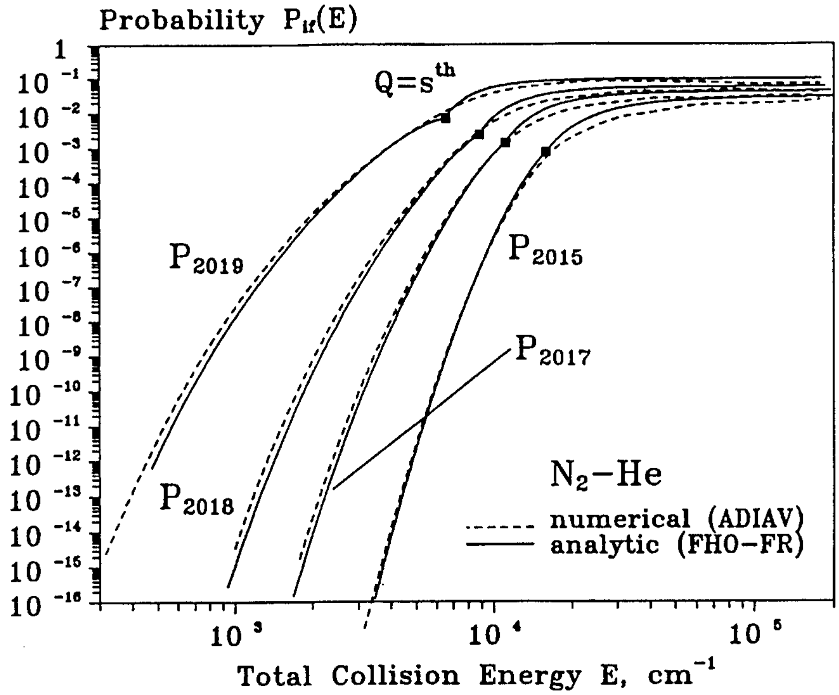

Figure 11. Comparison of the fully analytic FHO-FR probability of Eq. (24b) with the trajectory calculations by ADIAV for N_2-He.

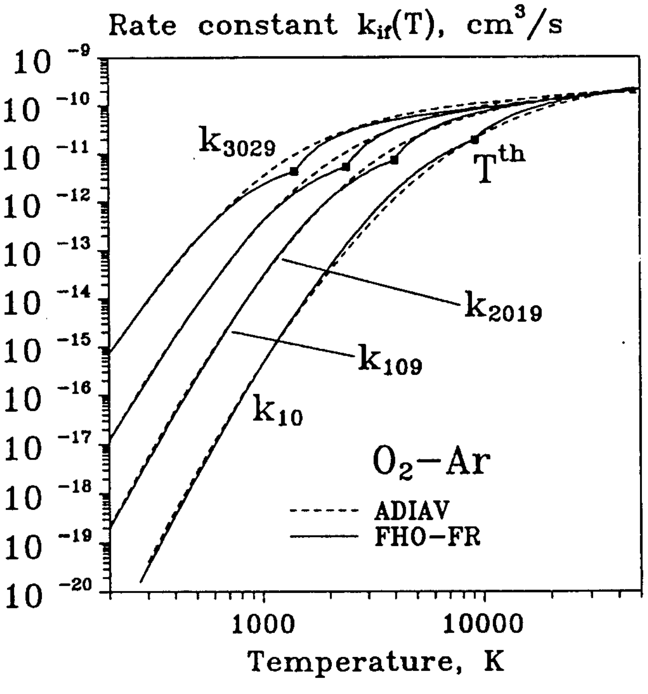

Figure 12. Comparison of the thermally averaged FHO-FR rate coefficients of Eqs. (26a,30a) with the trajectory calculations by ADIAV for O_2-Ar (single-quantum transitions, s=1).

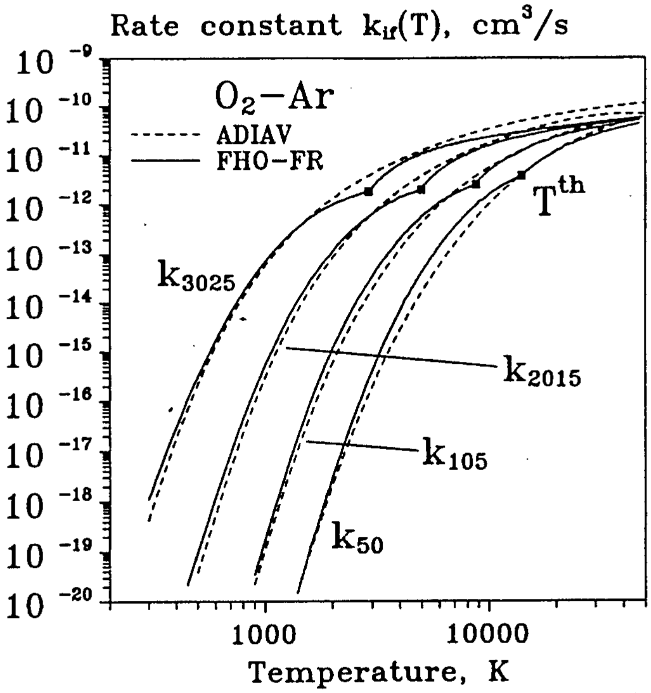

Figure 13. Comparison of the thermally averaged FHO-FR rate coefficients of Eqs. (26a,30a) with the trajectory calculations by ADIAV for O_2-Ar (multi-quantum transitions, s=5).

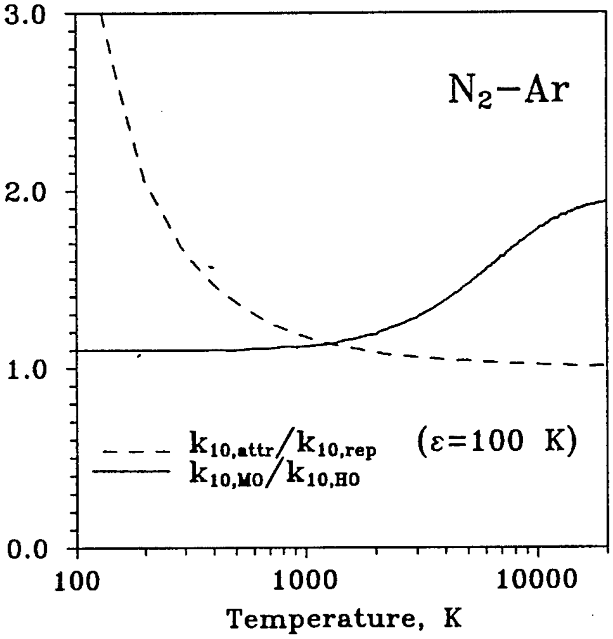

Figure 14. Comparison of the FHO-FR rate coefficients with the trajectory calculations by ADIAV using the *ab initio* CEPA potential energy surface for N_2-He [44], and with the experiment [46]. FHO-FR probability of Eqs. (10,12,14) is numerically averaged over the collision parameters ϑ, φ, ε, y, and E.

CHAPTER II.

THREE-DIMENSIONAL NONPERTURBATIVE ANALYTIC MODEL OF VIBRATIONAL ENERGY TRANSFER IN MOLECULE-MOLECULE COLLISIONS

1. Introduction

Vibrational energy transfer processes in collisions of diatomic molecules play an extremely important role in gas discharges, molecular lasers, plasma chemical reactors, high enthalpy gas dynamic flows, and in the physics of the upper atmosphere. In these nonequilibrium environments, the energy loading per molecule may be as high as 0.1-5.0 eV, while disequipartition among translational, vibrational, and electronic energy modes of heavy species, and with the free electron energy, may be very strong. This often results in development and maintaining of strongly nonequilibrium molecular vibrational energy distributions, which induce a variety of energy transfer processes among different energy modes and species, chemical reactions, and ionization [1-3]. The rates of these processes are determined by the populations of high vibrational levels of molecules, which are often controlled by vibration-vibration-translation (V-V-T) processes

$$AB(i_1)+CD(i_2)\rightarrow AB(f_1)+CD(f_2) \tag{1}$$

In Eq. (1), AB and CD represent diatomic molecules and an atom, respectively, and i_1, i_2, f_1, and f_2 are vibrational quantum numbers. Traditionally, these processes are separated into two separate modes, (i) vibration-translation (V-T) processes ($i_2=f_2$ in Eq. (1)), and (ii) vibration-vibration (V-V) processes ($i_1-f_1=f_2-i_2$ in Eq.(1)). At the low temperatures, the V-T processes are typically much slower than V-V energy transfer.

Quantitative data on the mechanisms and kinetic rates of these processes are needed for numerous practical applications, including novel chemical technologies, environmental pollution control, and radiation prediction in aerospace propulsion flows, in high altitude rocket plumes and behind shock waves. In addition, recent results demonstrate that strong vibrational disequilibrium can be sustained in CO-seeded atmospheric pressure air, optically pumped by a low-power c.w. CO laser [4]. This opens a possibility of creating stable large-volume high-pressure air plasmas. Insight into kinetics of these plasmas also requires knowledge of V-T and V-V rates in CO, N_2, and O_2.

There exists an extensive literature on the experimental study of V-T and V-V energy transfer, including recent state-specific rate measurements for highly vibrationally excited molecules, such as NO, O_2, and CO [5-9]. However, for many energy transfer processes among high vibrational quantum numbers the experimental rate data are still unavailable. As a result, most such rates used in applied kinetic modeling are based on theoretical scattering calculations. Among numerous theoretical rate models available, one can separate the following major approaches: (i) fully quantum calculations, (ii) classical, quasiclassical, and semiclassical numerical trajectory calculations, and (iii) analytic methods.

Since the exact quantum calculations are rather computationally laborious, they have been usually made for a simplified model of collinear collisions of harmonic oscillators and used as tests for more approximate approaches [10-12]. However, some three-dimensional calculations of the state-specific vibrational energy transfer rates for O_2-O_2 using vibrational close-coupling infinite-order sudden approximation (VCC-IOSA) have been recently published [13].

Classical and quasiclassical trajectory methods, such as used for calculations of vibrational relaxation rates for O_2-Ar [14], N_2-N, and O_2-O [15,16], are applicable only for calculation of rather large transition probabilities. For accurate predictions of small transition probabilities $P<<1$, a large number of collision trajectories, $N\sim1/P$, have to be averaged.

Among semiclassical calculations, one can mention the close-coupled method developed by Billing and validated by comparison with the exact quantum calculations, as well as with experimental data [17]. Trajectory calculations by this method have been made for a number of species such as H_2, N_2, O_2, and CO [18-23] in a wide range of collision energies and vibrational quantum numbers. These results comprise perhaps the most extensive and consistent vibrational energy transfer rate database.

In addition to some fundamental problems encountered in calculations by these advanced methods (such as the choice of the three-dimensional potential energy surface), their results are often difficult to interpret and use in kinetic modeling calculations. First, it is not always possible to identify the key energy transfer mechanisms that control the cross-sections obtained. Second, the number of the state-specific rates used as entries in modern master equation kinetic models for studies of strongly nonequilibrium gases and plasmas may reach 10^4-10^5. Even if some of these rate data are available from three-dimensional computer calculations, one has to rely on curve fitting, unreliable extrapolation, or inaccurate analytic parametrization to incorporate the rates into the model. As a result, such kinetic models do not provide new insight into kinetics, have limited applicability, and lack predictive capability.

Approximate analytic rate expressions are also widely used in kinetic modeling, mostly because of their simplicity. However, available analytic models have serious inherent flaws that make them much less reliable and accurate compared to numerical scattering calculations. First, most of these models, such as the Schwartz, Slawsky, Herzfeld (SSH) theory, Rapp-Englander-Golden model, Sharma-Brau theory etc. [24-27] are based on first-order perturbation theory (FOPT), and therefore cannot be applied at high collision energies, high quantum numbers, and for multi-quantum processes ($|i-f|>1$ in Eqs. (1,2)). An exception is the nonperturbative Forced Harmonic Oscillator (FHO) model [28-31], which takes into account the coupling of many vibrational states during a collision, and is therefore applicable for such conditions. Second, analytic models are typically developed only for collinear collisions of non-rotating molecules. A procedure commonly used to account for the effects of realistic three-dimensional collisions and molecular rotation is the introduction of adjustable correction parameters ("steric factors") into the resultant rate expression [32]. These coefficients, which are assumed to be temperature-independent, have very little or no theoretical basis and are found from comparison of a simple model with experiments or three-dimensional calculations.

There have been various attempts to develop non-empirical expressions for the steric factors and also to incorporate the effect of rotation into analytic models [32-35]. In most of them, the simplifying assumptions made, such as analyzing of collisions of arbitrarily oriented, but non-rotating, molecules [32], or, on the contrary, considering only collisions of rapidly rotating "breathing spheres" (i.e. isotropic three-dimensional oscillators) [33-35], were unrealistic. In addition, the coupled effects of orientation of colliding partners, molecular rotation, and non-zero impact parameter collisions have been analyzed separately. Finally, the procedure of comparison between the experimental relaxation rates and the analytic rates corrected for non-collinear orientation and rotation, used by some authors to validate theoretically obtained values of the steric factors, is hardly conclusive. It such cases, the agreement obtained might well be due to the formal adjustment of the intermolecular potential parameters used, i.e. to a curve fitting. The only credible procedure for analytic model validation would be comparing its predictions with the results of three-dimensional numerical calculations made for the same potential energy surface.

The present work discusses further development of a semiclassical analytic vibrational relaxation model that incorporates the effects of three-dimensional collisions and molecular rotation (Forced Harmonic Oscillator – Free Rotator, or FHO-FR model [36, 37]). It is a follow-up on our previous publication [37] where we analyzed energy transfer in collisions between a diatomic molecule and an atom. Previous results demonstrated not only remarkably good agreement between the analytic and numerical probabilities across a wide range of collision energies, but also showed that the analytic FHO-FR model correctly reproduces the probability dependence on other collision parameters such as rotation angle, angular momentum angle, rotational energy, impact parameter, and collision reduced mass. The model equally well predicted the cross-sections of single-quantum and multi-quantum transitions, up to very high collision energies and quantum numbers.

The main goal of the present study is development of analytic transition probabilities that are in agreement with trajectory calculations and that can be easily incorporated in nonequilibrium kinetic models. Such a model would give new insight into mechanisms of vibrational relaxation, as well as bridge the gap between state-of-the-art theoretical scattering techniques and their use for practical applications.

2. Collision trajectories and transition probabilities

The analysis of the dynamics of collisions between two rotating symmetric diatomic molecules is a straightforward extension of the procedure used for atom-molecule collisions in [37]. The translational motion and the three-dimensional rotation of the molecules are assumed to be uncoupled, and the latter is unaffected by the collision, i.e. free. Then the only effect of rotation on the collision trajectory is the periodic modulation of the interaction potential. The assumption of free rotation is quite similar to the basic assumption made in all semiclassical theories, which evaluate the translational-rotational trajectory uncoupled from the vibrational motion of the oscillator. Also, instead of relying on perturbation theory, the exact semiclassical solution of the Schrodinger equation (the FHO theory [28-31]) is used to evaluate the vibrational transition probabilities. This expands the applicability of the model to high collision energies and allows prediction of multi-quantum vibrational transition rates.

Consider a three-dimensional collision of two symmetric molecules (see Fig. 1). For the pairwise atom-to-atom interaction described by a repulsive exponential function, $U_i(R_i)=A\exp(-\alpha R_i)$, where R_i is the distance between the atoms, the atom-molecule interaction potential can be written as follows:

$$U(R,r,\vartheta_1,\varphi_1,\vartheta_2,\varphi_2) = 4Ae^{-\alpha R}\cosh\left[\frac{\alpha r}{2}\cos\vartheta_1\cos\varphi_1\right]\cosh\left[\frac{\alpha r}{2}\cos\vartheta_2\cos\varphi_2\right] \qquad (2)$$

In Eq. (2), R is the center-of-mass distance, r is the separation of atoms in a molecule, ϑ_1 and ϑ_2 are the rotation angles, and φ_1 and φ_2 are the angles between the plane of rotation and the velocity vector v (see Fig. 1). Since the rotation is assumed to be free, neither the magnitude nor the direction of the angular momentum vectors change in a collision. That gives $\vartheta_i(t)=\vartheta_{i0}+\Omega_i t$, $\varphi_i(t)=\varphi_{i0}$, where Ω_i are the constant angular velocities of molecular rotation, and the subscript "0" means "at the point of maximum interaction", where U is maximum. To calculate the semiclassical trajectory R(t), we also assume $r(t)=r_e$, where r_e is the equilibrium atom separation. One can see that the potential (2) consists of the exponential translational part modulated by the periodic rotational factors. If the rotation is not very rapid, the modulation can substantially change the shape of the time-dependent perturbation, $U(\tilde{R},t)$, where $\tilde{R}(t)=R(t)-R_0$, and R_0 is the "collision diameter" (the distance at the maximum interaction point). The classical equation of motion for this potential, $m\ddot{\tilde{R}}(t) = -\dfrac{\partial U(\tilde{R},t)}{\partial \tilde{R}}$ (m is the collision reduced mass), can be easily solved if the rotation is slow, so that the potential $U(R,r_e,t) = U(\tilde{R},t)$ can be expanded near the point of maximum interaction, R_0.

This approach also allows incorporation of non-zero impact parameter collisions by taking into account only radial relative motion of the colliding partners, R(t), in the vicinity of the maximum interaction point. Then the translational energy of collision, $E_{tr}=E-E_{rot,1}-E_{rot,2}$, is replaced by the energy of the radial motion, $E_{rad}=(E-E_{rot,1}-E_{rot,2})[1-b^2/R(t)^2]\cong(E-E_{rot,1}-E_{rot,2})(1-b^2/R_0^2)$ (the so-called modified wavenumber approximation [34]). Here E is the total collision energy, $E_{rot,i}=m_{o,i}\Omega_i^2 r_e^2/2$ are rotational energies of the molecules, $m_{o,i}$ are the oscillator reduced masses, and b is the impact parameter. This approach is justifiable for short-range repulsive interactions when the energy transfer is determined by a small portion of the trajectory near the maximum interaction point [38]. The resultant expression for the trajectory is

$$U(t)=\frac{E\gamma^2}{\cosh^2\left[\gamma\alpha t\sqrt{\frac{E}{2m}}\right]} \tag{3}$$

$$\begin{gathered}\gamma(\varepsilon,y,\vartheta_{10},\varphi_{10},\vartheta_{20},\varphi_{20})\approx\\ \max\left[0,-\frac{\sin 2\vartheta_{10}\cos\varphi_{10}}{2}\sqrt{\varepsilon_1}-\frac{\sin 2\vartheta_{20}\cos\varphi_{20}}{2}\sqrt{\varepsilon_2}+\sqrt{(1-\varepsilon_1-\varepsilon_2)(1-y)}\right]\end{gathered} \tag{4}$$

Eq. (3) describes a parametric set of three-dimensional trajectories with the same total collision energy E and various values of rotational energies, impact parameter, and orientation of collision partners, characterized by a single factor $\gamma=(\varepsilon,y,\vartheta_{10},\varphi_{10},\vartheta_{20},\varphi_{20})$, which is given by Eq. (4). In Eq. (4), $\varepsilon_i=E_{rot,i}/E$, and $y=b^2/R_0^2$. The factor $E\gamma^2$ in Eq. (3) can be interpreted as the effective collision energy. One can see that at $\varepsilon_i=y=\vartheta_{i0}=\varphi_{i0}=0$, one has $\gamma=1$, $E=E_{tr}$, and the trajectory coincides with the one-dimensional result for a head-on collinear collision of two non-rotating molecules [39].

The applicability of Eqs. (3,4) is limited to relatively slow molecular rotation [37], when

$$\varepsilon_1+\varepsilon_2=(E_{rot,1}+E_{rot,2})/E\lesssim\frac{1}{2}\frac{(1-y^2)}{(1-y^2/2)}, \tag{5}$$

so that the collision trajectory of a rapidly rotating molecule cannot be accurately predicted, especially at large impact parameters. However, the contribution of such collisions to the overall transition probability as a function of the total collision energy E is expected to be small (see discussion in [37]). Therefore, in the present work we disregard such collisions. Later we will show that this assumption is consistent with the results of the three-dimensional trajectory calculations.

Having calculated the free rotation collision trajectory (3,4), we can evaluate the semiclassical vibrational energy transfer probabilities $P(i_1,i_2 \rightarrow f_1,f_2)$, where i and f are initial and final vibrational quantum numbers, respectively. For this we will use the FHO theory [28-31], a nonperturbative analytic model, originally developed for collinear collisions of nonrotating diatomic molecules. This model is based on the exact solution of the Schrodinger equation for the intermolecular potential $U(R,r,\vartheta_i,\varphi_i)$ linearized in r and therefore takes into account the coupling of all vibrational quantum states during a collision. It is applicable up to high collision energies and vibrational quantum numbers, as well as for multiquantum transitions. The scaling law predicted by this model, i.e. the probability dependence on the vibrational quantum numbers, is independent of the interaction potential. Unfortunately, the exact FHO expression for a general V-V-T process probability, $P(i_1,i_2 \rightarrow f_1,f_2)$, is extremely cumbersome [30]. However, FHO probabilities of the V-T processes, $P(i_1,0 \rightarrow f_1,0)$, and of the V-V process, $P(i_1,i_2 \rightarrow f_1,f_2)$, $i_1-f_1=f_2-i_2$, are much simpler. They are given by the following relations [37,40,41]:

$$P(i_1,0 \rightarrow f_1,0) \approx \frac{(n_s)^s}{(s!)^2} Q^s \exp\left[-\frac{2n_s}{s+1}Q - \frac{n_s^2}{(s+1)^2(s+2)}Q^2\right],$$

$$s=|i_1-f_1|, \quad n_s=\left[\frac{\max(i_1,f_1)!}{\min(i_1,f_1)!}\right]^{1/s} \tag{6}$$

for the V-T processes, and

$$P(i_1,i_2 \rightarrow f_1,f_2) \approx \frac{(n_{s,1})^s (n_{s,2})^s}{(s!)^2} G^s \exp\left[-\frac{2n_s}{s+1}G - \frac{n_s^2}{(s+1)^2(s+2)}G^2\right],$$

$$s=|i_1-f_1|=|i_2-f_2|, \quad n_{s,1}=\left[\frac{\max(i_1,f_1)!}{\min(i_1,f_1)!}\right]^{1/s}, \quad n_{s,2}=\left[\frac{\max(i_2,f_2)!}{\min(i_2,f_2)!}\right]^{1/s} \tag{7}$$

for the V-V processes. In Eqs. (6,7), the potential-dependent parameters Q and G are the following trajectory integrals [28-30]:

$$Q = \frac{\langle 1|\tilde{r}|0\rangle_1^2}{\hbar^2}\left|\int_{-\infty}^{\infty}\left(\frac{\partial U(\tilde{R},\tilde{r},t)}{\partial\tilde{r}}\right)_{\tilde{r}=0} e^{i\omega_1 t}dt\right|^2 \tag{8}$$

and

$$G = \frac{\langle 1|\tilde{r}|0\rangle_1^2\langle 1|\tilde{r}|0\rangle_2^2}{\hbar^4}\left|\int_{-\infty}^{\infty}\left(\frac{\partial U(\tilde{R},\tilde{r},t)}{\partial\tilde{r}}\right)_{\tilde{r}=0} e^{i(\omega_1-\omega_2)t}dt\right|^2 \tag{9}$$

In Eqs. (8,9), $\tilde{r} = r - r_e$, $\omega_j = \frac{|E_{i_j} - E_{f_j}|}{s\hbar}$ is the average vibrational quantum for the transition $i_j \rightarrow f_j$, $\langle 1|\tilde{r}|0\rangle_j^2 = \frac{\hbar}{2m_o\omega_j}$ is the frequency corrected squared matrix element of the transition 0→1.

Using Eqs. (3,4), one obtains

$$Q(E,\varepsilon,y,\vartheta_{10},\varphi_{10},\vartheta_{20},\varphi_{20}) \approx \frac{\theta'}{4\theta}\frac{\cos^2\vartheta_{10}\cos^2\varphi_{10}}{\sinh^2\left[\frac{\pi\omega_1}{\alpha u\gamma(\varepsilon,y,\vartheta_{10},\varphi_{10},\vartheta_{20},\varphi_{20})}\right]} \tag{10}$$

and

$$G(E,\varepsilon,y,\vartheta_{10},\varphi_{10},\vartheta_{20},\varphi_{20}) \approx$$

$$\cos^2\vartheta_{10}\cos^2\varphi_{10}\cos^2\vartheta_{20}\cos^2\varphi_{20}\left[\frac{\gamma(\varepsilon,y,\vartheta_{10},\varphi_{10},\vartheta_{20},\varphi_{20})\alpha u}{2}\right]^2\frac{1}{\omega_1\omega_2}\left[\frac{\xi}{\sinh(\xi)}\right]^2, \tag{11}$$

$$\xi = \frac{\pi(\omega_1-\omega_2)}{\alpha u}$$

In Eq. (10,11), $\theta' = \frac{4\pi^2\omega_1^2 m}{\alpha^2 k}$, $\theta = \frac{\hbar\omega_1}{k}$, and $u = \sqrt{2E/m}$. Note that two different symbols, i.e. ϑ and θ, are being used throughout this chapter for the rotation angle and the characteristic vibrational temperature, respectively. The product $u\gamma$ can be interpreted as an effective collision velocity. One can see that at $\varepsilon=y=\vartheta_{i0}=\varphi_{i0}=0$, one has $\gamma=1$, $E=E_{tr}$, and Eqs. (10,11) coincide with the one-dimensional probabilities of the single-quantum transitions $0\to1$ and $1,0\to0,1$, predicted by the SSH theory [24,39]. The difference between the present FHO-FR model and the one-dimensional SSH theory result is that Eqs. (4,10,11) incorporate three-dimensional trajectories of rotating molecules as well as the coupling of vibrational states during a collision.

3. Comparison with trajectory calculations

To verify the accuracy of the present model, it has to be compared with three-dimensional semiclassical trajectory calculations for the diatom-diatom collisions, for the potential energy surface given by Eq. (2). For this purpose, we have used the computer codes DIDIAV and DIDIEX developed by Billing [42,43]. Both codes calculate classical translational-rotational collision trajectories. The main difference between the two codes is that DIDIAV uses the FHO formalism [28-30], modified by Kelley [31], to evaluate semiclassical vibrational transition probabilities of a frequency corrected harmonic oscillator, while in DIDIEX the semiclassical probabilities are evaluated by solving a set of coupled equations for the time-dependent expansion coefficients of the vibrational wavefunction over a basis of stationary states of the molecules. While the second approach is certainly more accurate, the calculation time using DIDIEX is about an order of magnitude longer. Both codes give close results (within 10-30%) except for the multi-quantum V-T probabilities at high collision energies, for which the DIDIEX predictions are preferred. Calculations were made for collisions of two N_2 molecules. The coupling matrix elements $\langle i|\tilde{r}|i\pm1\rangle$ used by DIDIEX were calculated for the frequency corrected harmonic oscillator (i.e. with harmonic wavefunctions but anharmonic energy spectrum), with up to 10 states used for the vibrational wavefunction expansion. The frequency corrected harmonic oscillator approximation also implies that parameter ω in the FHO-FR model is evaluated as the average vibrational quantum of a transition, i.e. $\omega = |E_i - E_f|/s\hbar$. The N_2 vibrational quantum, the anharmonicity, and the equilibrium atom separation were taken to be

ω_e=2359.6 cm^{-1}, $\omega_e x_e$=14.456 cm^{-1}, and r_e=1.094 A. The intermolecular repulsive potential parameters used were A=1730 eV, and α=4.0 A^{-1} [19].

The calculation results are summarized in Figs. 2-7. We emphasize that in the present work we will always compare the absolute values of the analytic FHO-FR probability and numerical probability, respectively, evaluated for two identical potential energy surfaces. We will also use the one-dimensional, collinear-collision SSH probabilities $P^{SSH}_{10,00}(E)=\frac{\theta'}{4\theta}\sinh^{-2}\left(-\frac{\pi\omega}{\alpha u}\right)$ and $P^{SSH}_{10,01}(E)=\left(\frac{\alpha u}{2\omega}\right)^2$ only as convenient scale factors. This procedure is more challenging than comparison of the two relative probabilities (i.e. analytic vs. numerical), both normalized on their respective values at some reference point, which is commonly used for validation of analytic rate models. For brevity, let us omit the subscript "0" remembering, however, that from now on the angles ϑ_i and φ_i are always evaluated at the maximum interaction point. Figure 2 shows the ratio of the three-dimensional FHO-FR V-T transition probability $P_{10,00}(E,\varepsilon_1,\varepsilon_2,y,\vartheta_1,\vartheta_2,\varphi_1,\varphi_2)$, given by Eqs. (4,6,10), to the SSH probability $P^{SSH}_{10,00}(E)$, as a function of the rotation angles ϑ_1, ϑ_2. All other collision parameters were held constant at E=10^3 cm^{-1}, $\varphi_1=\varphi_2=0$, $\varepsilon_1=\varepsilon_2=1/6$, $y=b^2/R_0^2=0$. Also shown in Fig. 2 is the ratio of the DIDIAV transition probability, evaluated for the same collision parameters, to the same factor $P^{SSH}_{10,00}(E)$. One can see that the FHO-FR probability peaks at similar values of the rotation angles as the DIDIAV probability ($\vartheta_1=\vartheta_2\cong-0.25\pi$ vs. $\vartheta_1=\vartheta_2\cong-0.3\pi$). Note that the optimum configuration for the V-T energy transfer is noncollinear. The maximum probability, which exceeds $P^{SSH}_{10,00}$ by more than three orders of magnitude, is also predicted quite accurately (within a factor of two). Figure 3 shows the ratios of the FHO-FR and DIDIAV V-V probabilities $P_{10,01}$, calculated at the same conditions as in Fig. 2, to the SSH probability $P^{SSH}_{10,01}(E)$. Both analytic and numerical probabilities are maximum for the collinear configuration ($\vartheta_1=\vartheta_2=0$), and the maximum probability is predicted by the FHO-FR model with accuracy of 20%. From Fig. 3, one can see that the analytic V-V probability is zero for the perpendicular orientation of at least one of the molecules at the point of maximum interaction ($\vartheta_1=\pm\pi/2$ and/or $\vartheta_2=\pm\pi/2$), while the numerical probability in these cases can be differ from zero. This illustrates that the free rotation approximation, which works well for the V-T processes induced over a small portion of the trajectory near the maximum interaction point, is less accurate for the resonance V-V processes that occur over a much longer portion of the trajectory (compare the integrals in Eqs. (8,9)). This "non-local" character of the resonance V-V energy transfer makes it rather sensitive to the change of the orientation angles due to the forced (i.e. non-free) molecular rotation during the collision.

Figure 4 plots the ratios of the FHO-FR and DIDIAV V-T probabilities $P_{10,00}(E,\varepsilon_1,\varepsilon_2,y)$, averaged over the orientation and angular momentum angles $\vartheta_1,\vartheta_2,\varphi_1,\varphi_2 \in [-\pi/2,\pi/2]$, to the SSH probability $P_{10,00}^{SSH}(E)$, as a function of the dimensionless rotational energies, $\varepsilon_1=E_{rot,1}/E$ and $\varepsilon_2=E_{rot,2}/E$. Once again, both probabilities peak at about the same values of ε_1 and ε_2, $\varepsilon_1 \cong \varepsilon_2 \cong 0.2$, and the maximum value is predicted within about 50% accuracy. Note that (i) the most efficient value of rotational energy is within the limits of applicability of the FHO-FR model, $\varepsilon_1+\varepsilon_2 \lesssim 1/2$, given by Eq. (5), and (ii) the DIDIAV transition probability sharply drops at $\varepsilon_1+\varepsilon_2 \to 1$, as discussed in Section 2. The last result justifies neglecting rapidly rotating molecule collisions (see Section 2).

Figure 5 displays the ratios of the FHO-FR and DIDIAV V-V probabilities $P_{10,01}(E,\varepsilon_1,\varepsilon_2,y)$, evaluated at the same conditions as in Fig. 5, to the SSH probability $P_{10,01}^{SSH}(E)$. One can see that the analytic probability linearly decreases with rotational energy, while the numerical probability at $\varepsilon_1,\varepsilon_2<1/2$ is weakly dependent on the rotational energy. Again, this difference shows that the free rotation approximation is less accurate for the resonance V-V processes than for the V-T processes. As discussed above, the "non-local" character of the resonance V-V energy transfer makes it sensitive to the change of the angular momentum vectors due to the forced rotation during the collision, which explains poor accuracy of the free rotation approximation in this case.

Figures 6,7 show the ratios of the FHO-FR and DIDIAV V-T and V-V probabilities, averaged over the orientation and angular momentum angles $\vartheta_1,\vartheta_2,\varphi_1,\varphi_2 \in [-\pi/2,\pi/2]$, to the SSH probabilities $P_{10,00}^{SSH}(E)$ and $P_{10,01}^{SSH}(E)$, respectively, as functions of the impact parameter b. Both figures show the probability ratios calculated at two collision energies, $E=10^3$ and 10^4 cm^{-1}, at $\varepsilon_1=\varepsilon_2=1/6$. One can see that both V-T and V-V analytic probabilities are within a factor of two of the numerical results, although the impact parameter dependence of the FHO-FR V-T probabilities is in much better agreement with the trajectory calculations. This again shows that the modified wavenumber approximation, discussed in Section 2, works better for the "local" V-T processes than for the "non-local" resonance V-V processes.

The fact that the ratios $P_{10}^{FHO-FR}/P_{10}^{SSH}$ and $P_{10}^{DIDIAV}/P_{10}^{SSH}$ both greatly exceed unity at $\vartheta_1,\vartheta_2,\varepsilon_1,\varepsilon_2\neq0$ (see Figs. 2,4), demonstrates that non-collinear collisions of rotating molecules are much more efficient for V-T energy transfer than head-on collinear collisions of non-rotating molecules considered by the SSH theory. The same effect, caused by the perturbation of the interaction potential near the maximum interaction point by molecular rotation, has been observed in atom-molecule collisions and discussed in [36,37].

Comparison of the two-quantum transition probabilities, $P_{20,00}$ and $P_{20,02}$, with the trajectory calculations by DIDIAV demonstrated the same kind of agreement (i.e. between a few tens of percent and a factor of two).

To compare the analytic and the numerical transition probabilities as functions of only the total collision energy E, we numerically averaged the probabilities $P_{VT}(i_1,0\to f_1,0,E,\varepsilon_i,y,\vartheta_i,\varphi_i)$, given by Eqs. (4,6,10), and $P_{VV}(i_1,i_2\to f_1,f_2,E,\varepsilon_i,y,\vartheta_i,\varphi_i)$, given by Eqs. (4,7,11), over the values of rotational energy, impact parameter, and orientation angles, using 10^5 points randomly chosen in phase space. The respective numerical transition probabilities in a collision energy range $E=10^2\text{-}10^6$ cm^{-1} were obtained by Monte Carlo averaging over 1000 randomly chosen trajectories with the same value of E, which provided 10-20% accuracy. The initial separation between a molecule and an atom was 15 A, and the maximum impact parameter was 2.5 A.

Figure 8 compares the FHO-FR and the DIDIEX V-T probabilities. One can see the remarkable agreement in the entire collision energy range considered, both for single-quantum and multi-quantum processes, up to s=5. Figure 9 shows that the agreement is also very good for the V-T probabilities at high vibrational quantum numbers, i~40. To illustrate a breakdown of the one-dimensional first-order perturbation theory (SSH theory), Fig. 9 also shows the SSH probability of the vibrational transition (40,0→39,0), which is in complete disagreement with both the three-dimensional model (FHO-FR) and the trajectory calculations. Note that calculations using DIDIEX are rather time-consuming, especially for multi-quantum processes, which require a large number of vibrational states in each molecule for the wavefunction expansion. Therefore the rest of calculations has been performed using a simpler code DIDIAV. The difference between the predictions of the two codes typically does not exceed 10-30%, except for the multi-quantum quantum processes at high collision energies ($E \geq 10^5$ cm^{-1} for transitions ($i,0 \rightarrow 0,0$) in nitrogen), when the difference increases up to a factor of 2-3. At these conditions, the predictions of DIDIEX are considered to be more accurate.

Figures 10-12 compare the FHO-FR and the DIDIAV V-V probabilities. Again, the agreement is quite satisfactory both for the resonance (Figs. 10,11) and non-resonance (Fig. 12) single-quantum and multi-quantum V-V processes. The SSH probability of the transition ($40,39 \rightarrow 39,40$), shown in Fig. 11, completely disagrees with both three-dimensional models in the entire collision energy range, which again illustrates that one-dimensional perturbation theories are inapplicable for the high vibrational quantum numbers.

The results of the model validation calculations discussed above demonstrate that the analytic FHO-FR formulae given by Eqs. (4,6,7,10,11) accurately predict the transition probability dependence on all collision parameters such as total collision energy, molecular orientation during the collision, rotational energies, and impact parameter. The model is applicable in a very wide range of collision energies and vibrational quantum numbers, as well as for processes of transfer of many vibrational quanta. Thus, taking into account (i) modulation of the interaction potential by the molecular rotation which is assumed to be free, (ii) non-zero impact parameters collisions using the modified wavenumber approximation, and (iii) many-state coupling using the FHO model, permits capturing the principal mechanism of molecule-to-molecule vibrational energy transfer and gives an accurate three-dimensional analytic rate model.

4. Averaging the probabilities and discussion

To make the FHO-FR model useful for practical calculations, we have to find the transition probabilities as functions of total collision energy E, that is to integrate the probabilities over the angles ϑ_1, ϑ_2, φ_1, φ_2, the rotational energies ε_1 and ε_2, and the impact parameter y. The multidimensional integral is evaluated by steepest descent method, which typically introduces an integration error of about 30-70%. Following the procedure [37], we first obtain the optimum configuration when the V-T probability at the given total collision energy E reaches maximum,

$$\vartheta_1^* = \vartheta_2^* = -\frac{\pi}{4}; \quad \varphi_1^* = \varphi_2^* = 0; \quad \varepsilon_1^* = \varepsilon_2^* = \frac{1}{6}; \quad y^* = 0; \quad \gamma^* = \sqrt{3/2} \qquad (12)$$

The location of the optimum configuration is in excellent agreement with the predictions of the trajectory calculations (see Section 3, Figs. 2,4,6). The maximum probability for this optimum configuration, $P(i_1,0\rightarrow f_1,0)^*$, is given by Eq. (6), where now

$$Q^* = \frac{\theta'}{2\theta}\exp\left[-\frac{2\pi\omega}{\alpha u\sqrt{3/2}}\right] \tag{13}$$

The superscript "*" will denote the optimum configuration parameters through the remainder of this chapter. One can see that zero impact parameter collisions ($y^*=0$) are most efficient for the vibrational energy transfer. However, the probability reaches maximum for a non-collinear collision ($\vartheta_1^*=\vartheta_2^*=-\pi/4$) of rotating molecules ($\varepsilon_1^*=\varepsilon_2^*=1/6$), when the angular momentum vector is perpendicular to the velocity vector **v** near the point of maximum interaction ($\varphi_1^*=\varphi_2^*=0$) (see Fig. 1). Expanding the probability of Eq. (6) in a series near the optimum configuration point (12) and integrating, one obtains

$$\begin{aligned} P(i_1,0\rightarrow f_1,0,E,Q^*<s^{th}) \approx {} & \frac{(n_s)^s}{(s!)^2}\left(\frac{3}{2}\right)^4\left(\frac{\alpha u}{\pi\omega s}\right)^4 (Q^*)^s \\ & \times\exp\left[-\frac{2n_s}{s+1}Q^* - \frac{n_s^2}{(s+1)^2(s+2)}Q^{*2}\right] \end{aligned} \tag{14}$$

where Q^* is given by Eq. (13) and

$$s^{th} = \frac{(s+1)(s+2)}{2n_s}\left(\sqrt{\frac{3s+2}{s+2}}-1\right) \quad , \tag{15}$$

At $Q^*\geq s^{th}$, i.e. at the high collision energies, the procedure for the probability integration becomes more cumbersome, since the optimum configuration of collision parameters, such as given by Eq. (12) is no longer unique (see discussion in [37]).

Repeating this procedure for the V-V processes, we obtain the optimum configuration, which in this case is collinear,

$$\vartheta_1^* = \vartheta_2^* = \varphi_1^* = \varphi_2^* = \varepsilon_1^* = \varepsilon_2^* = y^* = 0; \quad \gamma^* = 1, \tag{16}$$

Again, the location of this optimum configuration is in excellent agreement with the predictions of the trajectory calculations (see Section 3, Figs. 3,5,7). The maximum probability for the optimum configuration is given by Eq. (7), where

$$G^* = \left(\frac{\alpha u}{2}\right)^2 \frac{1}{\omega_1 \omega_2} \left[\frac{\xi}{\sinh(\xi)}\right]^2, \quad \xi = \frac{\pi(\omega_1 - \omega_2)}{\alpha u} \tag{17}$$

Expansion the probability of Eq. (7) in a series near the optimum configuration point (16) and integration over the angles, rotational energies, and impact parameters, gives

$$P(i_1, i_2 \rightarrow f_1, f_2, E, G^* < s^{th}) = \underbrace{\frac{\left(1 + \frac{1}{2^{s-1}}\right)^4}{2^{s+8}(s+1)^2}}_{F(s)} \frac{(n_{s,1})^s (n_{s,2})^s}{(s!)^2} (G^*)^s \times \exp\left[-\frac{2n_s}{s+1} G^* - \frac{n_s^2}{(s+1)^2 (s+2)} G^{*2}\right], \tag{18}$$

where now

$$s^{th} = \frac{(s+1)(s+2)}{2n_{s,1} n_{s,2}} \left(\sqrt{\frac{3s+2}{s+2}} - 1\right) \tag{19}$$

Note that at s=1 and $G^* \ll 1$, Eq. (18) looks almost exactly as the expression for the one-dimensional SSH probability (1,0→0,1) [39] except for the factor F(1)=1/128. This is the three-dimensional "steric factor" which describes the V-V probability reduction due to non-collinear orientation, molecular rotation, and non-zero impact parameter collisions. Again, at the high collision energies, such as $G^* \geq s^{th}$, non-uniqueness of the optimum configuration substantially complicates the analysis. The complete closed form expressions for the V-T and V-V probabilities that span both low and high collision energies, such as obtained for atom-molecule collisions in [37], will be given in our next publication.

Thermally averaged relaxation rate coefficients can be determined by averaging of the transition cross-sections over the Boltzmann distribution [42]:

$$k(i_1,i_2 \to f_1,f_2,T) = \langle u \rangle \int_0^\infty \sigma(\overline{E}) \exp\left(-\frac{\overline{E}}{T}\right) d\left(\frac{\overline{E}}{T}\right) = \pi R_0^2 \langle u \rangle \int_0^\infty \left(\frac{\overline{E}}{T}\right)^3 P(\overline{E}) \exp\left(-\frac{\overline{E}}{T}\right) d\left(\frac{\overline{E}}{T}\right) \qquad (20)$$

In Eq. (20), $\langle u \rangle = \left(\frac{8kT}{\pi m}\right)^{1/2}$, $\overline{E} = E + \Delta E/2 + (\Delta E)^2/16E$ is the symmetrized collision energy [42], ΔE is vibrational energy defect, $\sigma(\overline{E})$ is the cross-section, and $P(\overline{E})$ is the transition probability. The factor $\pi R_0^2 \cdot (\overline{E}/T)^3$ in the expression for the cross-section appears due to integration over the values of orbital kinetic energy (or orbital angular momentum) and two rotational energies (or rotational angular momenta) [42]. The maximum interaction distance R_0 is found as $U(R_0)=kT$, $R_0 \cong 2.5$ A at $T \sim 10^4$ K. Then the effective cross section for elastic collisions is $\langle\langle \sigma_{el} \rangle\rangle = \frac{k_{el}(T)}{\langle u \rangle} = 3\pi R_0^2 \approx 60\ A^2$, and the gas kinetic collision frequency is $Z = 3\pi R_0^2 \langle u \rangle$.

Evaluation of the integral in Eq. (20) using the V-T probability (14) yields

$$\begin{aligned} k(i_1,0 \to f_1,0,T) = {} & Z \frac{9}{2} \sqrt{\frac{2\pi}{3}} \frac{(n_s)^s}{(s!)^2} \left(\frac{\theta'}{2\theta}\right)^s \left(\frac{Ts^2}{\theta'}\right)^{1/6} \exp\left[-\frac{3}{2}\left(\frac{\theta' s^2}{(3/2)T}\right)^{1/3}\right] \\ & \times \exp\left\{-\frac{2n_s}{s+1} \exp\left[-\frac{3}{2}\left(\frac{\theta'}{(3/2)sT}\right)^{1/3}\right] - \frac{n_s^2}{(s+1)^2(s+2)} \exp\left[-3\left(\frac{\theta'}{(3/2)sT}\right)^{1/3}\right]\right\} \qquad (21) \\ & \times \exp\left\{\frac{\theta s}{2T}\left(1 - \frac{\theta}{4T}\left(\frac{(3/2)T}{\theta' s^2}\right)^{1/3}\right)\right\}, \end{aligned}$$

The last exponential factor in Eq. (21) originates from the symmetrization of collision energy in Eq. (20). Following the procedure suggested in [42], we evaluate the rates of exothermic processes. The endothermic rates can be found simply as $k_{endo} = k_{exo} \cdot \exp(-\theta s/T)$. Eq. (21) is valid only if $T \leq T^{th}$, where T^{th} is the threshold temperature that corresponds to the "switching" from the unique to the multiple optimum configuration regime (see [37]),

$$T^{th} = \frac{2\theta'}{33\ln^2\left[\frac{\theta'}{3s^{th}\theta}\right]} \tag{22}$$

The values of the threshold temperature for N_2-N_2 collisions, given by Eqs. (22), change from T^{th}=11,000 K for the transition 1→0 to T^{th}=1,300 K for the transition 40→39. More elaborate integration is needed to obtain the closed form analytic V-T rates at higher temperatures.

Integration of Eq. (20) using the V-V probability of Eq. (18) at $\xi=0$ (for the resonance V-V processes) yields

$$\begin{aligned} k(i_1,i_2 \rightarrow i_2,i_1,T) = Z &\underbrace{\frac{\left(1+\frac{1}{2^{s-1}}\right)^4}{2^{s+8}(s+1)^2}\,\frac{(s+3)!}{3!}}_{F(s)}\,\frac{(n_{s,1})^s(n_{s,2})^s}{(s!)^2}\left(\frac{\alpha^2 kT}{2m\omega^2}\right)^s \\ &\times\frac{1}{\left(1+\frac{2n_{s,1}n_{s,2}}{s+1}F(s)\,\frac{\alpha^2 kT}{2m\omega^2}\right)^{s+4}} \end{aligned} \tag{23}$$

One can see that the thermally averaged three-dimensional "steric factor" for single-quantum V-V exchange in Eq. (23), F(1)=1/32, is different from the value obtained by the modified SSH theory, 1/9 [24], and changes with the number of transmitted quanta, s. Integration at $\xi \neq 0$ becomes less straightforward and requires additional analysis, which we intend to complete in our next publication.

Eq. (23) is valid if $T \leq T^{th}$, where T^{th} is given by

$$T^{th} = \frac{2m\omega^2}{\alpha^2 k} s^{th} \tag{24}$$

For N_2-N_2 collisions, T^{th}=4,000 K for the transition 10,9→9,10 but drops to only T^{th}=250 K for the transition 40,39→39,40. Again, more elaborate integration is needed to obtain the closed form analytic V-V rates at higher temperatures.

While the complete analytic FHO-FR V-T and V-V rate expressions are not yet available, we compared the rates coefficients obtained by numerical integration of the analytic FHO-FR V-T probabilities given by Eqs. (6,10,20) and V-V probabilities given by Eqs. (7,11,20) over all collision parameters, with trajectory calculations for N_2-N_2. Figs. 13,14 show that the results are in remarkably good agreement in the temperature range of $200 \leq T \leq 10000$ K and vibrational quantum number range $0 \leq i \leq 40$. Although multi-quantum FHO-FR rate coefficients are not shown, comparison of the probabilities in Figs. 8-12 leaves no doubt that the agreement is equally good.

Finally, the FHO-FR model predictions for O_2-O_2 relaxation rates has been compared with (i) experimental data [6-8], (ii) three-dimensional semiclassical calculations by DIDIAV using the potential energy surface [20], which takes into account the long-range dispersion and quadrupole-quadrupole interaction terms, and (iii) three-dimensional quantum calculations using *ab initio* potential energy surface [13], rather than the simplified atom-to-atom potential [20]. Analytic FHO-FR relaxation rates have been evaluated using Eq. (3) with α=4.0 A^{-1}, which has been determined in [20] from the best fit of the short-range potential energy surface to ab initio data. The results, shown in Fig. 15, again demonstrate good agreement between experimental data, analytic model, and three-dimensional calculations.

5. Summary

Analysis of classical trajectories of free-rotating symmetric diatomic molecules acted upon by a repulsive potential allow extending a three-dimensional semiclassical nonperturbative analytic model of vibrational energy transfer (FHO-FR model) to molecule-molecule collisions. The model takes into account the following coupled effects: (i) interaction potential modulation by free rotation of arbitrarily oriented molecules during a collision, (ii) reduction of the effective collision velocity in non-zero impact parameter collisions of rotating molecules, and (iii) multi-state coupling in a collision.

The FHO-FR model predictions have been compared with close-coupled semiclassical trajectory calculations using the same potential energy surface. The comparison demonstrates not only very good agreement between the analytic and numerical probabilities across a wide range of collision energies, but also shows that the analytic model correctly reproduces the probability dependence on other collision parameters such as rotation angles, angular momentum angles, rotational energies, and impact parameter. The model equally well predicts the cross-sections of single-quantum and multi-quantum V-T and V-V transitions and is applicable up to very high collision energies and quantum numbers. The resultant analytic expressions for the probabilities do not contain any arbitrary adjustable parameters commonly referred to as "steric factors". The results obtained in the present work can be used for calculations of the state-specific V-T and V-V relaxation rates in collisions of symmetric or nearly symmetric molecules such as N_2-N_2, O_2-O_2, and N_2-O_2. Thus, the present work essentially completes development of the analytic rate database for vibrational energy transfer among air species, increasing the range of applicability of the FHO-FR model (previous results [37] are applicable for N_2-Ar, O_2-Ar, N_2-He, and O_2-He V-T relaxation). It remains an open question, however, whether the approach used here is applicable for calculations of vibrational energy transfer rates induced by the long-range multipole-multipole interaction, such as occurs in CO-CO and CO-N_2 collisions. Recently, FHO-FR model has also been used for prediction of nonequilibrium dissociation rates of diatomic molecules, showing satisfactory agreement with experimental measurements behind the shock waves [44].

The FHO-FR model provides new insight into kinetics of vibrational energy transfer and provides analytic expressions for state-specific transition probabilities and rate coefficients, applicable in the wide range of collision energies and temperatures that can be easily incorporated into existing nonequilibrium flow codes. FHO-FR V-T transition probabilities in molecule-molecule collisions have been recently used in DSMC modeling of nonequilibrium hypersonic flows [45]. Closed form analytic expressions for the V-T and V-V rates valid in a wide range of collision energies will be completed and published in the near future.

References

1. Gordiets, B.F., Osipov, V.A., and Shelepin, L.A., Kinetic Processes in Gases and Molecular Lasers, Gordon and Breach, London, 1988, Chaps. 3,4
2. Cacciatore, M., Capitelli, M., DeBenedictis, S., Dilonardo, M., and Gorse, C., "Vibrational Kinetics, Dissociation and Ionization of Diatomic Molecules under Nonequilibrium Conditions", Nonequilibrium Vibrational Kinetics, Springer-Verlag, Berlin, 1986, Chap. 2, pp. 5-46
3. Park, C., Nonequilibrium Hypersonic Aerodynamics, Wiley, New York, 1990, Chap. 3
4. W. Lee, M. Chidley, R. Leiweke, I. Adamovich, and W.R. Lempert, "Determination of O_2 and N_2 Vibrational State Distributions in CO Laser-Sustained Plasmas", AIAA Paper 99-3723, 30th AIAA Plasmadynamics and Lasers Conference, Norfolk, VA, June 28 – July 1, 1999
5. Yang, X., Kim, E.H., and Wodtke, A.M., "Vibrational Energy Transfer of Very Highly Vibrationally Excited NO", Journal of Chemical Physics, Vol. 96, No. 7, 1992, pp. 5111-5122
6. Price, J.M., Mack, J.A., Rogaski, C.A., and Wodtke, A.M., "Vibrational-State-Specific Self-Relaxation Rate Constant Measurements of Highly Excited $O_2(v=19\text{-}28)$", Chemical Physics, Vol. 175, No. 1, 1993, pp. 83-98
7. Park, H., and Slanger, T.G., "O (X, v=8-22) 300 K Quenching Rate Coefficients for O_2 and N_2, and $O_2(X)$ Vibrational Distribution from 248 nm O_3 Photo-dissociation", Journal of Chemical Physics, Vol. 100, No. 1, 1994, pp. 287-300
8. Klatt, M., Smith, I.W.M., Tuckett, R.P., and Ward, G.N., "State-Specific Rate Constants for the Relaxation of $O_2(X^3\Sigma_g^-)$ from Vibrational Levels v=8 to 11 by Collisions with NO and O ", Chemical Physics Letters, Vol. 224, Nos. 3,4, 1994, pp. 253-257
9. Deleon, R., and Rich, J.W., "Vibrational Energy Exchange Rates in Carbon Monoxide", Chemical Physics, Vol. 107, No. 2, 1986, pp. 283-292
10. Secrest, D., and Johnson, B.R., "Exact Quantum Mechanical Calculations of a Collinear Collision of a Particle with a Harmonic Oscillator", Journal of Chemical Physics, Vol. 45, No. 12, 1966, pp. 4556-4570
11. Chapuisat, X., Bergeron, G., and Launay, J.-M., "A Quantum-Mechanical Collinear Model Study of the Collision N_2-O_2", Chemical Physics, Vol. 20, No. 2, 1977, pp. 285-298

12. Chapuisat, X., and Bergeron, G., "Anharmonicity Effects in the Collinear Collision of Two Diatomic Molecules", Chemical Physics, Vol. 36, No. 3, 1979, pp. 397-405
13. R. Hernandez, R.Toumi, and D.C. Clary, "State-Selected Vibrational Relaxation Rates for Highly Vibrationally Excited Oxygen Molecules", Journal of Chemical Physics, Vol. 102, No. 24, 1995, pp. 9544-9558
14. Kuksenko, B.V., and Losev, S.A., "On the Theory of Vibrational Relaxation of Diatomic Molecules", High Temperature, Vol. 6, No. 5, 1968, pp. 794-799
15. Lagana, A., Garcia, E., and Ciccarelli, L., "Deactivation of Vibrationally Excited Nitrogen Molecules by Collision with Nitrogen Atoms", Journal of Physical Chemistry, Vol. 91, 1987, pp. 312-314
16. Lagana, A., and Garcia, E., "Temperature Dependence of $N+N_2$ Rate Coefficients", Journal of Physical Chemistry, Vol. 98, 1994, pp. 502-507
17. Billing, G.D., "Vibration-Vibration and Vibration-Translation Energy Transfer, Including Multiquantum Transitions in Atom-Diatom and Diatom-Diatom Collisions", Nonequilibrium Vibrational Kinetics, Springer-Verlag, Berlin, 1986, Chap. 4, pp. 85-111
18. R.E. Kolesnick, and Billing, G.D., "Rate Constants for Vibrational Transitions in Hydrogen and Isotopes", Chemical Physics, Vol. 170, No. 1, 1993, pp. 201-207
19. Billing, G.D., and Fisher, E.R., "VV and VT Rate Coefficients in N_2 by a Quantum-Classical Model", Chemical Physics, Vol. 43, No.3, 1979, pp. 395-401
20. Billing, G.D., and Kolesnick, R.E., "Vibrational Relaxation of Oxygen. State to State Rate Constants", Chemical Physics Letters, Vol. 200, No. 4, 1992, pp. 382-386
21. Cacciatore, M., and Billing, G.D., "Semiclassical Calculations of VV and VT Rate Coefficients in CO", Chemical Physics, Vol. 58, No. 3, 1981, pp. 395-407
22. Billing, G.D., "VV and VT Rates in N_2-O_2 Collisions", Chemical Physics, Vol. 179, No. 3, 1994, pp. 463-467
23. Cacciatore, M., Capitelli, M., and Billing, G.D., "Theoretical Semiclassical Investigation of the Vibrational Relaxation of CO Colliding with $^{14}N_2$", Chemical Physics, Vol. 89, No. 1, 1984, pp. 17-31
24. Herzfeld, K.F., and Litovitz, T.A., Absorption and Dispersion of Ultrasonic Waves, Academic, New York, 1959, Chap. 3
25. Rapp, D., and Sharp, T.E., "Vibrational Energy Transfer in Molecular Collisions Involving

Large Transition Probabilities", Journal of Chemical Physics, Vol. 38, No. 11, 1963, pp. 2641-2648

26. Rapp, D., and Englander-Golden, P., "Resonant and Near-Resonant Vibrational-Vibrational Energy Transfer between Molecules in Collisions", Journal of Chemical Physics, Vol. 40, No.2, 1964, pp. 573-575; Rapp, D., and Englander-Golden, P., "Erratum: Resonant and Near-Resonant Vibrational-Vibrational Energy Transfer between Molecules in Collisions", Journal of Chemical Physics, Vol. 40, No.10, 1964, pp. 3120-3121; Rapp, D., "Interchange of Vibrational Energy between Molecules in collisions", Journal of Chemical Physics, Vol. 43, No.1, 1965, pp. 316-317
27. Sharma, R.D., and Brau, C.A., "Energy Transfer in Near-Resonant Molecular Collisions Due to Long-Range Forces with Application to Transfer of Vibrational Energy from ν_3 Mode of CO_2 to N_2", Journal of Chemical Physics, Vol. 50, No. 2, 1969, pp. 924-930
28. Kerner, E.H., "Note of the Forced and Damped Oscillations in Quantum Mechanics", Canadian Journal of Physics, Vol. 36, No.3, 1958, pp. 371-377
29. Treanor, C.E., "Vibrational Energy Transfer in High Energy Collisions", Journal of Chemical Physics, Vol. 43, No.2, 1965, pp. 532-538
30. Zelechow, A., Rapp, D., and Sharp, T.E., "Vibrational-Vibrational-Translational Energy Transfer between Two Diatomic Molecules", Journal of Chemical Physics, Vol. 49, No. 1, 1968, pp. 286-299
31. Kelley, J.D., "Vibrational Energy Transfer Processes in Collision between Diatomic Molecules", Journal of Chemical Physics, Vol. 56, No. 12, 1972, pp. 6108-6117
32. Shin, H.K., "Vibrational Energy Transfer", Dynamics of Molecular Collisions, Plenum, New York, 1976, Part A, Chap. 4, pp. 131-210
33. Schwartz, R.N., and K.F. Herzfeld, Journal of Chemical Physics, Vol. 22, No. 2, 1954, pp. 767-
34. Takayanagi, K., Progress in Theoretical Physics (Kyoto), Vol. 8, 1952, pp. 8-
35. Mies, F.H., and Shuler, K., Journal of Chemical Physics, Vol. 37, No. 1, 1962, pp. 177-
36. I.V. Adamovich and J.W. Rich, "Three-Dimensional Nonperturbative Analytic Model of Vibrational Energy Transfer in Atom-Molecule Collisions", AIAA Paper 98-2953, 7th AIAA/ASME Joint Thermophysics and Heat Transfer Conference, June 1998, Albuquerque, NM

37. I.V. Adamovich and J.W. Rich, "Three-Dimensional Nonperturbative Analytic Model of Vibrational Energy Transfer in Atom-Molecule Collisions", Journal of Chemical Physics, vol. 109, No. 18, 1998, pp. 7711-7724
38. Nikitin, E.E., and Osipov, A.I., "Vibrational Relaxation in Gases", Kinetics and Catalysis, Vol. 4, VINITI, All-Union Institute of Scientific and Technical Information, Moscow, 1977, Chap. 2
39. Rapp, D., and Kassal, T., "The Theory of Vibrational Energy Transfer between Simple Molecules in Nonreactive Collisions", Chemical Reviews, Vol. 69, No. 1, 1969, pp. 61-102
40. Adamovich, I.V., Macheret, S.O., Rich, J.W., and Treanor. C.E., "Vibrational Relaxation and Dissociation Behind Shock Waves Part 1: Kinetic Rate Models", AIAA Journal, Vol. 33, No. 6, 1995, pp. 1064-1069
41. Adamovich, I.V., Macheret, S.O., Treanor, C.E., and Rich, J.W., "Vibrational Energy Transfer Rates Using a Forced Harmonic Oscillator Model", Journal of Thermophysics and Heat Transfer, Vol. 12, No. 1, 1997, pp. 57-
42. Billing, G.D., "Rate Constants and Cross Sections for Vibrational Transitions in Atom-Diatom and Diatom-Diatom Collisions", Computer Physics Communications, Vol. 32, No. 1, 1984, pp. 45-62
43. Billing, G.D., "Rate Constants for Vibrational Transitions in Diatom-Diatom Collisions", Computer Physics Communications, Vol. 44, 1987, pp. 121-136
44. Macheret, S.O., and Adamovich, I.V., "Nonequilibrium Dissociation at High Temperature - The Role of Vibrational and Rotational Energy", AIAA Paper 99-0351, 37th Aerospace Sciences Meeting and Exhibit, Reno, NV, Jan. 11-14, 1999
45. Gimelshein, S.F., Boyd, I.D., Sun, Q., and Ivanov, M.S., "DSMC Modeling of Vibration-Translation Energy Transfer in Hypersonic Rarefied Flows", AIAA Paper 99-3451, 33th AIAA Thermophysics Conference, Norfolk, VA, June 28 – July 1, 1999

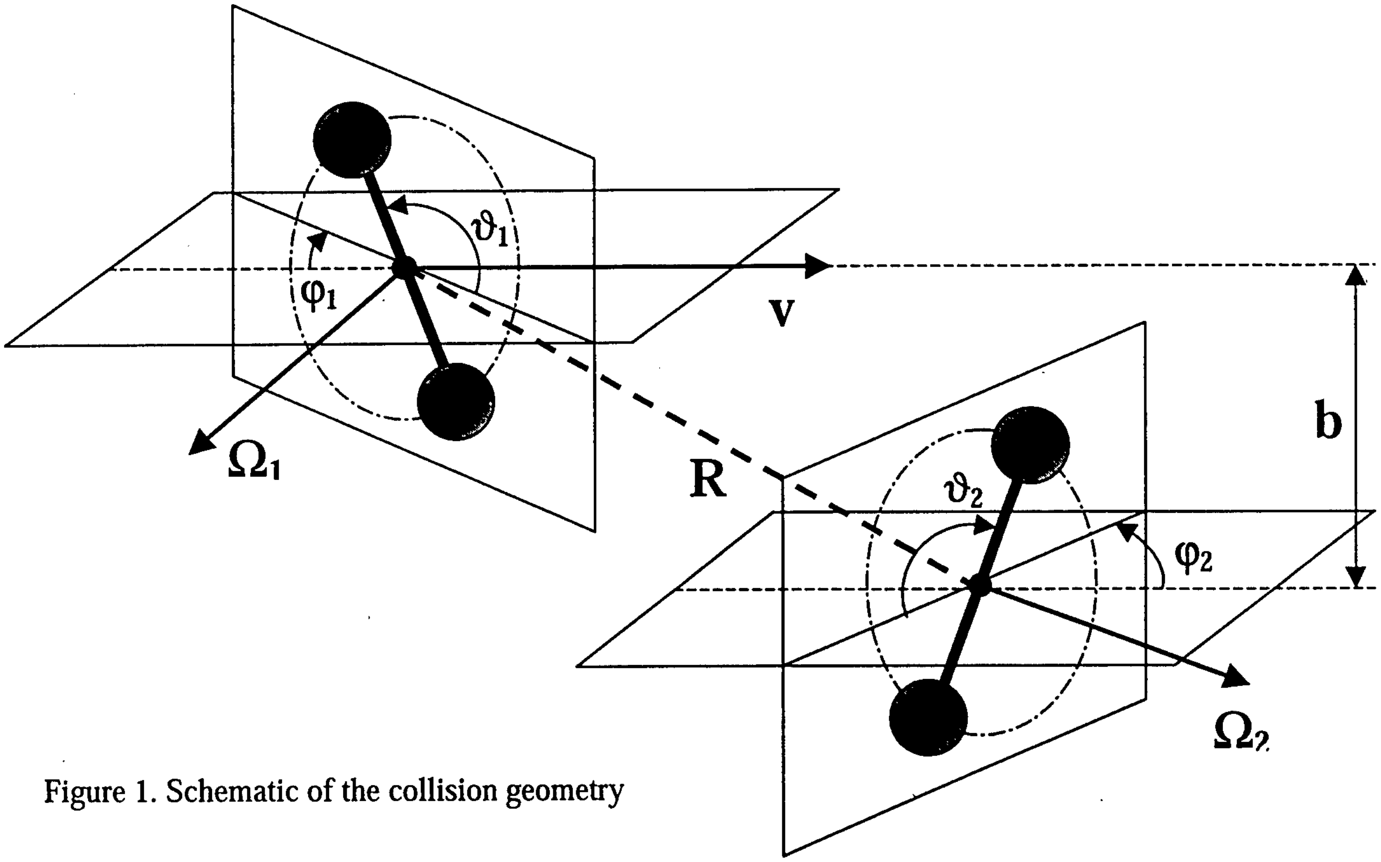

Figure 1. Schematic of the collision geometry

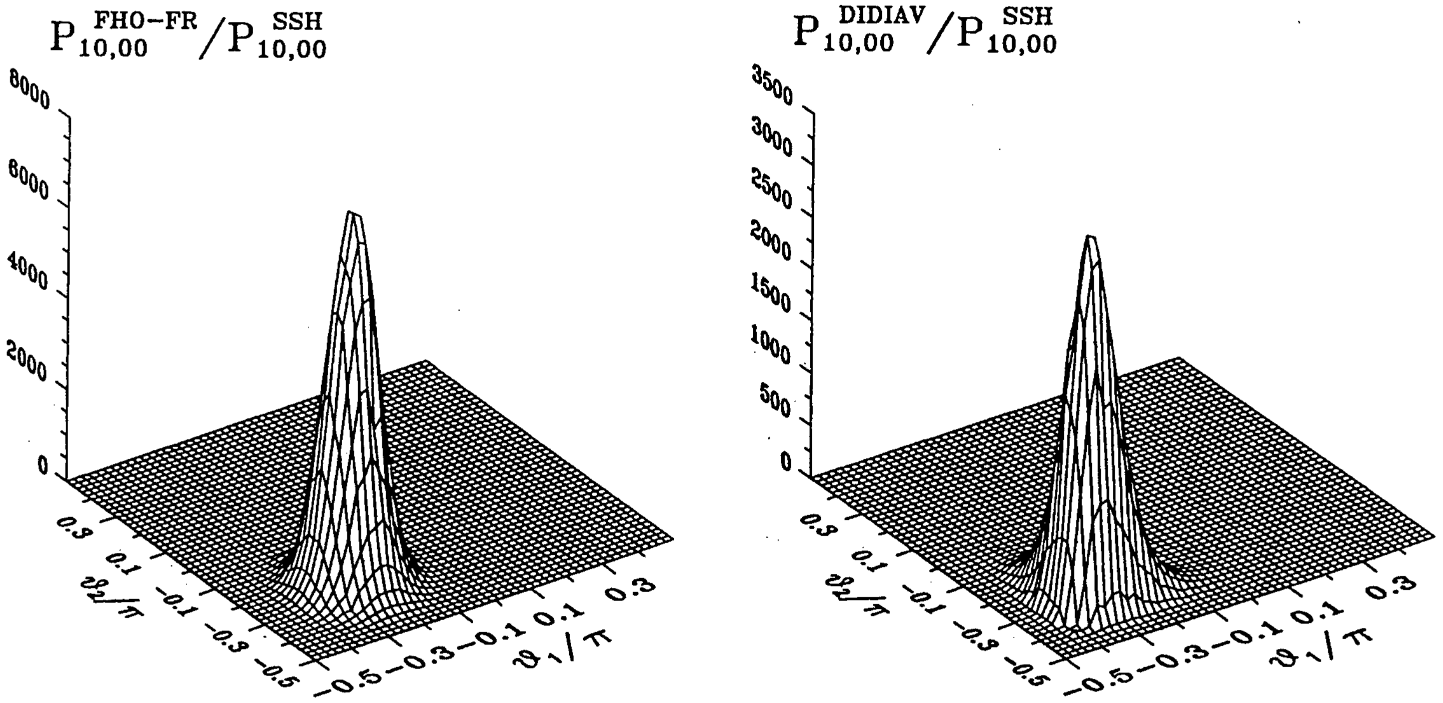

Figure 2. Comparison of the analytic FHO-FR probability and the numerical DIDIAV probability of the V-T transition (1,0→0,0) for N_2-N_2 as functions of the rotation angles ϑ_1 and ϑ_2. The total collision energy is E=1000 cm^{-1}, $\varepsilon_1=\varepsilon_2=1/6$, b=0.

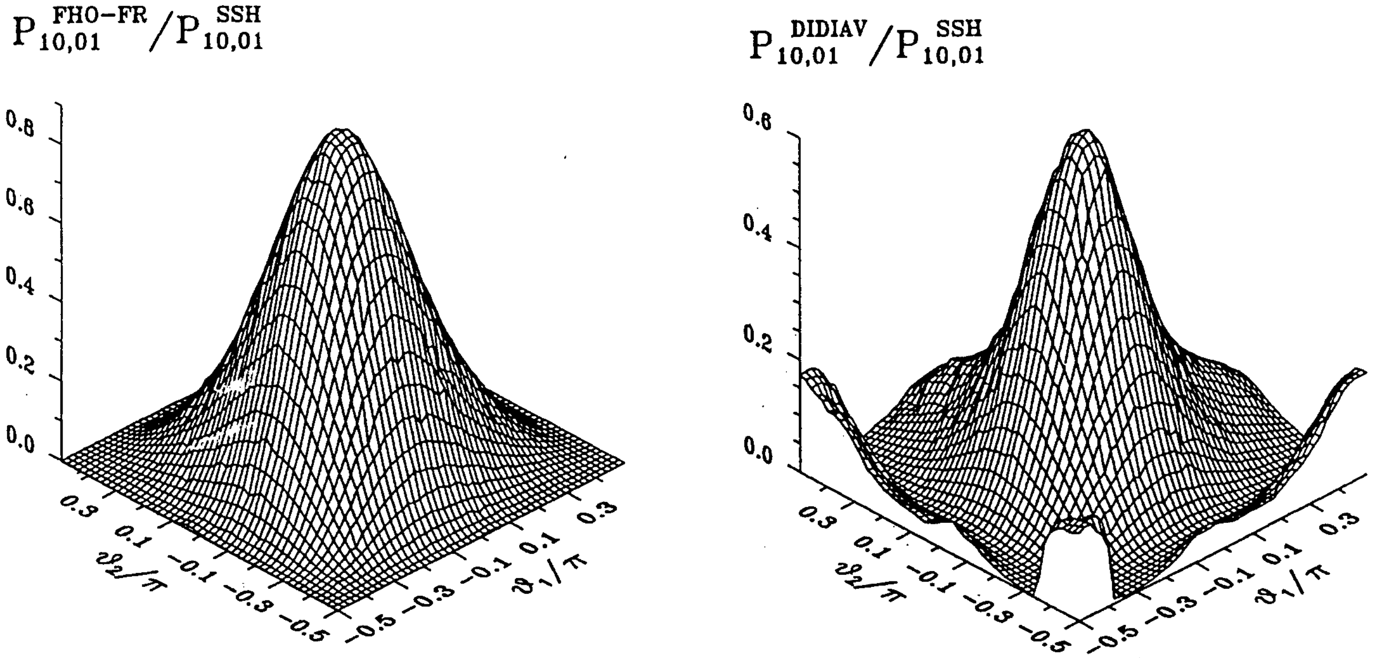

Figure 3. Comparison of the analytic FHO-FR probability and the numerical DIDIAV probability of the V-V transition (1,0→0,1) for N_2-N_2 as functions of the rotation angles ϑ_1 and ϑ_2. The total collision energy is E=1000 cm^{-1}, $\varepsilon_1=\varepsilon_2=1/6$, b=0.

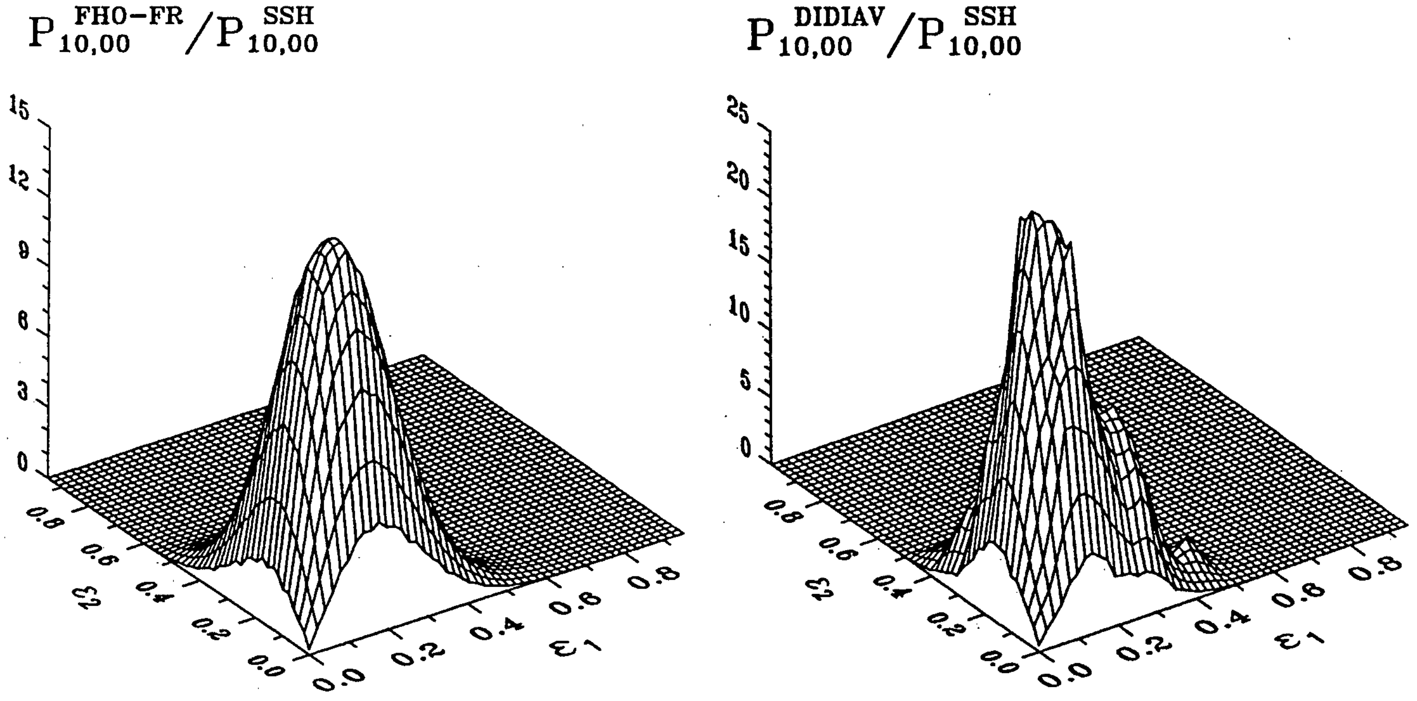

Figure 4. Comparison of the analytic FHO-FR probability and the numerical DIDIAV probability of the V-T transition (1,0→0,0) for N_2-N_2, both averaged over the collision angles $\vartheta_1, \vartheta_2, \varphi_1$, and φ_2, as functions of the rotational energies ε_1 and ε_2. The total collision energy is E=1000 cm^{-1}, b=0.

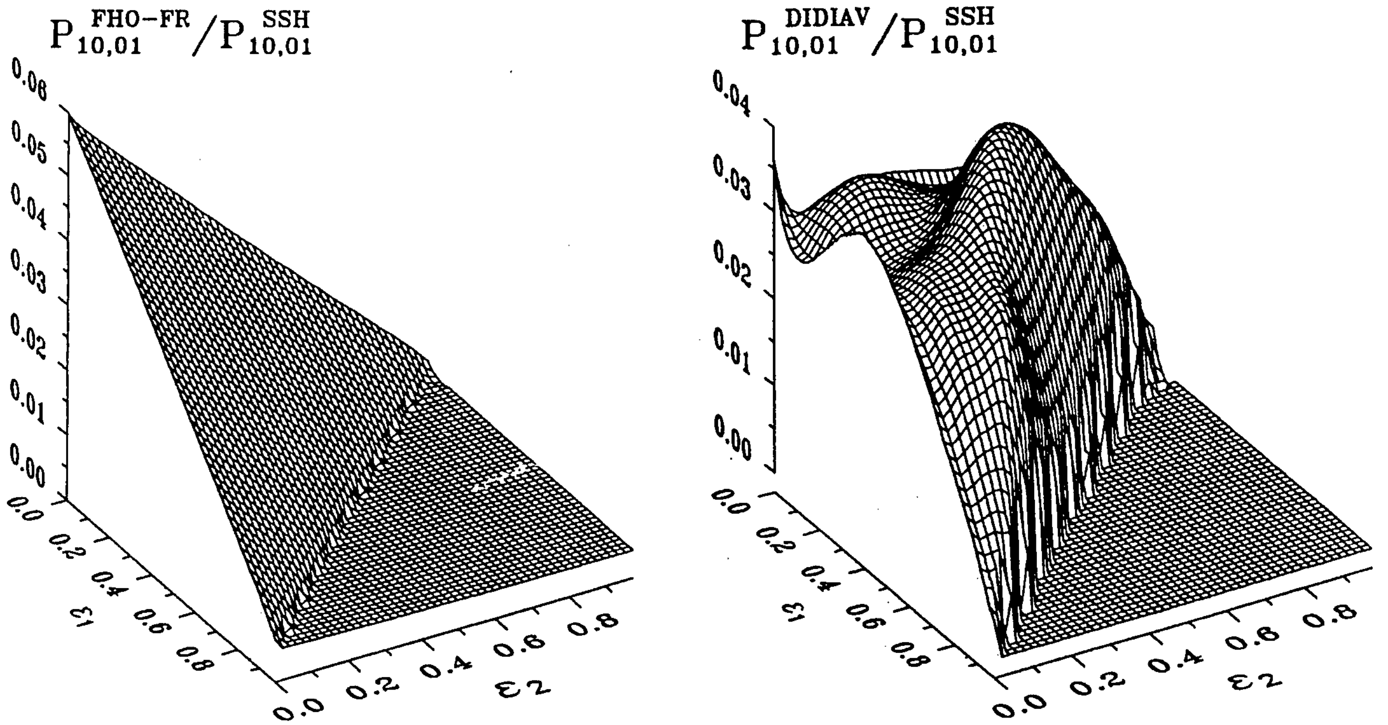

Figure 5. Comparison of the analytic FHO-FR probability and the numerical DIDIAV probability of the V-V transition (1,0→0,1) for N_2-N_2, both averaged over the collision angles $\vartheta_1, \vartheta_2, \varphi_1$, and φ_2, as functions of the rotational energies ε_1 and ε_2. The total collision energy is $E=1000$ cm^{-1}, b=0.

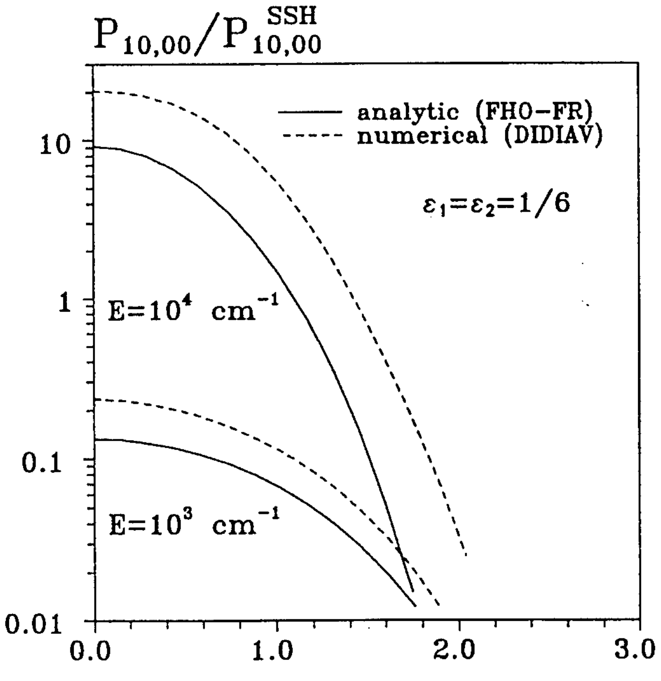

Figure 6. Comparison of the analytic FHO-FR probability and the numerical DIDIAV probability of the V-T transition (1,0→0,0) for N_2-N_2, both averaged over the collision angles ϑ_1, ϑ_2, φ_1, and φ_2, as functions of impact parameter b. $\varepsilon_1=\varepsilon_2=1/6$.

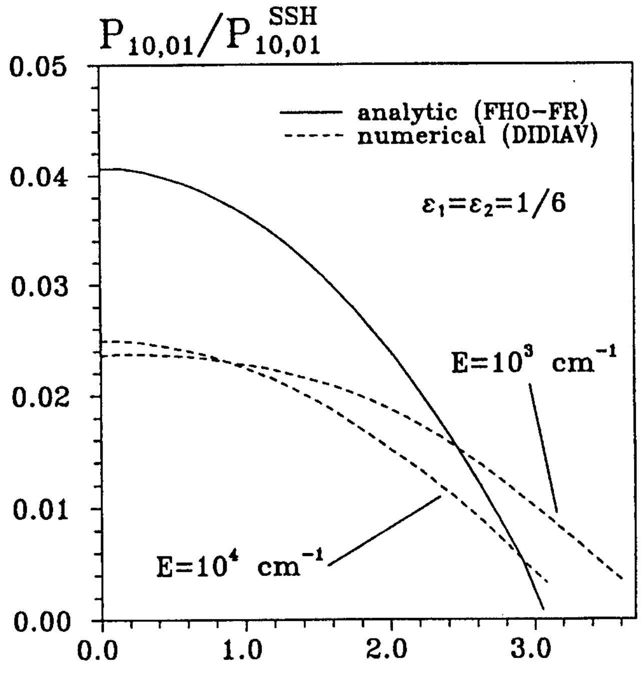

Figure 7. Comparison of the analytic FHO-FR probability and the numerical DIDIAV probability of the V-V transition (1,0→0,0) for N_2-N_2, both averaged over the collision angles ϑ_1, ϑ_2, φ_1, and φ_2, as functions of impact parameter b. $\varepsilon_1=\varepsilon_2=1/6$.

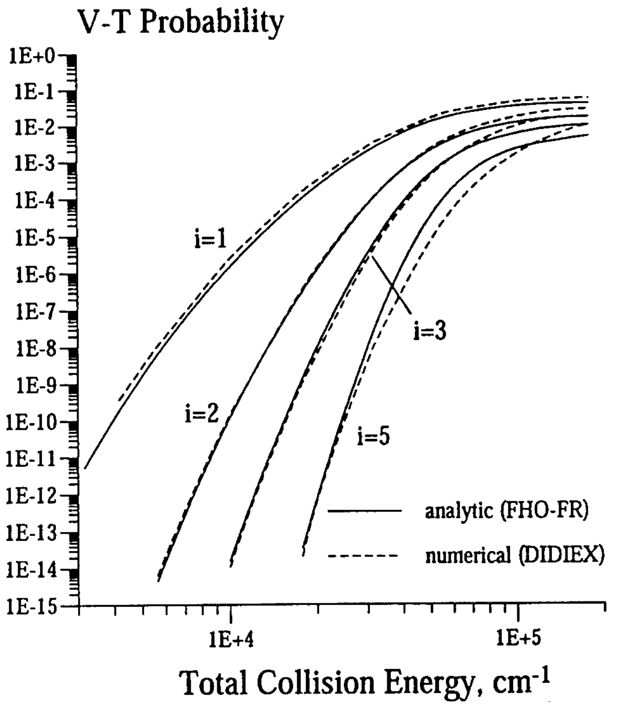

Figure 8. Comparison of analytic and numerical probabilities of V-T transitions (i,0→0,0) for N_2-N_2

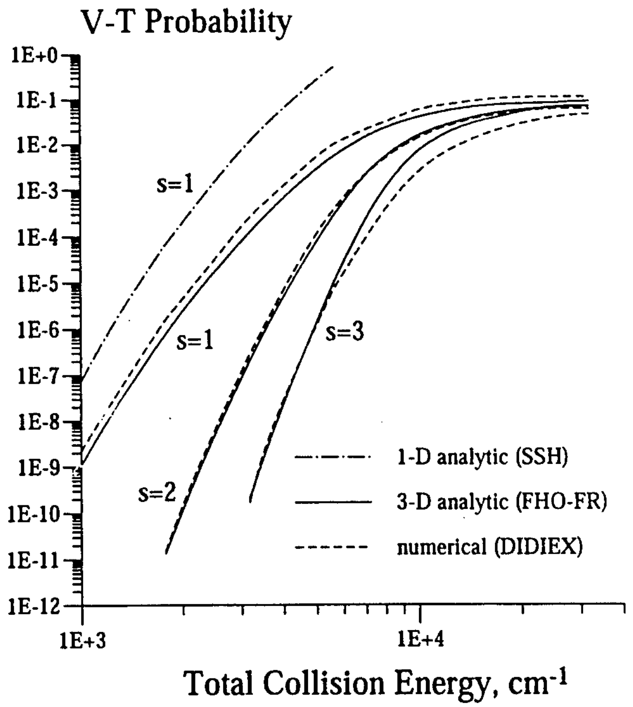

Figure 9. Comparison of analytic and numerical probabilities of V-T transitions (i,0→i-s,0) for N_2-N_2, i=40

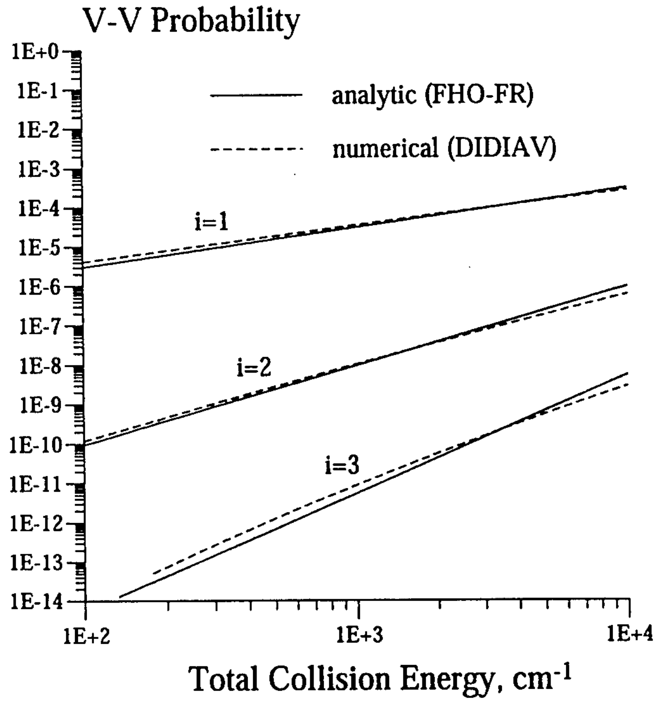

Figure 10. Comparison of analytic and numerical probabilities of resonance V-V transitions (i,0→0,i) for N_2-N_2

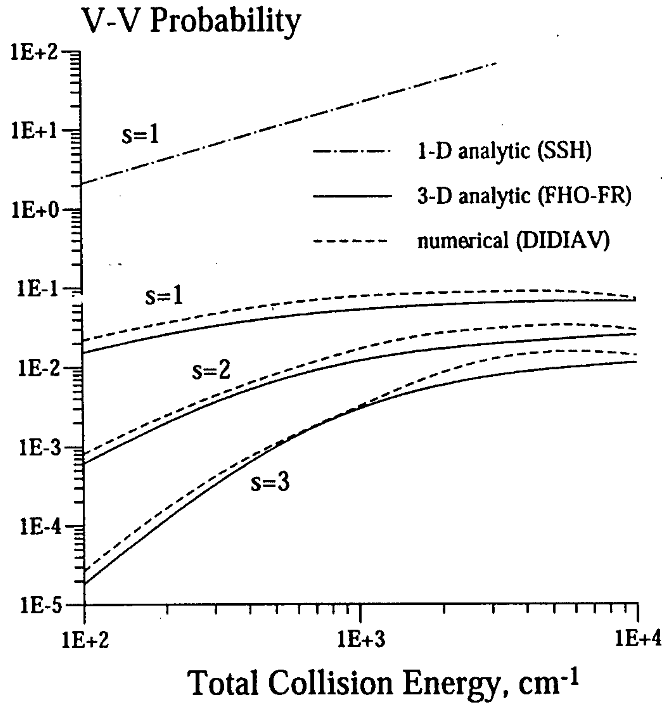

Figure 11. Comparison of analytic and numerical probabilities of resonance V-V transitions (i,i-s→i-s,i) for N_2-N_2, i=40

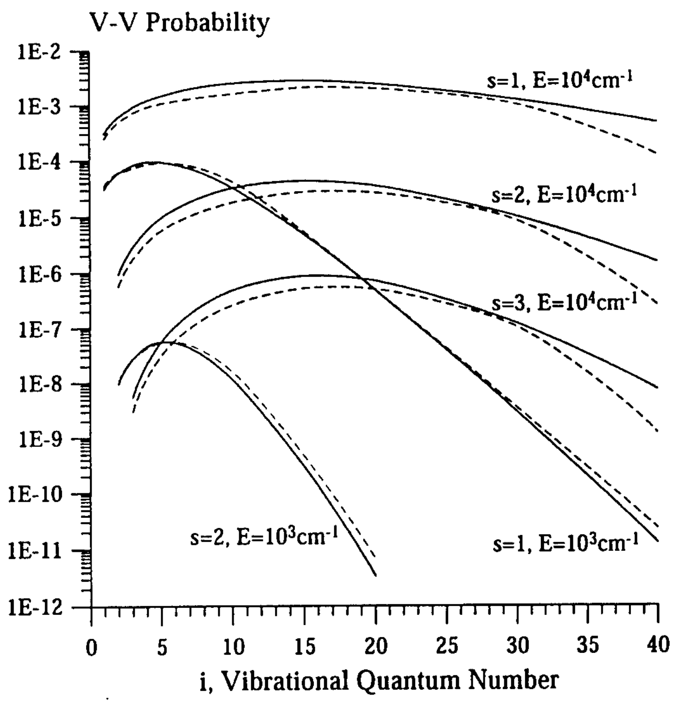

Figure 12. Comparison of analytic and numerical probabilities of non-resonance V-V transitions (i,0→i-s,s) for N_2-N_2. Solid lines, analytic (FHO-FR) model; dashed lines, trajectory calculations by DIDIAV

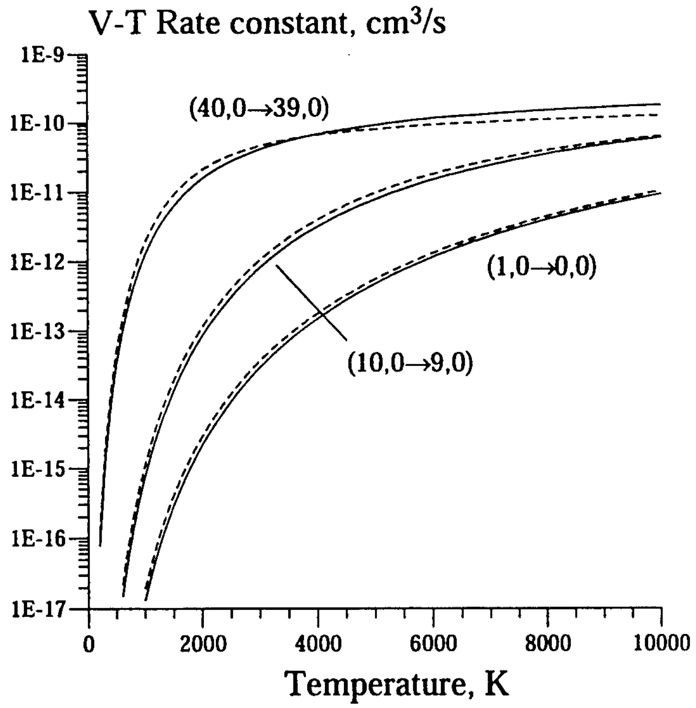

Figure 13. Comparison of analytic (solid lines) and numerical (dashed lines) rates of V-T transitions for N_2-N_2

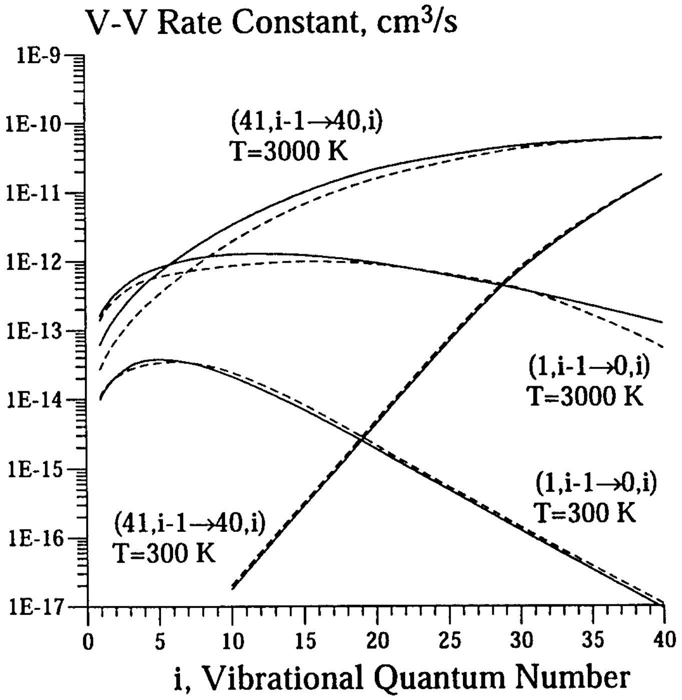

Figure 14. Comparison of analytic (solid lines) and numerical (dashed lines) rates of V-V transitions (1,i-1→0,i) and (41,i-1→40,i) for N_2-N_2

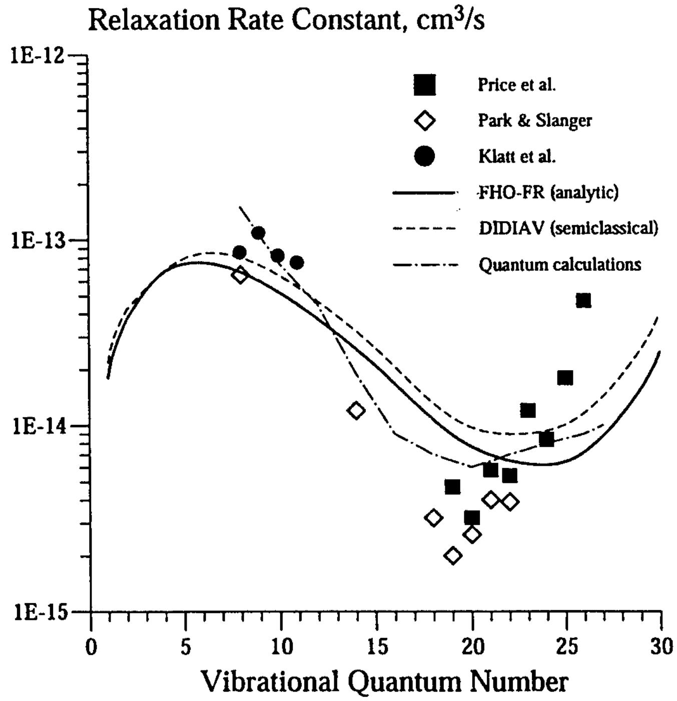

Figure 15. Comparison of analytic (solid line), semiclassical (dashed line), and quantum (dot-dashed line) calculations with experimental relaxation rates in O_2 at room temperature

CHAPTER III.

SEMICLASSICAL MODELING OF STATE-SPECIFIC DISSOCIATION RATES IN DIATOMIC GASES

1. Introduction

The vibration-dissociation coupling is of key importance to hypersonic reentry, significantly affecting aerodynamics, radiative and convective heat fluxes, and spectral signatures of vehicles flying at sub-orbital to super-orbital velocities in rarefied atmosphere. Over the last four decades, high-temperature dissociation and vibrational relaxation was a subject of a number of experimental and theoretical studies, reviewed by Park,[1] and, more recently, by Macheret.[2] A number of models, such as those suggested by Marrone and Treanor,[3] Losev,[4] and Park,[1, 6] have been used with some success to describe experimental data on nonequilibrium dissociation. Those models, however, are empirical or semiempirical, using adjustable parameters found from a fit to a limited number of experimental data, which cannot guarantee their validity outside of the calibration range.

Most models of vibrational relaxation, until recently, relied upon a first-order perturbation (FOP) method,[7] such as that used in SSH theory,[7, 8] with some modifications.[7, 9] Despite a reasonable agreement of the calculated overall relaxation times with experiments, FOP methods cannot pretend to adequately describe state-specific relaxation rates at high collision energies and temperatures typical of hypersonic bow shocks.

Recently, the authors and their colleagues have developed new theories of high-temperature relaxation[10-14] and dissociation[2, 15, 16], especially well suited for high-temperature environment. The principal idea of these theories is that at high energy of colliding particles a molecule can jump over many vibrational quantum states. These jumps can be both bound-bound (vibrational relaxation) and bound-free (dissociation), and they must be correctly accounted for even in the first approximation. For the relaxation problem, correct and convenient framework is provided by the Forced Harmonic Oscillator (FHO) model,[17-20] which naturally and consistently includes multi-quantum jumps. With relatively simple corrections for anharmonicity and enforcement of detailed balance, this model has been demonstrated to agree very well with both experimental data and sophisticated state-of-the-art quantum computations. The FHO approach was also used to model dynamics of populations of vibrational levels during relaxation, and to resolve a long-debated "bottleneck" problem.[12] Most recently, the approach was extended to explicitly account for three-dimensional motion of colliding particles and molecular rotation, resulting in a fully analytical, without adjustable parameters, non-perturbative theory of multi-quantum vibrational energy transfer.[13, 14] The important role of rotation and non-collinear collisions was clearly demonstrated, and the calculated rates agree well with experiments as well as with close-coupled quantum and semiclassical computations using full potential energy surfaces for N_2-He,[21-23] N_2-N_2,[24] and O_2-O_2.[25-29]

The recently developed dissociation model[2, 15, 16] also argued that because of availability of high kinetic energies of particles in the post-shock environment molecules can dissociate even from low vibrational states in a single collision. The model used classical impulsive (sudden) approximation to calculate both dissociation thresholds and probabilities to find the colliding pair near its optimum configuration. Vibrational state-specific and rotational energy dependent dissociation rates have been derived in closed analytical form. However successful, the model[2, 15, 16] is not free from problems. The impulsive approximation should certainly be correct as a high-energy asymptotic, but it is not clear if a real dissociating system is close to this limit. Additionally, the calculated probability factors[16] turned out to have singularities at certain energies, which calls for more sophisticated methods of evaluating the probabilities.

In the present work, we suggest a theory of state-specific dissociation rates of simple diatomic molecules. The approach is essentially a modified FHO model that allows to calculate probabilities of jumps across many quantum states, if an energy transferred to a classical initially non-vibrating oscillator can be determined. The latter value is derived for three-dimensional collisions of rotating molecules in two cases: free-rotation approximation and impulsive (sudden) limit. As a result, both state-specific and thermally-averaged dissociation rates are calculated, and roles of various degrees of freedom can be quantified.

2. The FHO-based dissociation model

Consider collisions of diatomic molecules AB with atoms M in the course of which the molecule changes its vibrational quantum state from i to f:

$$AB(i)+M \rightarrow AB(f)+M \tag{1}$$

If the molecule is modeled as a harmonic oscillator, and the collision's effect is treated as exerting a perturbing force on the oscillator, then the probability of the process (1) is:[7, 10, 11, 18]

$$P_{VRT}(i \to f,\ Q) = i!\ f!\ Q^{i+f} \exp(-Q) \left| \sum_{r=0}^{n} \frac{(-1)^r}{r!(i-r)!(f-r)!} \frac{1}{Q^r} \right|^2 \qquad (2)$$

where $n = \min(i,\ f)$, and $Q = \Delta E / \hbar\omega$ is the dimensionless energy (i.e. the average number of quanta) transferred to the initially non-vibrating classical oscillator in an AB-M collision.

The Forced Harmonic Oscillator (FHO) method is a consistent and convenient scaling tool, allowing close-coupled calculations of transitions across an arbitrary number of vibrational levels. This method reduces the complexity of the quantum problem to classical calculations of collisional energy transfer to an initially non-vibrating oscillator. The principal drawbacks of the FHO method are: i) anharmonicity of real molecules-oscillators, and ii) neglect of the reverse effect of the oscillator on the perturbing classical trajectory. The simplest way to account for the anharmonicity is to correct only frequency, and not the wavefunctions: for each transition $i \to f$, the quantity $\omega = |E_i - E_f| / (\hbar |i - f|)$, where E_i and E_f are the energies of the respective levels, is used as the effective oscillator frequency. To account for the oscillator feedback effect on the classical trajectory, a symmetrization procedure is commonly used whereby the effective initial velocity of the colliding pair is taken as an arithmetic average between the actual velocity and that calculated with the kinetic energy reduced by the oscillator energy increase, $E_i - E_f$.[30-32] These two simple corrections have proved to be successful in bringing the FHO-calculated vibrational energy transfer rates[10, 11, 13] into an excellent agreement with more sophisticated quantum calculations[21, 22, 24-26].

To model dissociation, we need to calculate probabilities of bound-free transitions. The original FHO theory, strictly speaking, cannot describe such transitions. First of all, the discrete energy spectrum of harmonic oscillator extends to infinity. Secondly, even for a truncated oscillator, calculating probabilities of bound-free transitions is difficult and is not done directly by the FHO theory. In this work, we will make use of the fact that, when molecular vibrations are modeled by a Morse oscillator with the lowest vibrational quantum and the anharmonicity constant equal to their known spectroscopic values, the depth of the resulting potential well exceeds the experimental value of the molecule's dissociation energy. This fact, of course, means that the Morse oscillator model is inaccurate at high vibrational levels, but it also gives an opportunity to formally model dissociation as a bound-bound transition. Specifically, we will consider transitions to any of the Morse oscillator quantum levels with energy equal to or above the experimental bond energy of the molecule to be dissociative. Obviously, transitions to the quantum levels with energies below the experimental bond energy, also approximated by the same Morse oscillator throughout the present work, are still interpreted as bound-bound transitions. The choice of the 'cutoff' bond energy is assumed to be independent of the rotational energy of the molecules. The parameters of the intermolecular Morse potential used are listed in Table I.

Table 1. Morse potential parameters

	Nitrogen	Oxygen
ω_e, cm^{-1}	2359.6	1580.3
x_e	$6.1265 \cdot 10^{-3}$	$7.639 \cdot 10^{-3}$
$D=\omega_e/4x_e$, cm^{-1}	96,287	51,718
D_{exp}, cm^{-1}	78,672	41,268
Total number of vibrational levels, $v_D=1/2x_e$	81	65
Number of bound vibrational levels ($E_v<D_{exp}$)	46	35

The total probability of collisional dissociation from vibrational level *i* is, therefore, a sum over all final "dissociative" Morse vibrational levels:

$$P_{diss}(i) = \sum_{E_f \geq D} P_{VRT}(i \to f) \tag{3}$$

where *D* is the molecule's dissociation (bond) energy, and the subscript "*VRT*" denotes vibration-rotation-translation energy transfer.

Similarly, for molecule-molecule (AB-CD) collisions:

$$AB(i_1)+CD(i_2) \to AB(f_1)+CD(f_2) \tag{4}$$

the dissociation probability can be defined as:

$$P_{diss}(i_1) = \sum_{E_{f_1} \geq D_{AB}} P_{VRT}(i_1 \to f_1) \tag{5}$$

As demonstrated earlier,[11, 12] in calculating probabilities of vibrational transitions in AB molecule at high kinetic energies or temperatures, vibration-vibration (VV) exchange between AB and CD can be neglected. Since this work is devoted to high-temperature dissociation processes, we will adopt this approximation. Additionally, summing over all possible vibrational states of CD molecule can be performed. The FHO transition probability scaling[11, 12] is then similar to that in the molecule-atom case:

$$P_{VRT}(i,\ \text{all}\rightarrow f,\ \text{all};\ Q_1)=i!\,f!\,Q_1^{i+f}\exp(-Q_1)\left|\sum_{r=0}^{n}\frac{(-1)^r}{r!(i-r)!(f-r)!}\frac{1}{Q_1^r}\right|^2 \tag{6}$$
$$=P_{VRT}(i\rightarrow f;\ Q_1)$$

Here $n=\min(i,\ f)$, and $Q_1=\Delta E/\hbar\omega_1$ is the dimensionless energy (i.e. the average number of quanta) transferred to the initially non-vibrating classical oscillator AB in an AB-CD collision.

Note that in Refs. 13 and 14, the exact FHO probabilities of Eqs. (2) and (6) have been reduced to the approximate analytic expressions using the asymptotic behavior of the series in the right-hand-sides of Eqs. (2) and (6) (e.g., see Ref. 11). This permitted straightforward analytic integration of the transition probabilities over the collision energies and obtaining the closed-form analytic expressions for the state-specific rate coefficients for vibrational energy transfer. Since developing a fully analytic dissociation model is beyond the scope of the present work, we are using the exact FHO scaling expressions.

3. Energy transfer to a classical rotating oscillator in 3D collisions: free-rotation and impulsive approximations

From the previous section, it is clear that to evaluate probabilities of vibrational transitions, including dissociation, an energy transferred to a classical initially non-vibrating oscillator has to be calculated. For this, an adequate potential energy surface should be determined, and then classical equations of motion should be integrated for the three- or four-atom system. We will use 2 approximations permitting analytic solutions.

3.1 Free-rotation approximation

Consider collisions between a rotating symmetric diatomic molecule and an atom. For the pairwise atom-to-atom interaction described by repulsive exponential functions, the atom-molecule interaction potential can be written as follows:[13, 21-23]

$$U(R,\ r,\ \vartheta,\ \varphi)=2Ae^{-\alpha R}\cosh\left(\frac{\alpha r}{2}\cos\vartheta\cos\varphi\right) \tag{7}$$

where R is the center-of-mass distance, r is the separation of atoms in a molecule, ϑ is the rotation angle (i.e. the angle between R and r), and φ is the angular momentum vector (i.e. the angle between the plane of rotation and the radius vector R). As in earlier work[13], we will assume that the rotation is free, that is, neither the magnitude nor the direction of the angular momentum vector change in a collision. Then the classical trajectory can be found analytically, and it is essentially an exponential function of $R(t)$ modulated by the periodic rotational factor. The resulting expression for the Q in Eq. (2) is:[13]

$$Q(E,\ \varepsilon,\ y,\ \vartheta,\ \varphi)=\frac{\theta'\xi}{4\theta}\frac{\cos^2\vartheta\cos^2\varphi}{\sinh^2\left[\dfrac{\pi\omega}{\alpha u\gamma(\varepsilon,\vartheta,\varphi,y)}\right]} \tag{8}$$

where $E=E_{tr}+E_{rot}$ is the total collision energy, $\varepsilon=E_{rot}/E$, $y=b^2/R_m{}^2$, b is the impact parameter, $R_m=2.5$ A is the hard-sphere diameter, $s=|i-f|$ is the number of quanta transferred, $\omega=|E_f-E_i|/s\hbar$ is the average vibrational quantum for the transition $i\rightarrow f$, $\theta'=\dfrac{4\pi^2\omega^2 m}{\alpha^2 k}$, $\theta=\dfrac{\hbar\omega}{k}$, $u=\sqrt{2E/m}$, m is the collision reduced mass, m_0 is the oscillator reduced mass, $2\xi=m/m_o$ is the ratio of the collision and oscillator reduced masses, and

$$\gamma(\varepsilon,\vartheta,\varphi,y)=\max\left[0,\ -\frac{\sin 2\vartheta\cos\varphi}{2}\sqrt{\xi\varepsilon}+\sqrt{(1-\varepsilon)(1-y)}\right] \tag{9}$$

The range of applicability of the free-rotation approximation was discussed in the earlier paper.[13] In the same paper, the FHO vibrational transition probabilities calculated with this approximation were found to agree very well with the full semiclassical modeling using full potential energy surface.[23]

An extension to 3D molecule-molecule collisions with rotation is straightforward.[14] The potential energy can be written as:

$$U(R,r,\vartheta_1,\varphi_1,\vartheta_2,\varphi_2)=4Ae^{-\alpha R}\cosh\left(\frac{\alpha r}{2}\cos\vartheta_1\cos\vartheta_2\right)\cosh\left(\frac{\alpha r}{2}\cos\vartheta_2\cos\varphi_2\right) \tag{10}$$

where R is the center-of-mass distance, r is the separation of atoms in the molecules, ϑ_i are the rotation angles (i.e., the angles between R and each r), and φ_i are the angular momentum vectors (i.e. the angles between the planes of rotation and the radius vector R). Having calculated the classical trajectory in this potential, assuming the free rotation, the energy transfer parameter Q turns out to be:[14]

$$Q_k\left(E,\varepsilon_1,\varepsilon_2,\vartheta_1,\varphi_1,\vartheta_2,\varphi_2,y\right)=\frac{\theta_k^{'}}{4\theta_k}\frac{\cos^2\vartheta_k\cos^2\varphi_k}{\sinh^2\left[\dfrac{\pi\omega_k}{\alpha u\gamma\left(\varepsilon_1,\varepsilon_2,\vartheta_1,\varphi_1,\vartheta_2,\varphi_2,y\right)}\right]}\ ;\ k=1,\ 2 \qquad (11)$$

Here $E=E_{tr}+E_{rot,1}+E_{rot,2}$ is the total collision energy, $\varepsilon_k=E_{rot,k}/E$, $y=b^2/R_m^2$, b is the impact parameter, R_m=2.5 A is the hard sphere diameter, $s_k=|i_k-f_k|$ is the number of quanta transferred, $\omega_k=|E_{f,k}-F_{i,k}|/s_k\hbar$ is the average vibrational quantum for the transition $i_k\rightarrow f_k$, $\theta_k'=\dfrac{4\pi^2\omega_k^2 m}{\alpha^2 k}$,

$\theta_k=\dfrac{\hbar\omega_k}{k}$, $u=\sqrt{2E/m}$, m is the collision reduced mass, and

$$\gamma\left(\varepsilon_1,\varepsilon_2,\vartheta_1,\varphi_1,\vartheta_2,\varphi_2,y\right)=\max\left[0,-\frac{\sin 2\vartheta_1\cos\varphi_1}{2}\sqrt{\varepsilon_1}-\frac{\sin 2\vartheta_2\cos\varphi_2}{2}\sqrt{\varepsilon_2}+\sqrt{\left(1-\varepsilon_1-\varepsilon_2\right)\left(1-y\right)}\right] \qquad (12)$$

3.2. Impulsive (sudden) approximation

In this approximation, AB is modeled by two hard spheres, A and B, connected by an initially non-deformed spring. Collision with an atom C, also modeled as a hard sphere, reduces to a hard-sphere collision of B and C. The center-of-mass kinetic energy, AB rotational energy, and the set of orientation angles at the moment of collision fully define the outcome of the collision. Applying energy and momentum conservation, the post-collision component of the velocity of B atom along the A-B axis can be determined, and the post-collision vibrational energy of the AB molecule calculated. Similarly, AB-CD collisions can be analyzed in the assumption that only hard spheres B and C collide directly.

The hard-sphere collision of B and C atoms can be treated as being either "smooth-sphere", where the collision is elastic along the line connecting centers of B and C, with no forces normal to that line, or "rough-sphere" one, where the collision is elastic along the line connecting B and C centers and fully inelastic perpendicular to that line.

When, in a collision, B atom receives a velocity increment Δv along the A-B axis, the initially non-vibrating AB molecule acquires vibrational energy

$$\Delta E=2\cdot\frac{1}{2}m\left(\frac{\Delta\text{v}}{2}\right)^2=\frac{1}{4}m\left(\Delta\text{v}\right)^2, \qquad (13)$$

where m is the mass of each of the atoms A and B. Since, in the present model, B collides directly only with C, it is convenient to introduce B velocity increments along the B-C axis, $\Delta v_{\parallel}$, and perpendicular to the B-C axis and parallel to the A-B-C plane, $\Delta v_{\perp}$, so that

$$\Delta v = \Delta v_{\parallel} \cos\theta + \Delta v_{\perp} \sin\theta . \tag{14}$$

Here θ is the angle between the A-B molecular axis and the B-C axis; $\theta \in [0,\ \pi/2]$. Note that the B atom velocity increment component perpendicular to both B-C axis and A-B-C plane does not contribute to Δv.

Consider now an AB-C collision in the AB-C center-of-mass system. Translational velocities of the colliding atoms B and C, $v_{B,\,tr}$ and $v_{C,\,tr}$, antiparallel to each other, are related to the center-of-mass kinetic energy, E_t, of the colliding pair by the momentum and energy equations:

$$2mv_{B,\,tr} = Mv_{C,\,tr};\ 2\cdot\frac{1}{2}mv_{B,\,tr}^{2} + \frac{1}{2}mv_{C,\,tr}^{2} = E_t , \tag{15}$$

where M is the mass of C atom. The direction of $v_{B,\,tr}$ and $v_{C,\,tr}$ can be characterized by α, the angle between the velocity of the C atom (in the AB-C center-of-mass system) and the B-C axis, and by φ, the angle between $v_{B,\,tr}$ or $v_{C,\,tr}$ and the straight line parallel to the A-B-C plane and normal to the B-C axis. The intervals of variation of these angles are: $\alpha \in [0, \pi/2]$ and $\varphi \in [\pi/2 - \alpha,\ \pi - \alpha]$.

Additionally, atom B has a rotational velocity, $v_{B,\,rot}$, whose magnitude can be expressed in terms of the initial rotational energy of AB, E_r:

$$2\cdot\frac{1}{2}mv_{B,\,rot}^{2} = E_r , \tag{16}$$

and whose direction (obviously, normal to the A-B axis) can be characterized by the angle β between $v_{B,\,rot}$ and the B-C axis; $\beta \in [\pi/2 - \theta,\ \pi/2 + \theta]$.

Considering an elastic collision of B and C atoms along the B-C line, from the energy and momentum conservation equations we obtain:

$$\Delta v_{\parallel} = \frac{2M}{M+m}\left[\left(v_{B,\,tr} + v_{C,\,tr}\right)\cos\alpha + v_{B,\,rot}\cos\beta\right] = \frac{2M}{M+m}\left[\sqrt{\frac{(M+2m)E_t}{Mm}}\cos\alpha + \sqrt{\frac{E_r}{m}}\cos\beta\right] \tag{17}$$

Here we expressed velocities $v_{B,\,rot}$, $v_{B,\,tr}$, and $v_{C,\,tr}$ through the energies E_r and E_t according to equations (15) and (16). Since in the smooth spheres case $\Delta v_{\perp}=0$, substituting Eqn. (17) into Eqn. (14), and inserting the result into Eqn. (13), we obtain the energy transferred to the initially non-vibrating oscillator in the **smooth spheres, molecule-atom** case:

$$\Delta E=\left[\frac{M}{M+m}\left(\sqrt{\frac{(M+2m)E_t}{M}}\cos\alpha+\sqrt{E_r}\cos\beta\right)\cos\theta\right]^2 \tag{18}$$

In the rough spheres case, one needs to calculate projections of all velocities of B and C atoms onto an axis perpendicular to the B-C line and parallel to the A-B-C plane. Then, from the energy and momentum equations for an absolutely inelastic collision of B and C atoms along that axis, one obtains:

$$\Delta v_{\perp}=\frac{M}{M+m}\left[\left(v_{B,\,tr}+v_{C,\,tr}\right)\cos\varphi-v_{B,\,rot}\cos\beta\cos\theta/\sin\theta\right] \tag{19}$$

Expressing velocities $v_{B,\,rot}$, $v_{B,\,tr}$, and $v_{C,\,tr}$ through the energies E_r and E_t according to equations (15) and (16), then substituting Eqns. (17) and (19) into Eqn. (14), and inserting the resulting formula for Δv into Eqn. (13), we obtain the energy transferred to the initially non-vibrating oscillator in the **rough spheres, molecule-atom** case:

$$\Delta E=\left\{\frac{1}{2}\cdot\frac{M}{M+m}\cdot\left[\sqrt{\frac{(M+2m)E_t}{M}}\left(2\cos\alpha\cos\theta+\cos\varphi\sin\theta\right)+\sqrt{E_r}\cos\beta\cos\theta\right]\right\}^2. \tag{20}$$

Similar derivations can be performed for molecule-molecule collisions. When writing energy and momentum conservation equations for B-C collisions, additional (compared with the molecule-atom case) C atom velocity components, corresponding to rotational and vibrational motion of CD molecule, have to be included, leading to additional terms in equations.

In the **molecule-molecule, smooth spheres** case:

$$\Delta E=\left[\frac{M}{M+m}\left(\sqrt{\frac{(M+m)E_t}{M}}\cos\alpha+\sqrt{E_r}\cos\beta+\sqrt{\frac{m}{M}E_v'}\cos\eta\cos\gamma_1+\sqrt{\frac{m}{M}E_r'}\cos\gamma_2\right)\cos\theta\right]^2 \tag{21}$$

Here, of course, we consider AB-CD collisions, with B and C atoms actually colliding. The mass of each of the atoms C and D equals *M*. E_v' and E_r' are the pre-collision vibrational and rotational energies of the CD molecule. Arguments of the new cosines are: η - the phase of CD oscillations in the moment of collision, γ_1 - the angle between B-C and C-D axes, and γ_2 - the angle between the rotational velocity of C atom and the B-C axis. The intervals of variation of the new arguments are:

$$\begin{aligned}&\eta \in [0,\ 2\pi];\ \gamma_1 \in [0,\ \pi];\\ &\gamma_2 \in [\pi/2-\gamma_1,\ \pi/2+\gamma_1],\ \text{if}\ \gamma_1 \in [0,\ \pi/2],\\ &\quad \in [\gamma_1-\pi/2,\ 3\pi/2-\gamma_1],\ \text{if}\ \gamma_1 \in (\pi/2,\ \pi].\end{aligned} \tag{22}$$

In the **molecule-molecule, rough spheres case:**

$$\begin{aligned}\Delta E = \Bigg\{ &\frac{1}{2}\cdot\frac{M}{M+m}\Bigg[\sqrt{\frac{(M+m)E_t}{M}}(2\cos\alpha\cos\theta+\cos\varphi\sin\theta)\\ &+\sqrt{E_r}\cos\beta\cos\theta+\sqrt{\frac{m}{M}E_v'}\cos\eta\,(2\cos\gamma_1\cos\theta+\cos\varphi_1\sin\theta)\\ &+\sqrt{\frac{m}{M}E_r'}(2\cos\gamma_2\cos\theta+\cos\varphi_2\sin\theta)\Bigg]\Bigg\}^2\end{aligned} \tag{23}$$

The new angles, φ_1 and φ_2, are the angles between vectors of vibrational and rotational velocity, respectively, of C atom and the straight line parallel to the A-B-C plane and perpendicular to the B-C axis. The intervals of their variation are:

$$\begin{aligned}&\varphi_1 \in [\pi/2-\gamma_1,\ \pi/2+\gamma_1],\ \text{if}\ \gamma_1 \in [0,\ \pi/2],\\ &\quad \in (\gamma_1-\pi/2,\ 3\pi/2-\gamma_1],\ \text{if}\ \gamma_1 \in (\pi/2,\ \pi]\end{aligned}$$

and

$$\begin{aligned}&\varphi_2 \in [\pi/2-\gamma_2,\ \pi/2+\gamma_2],\ \text{if}\ \gamma_2 \in [0,\ \pi/2],\\ &\quad \in (\gamma_2-\pi/2,\ 3\pi/2-\gamma_2],\ \text{if}\ \gamma_2 \in (\pi/2,\ \pi]\end{aligned} \tag{24}$$

4. Dissociation probabilities, cross sections, and rate coefficients

Formulas (8), (9), (11), (12), and (18)-(24) for Q and ΔE, when inserted into FHO scaling formulas (2) and (6), give sets of state-to-state transfer probabilities. Summing over the final states according to Eqs. (3) and (5), dissociation probabilities are found as functions of vibrational, rotational, and translational energies, and of the set of angles. Integrating over the angles, and assuming rotational-translational equilibrium with temperature *T*, gives the dissociation cross section as a function of vibrational quantum number *i*, total (translational plus rotational) collision energy *E*, and the temperature *T*.

The dissociation cross-section for molecule-atom collisions in the free-rotation approximation is:[31]

$$\begin{aligned}\sigma_{diss}(i,\ E,\ T) &= \frac{\pi\hbar^2}{2mT}\frac{\hbar^2}{2IT}\frac{1}{\pi^2}\int_0^{J_{\max}} dJ\,(2J+1)\int_0^{j_{\max}} dj\int_{|J-j|}^{J+j} dl\int_0^{\pi} d\vartheta\int_0^{\pi} d\varphi\cdot\sum_f P_{if} \\ &\approx \pi R_m^2\left(\frac{E}{T}\right)^2\frac{1}{\pi^2}\int_0^1 dy\int_0^1 d\varepsilon\int_0^{\pi} d\vartheta\int_0^{\pi} d\varphi\cdot\sum_f P_{if}(E,\ \varepsilon,\ \vartheta,\ \varphi,\ y)\end{aligned}\quad, \qquad (25)$$

where I is the moment of inertia of the AB molecule. For molecule-molecule collisions in the free-rotation approximation:[32]

$$\begin{aligned}\sigma_{diss}(i,E,T) &= \frac{\pi\hbar^2}{2mT}\frac{\hbar^2}{2I_1T}\frac{\hbar^2}{2I_2T}\int_0^{l_{\max}} dl\,(2l+1)\int_0^{j_{1\max}} dj_1\,(2j_1+1)\int_0^{j_{2\max}} dj_2\,(2j_2+1) \\ &\quad\cdot\frac{1}{\pi^4}\int_0^{\pi} d\vartheta_1\int_0^{\pi} d\varphi_1\int_0^{\pi} d\vartheta_2\int_0^{\pi} d\varphi_2\cdot\sum_f P_{if} \\ &\approx \pi R_m^2\left(\frac{E}{T}\right)^3\frac{1}{\pi^4}\int_0^1 dy\int_0^1 d\varepsilon_1\int_0^1 d\varepsilon_2\int_0^{\pi} d\vartheta_1\int_0^{\pi} d\varphi_1\int_0^{\pi} d\vartheta_2\int_0^{\pi} d\varphi_2 \\ &\quad\cdot\sum_f P_{if}(E,\varepsilon_1,\varepsilon_2,\vartheta_1,\varphi_1,\vartheta_2,\varphi_2,y)\end{aligned}\quad, \qquad (26)$$

where I_1 and I_2 are the moments of inertia of AB and CD molecules, respectively. Similar formulas can be written for the impulsive approximation. In Eqs. (25) and (26), the rigid rotor approximation has been used. The limits of integration over the angular momenta in Eqs. (25) and (26) are determined from the condition that the cross section is evaluated at the constant total energy E of the classical degrees of freedom (i.e. the sum of translational energies of the radial and the orbital motion and the rotational energies, $E=E_{rad}+E_{orb}+E_{rot,k}$).[31, 32] The approximate integration forms in the right-hand sides of Eqs. (25) and (26) are obtained by replacing integration over the rotational and orbital angular momenta by integration over the dimensionless rotational energies, $\varepsilon_k=E_{\mathrm{rot},k}/E$, and the dimensionless impact parameter $y=b^2/R_m^2$. In this procedure, replacing the appropriate integration limits for ε_k and y by unity does not significantly affect the integration accuracy since the dissociation cross section, σ_{diss}, was found to steeply drop both at the high values of rotational energies and the impact parameter (i.e. at the low values of the translational energy of the radial motion).

In this work, cross-sections were calculated at 60 values of total collision energy in the range 10^3-10^6 cm^{-1}. For each total collision energy E, 1000 randomly picked phase space points were used for evaluation of multi-dimensional cross-section integral. Previous calculations using this approach by Billing[24, 25] showed that the use of only 100-400 phase space points is sufficient to obtain a 20-30% confidence in the averaged cross sections. In the present calculations, the use of 1000 phase space points allows about 10-20% accuracy in the cross sections. To account for the oscillator reaction on the classical trajectory, or, in other words, to enforce the detailed balance, a symmetrization procedure[31, 32] was used, whereby the effective energy U was substituted for E, corresponding to the arithmetically averaging velocity before and after collision:

$$U = E + \frac{\Delta E_{if}}{2} + \frac{(\Delta E_{if})^2}{16E}; \quad E_{\min} = \Delta E_{if}/4 \tag{27}$$

Averaging the dissociation flux over Maxwellian energy distribution gives vibrational state-specific dissociation rate coefficient (v is the vibrational quantum number):[31, 32]

$$k_{diss}(v,T) = \left(\frac{8kT}{\pi m}\right)^{1/2} \int_0^{\infty} \sigma_{diss}(v,U,T) \exp\left(-\frac{U}{T}\right) d\left(\frac{U}{T}\right) \tag{28}$$

The integral in Eq. (28) is evaluated numerically by the RATECONS procedure[31] using all 60 values of the cross sections given by Eqs. (25) and (26). The estimated accuracy of numerical integration is about 10%. Further averaging of the state-specific rate coefficients over the vibrational energy mode distribution function would give the total dissociation rate coefficient. In the present work, this is done for both nonequilibrium and equilibrium vibrational mode energy distributions. In both cases, the energy distributions are assumed to be Boltzmann with vibrational temperature T_V and the gas temperature T, respectively. In the latter case, the thermal dissociation rate constant is obtained.

5. Results and discussion

To check the difference between vibrational energy transfer predicted by free-rotation and impulsive approximations, the parameter $Q = \Delta E / \hbar\omega$, averaged over collision angles, was calculated for O_2-Ar and O_2-O_2 collisions and plotted in Fig. 1 (a, b) as a function of the total (translational plus rotational) collision energy. In all free-rotation calculations done in this work, the parameters of the exponential repulsive potential of Eq. (7) were taken to be $\alpha = 4.0 \times 10^8\ cm^{-1}$, which is the commonly accepted number for nitrogen and oxygen,[10-13, 23, 24] and A=1730 eV.[24] As seen in Fig. 1 (a, b), there is virtually no difference between smooth and rough sphere impulsive approximations. At very high energies, free-rotation and impulsive approximations converge to close asymptotics, which is physically reasonable and provides a consistency check. At moderate and low energies, the impulsive approximation is seen to overpredict the energy transfer by orders of magnitude. Again, this could be expected, since in the impulsive approximation collision duration is assumed to be much shorter than the vibrational period, while low-velocity collisions last much longer than the period of vibrations, thus reducing the efficiency of energy transfer.

Fig. 2 (a, b) shows the dissociation probability from ground vibrational state versus total collision energy. Similar to Fig. 1, free-rotation and impulsive results are close to each other at high energies, while at low energies impulsive approximation predicts an excessively high dissociation probability.

An important step in validating any dissociation model is to compare predicted dissociation rates in thermal equilibrium with experimental data. Strictly speaking, this would require full master equation modeling, with dissociation, recombination, and energy transfer processes all taken into account. Such modeling can be done using the newly derived dissociation rates and FHO-based vibrational energy transfer rates,[10, 11, 13, 14, 16] similar to the modeling performed earlier.[11, 12, 16] However, such modeling is beyond the scope of this work. For the first-cut comparison, in this work we calculated thermal dissociation rates for nitrogen and oxygen assuming the equilibrium Boltzmann vibrational energy distribution function. Of course, if atom-atom recombination is weak, the irreversible dissociation would depopulate very high vibrational states, reducing the dissociation rate by perhaps a factor of 2-3.[1, 7, 33] If, on the other hand, recombination is significant, highly excited states would be close to equilibrium. Thus, a caution is needed when comparing computed thermal dissociation rates with experiments, as the degree to which highly excited states were close to thermal equilibrium in a specific experiment is often not clear.

In Fig. 3, a comparison with the dissociation rate inferred from shock tube measurements is shown for O_2-Ar collisions. Both free-rotation and impulsive energy transfer models in conjunction with FHO scaling give an excellent agreement with experiments in a very wide temperature range, especially considering that the experimental fit has an uncertainty range within a factor of 2-3. The agreement of the impulsive model with both experimental data and free-rotation predictions may seem somewhat surprising. The explanation lies in the fact that at thermal equilibrium the dissociation proceeds chiefly from very high vibrational levels, close to the dissociation threshold. This is well known from the literature,[7] and is confirmed in our calculations (see below). Since spacing between vibrational levels is very small near the dissociation threshold, the Massey parameter,[7] that is, the product of vibrational frequency and the collision duration, is small even for particles moving with mean thermal velocity. This means that most dissociative collisions at thermal equilibrium can be adequately described in the impulsive approximation.

Figure 4 shows calculated and experimental thermal dissociation rate coefficients in oxygen. One can see that both models somewhat underpredict the dissociation rate compared to the experimental data, $2.2\times10^{16}\exp(-59380/T)\left[1-\exp(-2240/T)\right]\ cm^3/(mole\cdot s)$.[38, 39] The impulsive model, which provides for more efficient rotational energy transfer into the dissociating bond than the free-rotation model does, appears to be closer to experiments in this case. It is also instructive to consider the ratio of thermal dissociation rate coefficients in O_2-O_2 and O_2-Ar collisions. Both free-rotation and impulsive models predict the ratio to be about 3 and to depend on temperature very weakly. That molecule-molecule collisions are more effective than molecule-atom ones demonstrates the role of rotational energy in dissociation and is qualitatively consistent with theoretical expectations.[7] Nikitin[7] argued that the vibrational energy E^*, that approximately separates the regions of single-quantum and multiquantum (including bound-free) transitions is determined by the criterion that the Massey parameter calculated with vibrational frequency at the energy level E^* be of the order of unity. On the basis of this criterion, Nikitin[7] estimated reduction in E^* due to efficient transfer of rotational energy of the non-dissociating molecule into vibrational mode of the highly-excited dissociating molecule and predicted the ratio of thermal dissociation rate coefficients in O_2-O_2 and O_2-Ar collisions to be about 10-20, independent of temperature. Experimental data quoted by Stupochenko, Losev, and Osipov,[33] specifically, O_2-O_2 data[34-36] and O_2-Ar data[37] seem to indicate that the dissociation rate ratio decreases from 30-40 at 3500 K to about 5-10 at 7000 K. Since at thermal equilibrium dissociation in both O_2-O_2 and O_2-Ar collisions is determined by the processes at very high vibrational states, one possible reason for the less than perfect agreement between our predictions and the experiment could be an error introduced by modeling the highly excited states by Morse oscillator. Further refinement of the theoretical model, especially with regard to the energy spectrum at high vibrational levels, would clarify the issue. However, experimental data of different authors also have to be treated with caution. For example, Losev *et. al.*,[4, 5, 38] based on experimental data of Losev and Shatalov,[39] recommend the dissociation rate value of $2.2\times10^{16}\exp(-59380/T)\left[1-\exp(-2240/T)\right]\ cm^3/(mole\cdot s)$ for O_2-O_2 collisions. Together with the O_2-Ar rate $6.0\times10^{13}(59380/T)\exp(-59380/T)\ cm^3/(mole\cdot s)$ of Camac and Vaughan,[37] this would give the ratio of thermal dissociation rate coefficients in O_2-O_2 and O_2-Ar collisions of about 10, weakly dependent on temperature (see Fig. 4). Considering the fact that both rates are known within a factor of 3 at best, this would mean a reasonably good agreement between our model and experiments. A detailed analysis of the experiments quoted, as well as further shock-tube experimental studies, could be helpful in developing a better understanding of dissociation processes.

Figures 5 and 6 depict calculated and experimental thermal dissociation rate coefficients for N_2-Ar and N_2-N_2 collisions. As seen from the figures, the agreement, within a factor of 2-3 experimental uncertainty, is uniformly excellent over the wide temperature range. Interestingly, the calculated ratio of the thermal dissociation rate coefficients for N_2-N_2 and N_2-Ar collisions is about 3, weakly changing with temperature, which is in a very good agreement with experiments.

As is well known,[1, 3, 4, 33] rotational relaxation behind shocks is quite fast, while vibrational relaxation is much slower. Thus, dissociation rate coefficient as a function of vibrational energy and translational-rotational temperature is quite useful for shock modeling. When averaged over nonequilibrium vibrational distribution, such vibrational energy-dependent rate coefficient could be converted into a two-temperature rate coefficient $k(T_v,T)$. The calculated vibrational energy-dependent rates normalized by the dissociation rate from the uppermost vibrational level at several temperatures are shown in Fig. 7 for N_2-Ar collisions. Very steep exponential increase of the rates with vibrational energy is clearly seen. Perhaps more informative is Fig. 8, where the rates from Fig. 7 have been multiplied by the equilibrium Boltzmann factor $f_E=\exp(-E_v/T)$. The plotted quantity, therefore, represents contributions of various vibrational states to the total thermal dissociation rate. As expected from theory,[7] the principal contribution to thermal dissociation comes from states with vibrational energy close to the dissociation threshold.

The plot in Fig. 8 is helpful in understanding the degree of preferentiality of dissociation. The well-known Marrone-Treanor model[3] assumes that the probability of dissociation from vibrational state with energy E_v becomes non-zero when translational collision energy exceeds the threshold $(D-E_v)$, and that there is an additional exponential increase of the probability with vibrational energy, so that the vibrational energy-dependent rate is proportional to

$$k_{MT}(E_v,T) \propto \exp\left(-\frac{D-E_v}{T}\right)\cdot\exp\left(-\frac{D-E_v}{U_{MT}}\right) \tag{29}$$

where the empirical parameter U_{MT} is a measure of preferentiality of the dissociation from higher vibrational states. The smaller U_{MT}, the more preferential dissociation is, while $U_{MT}=\infty$ corresponds to non-preferential dissociation. Multiplying the Marrone-Treanor rate [Eq. (29)] by the Boltzmann factor $\exp(-E_v/T)$, normalizing, and plotting the product in a semi-logarithmic scale would give a linear function of vibrational energy, with the slope determining the preferentiality parameter. In Fig. 8 that shows such a plot, the free-rotation approximation is seen to predict dissociation rates that are very preferential towards higher vibrational states. However, interpreting the rates in terms of a single constant parameter U_{MT} is quite difficult. First, the functions plotted in a semi-logarithmic scale in Fig. 8 deviate substantially from linearity. Second, slopes of the curves at each vibrational energy seem to decrease with increasing temperature, so that the effective parameter U_{MT} would increase with temperature, making dissociation less preferential at higher temperatures. The impulsive model, as seen in Fig. 8, gives rates that are less preferential than those given by the free-rotation model, so that at very high temperatures the impulsive-model rates are virtually non-preferential.

Finally, the new model was tested against experimental data on nonequilibrium dissociation of nitrogen. Losev *et. al.*[4, 5, 38, 42] have measured both vibrational and translational-rotational temperatures, and the nonequilibrium factor k(T$_v$,T)/k(T), i.e. the ratio of nonequilibrium and thermally-equilibrium dissociation rates, has been inferred from shock-tube experiments. In Ref. 38, the best fit to the measured nonequilibrium factor is obtained using a two-temperature dissociation model [4, 5],

$$\frac{k(T_v,T)}{k(T)} = \frac{1-\exp(-\theta/T_v)}{1-\exp(-\theta/T)}\cdot\exp\left[-\frac{D-\beta kT}{k}\left(\frac{1}{T_v}-\frac{1}{T}\right)\right] \quad , \tag{30}$$

with $\beta=3$. In Eq. (30), $\theta=3353$ K is the characteristic vibrational temperature of N_2. As shown in Fig. 9, the present model agrees well with the data inferred from the experiments (Eqn. (30) with $\beta=3$), considering that the latter are known within a factor of 2-3. The theoretical two-temperature dissociation rate $k(T_v,T)$ shown in Fig. 9 is obtained by averaging the state-specific rates $k(E_v,T)$ over the nonequilibrium Boltzmann distribution over the vibrational mode energy, with the vibrational temperature T_v. Note that Figs. 8 and 9 plot two essentially different characteristics of the dissociation process. Particularly, Fig. 8 shows the relative contribution of each vibrational level into the overall dissociation rate at thermal equilibrium, $k(E_v,T)f_{eq}(E_v,T)/k(T)$, where $f_{eq}(E_v,T)$ is the equilibrium relative population. On the other hand, Fig. 9 shows *the sum of contributions of all vibrational levels* into the overall dissociation rate at nonequlibrium conditions, at $T_v<T$. In fact, only the asymptotic limit of the ratio $k(T_v,T)/k(T)$ at $T_v \to 0$, plotted in Fig. 9 shows the relative contribution of vibrational level $v=0$ alone, i.e. $k(E_v=0,T)/k(T)$.

6. Conclusions

The new semiclassical theory of dissociation of diatomic molecules, suggested in this work, is based upon an anharmonicity-corrected and energy-symmetrized Forced Harmonic Oscillator (FHO) quantum scaling in conjunction with free-rotation or impulsive energy-transfer models. Although the theory is not fully analytical, it is computationally simple, and it can predict both state-specific and thermal dissociation rates, explicitly accounting for molecular rotation and three-dimensional collisions, without any adjustable parameters.

Calculated thermal dissociation rates of nitrogen and oxygen are in excellent agreement with shock-tube data over a wide temperature range. Agreement with experimental data on nonequilibrium dissociation of nitrogen is also quite good.

Predicted vibrational energy-dependent rates show that dissociation from very high vibrational states is strongly favored in the free-rotation approximation. However, the preferential nature of dissociation is difficult to interpret in terms of a single Marrone-Treanor parameter U_{MT}, as this parameter would be vibrational energy dependent and increase with temperature. The impulsive approximation for energy transfer results in dissociation rates with relatively little preference for high vibrational states.

A possible future refinement of the theory would involve using a more sophisticated and precise energy spectrum of highly vibrationally excited molecules. For practical application in CFD or DSMC analyses, the theory could be used to either generate a set of tabulated rates or to develop simple interpolation formulas.

References

[1] C.Park, *Nonequilibrium Hypersonic Aerothermodynamics* (Wiley, N.Y., 1990).

[2] S.O.Macheret, Paper AIAA 97-2501, 1997.

[3] P.V.Marrone and C.E.Treanor, Phys. Fluids **6**, 1215 (1963).

[4] S.A.Losev, Paper AIAA 96-2026, 1996.

[5] A.L.Sergievskaya, E.A.Kovach, S.A.Losev, and N.M.Kuznetsov, Paper AIAA 96-1895, 1996.

[6] C.Park, J. Thermophys. and Heat Transfer **2**, 8 (1988); ibid., **3**, 233 (1989).

[7] E.E.Nikitin, *Theory of Elementary Atomic and Molecular Processes in Gases* (Clarendon Press, Oxford, 1974), Chap. 7.

[8] R.N.Schwartz, Z.I.Slawsky, and K.F.Herzfeld, J. Chem. Phys. **22**, 767 (1954).

[9] S.P.Sharma, W.Huo, and C.Park, Paper AIAA 88-2714, 1988.

[10] I.V.Adamovich, S.O.Macheret, J.W.Rich, and C.E.Treanor, AIAA Journal **33**, 1064 (1995).

[11] I.V.Adamovich, S.O.Macheret, C.E.Treanor, and J.W.Rich, J. Thermophys. and Heat Transfer **12**, 57 (1998).

[12] I.V.Adamovich, J.W.Rich, and S.O.Macheret, J. Thermophys. and Heat Transfer **11**, 261 (1997).

[13] I.V.Adamovich and J.W.Rich, J. Chem. Phys. **109**, 7711 (1998).

[14] I.V.Adamovich and J.W.Rich, Paper AIAA 99-3565, 1999

[15] S.O.Macheret and J.W.Rich, Chem. Phys. **174**, 25 (1993).

[16] a) S.O.Macheret, A.A.Fridman, I.V.Adamovich, J.W.Rich, and C.E.Treanor, Paper AIAA 94-1984, 1994;.b) I.V.Adamovich, S.O.Macheret, J.W.Rich, C.E.Treanor, and A.A.Fridman, "Vibrational Relaxation, Nonequilibrium Chemical Reactions, and Kinetics of NO Formation Behind Strong Shock Waves", in M. Capitelli (ed.) "Molecular Physics and Hypersonic Flows", **NATO Advanced Study Institute Series**, vol. 482, Kluwer, 1996, p. 85-104

[17] E.H.Kerner, Can. J. Phys. **36**, 371 (1958).

[18] C.E.Treanor, J. Chem. Phys. **43**, 532 (1965).

[19] A.Zelechow, D.Rapp, and T.E.Sharp, J. Chem. Phys. **49**, 286 (1968).

[20] J.D.Kelley, J. Chem. Phys. **56**, 6108 (1972).

[21] A.J.Banks, D.C.Clary, and H.-J.Werner, J. Chem. Phys. **84**, 3788 (1986).

[22] G.D.Billing, Chem. Phys. **107**, 39 (1986).

[23] M.M.Maricq, E.A.Gregory, C.T.Wickham-Jones, D.J.Cartwright, and C.J.S.M.Simpson, Chem. Phys. **75**, 347 (1983).

[24] G.D.Billing and E.R.Fisher, Chem. Phys. **43**, 395 (1979).

[25] G.D.Billing and R.E.Kolesnick, Chem. Phys. Lett. **200**, 382 (1992).

[26] R.Hernandez, R.Toumi, and D.C.Clary, J. Chem. Phys. **102**, 9544 (1995).

[27] J.M.Price, J.A.Mack, C.A.Rogaski, and A.M.Wodtke, Chem. Phys. **175**, 83 (1993)

[28] H.Park and T.G.Slanger, J. Chem. Phys. **100**, 287 (1994).

[29] M.Klatt, I.W.M.Smith, R.P.Tuckett, and G.N.Ward, Chem. Phys. Lett. **224**, 253 (1994)

[30] G.D.Billing, in *Nonequilibrium Vibrational Kinetics*, ed. by M.Capitelli (Springer, Berlin, 1986), p. 85.

[31] G.D.Billing, Computer Physics Communications **32**, 45 (1984)

[32] G.D.Billing, Computer Physics Communications **44**, 121 (1987)

[33] Ye.V.Stupochenko, S.A.Losev, and A.I.Osipov, *Relaxation in Shock Waves* (Springer-Verlag, New York, 1967).

[34] S.A.Losev, Doklady Acad. Sci. SSSR **141**, 894 (1961).

[35] D.L.Matthews, Phys. Fluids **2**, 170 (1959).

[736] S.R.Byron, J. Chem. Phys. **30**, 1380 (1959).

[37] M.Camac and A.Vaughan, J. Chem. Phys.**34**, 460 (1961).

[38] S.A.Losev and G.G.Chernyi, eds., "Analysis of Russian Experimental Investigations for Validation of Kinetic Models for Hypersonic Flows in Thermal Nonequilibrium," Final Report on the Research Grant No. 93-0987-01 by and between the North Carolina State University and Avogadro Center of Institute of Mechanics (Moscow State University, 1993).

[39] S.A.Losev and O.P.Shatalov, Doklady Acad. Nauk SSSR **185**, 293 (1969) [Russian].

[40] J.P.Appleton, M.Steinberg, and D.J.Liquornik, J. Chem. Phys. **48**, 599 (1968).

[41] S.Byron, J. Chem. Phys. **44**, 1378 (1966).

[42] S.A.Losev and M.S.Yalovik, Khimiia Vysokikh Energii (High Energy Chemistry) **4**, 202 (1970) [Russian].

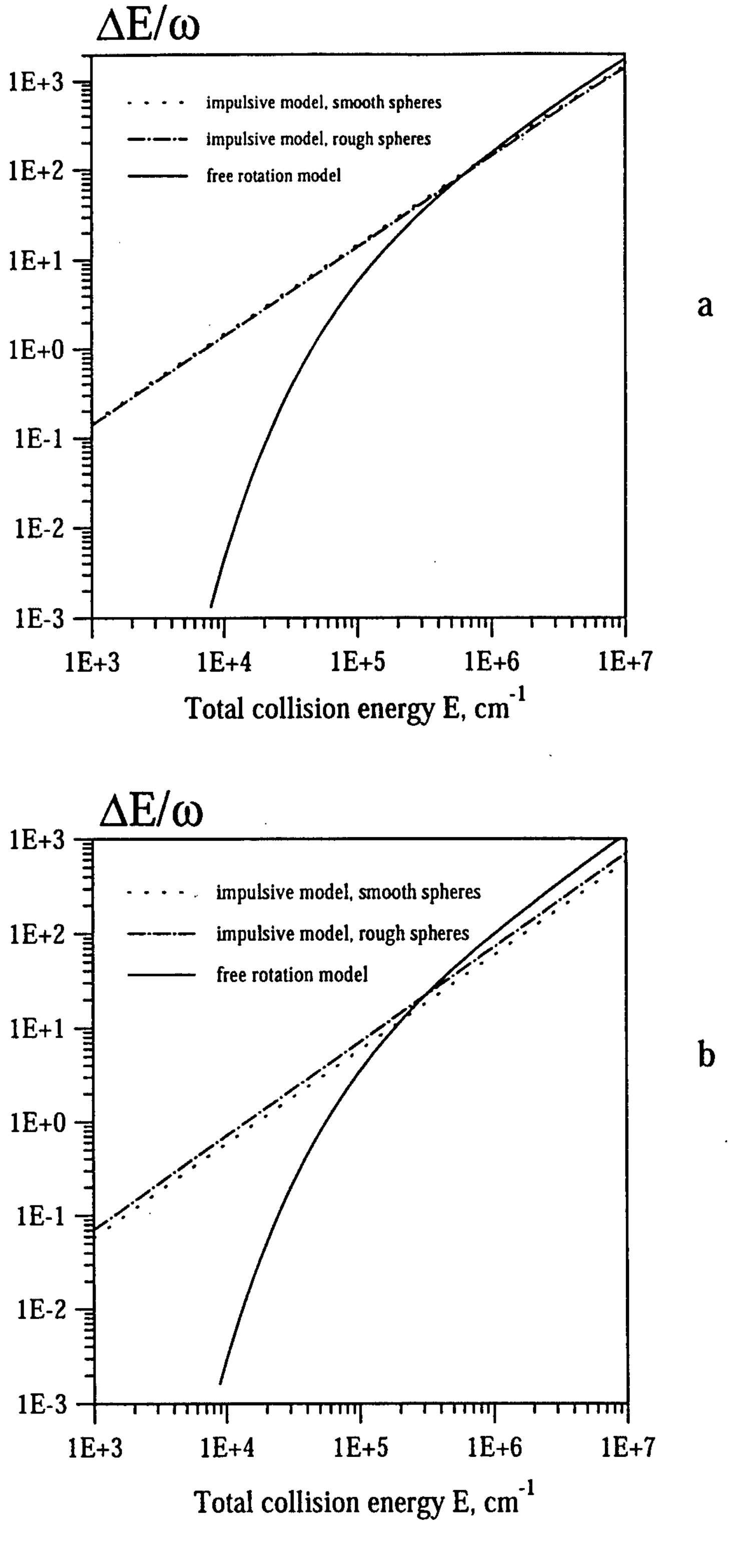

Fig.1a, b. Average number of quanta transferred to initially non-vibrating oxygen molecule versus total collision energy, as given by impulsive and free-rotation models. (a) O_2-Ar collisions; (b) O_2-O_2 collisions

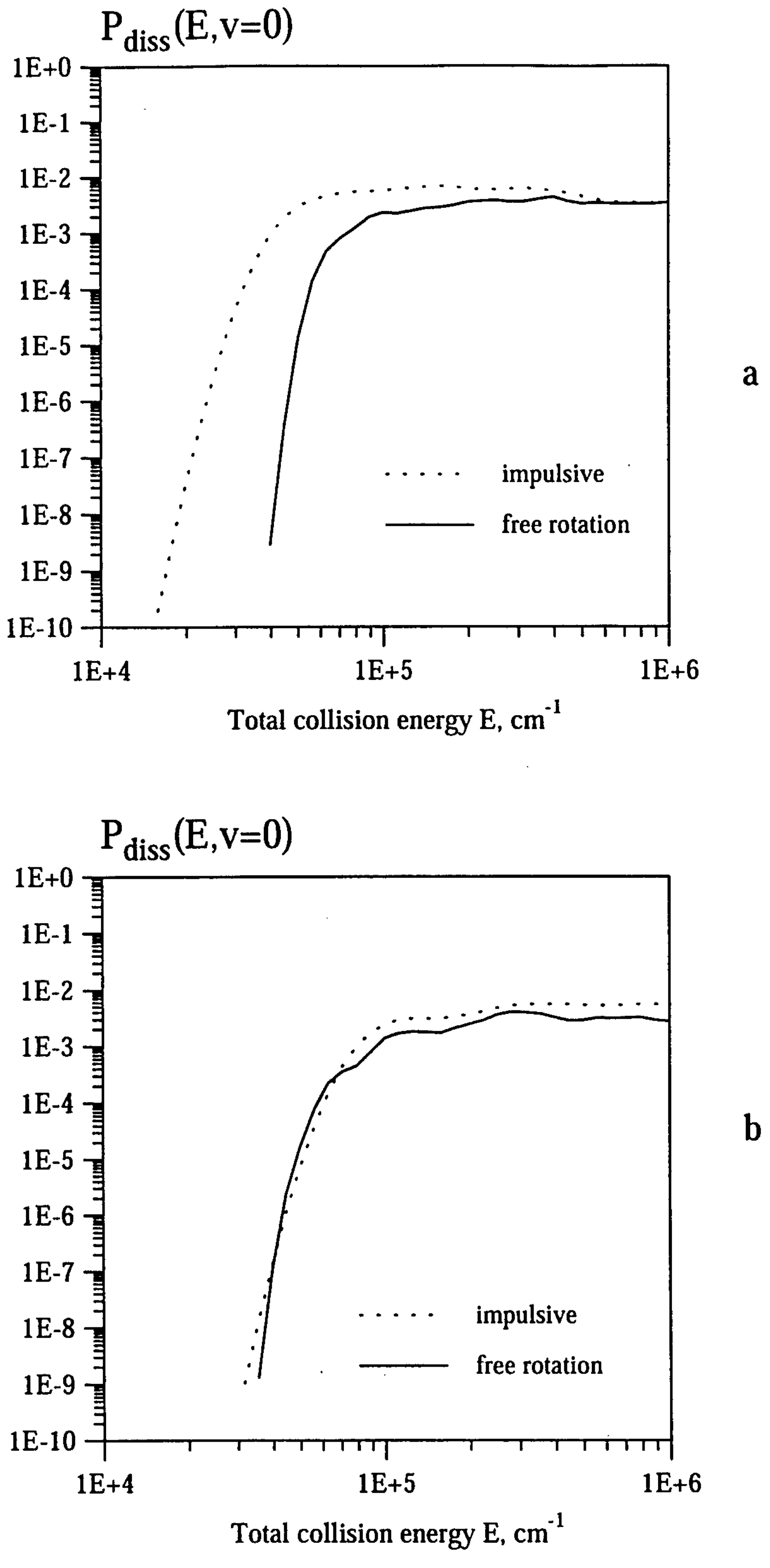

Fig. 2 a, b. Probability of oxygen molecule dissociation from the ground vibrational state versus total collision energy, as calculated with impulsive and free-rotation models. (a) O_2-Ar collisions; (b) O_2-O_2 collisions

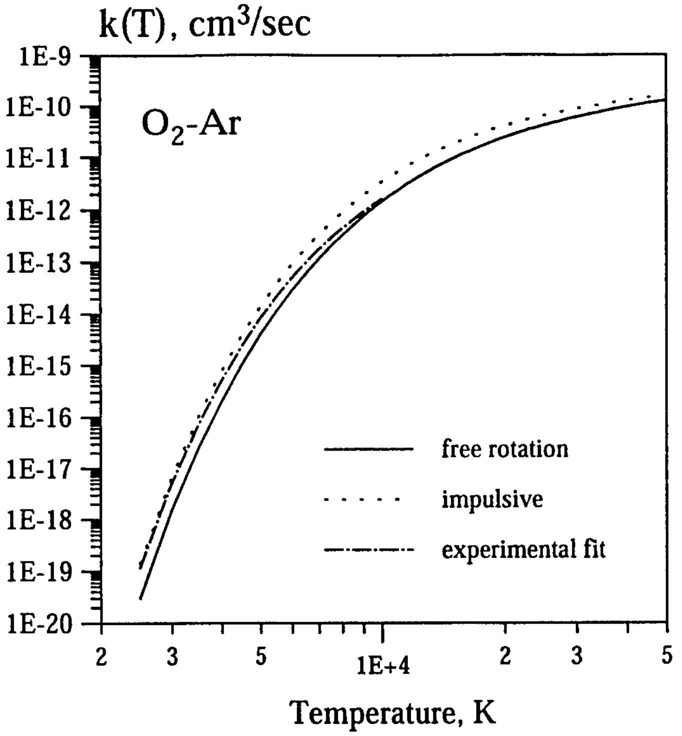

Fig. 3. Computed and inferred from experiments[37] thermal dissociation rate constant for oxygen diluted in argon

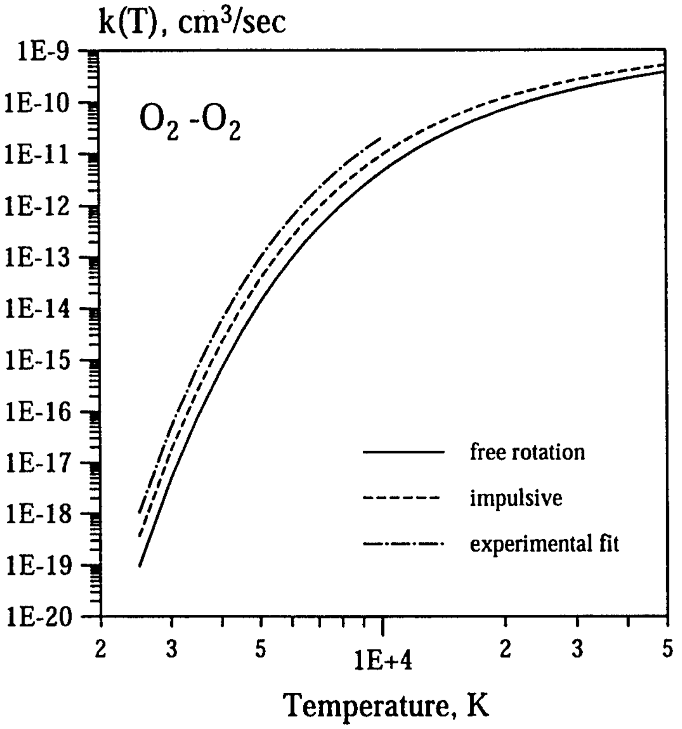

Fig. 4. Computed and inferred from experiments[34-36] thermal dissociation rate constant for oxygen

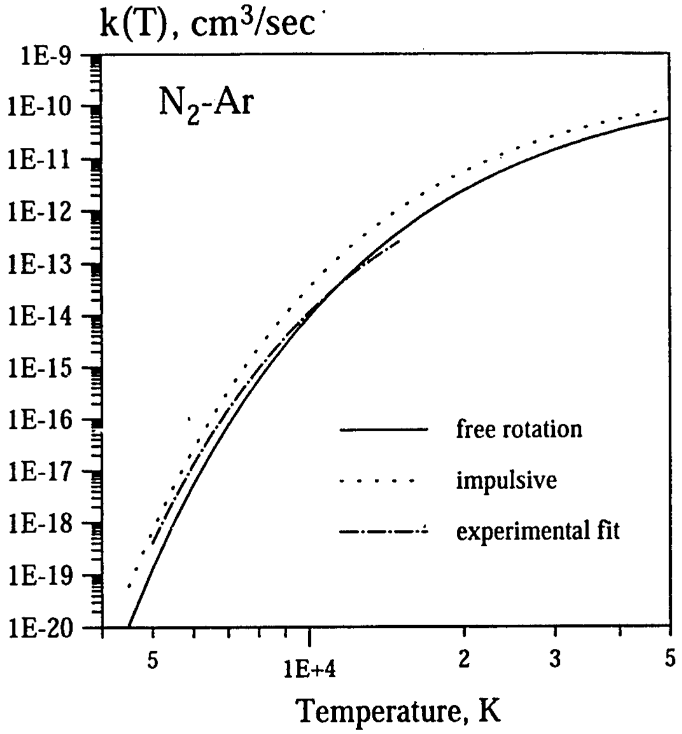

Fig. 5. Calculated and experimental[40] nitrogen thermal dissociation rates in N_2-Ar collisions versus temperature.

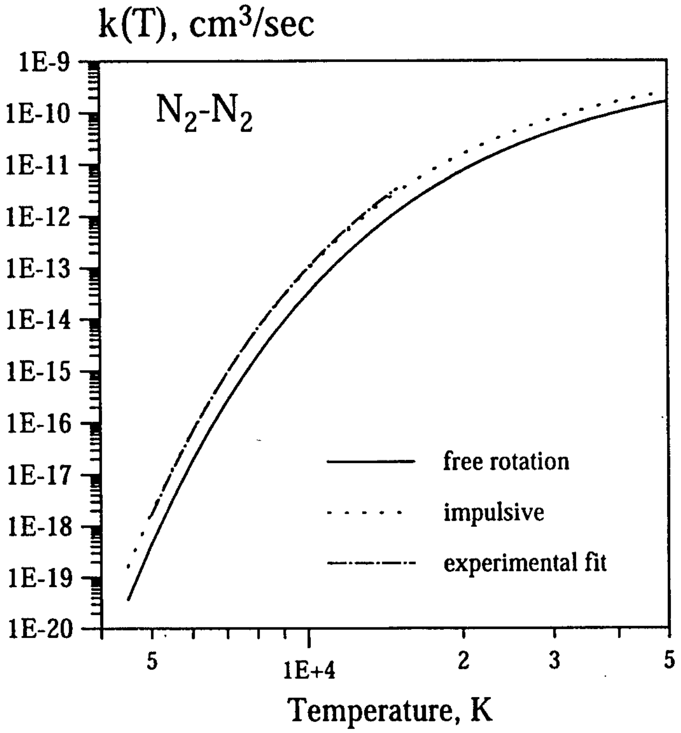

Fig. 6. Calculated and experimental[41] thermal dissociation rate of nitrogen in N_2-N_2 collisions versus temperature.

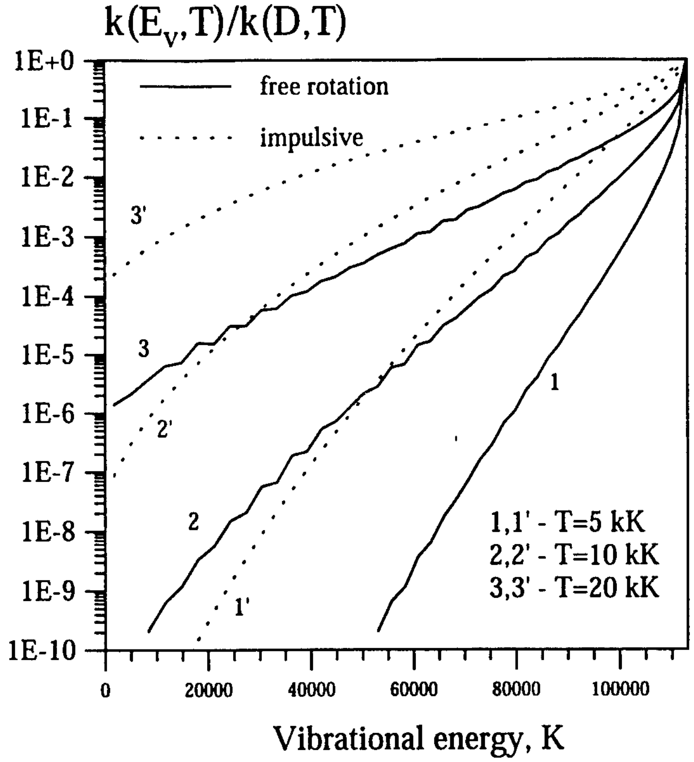

Fig. 7. Calculated state-specific dissociation rates in N_2-Ar collisions, normalized by the dissociation rate from the uppermost vibrational level.

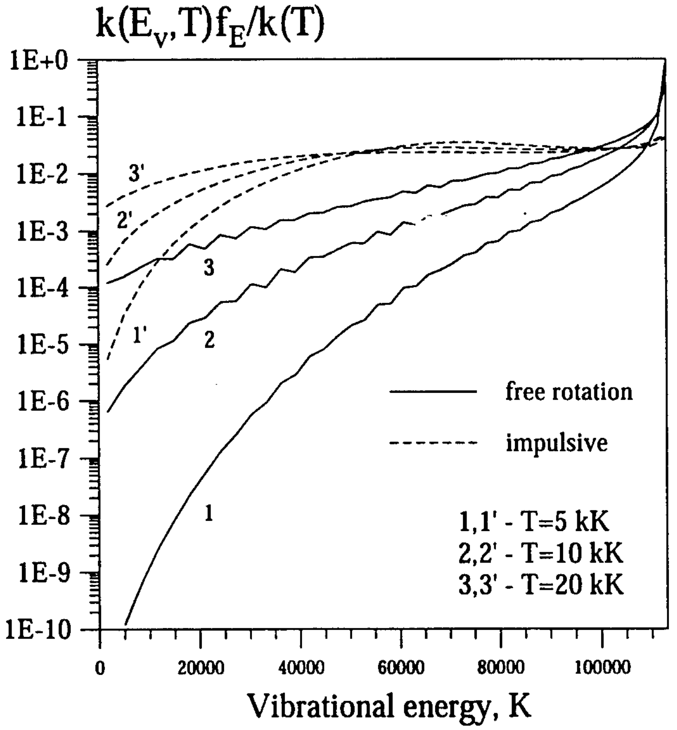

Fig. 8. Calculated state-specific dissociation rates in N_2-Ar collisions, multiplied by the Boltzmann population factor and normalized by the thermal dissociation rate.

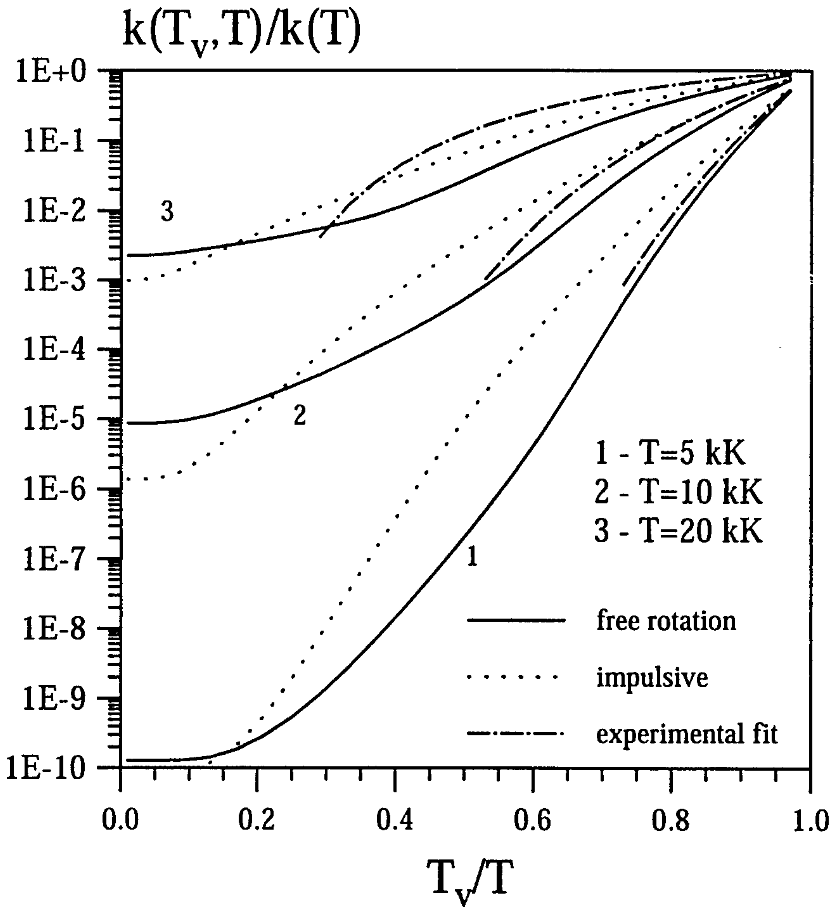

Fig. 9. Comparison of calculated and experimental[4, 5, 38, 42] nonequilibrium factors, i.e., the ratios of nonequilibrium and equilibrium dissociation rates, in pure nitrogen versus the ratio of vibrational and translational-rotational temperatures.

CHAPTER IV.

TIME-RESOLVED FOURIER TRANSFORM INFRARED SPECTROSCOPY OF OPTICALLY PUMPED CARBON MONOXIDE

1. Introduction

Nonequilibrium vibrational kinetics of diatomic and small polyatomic molecules has been a focus of attention for many years in gas discharge plasmas, molecular lasers, upper atmosphere chemistry, and gas dynamic flows [1,2]. The rate of energy transfer between the vibrational molecular modes and the "external" modes of rotation and translation is, in particular, a determining process in many high enthalpy fluid environments. The details of the actual distribution of energy among the vibrational quantum states is important in a more restricted range of problems, but is certainly key in non-thermal plasma chemical reactor design, in predicting radiation from supersonic nozzle expansions, and in the design of a variety of molecular gas lasers [3]. This energy distribution is primarily controlled by vibration-to-vibration (V-V) energy exchange processes [4,5],

$$AB(v) + AB(w-k) \rightarrow AB(v-k) + AB(w)\,, \tag{1}$$

which for a broad range of parameters are known to be much faster than vibration-to-translation (V-T) relaxation,

$$AB(v) + M \rightarrow AB(v-k) + M\,. \tag{2}$$

In Eqs. (1,2), AB and M stand for diatomic molecule and atom, respectively, v and w are vibrational quantum numbers, k is the number of quanta transmitted in a collision. The rates of the near-resonance V-V exchange processes of Eq. (1) among the high vibrational quantum levels (v~w, v,w>>1) are of particular importance, since molecules on the high vibrational levels can also participate in nonequilibrium chemical reactions, as well as produce electronic excitation and ionization. In particular, the vibration-to-electronic (V-E) processes, in which energy is transferred from highly vibrationally excited levels of the ground electronic state to a low-lying excited electronic state, with subsequent ultraviolet and visible band radiation, have been observed in optical pumping experiments in both CO [6-8] and NO [9,10]. Ionization in collisions of two vibrationally excited CO molecules pooling their energies together has been studied in [11,12]. Predictive analysis of kinetics of these energy transfer processes, coupled to the high vibrational level populations, require precise knowledge of the V-V rates.

The present work addresses recent measurements of the V-V rates in strongly vibrationally excited carbon monoxide. The V-V rates for CO-CO have previously been measured using a variety of spectroscopic techniques (see [6] and references therein), including experiments by Brechignac and co-workers [13-15] and DeLeon and Rich [6] who inferred the near-resonance V-V rates up to v≤29 and v≤35, respectively. The main advantage of the present study over the previous experiments is the use of time-resolved step-scan Fourier transform infrared (FTIR) emission spectroscopy. Step-scan FT spectrometers, such as the system used in the present study, have become available only relatively recently. These instruments provide the ability to record emission spectra in a broad wavelength range with high time resolution. The time resolution is limited by the response time of the detector system and data acquisition capabilities. In the present study, a fast response InSb detector with a high bandwidth DC preamplifier allows time resolution of up to a few nanoseconds. In other words, instead of measuring the time-dependent emission signal in a narrow wavelength range, the population of each radiating vibrational-rotational state can be monitored simultaneously. The step-scan technique requires a repetitively pulsed experiment, which is arranged in the present study; note that the technique could not be used for single-pulse experiments, such as in shock tunnels. An emission experiment is advantageous with this instrument, since absorption spectroscopy introduces noise complications from the incident absorption source. In addition, FT spectrometers provide throughput and multiplex advantages compared to conventional narrow-slit monochromators, improving the signal-to-noise ratio at high spectral resolution. Step-scan FT spectroscopy has been recently used to study energy transfer in vibrationally excited NO_2 [16,17].

Thus, in the present study, the time evolution of all vibrational states populated by the V-V processes up to extreme vibrational disequilibrium can be monitored simultaneously.

2. Experimental Setup

Fig. 1 shows a schematic of the experimental setup for the study of vibrational energy transfer in CO. A carbon monoxide laser is used to irradiate a gas mixture of CO and Ar, which is slowly flowing through the pyrex glass optical absorption cell shown. The residence time of the gas mixture in the cell is about 1 sec. The liquid nitrogen cooled CO laser was designed in collaboration with the University of Bonn and fabricated at Ohio State. It produces a substantial fraction of its power output on the v = 1→ 0 fundamental band component in the infrared. The laser can operate at more than 100 W continuous wave (c.w.) power. However, in the present experiment, the laser is typically operated at 10 W c.w. broadband power on the lowest ten fundamental bands, with up to ~0.3 W on the v = 1→ 0 component (see Table 1). The output on the lowest bands (1→ 0 and 2→ 1) is necessary to begin the absorption process in cold CO (initially at 300 K) in the cell.

Table 1. CO laser spectrum

Laser line	Power, W
1→0 P(15)	0.29
2→1 P(15)	0.62
2→1 P(16)	0.57
3→2 P(14)	0.79
3→2 P(15)	1.52
4→3 P(13)	0.31
4→3 P(14)	1.14
4→3 P(15)	0.80
5→4 P(13)	0.24
5→4 P(14)	0.95
5→4 P(15)	0.35
6→5 P(12)	0.42
6→5 P(13)	0.20
6→5 P(14)	0.56
7→6 P(12)	0.32
7→6 P(13)	0.44
8→7 P(12)	0.45
9→8 P(11)	0.13
9→8 P(12)	0.10
10→9 P(10)	0.05
10→9 P(12)	0.09

The present use of CO laser pumped absorption cells to study the V-V process is a further development of a technique with a considerable literature [6-11,18].

In the time-resolved experiments, intended to obtain a more precise measurement of the mechanism and rates of the V-V exchange processes, the laser beam is interrupted by a mechanical chopper, giving a nearly square wave input of laser power to the cell (see Fig. 2). After the laser is turned on, the lower states, $v \leq 10$, are populated by direct resonance absorption of the pump radiation in combination with the much more rapid redistribution of population by the V-V exchange processes. The time-dependent transmitted laser pulse shapes are also shown in Fig. 2 for different CO partial pressures in the cell. The V-V processes then continue to populate the higher vibrational levels above $v = 10$, which are not directly coupled to the laser radiation. When the laser is turned off, the vibrational levels are depopulated, again mainly by the V-V energy transfer, and the vibrational energy distribution approaches the Boltzmann distribution at the translational temperature. The chopper is operated at a low frequency of 13 Hz with a low duty cycle of $\cong 1/11$, so that the laser pulse duration is 6.8 msec, and the time between the pulses is about 75 msec. The low duty cycle is deliberately chosen to allow complete vibrational relaxation between the laser pulses.

In the steady-state measurements, the laser remains on all the time, so that a complete steady state is reached. Note that the vibrational energy stored in the molecule is constantly converted into heat both in V-V and V-T processes. However, the large heat capacity of the Ar diluent, as well as conductive and convective cooling of the gas flow, allow us to control the translational/rotational mode temperature in the cell. Even in steady-state conditions, when the average vibrational mode energy of the CO would correspond to a few thousand degrees Kelvin, the temperature never rises above a few hundred degrees. Thus a strong disequipartition of energy can be maintained in the cell, characterized by very high vibrational mode energy and a low translational/rotational mode temperature. Similar nonequilibrium conditions exist in a variety of rapid supersonic expansions, in glow plasma discharges, and in a number of other thermodynamic environments. The present setup allows us to study the energy transfer and kinetic processes in a closely controlled environment, without the complications of numerous electron impact processes which occur in electric discharges or the experimental difficulties of creating and controlling a supersonic flow.

As shown in Fig. 1, the population of the vibrational states of the CO in the cell is monitored by infrared emission spectroscopy. For this purpose, a Bruker step-scan Fourier transform IFS 66 spectrometer with step-scan and rapid-scan capabilities is used to record the spontaneous emission from the CO fundamental, first and second overtone bands through a window on the side of the cell. The FT spectrometer can be used for recording of both steady-state and time-resolved spectra. Steady-state spectra are typically recorded in rapid-scan mode at a spectral resolution of 0.25 cm^{-1}. In time-resolved measurements, a few hundred "time slices" are recorded in step-scan mode with a lower spectral resolution of 8.0 cm^{-1}, and a time resolution ranging from 5 μsec to 50 μsec, thereby spanning a time period of a few msec to a few tens of msec.

The Gaussian laser beam, which has a diameter of ~0.5 cm, does not have to be focused to provide substantial vibrational mode energy in the cell gases. However, in the present experiments it is focused to increase the power loading per CO molecule and accelerate the V-V up-pumping, providing an excitation region in the cell of ~1 mm diameter. The measurements reported here are made at the same Ar partial pressure of 100 torr, and at seven CO partial pressures varying from 0.5 torr to 3.5 torr.

3. Kinetic Model and the V-V Rate Parametrization

To interpret the results of both steady-state and time-resolved measurements, and to infer the V-V rates for CO-CO, we use a state-specific kinetic model of excitation and relaxation of optically pumped anharmonic oscillators in inhomogeneous media. It is based on the master equation model described in detail in [18]; two significant upgrades are (i) incorporation of laser power distribution and transport processes (diffusion and heat conduction) across the Gaussian laser beam, and (ii) incorporation of the multi-quantum V-V processes ($|k|>1$ in Eq. (1)). The model evaluates the time-dependent vibrational level populations in CO-Ar mixture excited by a laser beam:

$$\frac{\partial n_v(r,t)}{\partial t} = \frac{1}{r}\frac{\partial}{\partial r}\left[rD\frac{\partial n_v(r,t)}{\partial r}\right] + VV_v + VT_v + SRD_v + VE_v + PL_v$$

$$\left.\frac{\partial n_v(r,t)}{\partial r}\right|_{r=0} = 0\,; \quad n_v(r,t)\big|_{r=\infty} = n_v(r,t)\big|_{t=0} = n_v(T_0) \tag{3}$$

$$v = 0, v_{\max}$$

$$\rho c_p \frac{\partial T(r,t)}{\partial t} = \frac{1}{r}\frac{\partial}{\partial r}\left[r\lambda\frac{\partial T(r,t)}{\partial r}\right] + HVR$$

$$\left.\frac{\partial T(r,t)}{\partial r}\right|_{r-0} = 0\,; \quad T(r,t)\big|_{r=\infty} = T(r,t)\big|_{t=0} = T_0 \tag{4}$$

In Eqs. (3,4), $n_v(r,t)$ is the population of the vth vibrational level of CO, $n_v(T_0)$ is the initial equilibrium population at T_0=300 K, n_{CO} is the CO concentration, r is the distance from the beam axis, D and λ are the diffusion and heat transfer coefficients, respectively, ρ and c_p are density and specific heat at constant pressure. The rest of the notation is the same as in [18]: VV, vibration-vibration term; VT, vibration-translation term; SRD, spontaneous radiative decay (infrared); VE, vibration-electronic coupling; PL, laser pumping; HVR, gas heating by vibrational relaxation. The explicit expressions for these terms are given in [18] and will not be repeated here, with the exception of the V-V term, which in the presence of the multi-quantum processes is modified as follows:

$$\begin{aligned} VV_v = &\sum_{w,k} Q(v, w-k \to v-k, w)\cdot n_v n_{w-k} \\ &-\sum_{w,k} Q(v-k, w \to v, w-k)\cdot n_{v-k} n_w \end{aligned} \tag{5}$$

$$|\Delta k| \le \Delta v_{\max}$$

In Eq. (5), Q(v,w-k→v-k,w) is the rate of V-V energy exchange. Since the flow velocity is quite slow, a few cm/sec, convective cooling in the energy equation (4) is neglected.

The objective of upgrading the model is the study of the effects of nonuniform intensity distribution across the laser beam and vibrational energy transport by diffusion (see [19]), as well multi-quantum energy transfer, on the excitation and relaxation processes.

The Gaussian intensity distribution across the laser beam results in a faster V-V pumping near the beam axis. Pump power is highest on the axis, and it is here where the vibrational level populations most rapidly reach steady state. There is slower excitation far from the axis, where pump power is less. The same qualitative scenario (i.e. faster relaxation near the axis) can be observed during the relaxation after the laser is turned off. This occurs because V-V exchange between two excited molecules is a nonlinear kinetic process with a rate proportional to the product of the two level populations. For example, $[dn_2/dt]_{VV}\sim Q_{VV}(1,1\rightarrow 2,0)n_1n_1$, and the first-order "time constant" $\tau_{VV}\sim[Q_{VV}(1,1\rightarrow 2,0)n_1]^{-1}\neq$const is inversely proportional to n_1, which tends to increase with the pump laser power density. Note that emission spectroscopy is essentially a line-of-sight measurement. The line-of-sight integration of the time-dependent signal by the spectrometer will create an impression that the high level populations rapidly rise and decay, because of the contribution of the central portion of the beam where the power density is high and kinetics is fast. The described effect does not appear in linear or quasilinear kinetic processes, such as V-T relaxation or V-V exchange with the ground vibrational state, v=0. For these two cases, the first-order time constants, $\tau_{VT}\sim[P_{VT}(1\rightarrow 0)N]^{-1}$ and $\tau_{VV}\sim[Q_{VV}(1,0\rightarrow 0,1)n_0]^{-1}$, are indeed constant ($n_0$ changes fairly weakly during the excitation) and independent of the laser power.

Focusing of the laser beam is likely to reduce this effect due to the more rapid diffusion of vibrationally excited molecules across the narrow beam. However, a greater effect of diffusion when the beam diameter is reduced will further complicate the analysis. For example, previous time-resolved experiments [6,18] show that the typical rise and decay times for the infrared radiation from the high CO vibrational levels excited by the focused laser beam are of the order of a few milliseconds. On the other hand, simple estimates show that the characteristic time for diffusion of vibrational energy out of the excited volume is of the same order of magnitude: $\tau_{diff}\sim R^2/D\sim 10$ msec. Here R~1 mm is the focused laser beam diameter, and D~1 cm^2/sec is the diffusion coefficient of CO at P~100 torr. This results in a competition between the V-V energy transfer and energy transport by diffusion.

Finally, three-dimensional semiclassical trajectory calculations of the V-V rates for CO-

CO by Cacciatore and Billing [20] predict the rates of the near-resonance multi-quantum processes collisions involving exchange of two or more quanta ($|k|\geq 2$ in Eq. (1)) to be comparable with those of the single-quantum processes for high vibrational levels (v,w>10 in Eq. (1)). This prediction is consistent with the results of the previous experiments [6], which inferred the near-resonance single-quantum V-V rates to be an order of magnitude greater than the gas kinetic collision frequency. This result might be attributed to the latent contribution of the multi-quantum processes, not accounted for in the kinetic model used.

All this suggests that the spatial power distribution, diffusion, and multi-quantum relaxation might well be significant factors in the present experiments.

In the present model, the rates of the energy transfer processes, except for CO-CO V-V rates, are the same as described in [18]. The V-V rates are the remaining parameters in the model calculations that are only known with some uncertainty. Therefore they are varied to provide better agreement with the experiment. In the calculations, two different sets of rates are used. In the first baseline series of modeling calculations, we used a V-V rate model based on the analytic parametrization suggested by Jeffers and Kelley [21], developed from perturbation theory for the cross sections, and correlated with the body of experimental data obtained in several previous measurements (see [6] and references therein). These rates constitute Set I (see Fig. 3). This rate model is applicable only for single-quantum V-V exchange processes. The explicit V-V rate expressions used can be found in Appendix. In the second series of calculations, we used an analytic non-perturbative theory of vibrational energy transfer [22-24] that provides a convenient parametrization of the results of the trajectory calculations by Cacciatore and Billing [20], considered to be the most reliable theoretical data available. This "forced harmonic oscillator" (FHO) theory takes into account the coupling of many vibrational states during a collision and is therefore applicable for multi-quantum processes. Since the published set of the CO-CO rates [20] is somewhat incomplete, we have used the computer codes DIDIAV and DIDIEX developed by Billing [25,26] to extend the calculations up to $|k|\leq 5$, for the same CO-CO potential as used in [20]. The comparison of these rate data with the FHO parametrization, given in the Appendix, is shown in Figs. 3, 4. These V-V rates constitute Set II.

In addition, the code DIDIEX was also used to calculate the rates of the asymmetric one-by-two quanta near-resonance V-V exchange process

$$CO(0) + CO(w) \rightarrow CO(1) + CO(w-2)\,, \quad v = 35-50, \qquad (6)$$

(see Fig. 5). This process, incorporated in all subsequent calculations (using both sets of V-V rates) was suggested by Napartovich and co-workers to be very important in kinetics of high vibrational levels of CO [27]. Note that calculations of the rates of process (6) require the use of accurate CO spectroscopic constants [28]; otherwise the quantum number at which the rate (6) reaches maximum can be shifted by a few levels.

We emphasize the necessity of the use of analytic parametrization for rate inference. Even if only transitions between adjacent quantum levels are incorporated in the time-resolved experiment analysis, there are potentially 40 x 40 specific rates involved for a pump up to v = 40. As is well known, deconvolution of all the specific rates from the time-dependent population measurements alone would require far greater accuracy than achieved in the present data. We therefore require theoretical models of the quantum number dependence of these rates, as discussed above, to greatly reduce the number of parameters involved.

The system of equations (3,4) for 50 vibrational levels of CO is solved using a standard solver for stiff partial differential equations, PDECOL [29]. In the calculations, a 31-point nonuniform grid, with most points located near the beam axis, is typically used. The laser line intensity distributions are given by the equation $I_i(r)=0.5\cdot(I_{0i}+I_{0t})\cdot[2/\pi R^2\cdot \exp(-2r^2/R^2)]$, where I_{0i} and I_{0t} are the incident and the transmitted line intensities in W, and parameter R=0.28 mm in the Gaussian intensity distribution across the focused laser beam is calculated by the code STRAHL developed at University of Bonn [30]. A synthetic spectrum code is then used to generate the model spectra. Rotational level populations are assumed to be in equilibrium with the translational temperature T(r). Both the vibration-rotation level populations and the emission intensity are integrated along the optical path of the spectrometer (i.e. across the laser beam). The code uses the spectroscopic data for CO molecule [28] and accurate Einstein coefficients for spontaneous emission and absorption coefficients for the CO infrared bands [31] as inputs. As usual, the synthetic spectra are corrected for the blackbody-calibrated instrument response function.

4. Results and Discussion

4.1. Steady-State Measurements

Under the conditions described in Section 2, with the laser left on, a highly nonequilibrium distribution of vibrational energy is created in the CO in the cell. The second overtone, first overtone, and part of the fundamental emission from CO excited by the focused laser beam is shown in Fig. 6, as recorded by the FT spectrometer at a resolution of 0.25 cm^{-1}. The second overtone bands can be seen at the highest frequencies on the left ($\nu>4300$ cm^{-1}), the first overtone bands dominate at the lower frequencies (2250 $cm^{-1}<\nu<4300$ cm^{-1}), and the high frequency tail of the R-branch of the $v = 1 \rightarrow 0$ fundamental is the tall peak on the right. A long wavelength cut-off filter is used to prevent any more of the very intense fundamental band emission at frequencies $\nu<1950$ cm^{-1} from being recorded by the detector, and swamping the overall signal. While this resolution is approximately 1/10 the rotational spacing of the CO molecule, there is a dense array of individual vibrational-rotational lines, due to the overlapping of the various band components. The vibrational population distribution functions (VDF) inferred from such high-resolution spectrum using the standard technique [32] are shown in Figs. 7, 8 for different CO partial pressures. Typically, the vibrational level populations for $v<30$ are inferred with the accuracy of a few per cent, while for $v\geq30$ the accuracy becomes somewhat worse, up to 20-30%. The translational/rotational temperatures at these conditions, inferred from the rotationally resolved R-branch of the $1\rightarrow0$ fundamental band with the accuracy of ±10 K, are also shown in Fig. 8. The distributions shown in these figures are the well-known "V-V pumped" distributions [4,5], maintained by the rapid redistribution of vibrational energy by the V-V processes, which pump energy into the higher vibrational levels. They are obviously extremely non-Boltzmann, and characterized by high population of the upper vibrational levels. Although there are more than 80 bound vibrational levels in the CO ground electronic state, only the lowest 40 levels are populated by the V-V process. Note that V-V pumping of CO above level $v\sim40$ has not been achieved in the previous experiments with vibrationally excited carbon monoxide [6,8,11,18,33,34] in a broad range of translational temperatures T=90-700 K, regardless of available pumping power. This includes measurements in electric discharges and in laser absorption cells (both in gas and in liquid phase).

The reason for this persistent termination of the up-pumping has been discussed in the literature for some time [6,8,27,33,35]. The three most likely kinetic processes responsible for this effect are (i) asymmetric one-by-two quanta near-resonance V-V exchange (6) [27], (ii) near-resonance vibration-to-electronic (V-E) energy transfer from v~40 of the ground electronic state, $X^1\Sigma$, to the low levels of the excited electronic state $A^1\Pi$,

$$\begin{aligned} &CO(X^1\Sigma, v\sim 40)+CO\rightarrow CO(A^1\Pi, v\sim 0)+CO \\ &CO(A^1\Pi)\rightarrow CO(X^1\Sigma)+h\nu \\ &CO(A^1\Pi)+M\rightarrow CO(X^1\Sigma)+M\,, \end{aligned} \tag{7}$$

suggested in [6] based on the measurements of time-resolved radiation from CO 4th positive electronic bands $A^1\Pi\rightarrow X^1\Sigma$, coupled with the population of v~35, and (iii) rapid V-T relaxation on the products of vibrationally-induced chemical reactions initiated by the process,

$$CO(v)+CO(w)\rightarrow CO_2+C, \tag{8}$$

such as C, C_2, C_2O, etc. (vibrationally-induced chemistry was first observed in optically pumped CO in [36]). Finally, both theoretical calculations of the V-T rates for CO-CO [20] and measurements of the V-T rates CO-Ar at high vibrational levels [37] show them to be far too slow to affect the vibrational level populations at v~40, especially at the low temperatures of T=100-300 K. Note that dramatic increase of the state-specific vibrational relaxation rates above a threshold vibrational quantum level, induced by chemical reactions or intermolecular electronic coupling, has been also previously observed in NO (v>14) [38], O_2 (v>26) [39], and NO_2 (vibrational energy greater than 10,000-12,000 cm^{-1}) [40].

To analyze the effect of these processes on the observed up-pumping termination, we calculated the steady-state distributions when turning processes (6) and (7) on and off separately, for both sets of V-V rates discussed in Section 3. The results are summarized in Figs. 7, 8. First, calculations using the V-V rates of Set I show that the asymmetric V-V exchange (6) truncates the VDF at higher quantum numbers than observed in the experiment, i. e. at v~45, where the asymmetric V-V rate reaches maximum (see Fig. 5). Replacing process (6) by the V-E energy transfer (7) predicts VDF truncation in satisfactory agreement with the low temperature data (see Fig. 7). However, as the CO partial pressure and the translational temperature both increase, the experimental VDF crashes at the lower quantum numbers than predicted using the near-resonance V-E transition (7) (see Fig. 8).

These results are consistent with the studies of the V-E energy transfer in CO by Wallaart and co-workers [8]. First, Wallaart et al. concluded that the measured steady-state populations of CO($A^1\Pi$,v=1-11) best correlate not with the ground state level v=40 but with v=33, and therefore suggested a more complicated multi-step mechanism of CO($A^1\Pi$) population via mediation of the triplet electronic states with excitation energies between 7 and 8 eV. In addition, their measurements of the CO($A^1\Pi$) concentrations, $n_{CO(A)}=10^5$-10^6 cm^{-3}, lead us to conclude that the maximum power removed by both radiation and collisional quenching of the A state, is $n_{CO(A)}E_A/\tau \sim 10^{-5}$-$10^{-4}$ W/cm^3, which is negligible compared with the absorbed laser power of 2 W. Here E_A=8 eV is the excitation energy of the A state, and $\tau \sim 10^{-8}$ sec is its radiative lifetime, which at P=100 torr is comparable with the collisional lifetime. On the other hand, in our previous paper [19] we have shown that an energy sink at the level $v_a \sim 40$ that cuts off the V-V pumped VDF with the Treanor minimum at $v_0 \sim 10$ must remove a much larger fraction of the power added to the vibrational mode of the oscillator, $[1-x_e(v_a+v_0)]/(1-2x_ev_0) \sim 80\%$, the other 20% being removed by the V-V exchange. These estimates demonstrate that regardless of the details of kinetics of the V-E transition $X^1\Sigma \rightarrow A^1\Pi$, it is unlikely to be responsible for the up-pumping truncation at the conditions of experiments [8] (T=700 K), since it apparently does not remove enough power from the vibrational mode of CO. We note, however, that the CO($A^1\Pi$,v) populations measured in Ref. [8] might conceivably be underestimated due to the strong self-absorption of the CO fourth positive bands.

Quite obviously, chemical reactions such as (8) can truncate the V-V pumped distribution only if the reaction rate coefficient, k_r, is comparable with the near-resonance V-V rate that sustains the VDF at v~40, $k_r \sim Q_{vv} \sim 10^{-10}$ cm^3/s. This gives an unrealistic reaction rate $k_r n_{CO(v)} n_{CO(w)} \sim 10^{-10} \cdot 10^{14} \cdot 10^{14} = 10^{18}$ 1/cm^3/sec, or ~100 torr CO per second. We therefore tentatively suggest that the VDF cutoff at v<40 can be at least partially attributed to the fast V-T relaxation of CO on the products of chemical reaction (8). This mechanism may be most prevalent at the higher cell temperatures. At the same time, previous experimental data (in particular, the VDF crash at v~40 observed at cryogenic temperatures T=90-100 K [33,34], when the V-T relaxation becomes extremely slow) still suggest that the V-E transition (8) might also play a role in the VDF truncation at the low temperatures.

Returning to the discussion of Fig. 7, we note that calculations using the V-V rates of Set II demonstrate a similar although somewhat weaker effect of processes (6) and (7) on the VDF at v~40-45. In addition, the slope of the VDF calculated using Set II V-V rates becomes much steeper than in the experiment (see Fig. 7). Varying Δv_{max} in the calculations showed that this occurs due to a rapid increase of the multi-quantum V-V rates at high vibrational quantum numbers, even though the rates of the single-quantum processes of Set II are somewhat slower than those of Set I (see Figs. 3, 4). It therefore appears that Set II substantially overpredicts the multi-quantum V-V rates at the high v's.

Before we proceed with the discussion of the time-resolved measurements, we tentatively conclude that the use of the rates of Set I together with the V-E process (7) instead of the asymmetric V-V exchange (6) provide better agreement with the low-temperature steady-state data. We would like to emphasize that, apparently, the details of the VDF truncation kinetics, which are still not well understood, have little effect on the vibrational populations at v<40 (see Fig. 7). This fact allows inference of the V-V rates from the time-resolved measurements. Finally, Fig. 9, which shows the VDF's and the values of the first level vibrational temperature,

$$T_v = \frac{\omega_e(1-2x_e)}{\ln(f_o / f_1)}, \tag{9}$$

at different distances from the beam axis, demonstrates the strong spatial nonuniformity of the modeled V-V pumped region.

4.2. Time-Resolved Measurements

Fig. 10 shows a typical time-resolved step-scan spectrum obtained in the experiment. In this three-dimensional projection, emission intensity in arbitrary units is on the vertical axis, frequency in cm^{-1} is on the horizontal axis, and the diagonal axis is the time in microseconds. The overtone bands (see Section 4.1) are used as the primary diagnostic to infer the vibrational state populations, as the gas is optically thin on all these transitions. The resolution here is 8 cm^{-1}, so that the rotational line structure is not resolved, although the individual vibrational band component structure is clearly seen. The time resolution is 50 microseconds here, and every spectrum obtained at these intervals is being displayed. The broadband structure visible at t=0 is the blackbody background, subtracted in the subsequent analysis. The laser is switched on at t = 0, reaches its steady state intensity in about 200 microseconds, and is switched off at t=6.6

milliseconds (see Fig. 2). In addition to the low time resolution spectrum shown in Fig. 10, a 5 microsecond time resolution spectrum is taken for each CO partial pressure to better resolve the initial 2 msec stage of the up-pumping after the laser is turned on. For each step-scan CO emission spectrum, a time-dependent laser spectrum was also measured; the time-dependent transmitted laser power obtained from these laser spectra is shown in Fig. 2.

Figs. 11 and 12 display slice-by-slice comparison between the experimental and the synthetic spectra using the model described in Section 3 and the first set of the V-V rates. Although the spectra are shifted along the y-axis for illustrative purpose, they are shown in the same scale. In this experiment, the CO partial pressure is 3.5 torr. One can see that although the model is in very good agreement with the time-resolved relaxation data (see Fig. 12), it fails to reproduce the time-dependent spectra during the excitation (see Fig. 11, only two synthetic spectra at t=0.45 msec and t=4.45 msec are shown). Basically, the model predicts much faster laser radiation absorption and the CO up-pumping after the laser is turned on, so that the V-V pumped distribution reaches the steady state within a few hundred of microseconds instead of a few milliseconds (see Fig. 11). The same kind of disagreement between theoretical and experimental excitation spectra has been also observed at other CO partial pressures.

Figure 13 displays the slice-by-slice comparison with the relaxation data at P=0.5 torr. The scale in this figure is different from the scale used in Figs. 11 and 12 (the emission intensity is roughly proportional the CO partial pressure). However, all time slices within each figure are still shown in the same scale.

It is disappointing that the model is at variance with the time-resolved excitation data. Note that varying the adjustable parameters in the Set I parametrization or the use of Set II had not resulted in substantial improvement of the agreement. This fact, as well as good agreement of the model with the relaxation data in a wide range of CO partial pressures (see Figs. 12, 13), suggests that the observed slow up-pumping is not related to the V-V rates. On the other hand, the time dependence of the absorbed laser power (e.g. shown in Fig. 2), and therefore the overall rate of CO up-pumping were found to be very sensitive to the laser spectrum. We therefore believe that the observed slow excitation is due to the following two effects. First is the laser "line hopping" (i. e. laser output power change on individual lines) detected in the time-resolved laser spectra, which is significant even though the total laser power remains fairly stable (see Fig. 2). Second is the fast V-T relaxation on the chemical reaction products, which is the "bottleneck" at the first stage of excitation when the rate of the V-V process that triggers the up-pumping, $CO(1)+CO(1)\rightarrow CO(0)+CO(2)$, is comparable with that of the V-T relaxation, $CO(1)+M\rightarrow CO(0)+M$. Since the V-T relaxation rates for CO-CO and CO-Ar are extremely slow, relaxation on reaction products may change the effective rate of the V-T relaxation by several orders of magnitude, thereby delaying the onset of the up-pumping. We plan to verify these assumptions in our on-going time-resolved experiments on optical pumping of NO [41]. In these experiments, a stable single-line CO laser is used, while the rapid self-relaxation NO-NO is the dominant V-T process with well-known rates [38], so there should be much less uncertainty in the up-pumping delay. Finally, even though achieving better agreement with the experimental excitation data is certainly desirable, we believe that the relaxation data allow more straightforward inference of the V-V rates. Indeed, in this case the model does not need to incorporate the laser-related processes (i.e. absorption and induced radiation), and the model predictions are less dependent on the laser spectrum and intensity profile, which reduces the uncertainty in the inferred V-V rates.

Figure 14 shows the time-resolved relaxation spectra using the second set of the V-V rates for the conditions shown in Fig. 13 (at P_{CO}=0.5 torr). Comparing these two figures, one can see that the use of the rates of Set II results in a somewhat worse agreement with the experiment, just as has been observed in the steady-state calculations (see Section 4.1). In particular, the radiation intensity from $v>20$ ($\nu<3400$ cm^{-1}) calculated using the Set II rates is noticeably weaker than both in the experiment and in the Set I calculations (see Figs. 13, 14). This is consistent with the lower steady-state vibrational populations calculated using the rates of Set II, compared with the Set I results (see Fig. 7). We therefore confirm the conclusion of Section 4.1 that calculations by Cacciatore and Billing substantially overpredict the multi-quantum V-V rates among the high vibrational quantum numbers. Note that recent semiclassical calculations by Coletti and Billing [42], where a more accurate potential energy surface has been used, also predict somewhat lower values of the V-V rates.

Figure 15 displays the time-dependent VDF's for the conditions of Fig. 12, i.e. relaxation at P_{CO}=3.5 torr (solid lines). It shows that the relaxation occurs through a succession of distributions with long plateaus, known to be dominated by near-resonance V-V exchange [4,5]. Another well-pronounced feature is the development of a total population inversion at a late stage of the relaxation process, for $v>10$, created by the diffusion of the vibrationally excited molecules out of the beam region (compare with the steady-state VDF's at large distances from the beam center shown in Fig. 9). Figure 15 also shows that the calculated vibrational level populations drop by a factor 20-100 during the relaxation, i.e. that the experimental step-scan data cover a substantial portion of the entire relaxation process. Dashed lines in Fig. 15 show the vibrational distributions calculated assuming a spatially uniform excited region and neglecting diffusion. The latter calculation starts from a VDF that is close to the line-of-sight integrated VDF predicted by the model incorporating nonuniformity and diffusion, and the V-V rates are the same in both cases. Qualitative difference between these two calculations can be easily seen. Relaxation in a nonuniform region occurs much faster because of the higher vibrational populations near the beam axis (see discussion in Section 3 and Fig. 9). The vibrational level populations calculated without nonuniformity and diffusion drop by only a factor 4-5, which is inconsistent with the step-scan relaxation spectra (see Fig. 12). Also, in this calculation the total population inversion does not form. This clearly shows the importance of taking into account spatial nonuniformity of the excited region as well as the transport processes.

Parametric calculations using the rates of Set I, where we replaced the V-E transfer (7) by the asymmetric V-V exchange (6) showed that both the VDF for $v<40$ and the synthetic spectra shown in Figs. 12,13 are primarily influenced by the V-V rates, and only weakly sensitive to the rates of other energy transfer processes. Finally, varying the adjustable parameters for Set I shown in the Appendix showed that their values chosen in [6] provide the most consistent agreement with the step-scan relaxation spectra for P_{CO}=0.5-3.5 torr.

The time-resolved measurements discussed in this section are made at translational temperatures fairly close to room temperature. Indeed, from Fig. 16 which shows the temperature change at the beam axis during the excitation and relaxation one can see that the maximum temperature rise at P_{CO}=3.5 torr is about 100 K. However, good agreement between the steady-state data and the modeling calculations for $v<30$ in the temperature range T=400-730 K (see Fig. 8) shows that the Set I rate parametrization is also applicable at these temperatures. As has been discussed in Section 4.1, the difference between the calculated and the experimental VDF's at $v>30$ in Fig. 8 is due to the effect of the processes unrelated to the V-V exchange.

5. Summary

In the present work, time-resolved step-scan Fourier transform infrared spectroscopy of optically pumped carbon monoxide is used to study the kinetics of vibrational energy transfer processes (primarily V-V exchange) in strongly vibrationally nonequilibrium CO. Time evolution of all vibrational states populated by the V-V processes up to extreme vibrational disequilibrium is monitored simultaneously. The V-V rates are inferred from these data using a kinetic model that incorporates the pump laser spatial power profile and transport processes, and allows incorporation of multi-quantum V-V processes. The model predictions agree well with the step-scan relaxation spectra. Comparison of calculations using two different sets of V-V rates with experimental spectra showed that the use of the V-V rates of Set I provides better agreement with experiment. It is also shown that the multi-quantum V-V rates of Set II (i.e. analytic parametrization of semiclassical trajectory calculations by Cacciatore and Billing) are overpredicted at high vibrational quantum numbers.

These results provide new insight into nonequilibrium vibrational kinetics, and also demonstrate the capabilities of the time-resolved step-scan Fourier-transform spectroscopy for studies of molecular energy transfer processes and validation of theoretical rate models.

6. Appendix

6.1. DeLeon-Rich single-quantum V-V rate parametrization (Set I) [6,18]

$$Q(v, w-1 \to v-1, w) = Z(S^{v,v-1}_{w-1,w} + L^{v,v-1}_{w-1,w})e^{-\Delta E/2T}\ , \quad \Delta E = 2\omega_e x_e (v-w)$$

$$S^{v,v-1}_{w-1,w} = S(T)\frac{v}{1-x_e v}\frac{w}{1-x_e w}F(\lambda^{v,v-1}_{w-1,w})$$

$$F(\lambda) = \frac{1}{2}(3-e^{-2\lambda/3})e^{-2\lambda/3}\ , \quad \lambda^{v,v-1}_{w-1,w} = 2^{-3/2}\sqrt{\frac{c}{T}}|\Delta E|$$

$$L^{v,v-1}_{w-1,w} = L(T)\left(\frac{g^{v,v-1}}{g^{1,0}}\right)^2\left(\frac{g^{w-1,w}}{g^{1,0}}\right)^2\exp\left(-\frac{\Delta E^2}{bT}\right)$$

$$\left(\frac{g^{v,v-1}}{g^{1,0}}\right)^2=\left(\frac{a+1}{a+3-2v}\right)^2\frac{v(a+2-2v)(a+4-2v)}{a(a+3-v)}, \quad a=1/x_e$$

Gas-kinetic collision frequency, $Z=3\cdot10^{-10}(T/300)^{1/2}$ cm^3/s

Parameters:

Short-range interaction, $S(T)=4.93\cdot10^{-4}$ (T/300) cm^3/s, $c=0.456$ K^{-1}

Long-range interaction, $L(T)=5.37\cdot10^{-3}$ (300/T) cm^3/s, $b=40.36$ K

6.2. FHO parametrization of Cacciatore-Billing V-V rates (Set II) [20,24]

$$Q(v,w-k\to v-k,w)=\frac{\left(S_{w-k,w}^{v,v-k}\right)^k}{k!\left(1+\frac{3}{2}\frac{S_{w-k,w}^{v,v-k}}{k+1}\right)^{k+1}}+\frac{\left(L_{w-k,w}^{v,v-k}\right)^k}{k!\left(1+\frac{3}{2}\frac{L_{w-k,w}^{v,v-k}}{k+1}\right)^{k+1}},$$

$$S_{w-k,w}^{v,v-k}=S(T)\cdot\left(\frac{v!}{(v-k)!}\frac{w!}{(w-k)!}\right)^{1/k}F(\lambda_{w-k,w}^{v,v-k})$$

$$F(\lambda)=\frac{1}{2}(3-e^{-2\lambda/3})e^{-2\lambda/3}, \quad \lambda_{w-k,w}^{v,v-k}=2^{-3/2}\sqrt{\frac{c}{T}}\frac{|\Delta E|}{k}$$

$$L_{w-k,w}^{v,v-k}=L(T)\cdot\left(\frac{v!}{(v-k)!}\frac{w!}{(w-k)!}\right)^{1/k}\exp\left(-\frac{(\Delta E/k)^2}{kb\sqrt{T}}\right)$$

$$\Delta E=2k\omega_e x_e(v-w)$$

Parameters:

Short-range interaction, $S(T)=8.73\cdot10^{-4}$ (T/300) cm^3/s, $c=0.475$ K^{-1}

Long-range interaction, $L(T)=3.36\cdot10^{-3}\,(300/T)^{1/2}$ $\mathrm{cm^3/s}$, $b=1386$ $\mathrm{K^{3/2}}$

6.3. Asymmetric V-V rate parametrization (used with both V-V rate sets) [24]

$$Q(0, w\rightarrow 1, w-2) = Z(S^{1,0}_{w-2,w} + L^{1,0}_{w-2,w}) \cdot x_e \frac{w(w-1)}{2}$$

$$S^{1,0}_{w-2,w} = S(T) \cdot F(\lambda^{1,0}_{w-2,w})$$

$$L^{1,0}_{w-2,w} = L(T) \cdot \exp\left(- \frac{\Delta E^2}{b\sqrt{T}} \right)$$

S(T), L(T), c, b, and F(λ) are the same as in 7.2.

References

1. "Nonequilibrium Vibrational Kinetics", ed. M. Capitelli, Springer, Berlin, 1986
2. C. Park, "Nonequilibrium Hypersonic Aerodynamics", Wiley, New York, 1990
3. J. W. Rich, S.O. Macheret, and I.V. Adamovich, "Aerothermodynamics of Vibrationally Nonequilibrium Gas", Experimental Thermal and Fluid Science, vol. 13, 1996, p. 1
4. J. W. Rich, "Relaxation of Molecules Exchanging Vibrational Energy", in "Applied Atomic Collision Physics", vol. 3, "Gas Lasers", ed. E.W. McDaniel and W.L. Nighan, Academic Press, New York, 1982, pp. 99-140
5. B.F. Gordiets, V.A. Osipov, and L.A. Shelepin, "Kinetic Processes in Gases and Molecular Lasers", Gordon and Breach, London, 1988
6. R.L. DeLeon and J.W. Rich, Chem. Phys., vol. 107, 1986, p. 283
7. W. Urban, J.X. Lin, V.V Subramaniam, M. Havenith, and J.W. Rich, Chem. Phys., Vol. 130, 1989, p. 389
8. H.L. Wallaart, B. Piar, M.Y. Perrin, and J.P. Martin, Chem. Phys., Vol. 196, 1995, p. 149
9. H. Dunnwald, E. Siegel, W. Urban, J.W. Rich, G.F. Homicz, and M.J. Williams, Chem. Phys., Vol. 94, 1985, p. 195
10. S. Saupe, I. Adamovich, M.J. Grassi, and J.W. Rich, Chem. Phys., vol. 174, 1993, p. 219
11. I. Adamovich, S. Saupe, M.J. Grassi, O. Schulz, S. Macheret, and J.W. Rich, Chem. Phys., vol. 173, 1993, p. 491
12. I.V. Adamovich and J.W. Rich, J. Phys. D: Appl. Phys., vol. 30, 1997, p. 1741
13. Ph. Brechignac, J.P. Martin, and G. Taieb, IEEE J. Quant. Electr., QE-11, 1975, p. 797
14. Ph. Brechignac, G. Taieb, and F. Legay, Chem. Phys. Lett., vol. 36, 1975, p. 242
15. Ph. Brechignac, Chem. Phys., vol. 34, 1978, p. 119
16. G.V. Hartland, D. Qin, and H.L Dai, J. Chem. Phys., vol. 100, 1994, p. 7832
17. G.V. Hartland, D. Qin, and H.L Dai, J. Chem. Phys., vol. 101, 1994, p. 8554
18. C. Flament, T. George, K.A. Meister, J.C. Tufts, J.W. Rich, V.V. Subramaniam, J.-P. Martin, B. Piar, and M.-Y. Perrin, Chem. Phys., vol. 163, 1992, p. 241
19. I.V. Adamovich, S.O. Macheret, and J.W. Rich, Chem. Phys., vol. 182, 1994, p. 167
20. M. Cacciatore and G.D. Billing, Chem. Phys., vol. 58, 1981, p. 395
21. W.Q. Jeffers and J.D. Kelley, J. Chem. Phys., vol. 55, 1971, p. 4433

22. A. Zelechow, D. Rapp, and T. Sharp, J. Chem. Phys., Vol. 49, 1968, p. 286
23. I.V. Adamovich, S.O. Macheret, J.W. Rich and C.E. Treanor, AIAA J., vol. 33, 1995, p. 1064
24. I.V. Adamovich, S.O. Macheret, J.W. Rich and C.E. Treanor, J. Thermophys. Heat Trans., Vol. 12, 1998, p. 57
25. G.D. Billing, Comp. Phys. Comm., Vol. 32, 1984, p. 45
26. G.D. Billing, Comp. Phys. Comm., Vol. 44, 1987, p. 121
27. A.V. Demyanov, I.V. Kochetov, A.P. Napartovich, V.G. Pevgov, and A.N. Starostin, Sov. High Temp. Phys., vol. 18, 1980, p. 918
28. K.P. Huber and G. Herzberg, "Molecular Spectra and Molecular Structure", Vol. 4, "Constants of Diatomic Molecules", New York, Van Nostrand, 1979
29. N.K. Madsen and R.F. Sincovec, ACM Trans. Math. Software, vol. 5, 1979, p. 326
30. A. Yariv and P. Yeh, "Optical Waves in Crystals: Propagation and Control of Laser Radiation", Wiley, New York, 1984; U. Sterr and W. Ertmer (Univ. Of Bonn, Germany), private communication
31. C. Chackerian, Jr., R. Farrenq, G. Guelachvili, C. Rosetti, and W. Urban, Can. J. Phys., Vol. 62, 1984, p. 1579
32. K.P. Horn and P.E. Oettinger, J. Chem. Phys., vol. 54, 1971, p. 3040
33. R. Farrenq, C. Rosetti, G. Guelachvili, and W. Urban, Chem. Phys., vol. 92, 1985, p. 389; R. Farrenq and C. Rosetti, Chem. Phys., vol. 92, 1985, p. 401
34. I.V. Adamovich, J.W. Rich, and C.E. Treanor, "Energy Transfer Processes in High Enthalpy Nonequilibrium Fluids", AIAA Paper 96-1982, presented at 27th AIAA Fluid Dynamics Conference, June 1996, New Orleans, LA
35. J.W. Rich, R.C. Bergman, and M.J. Williams, in: Gas-Flow and Chemical Lasers, ed. J.H. Wendt, Hemisphere, Washington, 1978
36. J.W. Rich and R.C. Bergman, Chem. Phys., Vol. 44, 1979, p. 53
37. J.W. Rich, R.C. Bergman, and M.J. Williams, Measurement of Kinetic Rates for Carbon Monoxide Laser Systems, Final Contract report AFOSR F49620-77-C-0020 (November 1979)
38. X. Yang, E.H. Kim, and A.M. Wodtke, J. Chem. Phys., vol. 96, 1992, p. 5111
39. J.M. Price, J.A. Mack, C.A. Rogaski, and A.M. Wodtke, Chem. Phys., vol. 175, 1993, p. 83

40. G.V. Hartland, D. Qin, H.L. Dai, and C. Chen, J. Chem. Phys., vol. 107, 1997, p. 2890

41. A.V. Saveliev, P.F. Ambrico, I.V. Adamovich, and J. W. Rich, "Vibrational Transfer Among High Vibrational Levels of Nitric Oxide", AIAA Paper 95-0630, presented at 33rd Aerospace Sciences Meeting and Exhibit, January 1995, Reno, NV

42. C. Coletti and G.D. Billing, Chem.Phys., vol. 111, 1999, p. 3891

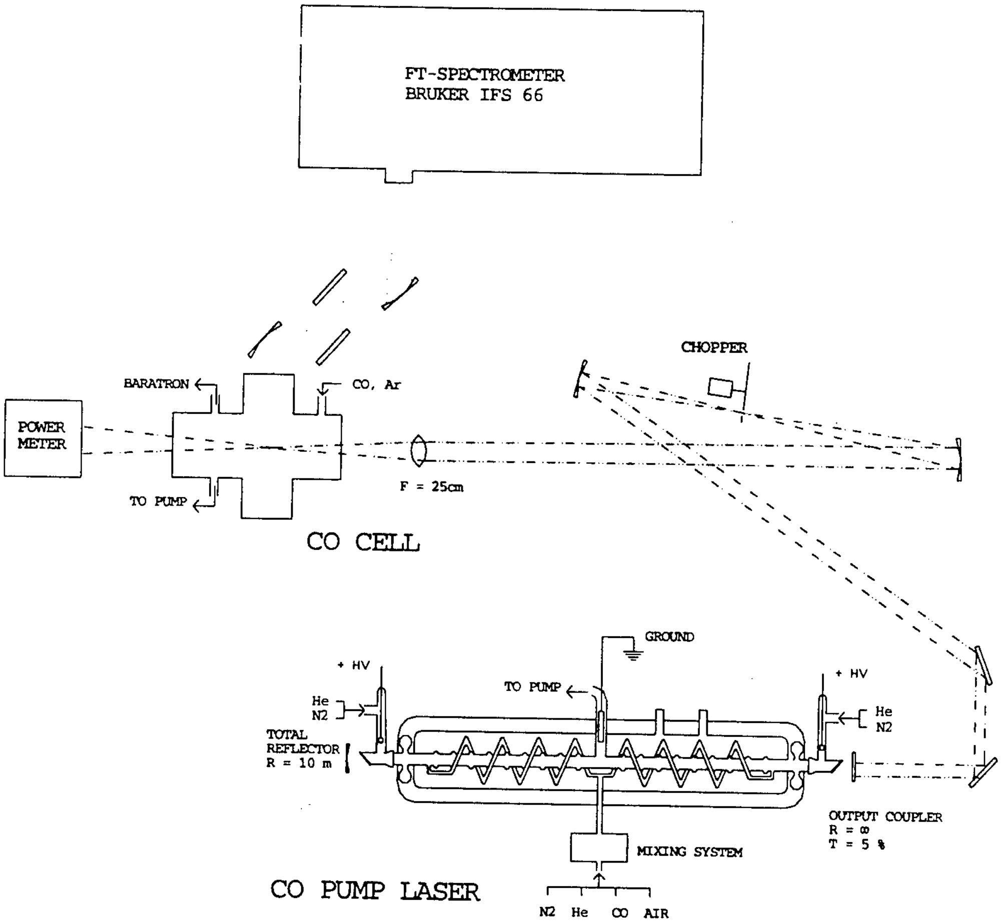
FT-SPECTROMETER
BRUKER IFS 66
CHOPPER
BARATRON
CO, Ar
POWER METER
TO PUMP
F = 25cm
CO CELL
GROUND
+ HV
TO PUMP
+ HV
He
N2
He
N2
TOTAL REFLECTOR
R = 10 m
OUTPUT COUPLER
R = ∞
T = 5 %
MIXING SYSTEM
CO PUMP LASER
N2
He
CO
AIR

Figure 1. Schematic of the experimental setup

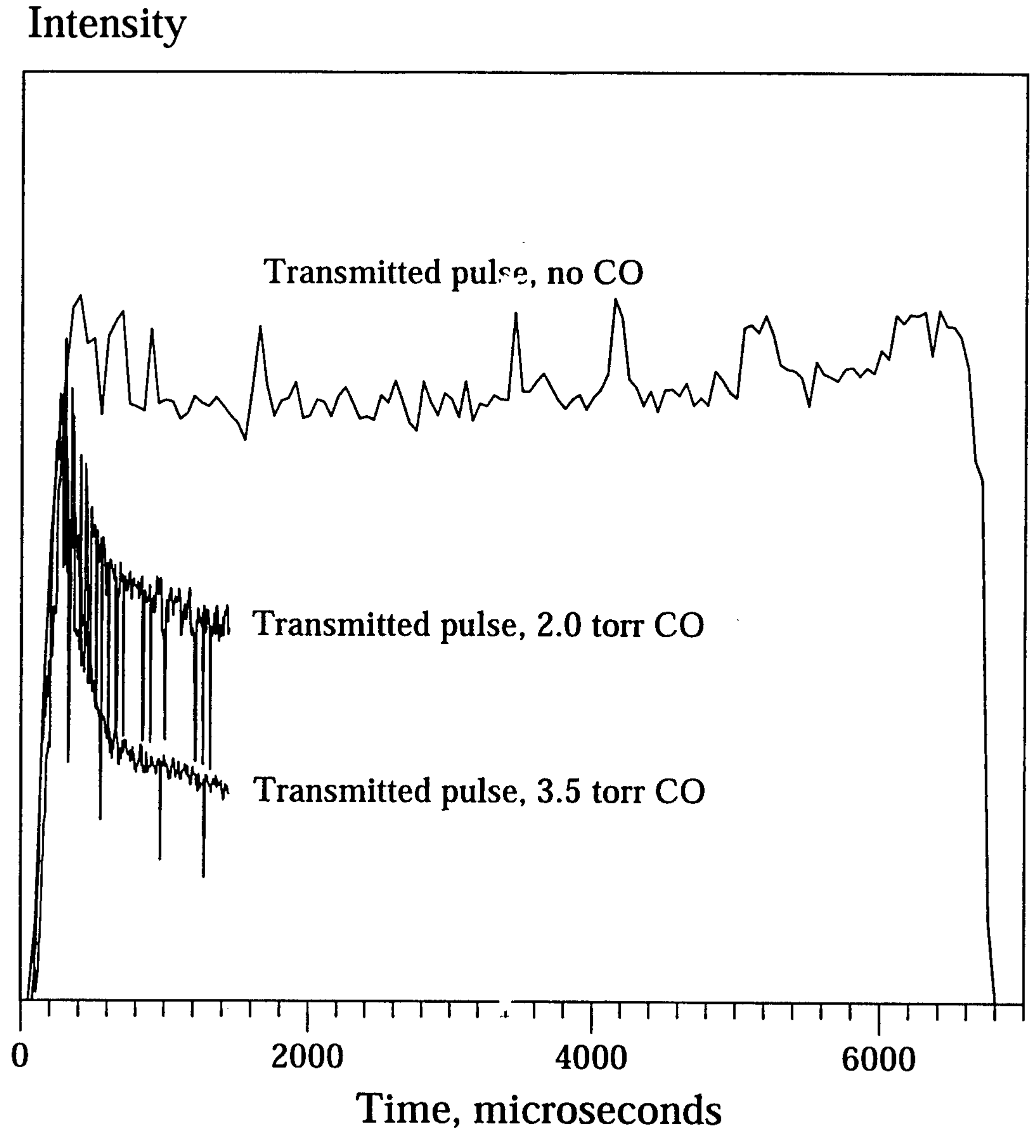

Figure 2. Transmitted CO laser pulse shape at different CO partial pressures in the cell

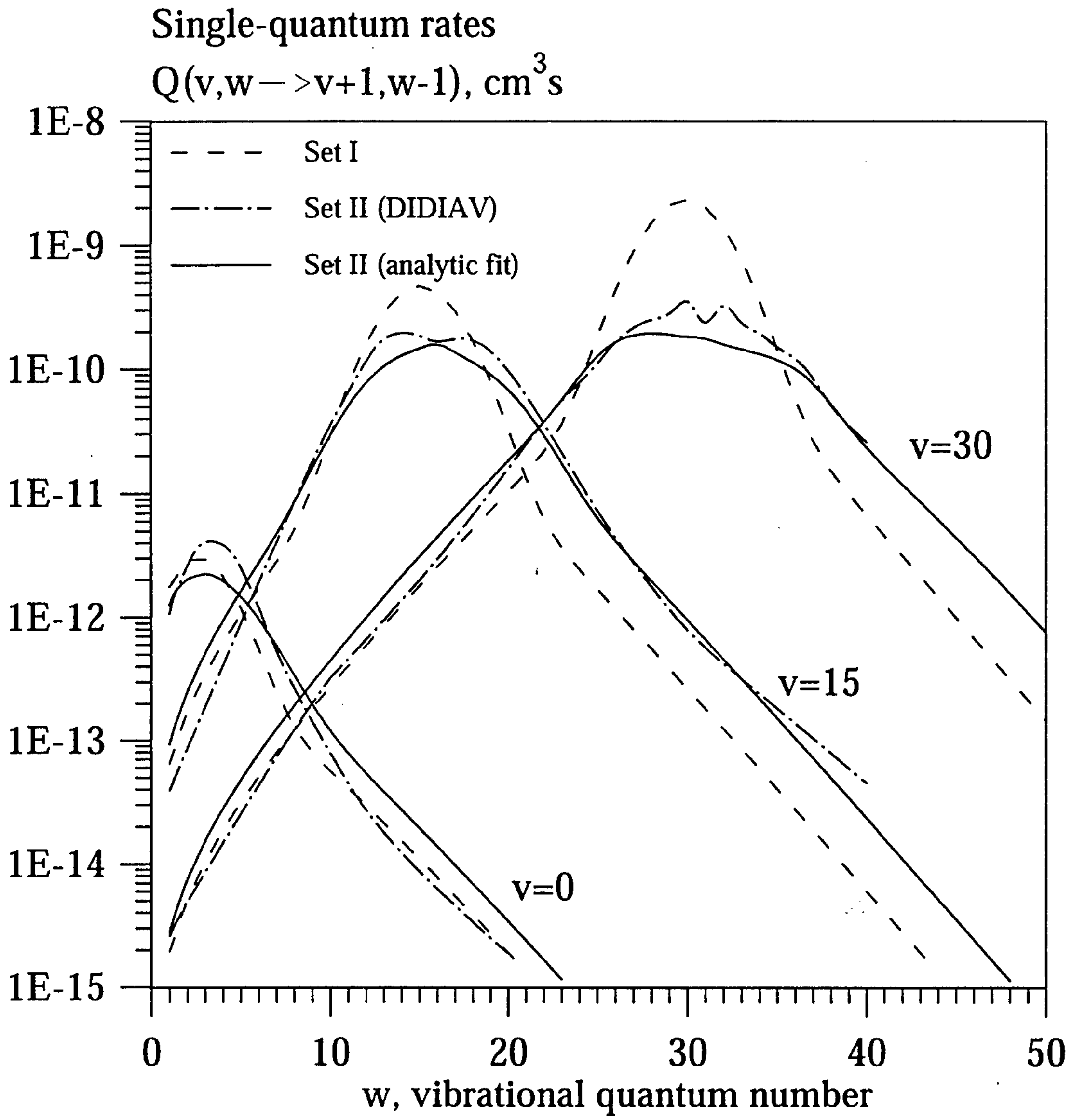

Figure 3. Set I and Set II single-quantum rates at T=300 K

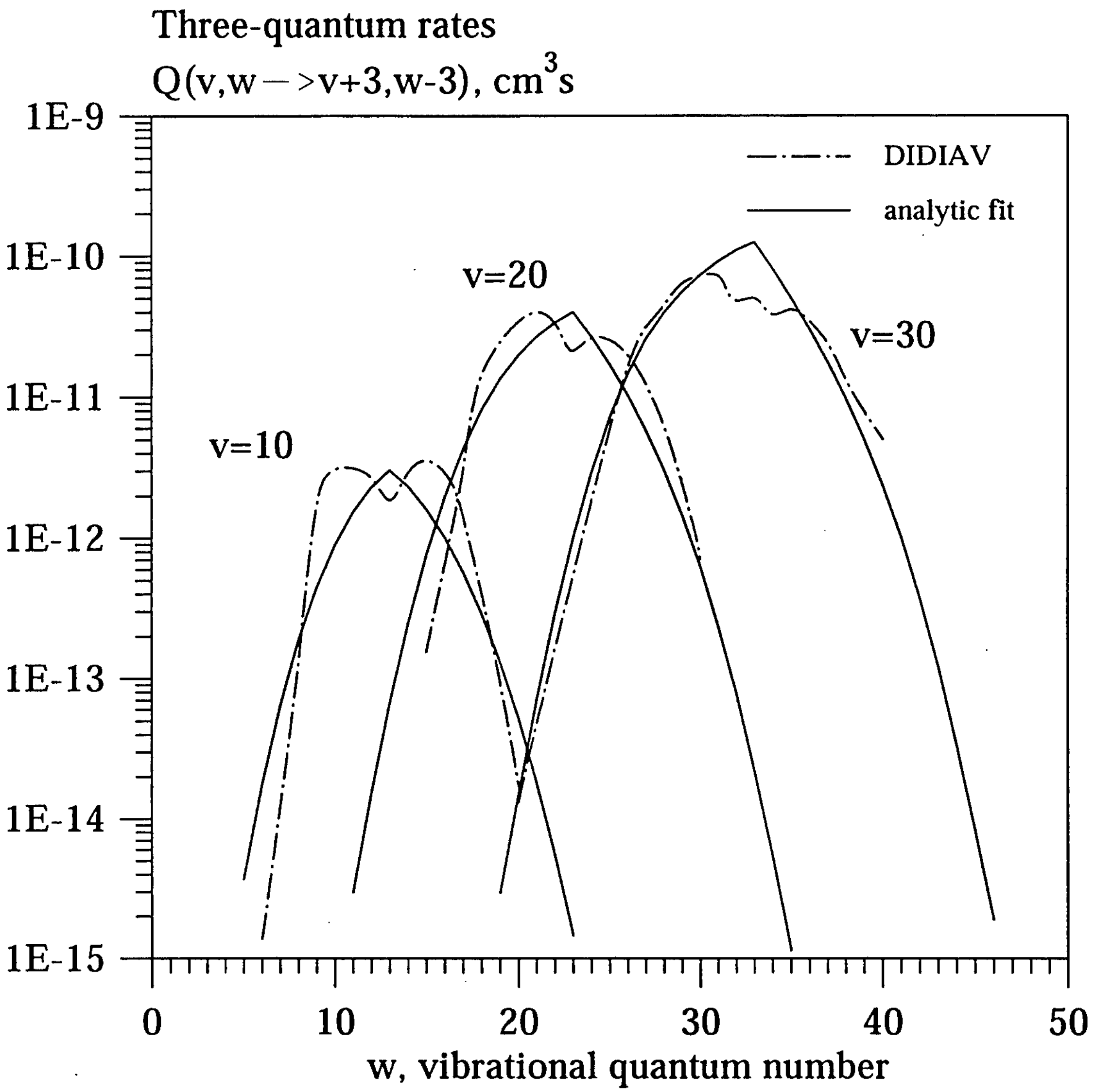

Figure 4. Set II: three-quantum rates at T=300 K

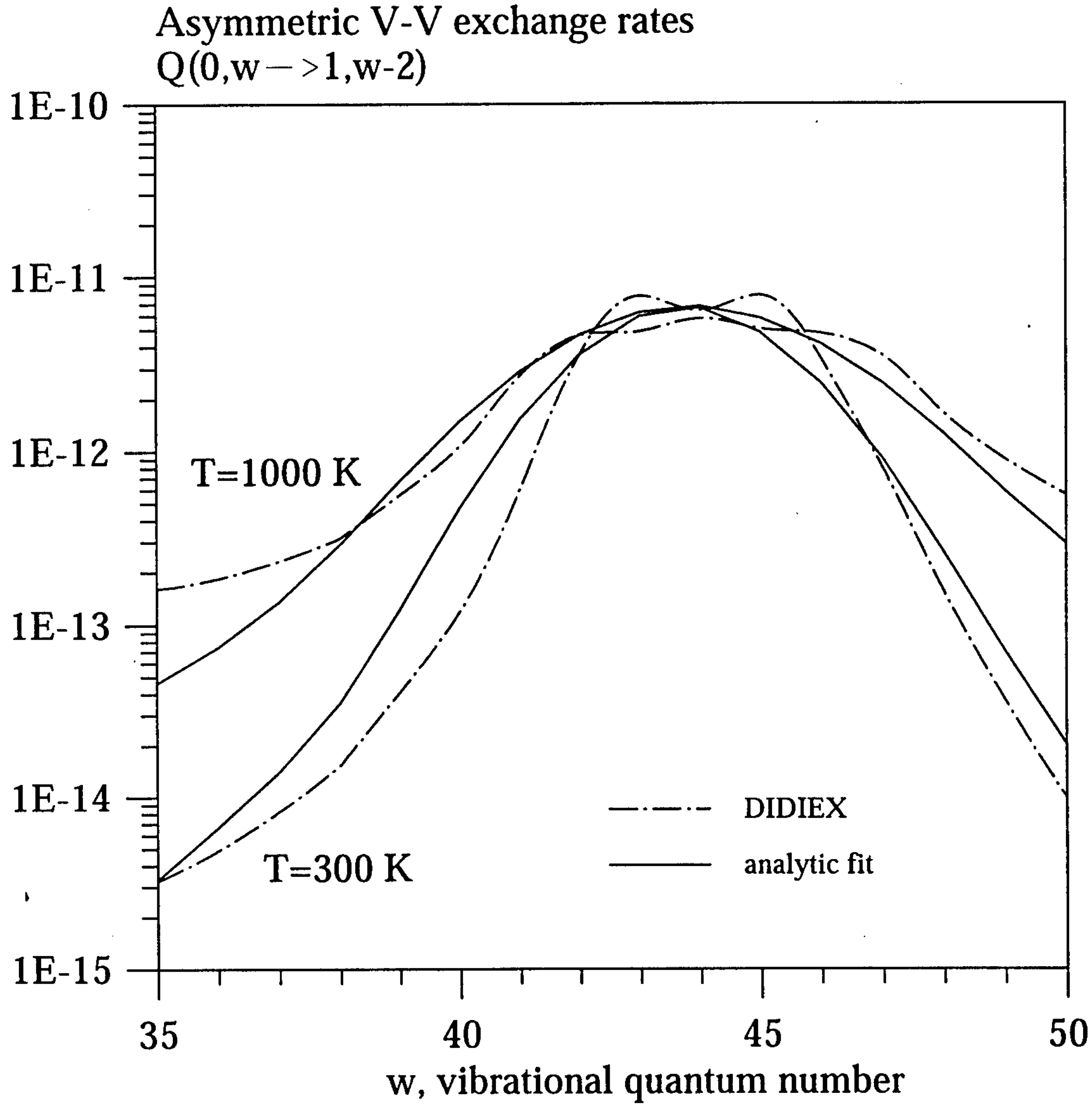

Figure 5. Asymmetric near-resonance V-V rates

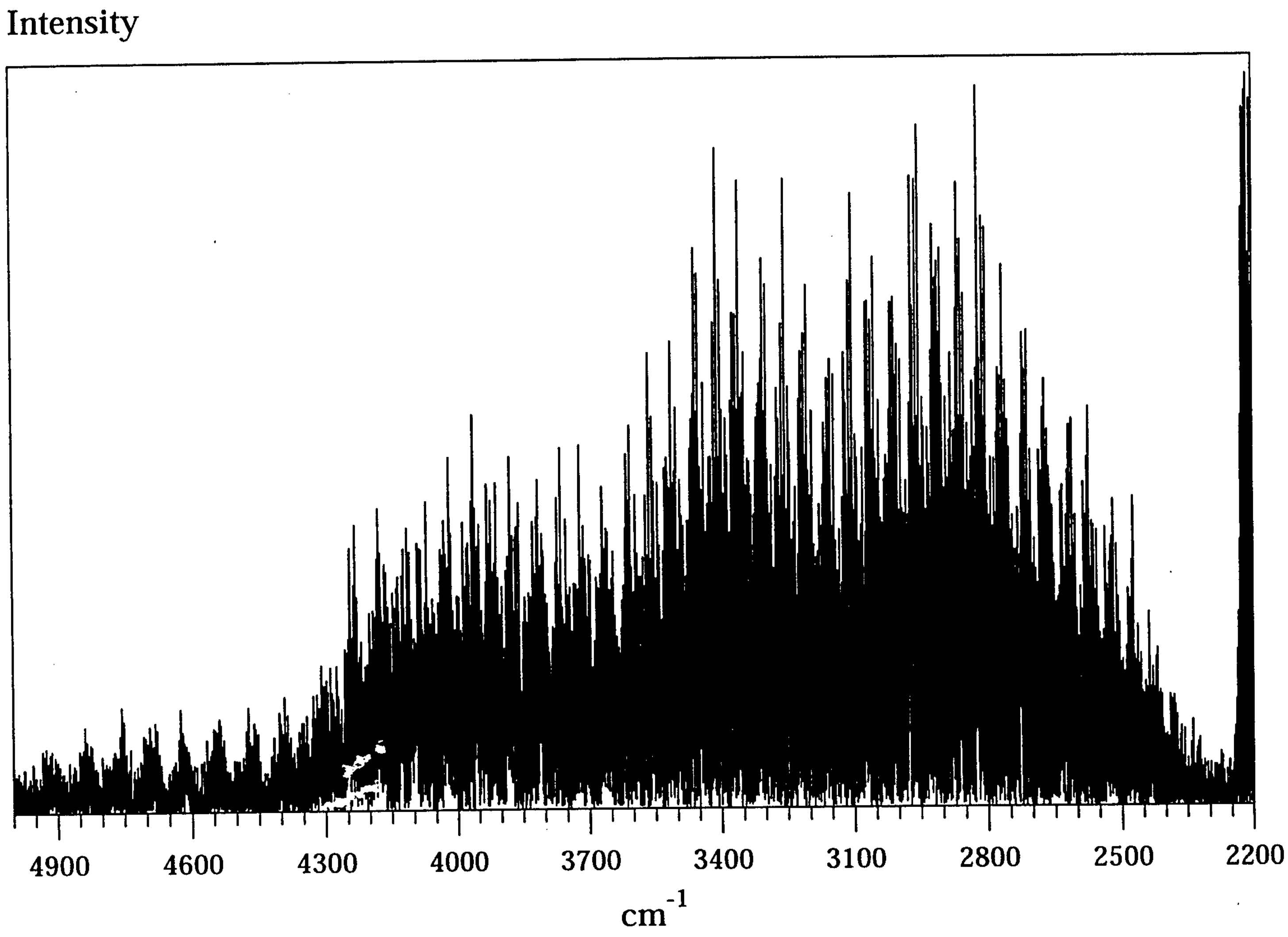

Figure 6. High-resolution steady-state CO FT spectrum. P_{CO}=0.5 torr

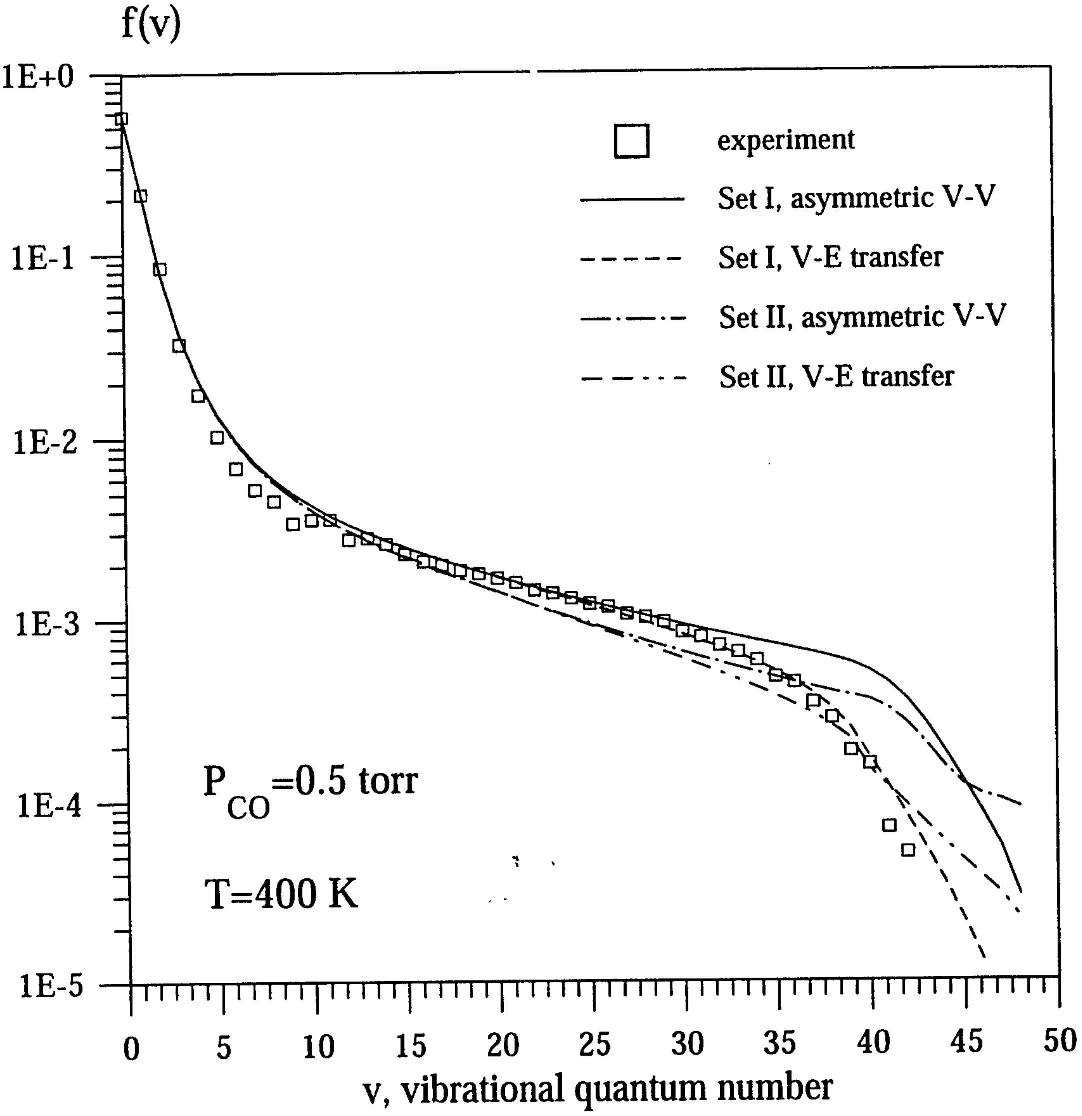

Figure 7. Experimental and theoretical steady-state CO distribution functions at P_{CO}=0.5 torr

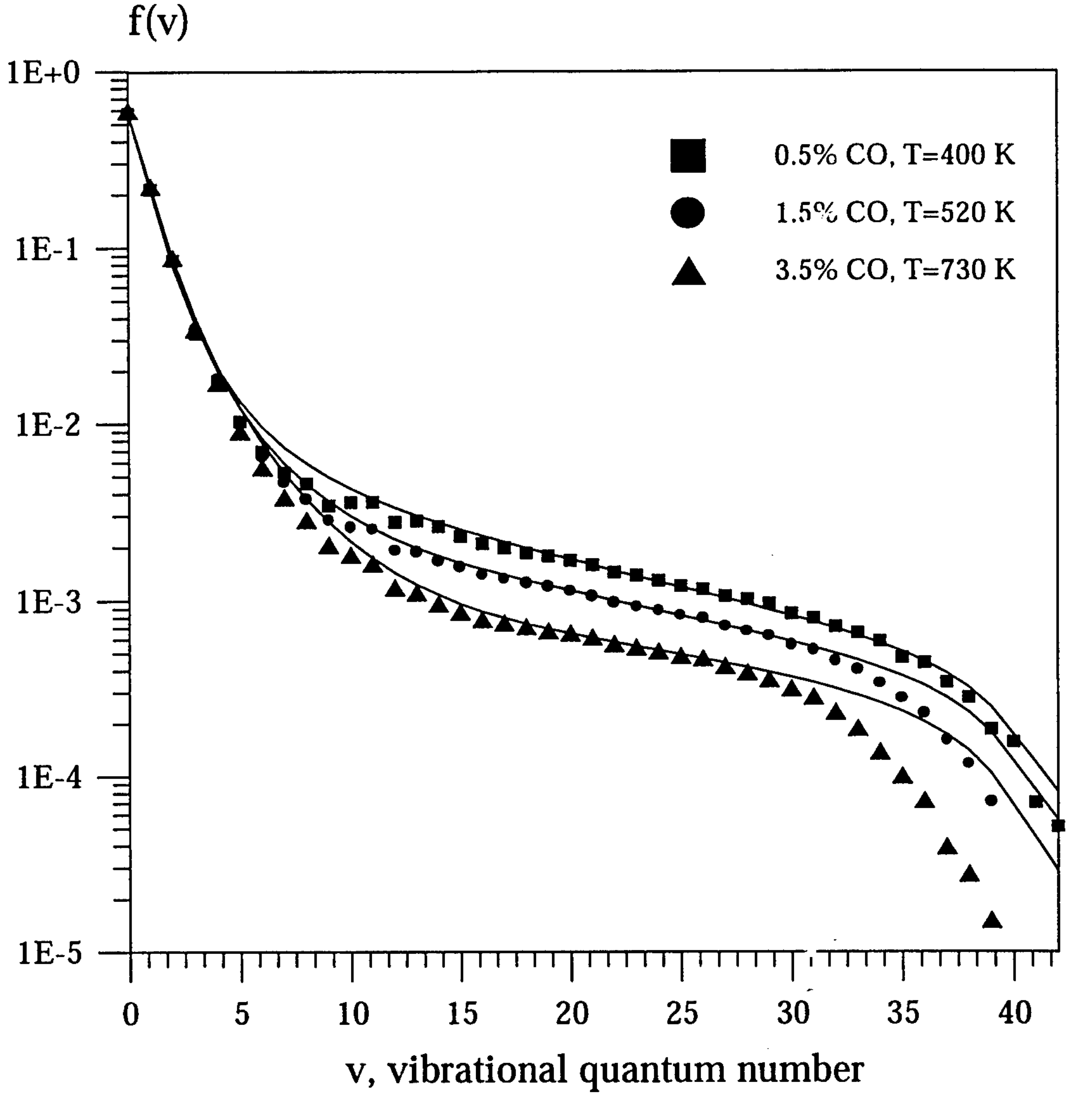

Figure 8. Experimental and theoretical steady-state vibrational distribution functions at different CO partial pressures

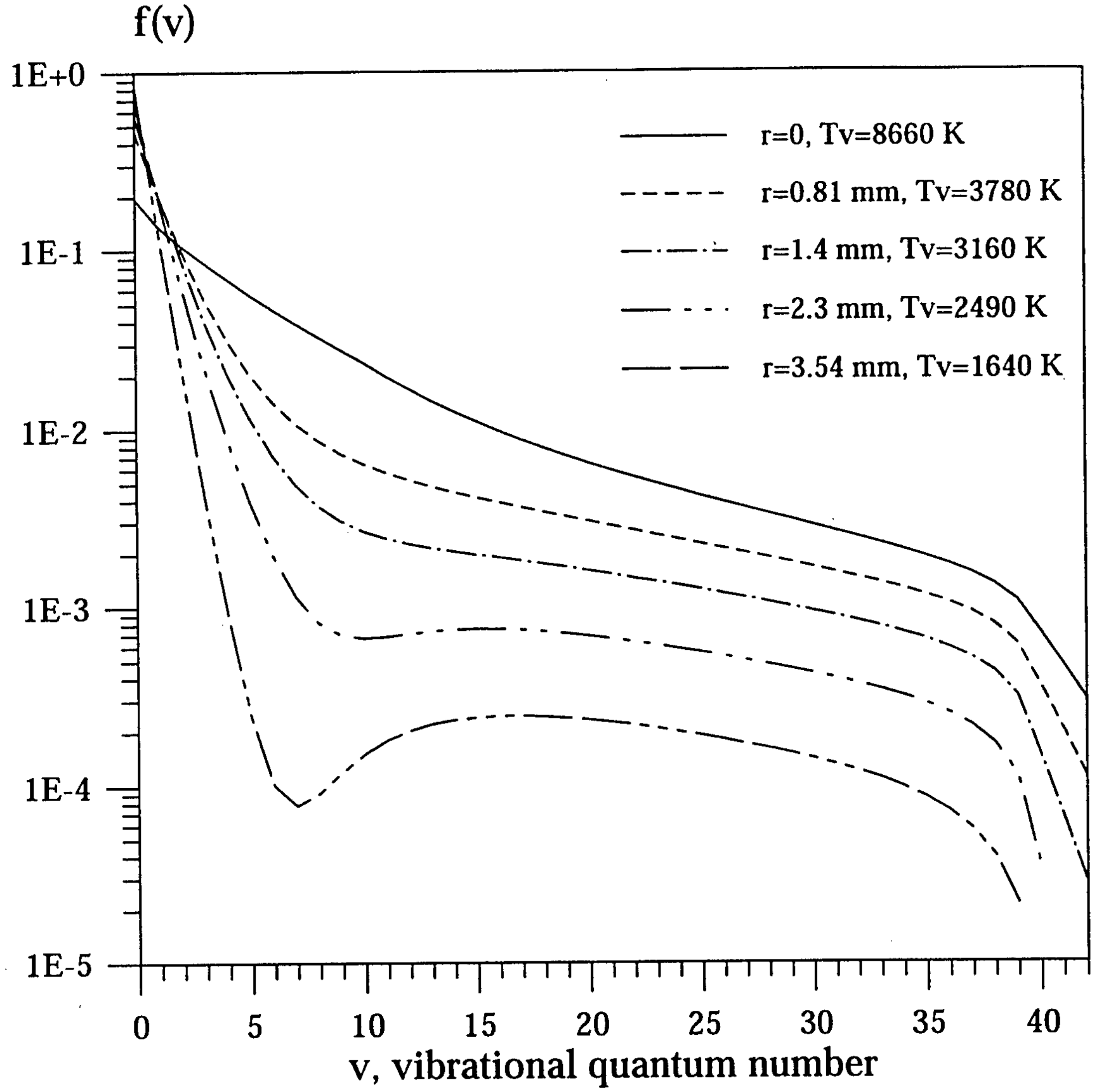

Figure 9. Steady-state vibrational distribution functions at different distances from the beam axis. P_{CO}=0.5 torr

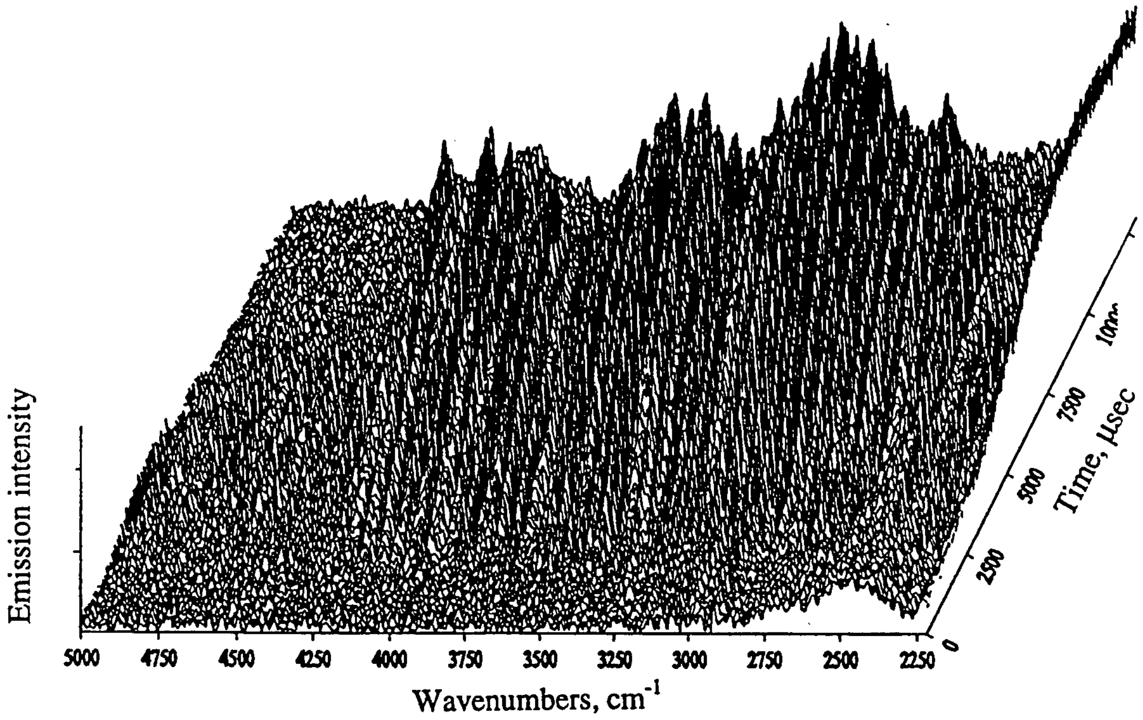

Figure 10. Typical CO step-scan infrared emission spectrum

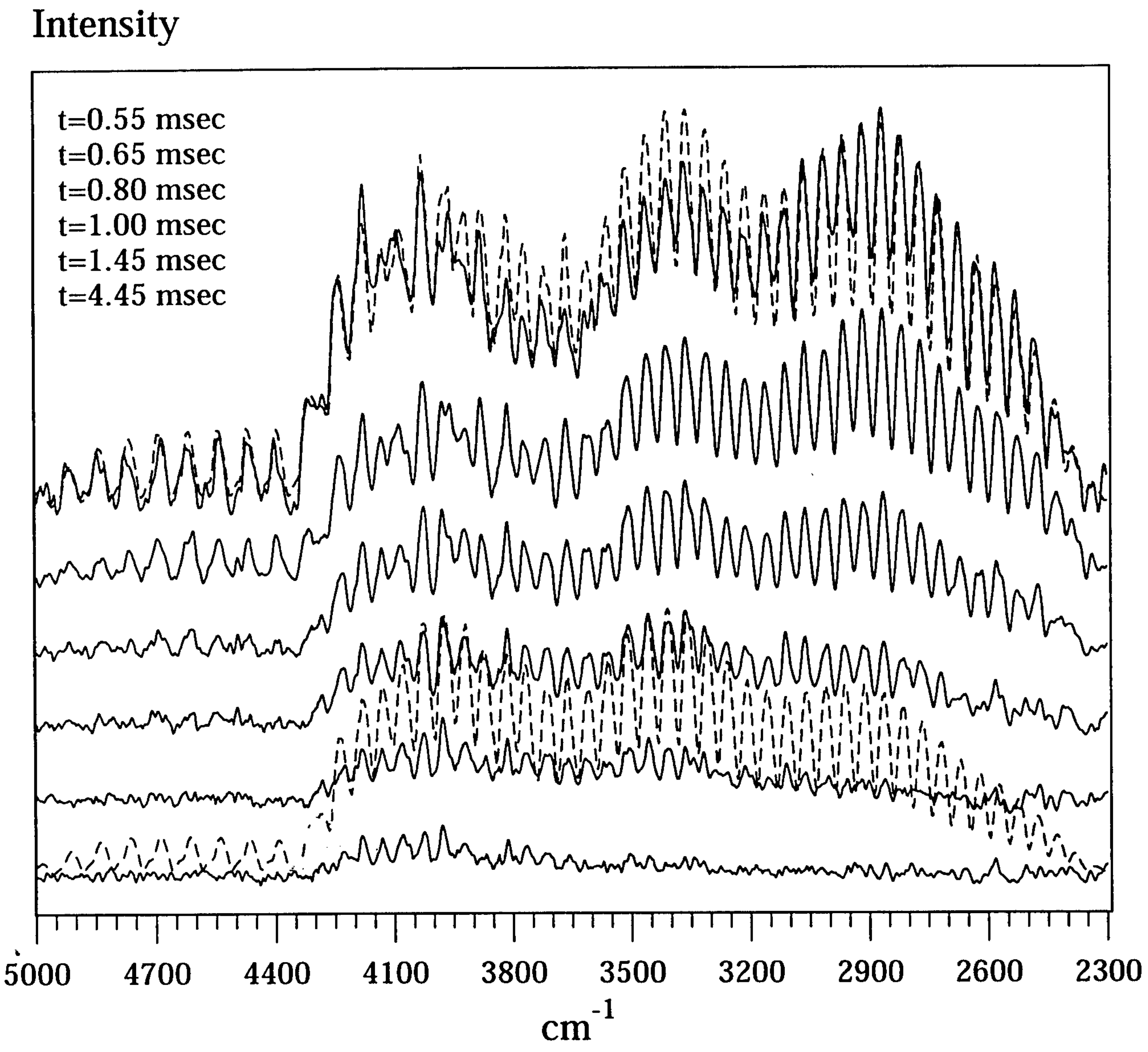

Figure 11. Time-resolved CO emission spectra during excitation. P_{CO}=3.5 torr. Solid lines, experiment; dashed lines, calculations using Set I of the V-V rates (only two synthetic spectra, at t=0.55 msec and at t=4.45 msec are shown). Time slices shown in the legend are bottom to top.

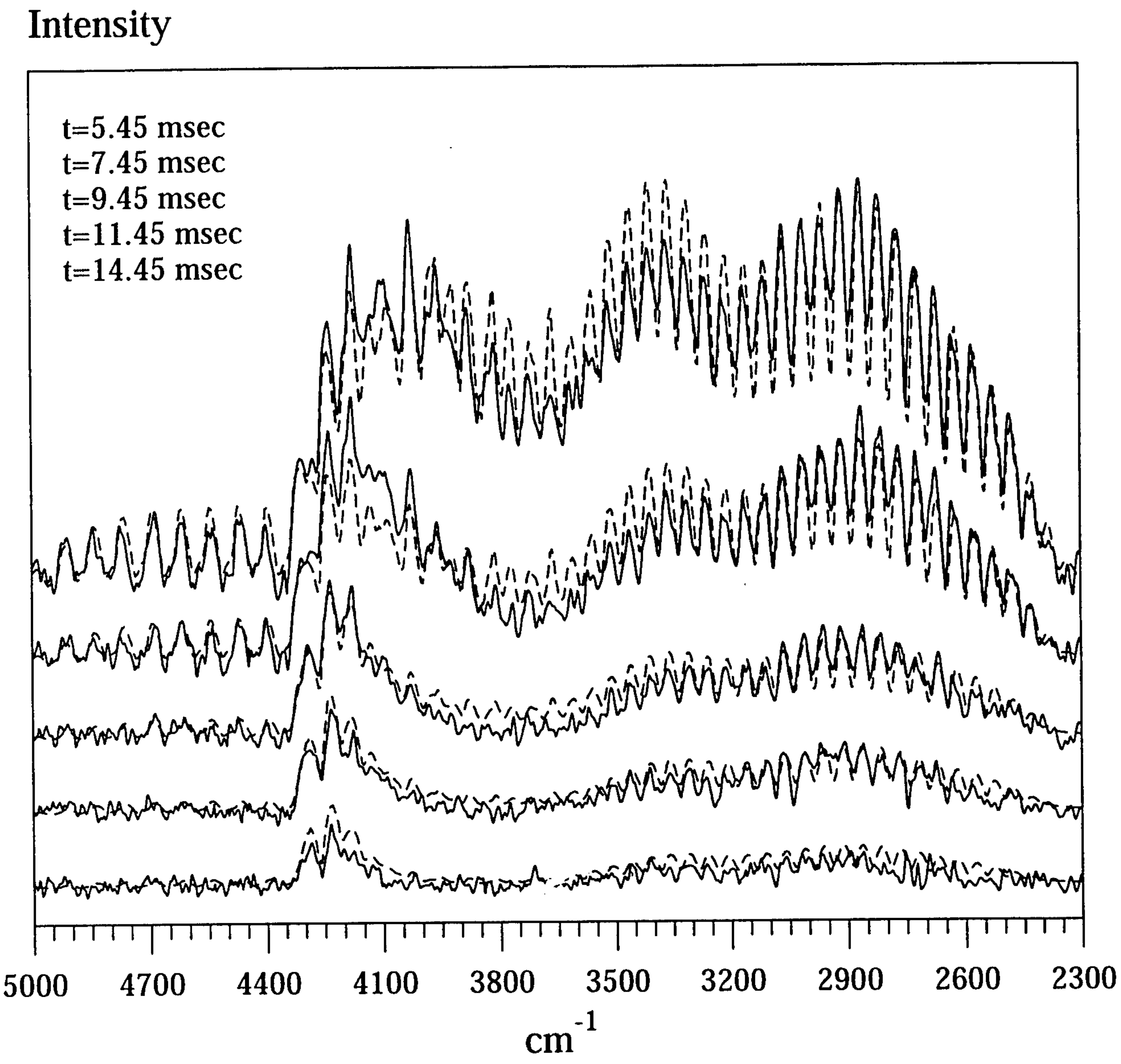

Figure 12. Time-resolved CO emission spectra during relaxation. P_{CO}=3.5 torr. Solid lines, experiment; dashed lines, calculations using Set I of the V-V rates. Time slices shown in the legend are top to bottom.

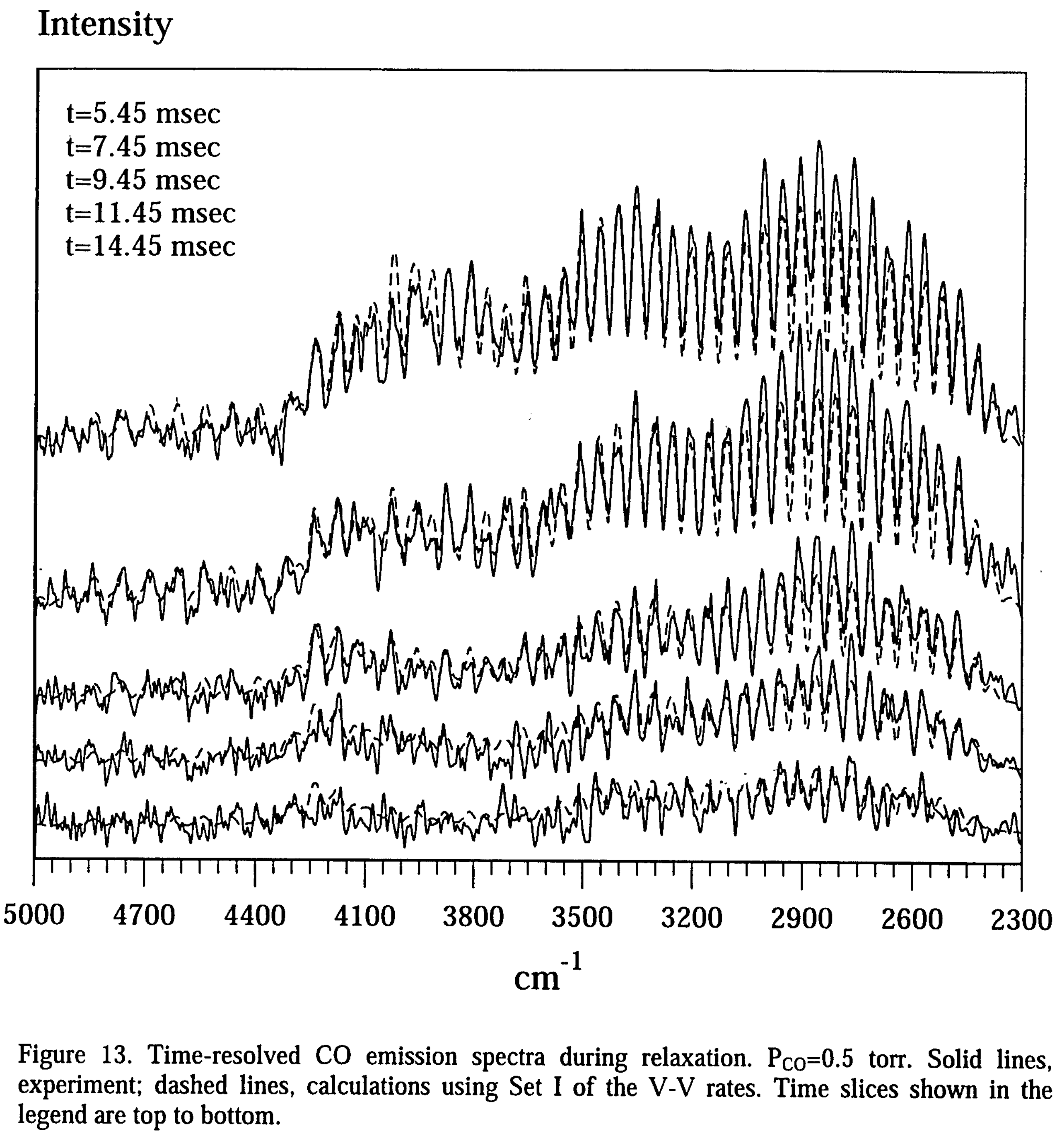

Figure 13. Time-resolved CO emission spectra during relaxation. P_{CO}=0.5 torr. Solid lines, experiment; dashed lines, calculations using Set I of the V-V rates. Time slices shown in the legend are top to bottom.

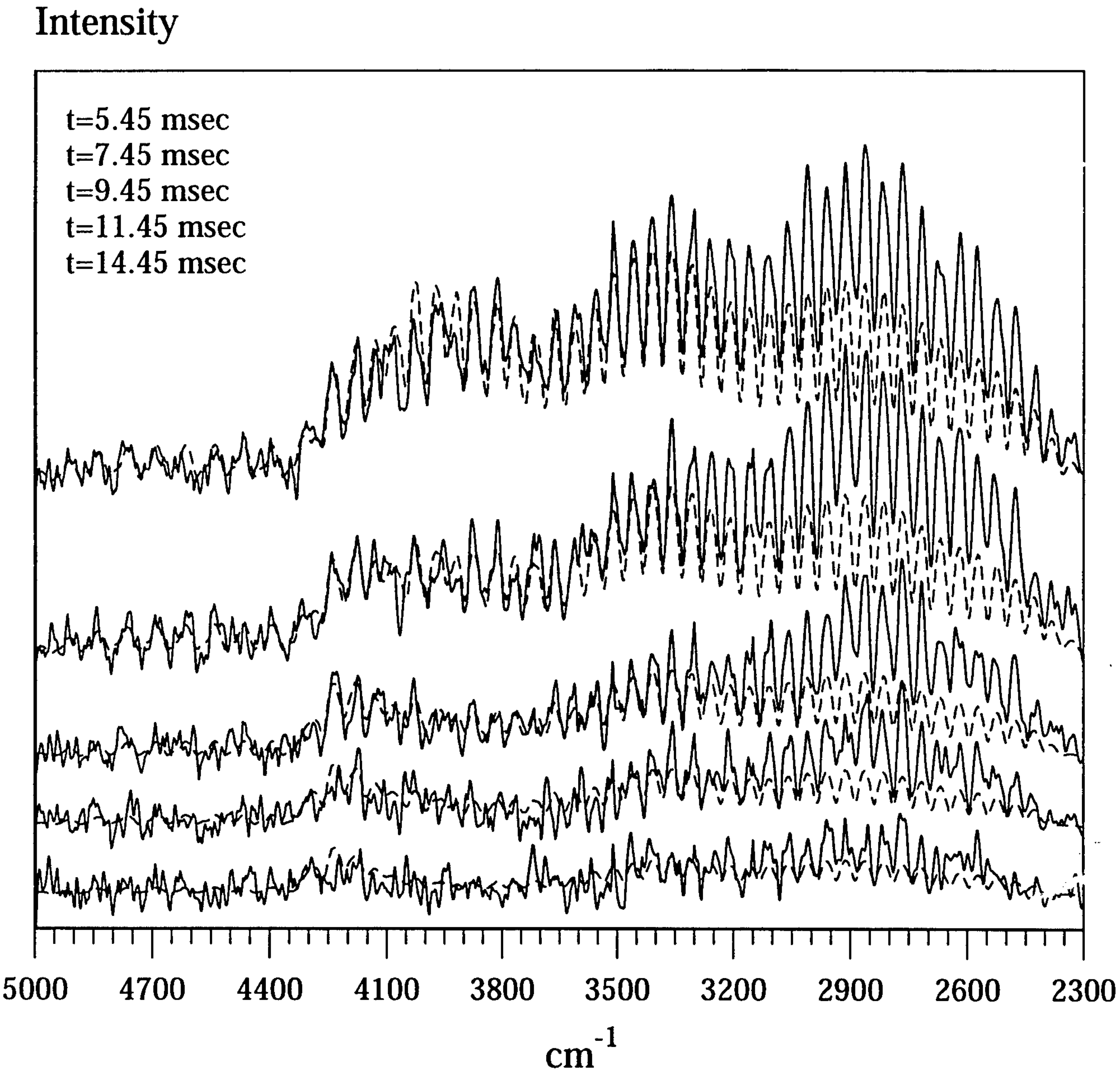

Figure 14. Time-resolved CO emission spectra during relaxation. P_{CO}=0.5 torr. Solid lines, experiment; dashed lines, calculations using Set II of the V-V rates. Time slices shown in the legend are top to bottom.

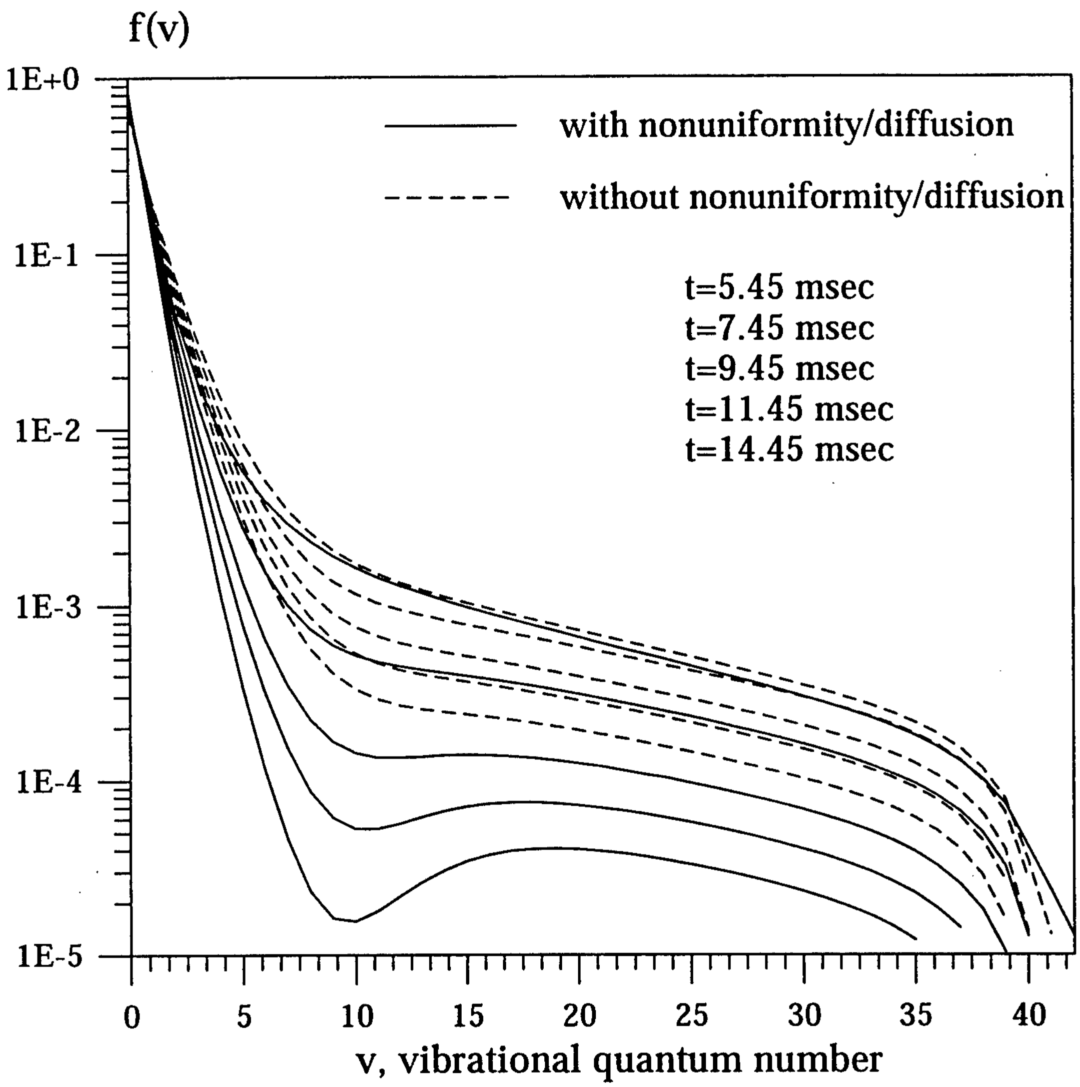

Figure 15. Vibrational distribution functions during the relaxation at P_{CO}=3.5 torr. Time slices shown in the legend are top to bottom.

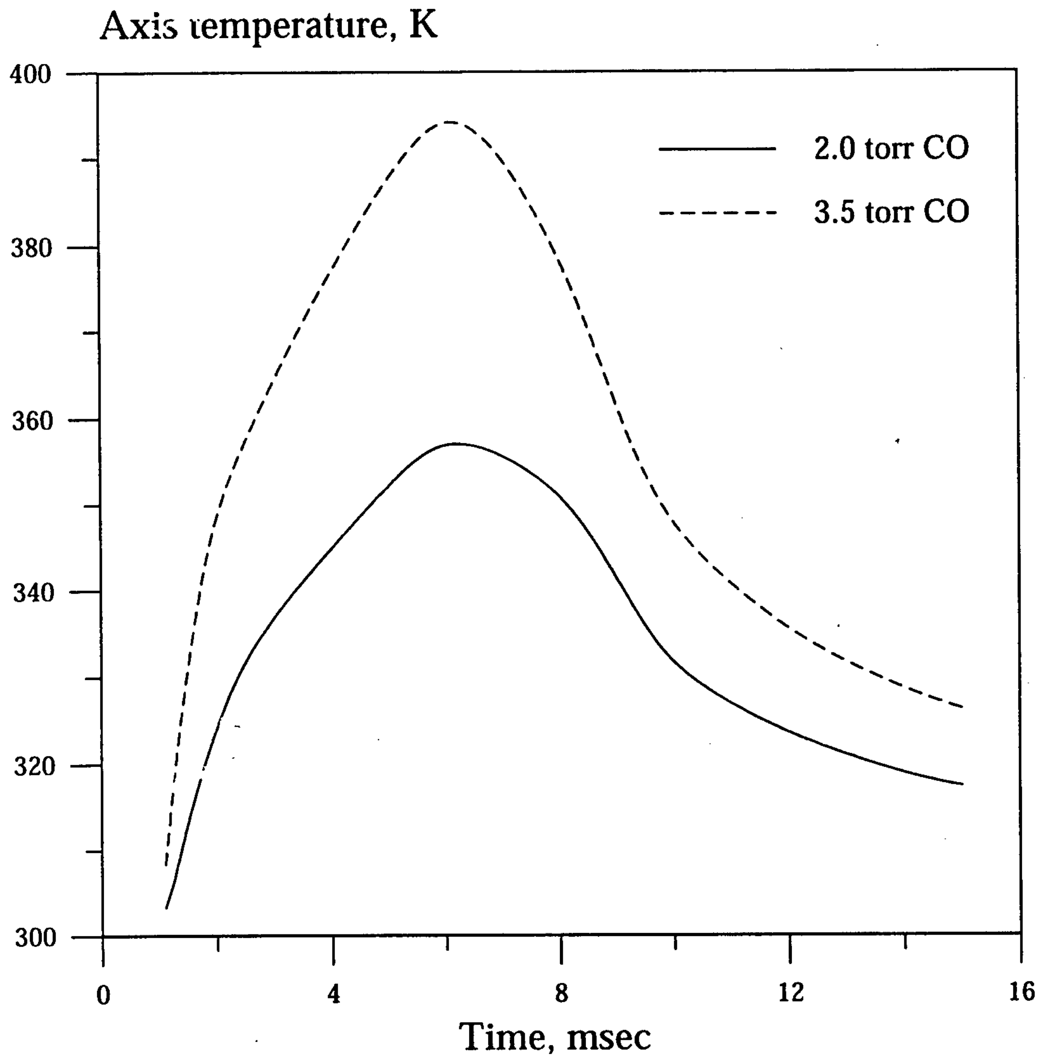

Figure 16. Translational temperature at the beam axis

CHAPTER V.

VIBRATIONAL ENERGY TRANSFER AMONG HIGH VIBRATIONAL LEVELS OF NITRIC OXIDE

1. Introduction

Vibrational and electronic energy transfer in nitric oxide (NO) is known to be of great importance for many applied problems of nonequilibrium gas dynamics and chemical physics, such as in ultraviolet radiation from rocket plumes and hypersonic shock waves, in upper atmosphere kinetics, in environmental clean-up problems and in plasma chemical reactors. There exists considerable experimental evidence that in these nonequilibrium environments, where a considerable amount of energy is stored in molecular vibrations, NO has a strongly non-Boltzmann vibrational-mode energy distribution, maintained by vibration-to-translation (V-T) and vibration-to-vibration (V-V) energy exchange in molecular collisions. For example, NO in its ground electronic state $X^2\Pi$ was shown to be excited by V-V pumping up to vibrational level v=15-16 in glow discharge and optical pumping experiments [1-3], and up to level v=28 in RF discharge experiments [4]. The strong vibrational excitation of NO also leads to the excitation of its electronic levels $NO(A^2\Sigma,B^2\Pi)$ with the subsequent UV radiation, and induces chemical reactions [2,5,6]. However, nonequilibrium kinetics of nitric oxide is still not well studied. Experimental data on the rates and mechanisms of the energy exchange processes, involving highly excited vibrational quantum states, are scarce [7,8], while reliable theoretical models are still not available.

This paper continues studies of the NO kinetics using optical pumping of nitric oxide by a CO laser. The main advantage of this approach over electric discharge excitation methods is that vibrational levels above v=1 are populated by the processes of V-V exchange only. The results of the steady-state experiments have been published previously [2,9]. In the present work, time-resolved optical pumping is used to study the mechanism of population of high vibrational and electronic states of NO, and to infer the V-V rates for NO-NO. This technique has previously been applied for measurements of the V-V rates for CO-CO [10].

2. Experimental

Fig. 1 shows the schematic of the experimental setup. Radiation from a liquid nitrogen cooled CO gas laser (1) is used to optically pump nitric oxide in a flowing-gas absorption cell (4). The laser used in the present study is similar in design and characteristics to the laser described in detail in [2]. In the present experiments, the laser is grating tunable and operates in the single line cw regime. In particular, it produces up to 5 W power on the CO fundamental transition P(11) 8→7, which is in very close resonance with the NO absorption line 1/2R(12.5) 0→1. The energy displacement between the CO laser line and the lower-frequency component of the NO Λ-doublet is $\sim 2 \cdot 10^{-3} \mathrm{cm}^{-1}$ [11,12], which is less than the Doppler width of the NO line [6]. Since the laser transition has no good resonance with any of the NO fundamental transitions on higher bands, it can directly excite only vibrational level v=1 of nitric oxide.

The laser radiation is focused into the absorption cell (4) by a 300 mm focal length CaF_2 lens (5). The position of the focus in the cell can be displaced by moving the lens mount. The focusing area is approximately 0.1 mm^2, which gives the maximum power density in the cell of about 5 $\mathrm{kW/cm}^2$ for a typical laser power, and clearly excludes the possibility of the multi-photon absorption. The laser beam path is purged with dry nitrogen to avoid atmospheric water absorption.

The NO-Ar gas mixture is flowing through an aluminum absorption cell with 8 mm ID and an absorption length of 8 cm, sealed with CaF_2 windows. The cell design has also been described in greater detail previously [2]. To reduce the concentration of possible chemical products in the cell, and to provide thermal inertia, the nitric oxide was diluted with argon. The NO partial pressure in the cell was varied from 0.1 to 1 torr, with the Ar pressure being constant at 80 torr. To keep down the cell temperature, the gas flow velocity was quite high, with the residence time being varied in the range 10-40 msec. The gases used are Matheson CP grade NO and Ar (99.9% purity).

To produce square-shaped pumping pulses, the laser beam is modulated by a mechanical chopper (6). The chopper, with a stabilized frequency of 50 Hz, and a variable duty cycle, provides a rise time for the pumping of the laser beam of about 100 μsec. The 15% cycle (3 msec on / 17 msec off), used in most of the experiments, allowed reaching steady-state nonequilibrium conditions, when the laser pulse is on, and complete relaxation, when the pulse is off. At the exit of the cell, the transmitted laser beam was focused by a lens (7) in a HgCdTe detector (9) through a series of filters (8). This provided time-resolved measurements of the transmitted laser power. The average absorbed laser power is measured as a difference between the transmitted power with and without NO by introducing a power meter (16) behind the cell.

The infrared and ultraviolet emission from the cell is collected perpendicular to the laser beam by CaF_2 lenses. The infrared signal is analyzed using a series of narrow band filters mounted on a filter wheel (10) and backed by an InSb infrared detector (11). The filter transmission curves are shown in Fig. 2, overlapped with the NO first overtone emission spectrum, obtained previously in the steady-state optical pumping experiments [2]. The filter band centers are close to the following NO first overtone band centers: v=3→1 (λ=2.72 μm), 5→3 (λ=2.80 μm), 9→7 (λ=3.01 μm), 13→11 (λ=3.20 μm), and 14→12 (λ=3.29 μm); however, the measured filter signals obviously originate from several adjacent overlapping vibrational bands. The peak transmission of the filters reaches 70-75%, which allowed much better quality of the signal compared to that obtained using a monochromator. For the time-resolved measurement of the UV emission from the cell a 1/3 m monochromator with a photomultiplier (12) was used. The rise time of the detector circuits used in the present study are better than 30 μsec.

The signals from the IR detectors and photomultiplier are sampled and averaged by a HP 54501A digitizing oscilloscope (14) interfaced with a PC (15). The triggering signal is delivered from the optical sensor monitoring the mechanical chopper. The sampling time of the acquisition system is better than 3 μs. To increase the signal-to-noise ratio, the emission signal is typically averaged over one thousand laser pulses.

3. Results

Figs. 3,4 show the laser pulse shape and the time evolution of the NO infrared emission signals from four of the five IR filters, as well as the time-dependent UV signal. The data are shown for two different NO partial pressures of 0.5 and 1 torr, and at two different scales, to show the rising parts of the curves in greater detail. From both figures it is clear that at these experimental conditions quasi-steady-state conditions are achieved during the laser excitation. At the high NO pressure, there is a pronounced overshoot in the IR signals from the higher vibrational levels, and also in the UV signal, which may be attributed to the increasing deactivation of the high NO quantum states with rising temperature. All the data curves are normalized on the maximum value of the corresponding signal. It can be seen from Figs. 3,4 that the optical pumping occurs as a diffusion-type process, with the consecutive excitation of increasing vibrational levels and subsequent electronic excitation. The 50% rise times for the signals, chosen for the analysis of the excitation process, increase with the energy of the excited state. Note that we never registered any signal from the v=14 IR filter. We believe the lack of signal here is due to the narrow band pass of this filter (see Fig. 2). In previous steady-state optical pumping experiments [2,3] the NO vibrational distribution function (VDF) was measured up to v=16, without any evidence of a cut-off of the vibrational populations.

Fig. 5 shows the steady-state IR filter signal intensities (for the high NO pressure - IR signals at their maxima), normalized on that of v=5, for different experimental conditions. One can see that the populations of the high vibrational states decrease with the NO partial pressure.

Two separate series of experiments were performed to determine the dependence of the pumping process characteristics (UV rise time and intensity) on the laser power density. First, the focusing lens ((5) of Fig. 1) was moved to displace the focusing point along the cell. Second, the signal was collected from the different regions of the cell using a narrow diaphragm, without moving the focusing lens. Both measurements were performed for the low and high NO partial pressure (0.2 and 1 torr, respectively). We found out that these two procedures only weakly affect the UV delay time, both at the low and high NO pressure. For example, Figs. 6,7 present the results of the UV radiation measurements obtained by moving a diaphragm. As can be seen, the UV delay time is very nearly the same for all diaphragm positions. Therefore, we conclude that the NO $v=0 \rightarrow 1$ transition is close to saturation, with the populations of the levels v=0 and v=1 being approximately equal.

4. Kinetic modeling and discussion

To interpret the results of the experimental measurements, and to infer the kinetic rates of vibrational energy exchange in NO, we used master equation modeling. A detailed description of the master equation kinetic model used in the present calculations has been given previously [6]; here we give only a brief summary. The time-dependent population of each vibrational level of NO is expressed as follows:

$$\frac{df_v}{dt} = \mathrm{PUMP} + \mathrm{SRD} + \mathrm{VT} + \mathrm{VV} + \mathrm{CHEM}\,, \quad v=1\text{–}20 \qquad (1)$$

where f_v is the relative population of a vibrational level, PUMP is the laser excitation of level v=1, SRD is spontaneous radiative decay, VT and VV are vibration-translation and vibration-vibration energy exchange terms, and CHEM describes vibrationally induced chemical reactions. Subsequently in this paper, f_v is referred to as the vibrational distribution function, or "VDF". This system of equations was supplemented by kinetic equations for concentrations of chemical components such as N, O, NO, N_2, O_2, N_2O, NO_2, and by the energy equation, which calculates the gas temperature change in relaxation processes and chemical reactions. Since the measured rise times for IR and UV signals are rather short ($\tau_{ex} \leq 1$ msec), one can neglect diffusion of excited NO out of the excitation volume ($\tau_{diff} \sim d^2/D \sim 10$ msec, where d~1 mm is the laser beam diameter). Also, since the V-V pumped area is shown to be rather uniform along the cell, we neglect the influence of the flow on relaxation.

The rates of resonance absorption of the CO laser power $v=0\rightarrow1$ and of induced radiation $v=1\rightarrow0$ can be evaluated, using the known values of NO spectroscopic constants, the Einstein coefficient for spontaneous radiation A_{10}, the energy displacement between the laser line and the NO absorption line, and the absorption line shape factor, which is a known function of the gas mixture temperature, pressure, and chemical composition (see [6] for details of calculations). These rates are also proportional to the laser power density, which is only known with a substantial uncertainty. However, the flow uniformity tests (see Section 3) indicate that the absorbing transition is saturated. The calculations also show that at $P_{NO} \leq 1$ torr and laser power density ≥500 W/cm^2 at the line P(11) $8\rightarrow7$ the NO $v=0\rightarrow1$ transition is indeed very close to saturation. Obviously, the results of kinetic modeling in the saturation limit become only weakly sensitive to the power density.

The spontaneous radiative decay term is simply proportional to the Einstein coefficients, taken from [13,14]. The calculated first-overtone radiation signal intensity for each of the IR filters, used for comparison of the model predictions with the experimental results, was evaluated as a superposition of all individual vibrational-rotational lines (P,Q and R-branches), transmitted by the filter (see Fig. 2). The filter transmission curves, multiplied by the InSb detector response function, were used as entries in the computer code. In calculation of the vibrational-rotational line intensities, we assumed rotational-translational and spin-orbit equilibrium, which is appropriate for the present experimental conditions.

The V-T relaxation rate NO-NO for v=1 has been measured by several authors (see [15] and references therein) over a wide temperature range. In the present calculations we use the room-temperature value $k_{NO}(1\rightarrow0)=8.5\cdot10^{-14}$ cm^3/s [15]. The V-T rates at the high v's were determined in [7,8] as total NO(v) decay rates at T=300K for vibrational levels v=8-25, prepared with high specificity by stimulated emission pumping (SEP) (see Fig. 8). However, from the results of the SEP experiments it is not completely clear what part of the NO relaxation rate at v≥14 is accounted for by the single-quantum and double-quantum V-T relaxation process, respectively,

$$NO(v) + NO(0) \rightarrow \begin{cases} NO(v-1) + NO(0) \\ NO(v-2) + NO(0) \end{cases}, \tag{2}$$

by the near-resonance V-V exchange

$$NO(v) + NO(v) \rightarrow NO(v-1) + NO(v+1) , \tag{3}$$

and by chemical reaction

$$NO(v) + NO(w) \rightarrow N_2O + O , \tag{4}$$

which has the activation energy $E_a \sim 23{,}400$ cm^{-1} [16], corresponding to approximately v=14 of NO. We also note that none of the existing adiabatic V-T rate theories explains all of the anomalous features of NO self-relaxation: extremely high absolute value at room temperature (by several orders of magnitude higher than those of CO and O_2), anomalous temperature dependence with a minimum at about T=300 K [15], and very weak linear quantum number dependence, compared to what is predicted by adiabatic theories [17]. Nonadiabatic theory [18] shows that V-T relaxation NO-NO occurs via vibrational-electronic transition

$$NO(X^2\Pi_{1/2}, v \rightarrow X^2\Pi_{3/2}, v-1), \tag{5}$$

between the components of the split double degenerate ground electronic state. Although this semi-qualitative analytical theory correctly predicts the order of magnitude of the NO(1→0) relaxation rate, it may be used only as an estimate, since the electronic terms of the NO+NO system cannot be evaluated to the desired accuracy. Trajectory calculations using realistic NO-NO potential energy surfaces are not available. In the present calculations we neglect the effect of the NO-Ar V-T relaxation, because it is known to be much slower than NO-NO relaxation [19,20].

The current situation with the NO V-V rates is even more uncertain. The only rate determined in the experiments is $k_{NO}(1,1 \rightarrow 2,0)$ (see [21] and references therein; here we use the value $2.9 \cdot 10^{-12} cm^3/s$, measured in careful experiments by Wysong [21] at T=300 K), while the quantum number dependence has never been measured. Although the $k_{NO}(1,1 \rightarrow 2,0)$ rate is close to the corresponding CO-CO V-V rate, $k_{CO}(1,1 \rightarrow 2,0)=3.2 \cdot 10^{-12}$ cm^3/s [10], and masses and vibrational quanta of both molecules are also similar, this of course does not necessarily mean that the two V-V rate sets have similar temperature and quantum number dependence. It is possible that V-V exchange in nitric oxide also occurs by non-adiabatic mechanism, involving a vibrational-electronic transition (5), as is the case for the NO-NO V-T relaxation. For this reason it is not immediately clear what kind of parametrization can be used to represent the NO-NO V-V rates.

In the present study, we assume that the rates of the V-V transitions (so far limited to single-quantum transitions only) are simply proportional to the product of squares of the corresponding adiabatic matrix elements, and to some energy defect function F, decreasing with the energy defect ΔE,

$$k(v+1,w \rightarrow v,w+1) = (v+1)(w+1)\cdot k(1,0\rightarrow 0,1)\cdot F(\delta,\Delta E), \quad \Delta E = 2\omega_e x_e (v-w) \qquad (6)$$

where δ is radius of V-V exchange, considered as an adjustable parameter. This follows from an assumption that the total matrix element of the vibrational-electronic transition (5), if it does occur, can be represented as a product of the matrix element of a purely vibrational transition, $v \rightarrow v-1$, and the matrix element of the purely electronic transition, $\Omega = 1/2 \rightarrow 3/2$ (see [18]), considered to be weakly dependent on the vibrational quantum number. This assumption is justified to some extent by the approximately linear quantum number dependence of the non-adiabatic NO V-T rates $k(v \rightarrow v-1) \sim v \cdot k(1 \rightarrow 0)$ up to $v \sim 14$ [7,8].

From numerical solution of master equation (1) with different parametrizations of $F(\delta,\Delta E)$ we found out that both the calculated IR signal rise times and the steady-state vibrational distribution function (VDF), very much sensitive to the V-V exchange radius δ, are only weakly dependent on the type of parametrization. This effect can best be explained in terms of the diffusion theory of V-V exchange [22], developed for the case of the "strong" excitation regime, when there exists an extensive gently decreasing plateau in the VDF (see Fig. 9), supported by near-resonance V-V exchange, which is much faster than the V-T relaxation. Qualitatively, results of this theory may be applied to the present experimental conditions, where the plateau in the VDF is not so well pronounced, and the V-T relaxation is not negligibly slow. According to the diffusion theory, both the time-dependent and the steady-state VDF are determined not so much by the individual V-V rates, as by the integral diffusion coefficient of the vibrational quanta in vibrational number space, independent of vibrational quantum numbers [24],

$$D = \frac{\omega_e x_e}{T} k(1,0\rightarrow 0,1) \int_{-\infty}^{+\infty} F(\delta,v-w)\cdot(v-w)^2 \, d(v-w) \qquad (7)$$

In particular, the time-dependent VDF on the plateau is given by the equation [24,25]

$$\frac{\partial q}{\partial t} = (v+1)\cdot\frac{\partial}{\partial v}\left(j_{vv} - j'\right) = (v+1)\cdot\frac{\partial}{\partial v}\left(D\frac{\partial q^2}{\partial v} - j'\right) \qquad (8)$$

where $q=(v+1)f_v$ is the vibrational quanta density, and j' is the vibrational quanta loss rate due to some sink such as V-T relaxation, chemical reactions, diffusion etc. The steady-state flow of quanta on the plateau is [25]

$$\Pi(v) = Dq^2 - \int j' dv \cong \text{const} , \text{ if } \int j' dv \ll Dq^2 , \tag{9}$$

where the constant is determined by the pumping power. For the two well-known adiabatic parametrizations,

$$F(\delta_{VV},\Delta E) = \exp(-\delta_{VV}|v-w|) \tag{10}$$

for the V-V rates induced by short-range repulsive forces, and

$$F(\Delta_{VV},\Delta E) = \exp(-\Delta_{VV}(v-w)^2) \tag{11}$$

for the V-V rates induced by long-range dipole-dipole interaction, the diffusion coefficient is

$$D \sim \frac{\omega_e x_e}{T} \frac{1}{\delta^3_{VV}} k(1,0\to 0,1) \tag{12}$$

and

$$D \sim \frac{\omega_e x_e}{T} \frac{1}{\Delta^{3/2}_{VV}} k(1,0\to 0,1) , \tag{13}$$

respectively. One can see that the VDF, given by Eqs. (8,9) is independent of the type of the V-V parametrization, and determined by a single parameter in the energy defect function. Our objective now is to determine the adjustable parameter δ in equation (6) by fitting the results of kinetic modeling calculations to the results of both time-resolved and quasi-steady-state measurements. For this purpose, we used the V-V parametrization (11).

The chemical reaction term CHEM describes the NO VDF change due to the chemical reaction (4) which can possibly affect the populations of the high vibrational levels of NO. Two other possible channels of the reaction (4), with the formation of NO_2 and N, N_2 and O_2, respectively, also taken into account by the model, are much less probable [16]. The state-to-state rate constant of this reaction as a function of vibrational energy of reactants was evaluated by statistical theory [18,24],

$$k(v,w\to) = \theta(E_v+E_w-E_a)\cdot\left(\frac{E_v+E_w-E_a}{E_v+E_w}\right)^2 , \tag{14}$$

where $\theta(x)$ is a step function, and normalized on the equilibrium rate constant, k =

$5 \cdot 10^{-12} \cdot \exp(-33{,}664/T)$ [16].

In the present calculations, we assumed that electronic excitation of NO occurs in the vibrational energy pooling reaction

$$NO(X,v) + NO(X,w) \rightarrow NO(A,B) + NO(X) \qquad (15)$$

$$E_v + E_w \geq E(A) \sim E(B) \ ,$$

which has approximately the same vibrational energy threshold v~14 as the reaction (4). Other possible mechanisms, such as recombination of N and O atoms

$$N + O + M \rightarrow NO(A,B) + M \ , \qquad (16)$$

and resonance vibration-to-electronic (V-E) energy transfer

$$NO(X,v{\sim}35) + M \rightarrow NO(A,B,v{\sim}0) + M \ , \qquad (17)$$

previously discussed in [2], were neglected. Mechanism (16) was shown to be very unlikely on the basis of the steady state experimental data (see discussion in [2]), while mechanism (17) was considered to be unsignificant since it predicts a much longer UV rise time than is predicted by the energy pooling reaction (15).

In the first series of modeling calculations, the chemical reaction term was ignored, assuming the NO(v) relaxation rates [7,8] to be purely V-T rates. In this series, we failed to obtain any reasonable agreement with the experimental results in a wide range of values of parameter Δ_{VV} in Eq. (11). In particular, at high Δ_{VV} (low diffusion coefficient), the model correctly reproduced the steady-state intensities of the IR filter signals, shown in Fig. 5, but the IR and UV rise times were much longer than was obtained in the experiment. On the other hand, the decrease of Δ_{VV} (high diffusion coefficient), leading to a reasonable correspondence of the rise times with the experimental values, gave much higher intensities of v=9 and v=12 filters than have been measured. However, it was found that the increase of the vibrational quanta loss rate (sink j′ in Eqs. (8,9)) leads to much better agreement with the experiment for some values of Δ_{VV}. The same result was obtained with the alternative type of the V-V parametrization given by Eq. (10).

In the second series of calculations, we introduced the chemical reaction term. The NO V-T relaxation rates among the high levels v≥14 were now evaluated from the linear extrapolation of the low-quantum-number V-T rates [8], rather than taken to be equal to the values inferred from the experiment (see Fig. 8). It is interesting that the superposition of these "extrapolated" V-T rates and the state-to-state chemical reaction rates (14) turns out to be very close to the total NO(v) relaxation rates measured in [8] (see Fig. 8). However, the quanta loss rate j′ now becomes much faster, since each act of vibrationally-induced chemical reaction (4) removes many quanta from the vibrational mode, instead of one or two in V-T relaxation. In this series, a reasonable agreement with the experimental results was obtained at Δ_{VV}=0.10 (see Figs. 5,10). Fig. 10 shows experimental and calculated IR and UV 50% rise times, which are also in fairly good agreement. The agreement between the experimental and calculated UV rise times suggests that NO electronic excitation indeed correlates with vibrational excitation of the ground electronic state vibrational levels v~14, which justifies the use of the mechanism (15).

Due to the short laser excitation time ~3 ms, the concentrations of chemical products in the cell were found to be only a small fraction of the NO concentrations, which permitted neglect of the effects of reverse reactions and of NO relaxation by the reaction products.

Finally, Fig. 11 shows the NO-NO V-V rates inferred from the comparison of the modeling calculations with the experiment. These rates are close to the CO-CO V-V rates (see [10]), which allows suggesting that the V-V exchange in NO occurs by an adiabatic mechanism, and is induced by long-range dipole-dipole interaction. Also, we note that at v≥15 the near-resonance NO-NO V-V rates exceed the gas-kinetic frequency, which indicates possible importance of the multi-quantum V-V transitions for these vibrational levels, as is the case for CO-CO [27].

Since the translation temperature increase due to relaxation appears to be insignificant at the measured rise time scale of ≤ 1 ms (less that 50 K for P_{NO}=1 torr, according to vibrational energy balance model calculations), the inferred V-V rates may be regarded as the room-temperature rates. Recent experimental measurements [21] of the $k_{NO}(1,1\rightarrow2,0)$ rate show slightly negative temperature dependence (~10% as temperature drops from T=300 K to T=240 K), as should be expected for the dipole-dipole induced transitions [27]. On the other hand, at higher temperatures V-V exchange is more likely to be induced by repulsive intermolecular forces, and one may expect the rates to rise. More information on the quantum number and temperature dependence of the NO-NO V-V rates is expected to be obtained using time-resolved step-scan FTIR spectrometer diagnostics.

Summarizing, the model rates shown in Fig. 11, which best fit the experimental data, are given by the following function, obtained by combining Eqs. (6,11):

$$k(v+1,w \rightarrow v,w+1) = (v+1)(w+1)\cdot k(1,0\rightarrow0,1)\cdot \exp(-\Delta_{VV}(v-w)^2) , \qquad (16)$$

where Δ_{VV}=0.1, and $k(1,0\rightarrow0,1) = 1/2\cdot k(1,1\rightarrow2,0)\cdot \exp(\Delta_{VV}) = 1.6\cdot10^{-12}$ cm^3/s at T=300 K.

References

1. R.C. Bergman, M.J. Williams and J.W. Rich, Chem. Phys., 66 (1982) 357
2. S. Saupe, I. Adamovich, M.J. Grassi, J.W. Rich, Chem. Phys., 174 (1993) 219
3. R.C. Bergman and J.W. Rich, unpublished. Some of the results are presented in [2].
4. S. DeBenedictis and G. Dilecce, private communication, 1994
5. J. Kosanetzky, H. Vormann, H. Dunnwald, W. Rohrbeck and W. Urban, Chem. Phys. Lett., 70 (1980) 60
6. H.Dunnwald, E.Siegel, W.Urban, G.F.Homicz and M.J.Williams, Chem. Phys., 94 (1985) 195
7. X. Yang and A.M. Wodtke, J. Chem. Phys., 92 (1990) 116
8. X. Yang, E.H. Kim and A.M. Wodtke, J. Chem. Phys., 96 (1992) 5111
9. I.V.Adamovich, S.Saupe, M.J.Grassi, S.O.Macheret and J.W.Rich, AIAA Paper 93-3199
10. R.L. DeLeon and J.W. Rich, Chem. Phys., 107 (1986) 283
11. NBS Technical Note, 1321 (US GPO, Washington, 1988)
12. National Institute of Standards and Technology Special Publication, 821 (1991)
13. F.P. Billingsley II, J. Mol. Spectroscopy, 61 (1976) 53
14. W.T.Rawlins, M.E.Fraser, S.M.Miller and W.A.M.Blumberg, J.Chem.Phys., 96 (1992) 7555
15. L. Doyennette and M. Margottin-Maclou, J. Chem. Phys., 84 (1986) 6668
16. O.E. Krivonosova, S.A. Losev, V.P. Nalivaiko, Yu.K. Mukoseev, and O.P. Shatalov, "Recommended Data on Chemical Reactions Rate Constants of Molecules Consisting of N and O Atoms", in "Plasma Chemistry" series, ed. by B.M. Smirnov, vol. 14, pp. 3-31, Moscow, Energoizdat, 1987
17. D. Rapp and T. Kassal, Chem. Rev., 69 (1969) 61
18. E.E. Nikitin, "Theory of Elementary Atom and Molecular Processes in Gases", Clarendon Press, Oxford, 1974
19. J.C. Stephenson, J. Chem. Phys, 59 (1973) 1523; 60 (1974) 4289
20. J. Kosanetzky, U. List, W. Urban, and H. Vormann, Chem. Phys. 50 (1980) 3605
21. I.J. Wysong, J. Chem. Phys., 101 (1994) 2800
22. B.F. Gordiets, A.I. Osipov, and L.A. Shelepin, "Kinetic Processes in Gases and Molecular Lasers", New York, Gordon and Breach, 1980
23. Yu.S. Akishev, A.V. Demyanov, I.V. Kochetov et al., Sov. High Temperature Physics, 20 (1982) 818
24. A.A. Likal'ter, G.V. Naidis, "Vibrational Distributions in Strongly Excited Molecular Gases", in "Plasma Chemistry" series, ed. by B.M. Smirnov, vol. 8, pp. 156-188, Moscow, Energoizdat, 1981
25. S.A. Zhdanok, A.P. Napartovich and A.I. Starostin, Sov. Phys. JETP, 49 (1979) 66
26. Rusanov, Fridman, Sholin, Sov. Physics - Doklady, 22 (1977) 757
27. M. Cacciatore, G.D. Billing, Chem. Phys., 58 (1981) 395

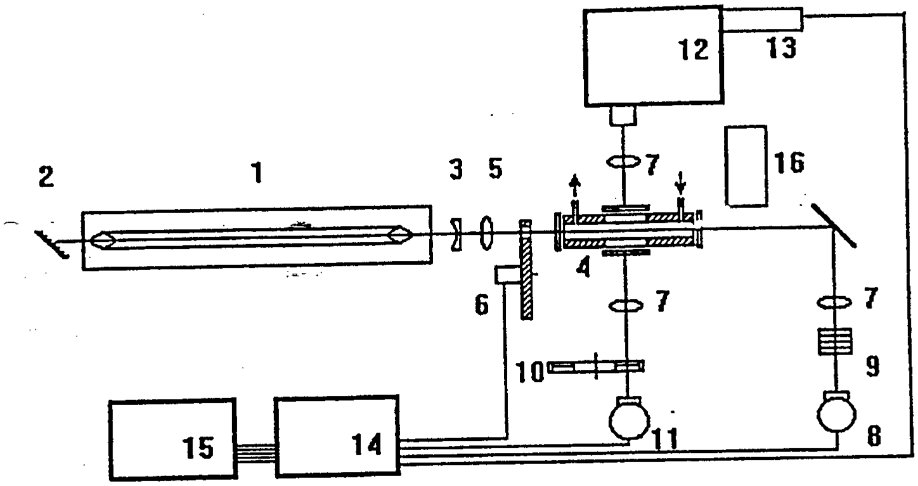

Figure 1. The experimental setup. (1) CO laser; (2) grating; (3) output coupler; (4) absorption cell; (5) focusing lens; (6) chopper; (7) collection optics; (8) HgCdTe detector; (9) filters; (10) filter wheel with IR filters; (11) InSb detector; (12) monochromator; (13) photomultiplier; (14) digitizing oscilloscope; (15) computer

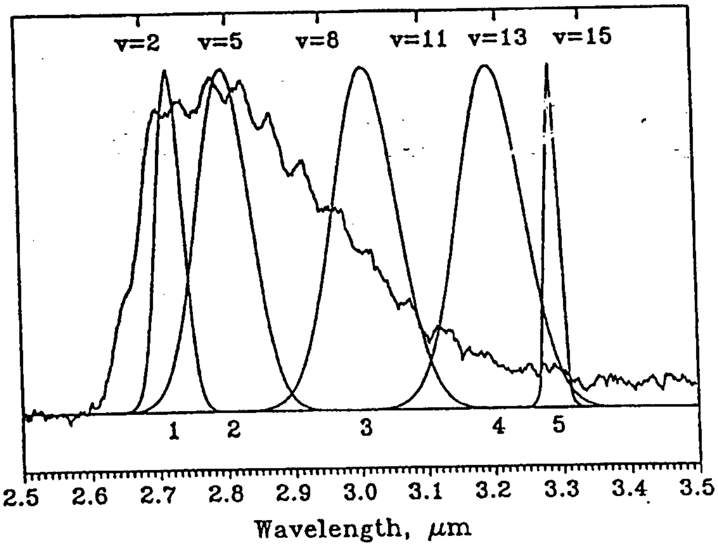

Figure 2. Steady state NO first overtone emission spectrum [2] and filter transmission curves

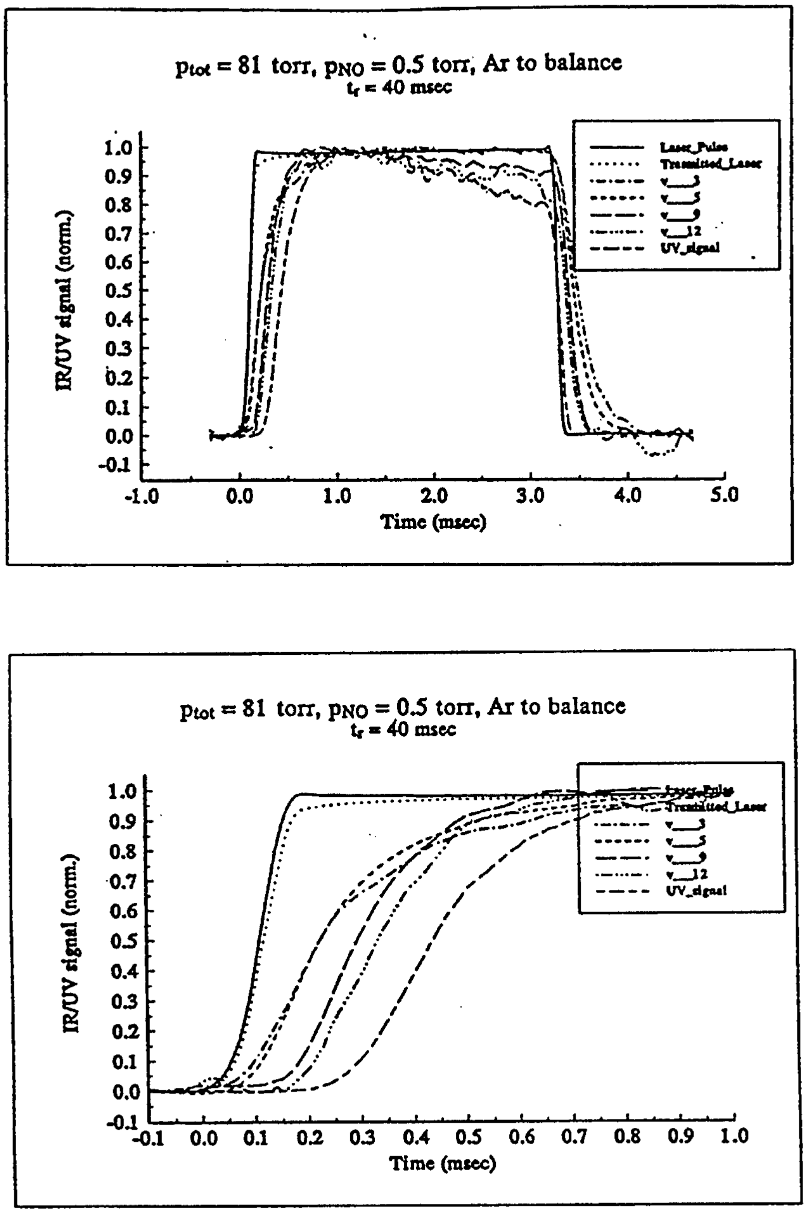

Figure 3. Time-dependent IR and UV emission from the optically pumped NO in the cell. P_{NO}= 0.5 torr

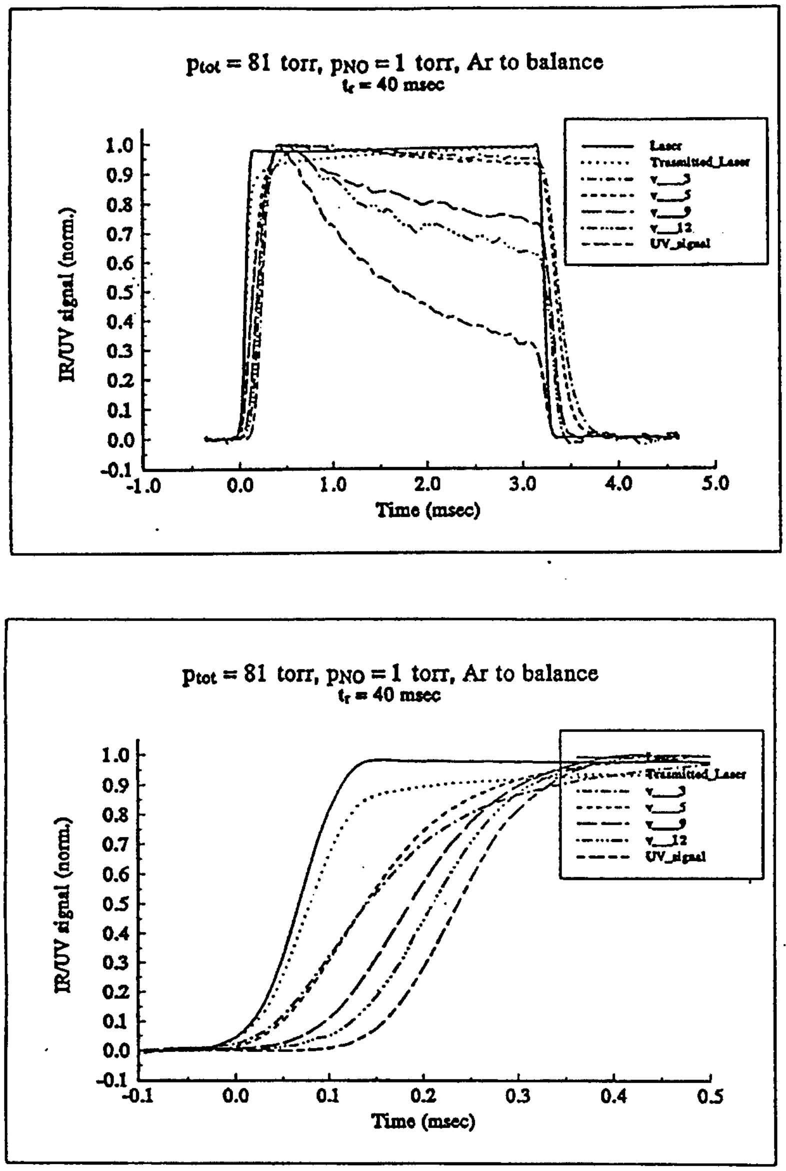

Figure 4. Time-dependent IR and UV emission from the optically pumped NO in the cell. P_{NO}= 1.0 torr

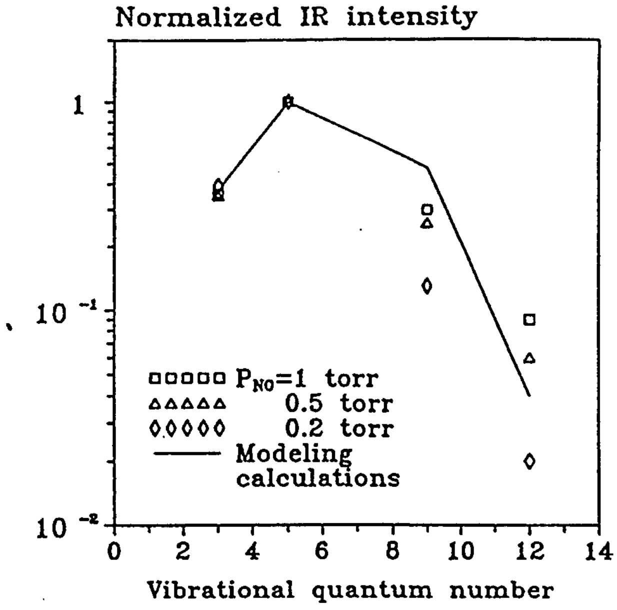

Figure 5. Steady state IR filter signal intensities.

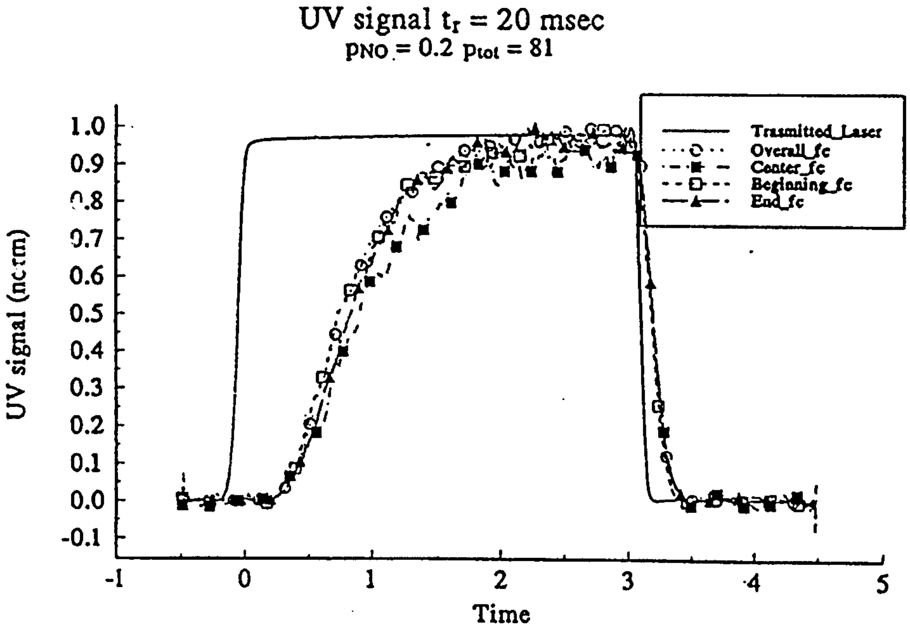

Figure 6. Time-resolved UV emission from the cell at different positions of a diaphragm. P_{NO}=0.2 torr

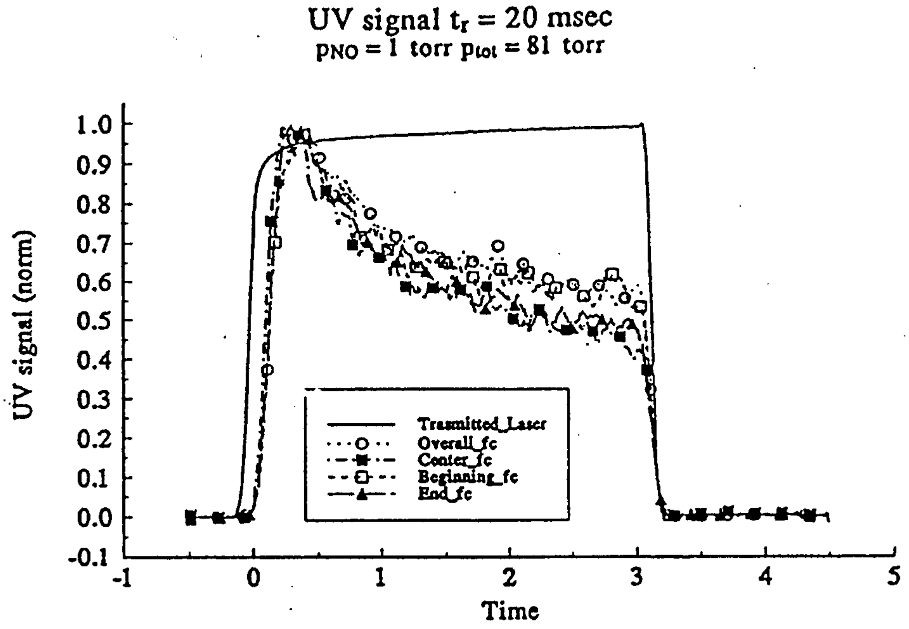

Figure 7. Time-resolved UV emission from the cell at different positions of a diaphragm. P_{NO}=1.0 torr

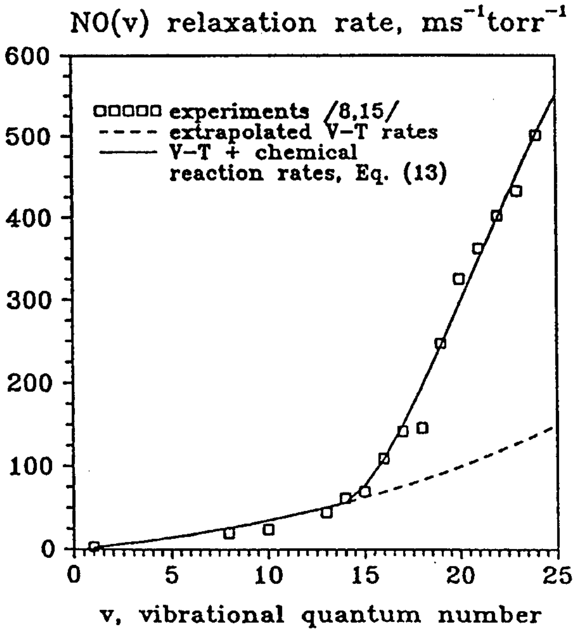

Figure 8. NO(v) relaxation rates [8,15] (symbols); extrapolation of the low level experimental data (dashed curve); sum of the extrapolated V-T rates and state-to-state rates of chemical reaction (4), given by Eq. (14)

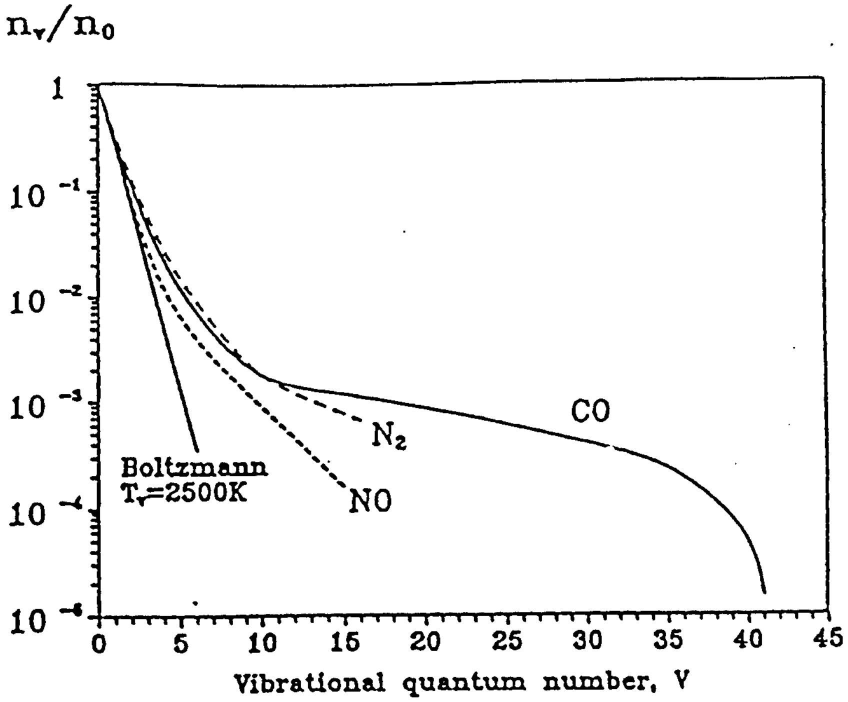

Figure 9. Measured nonequilibrium vibrational distribution functions in diatomic gases. N_2: pulsed electric discharge [23]; NO: optical pumping [2]; CO: optical pumping [10].

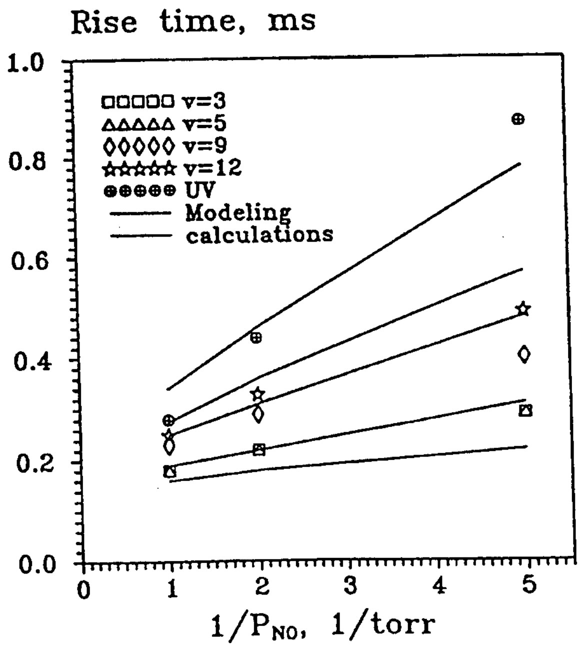

Figure 10. Experimental and calculated IR and UV 50% rise times.

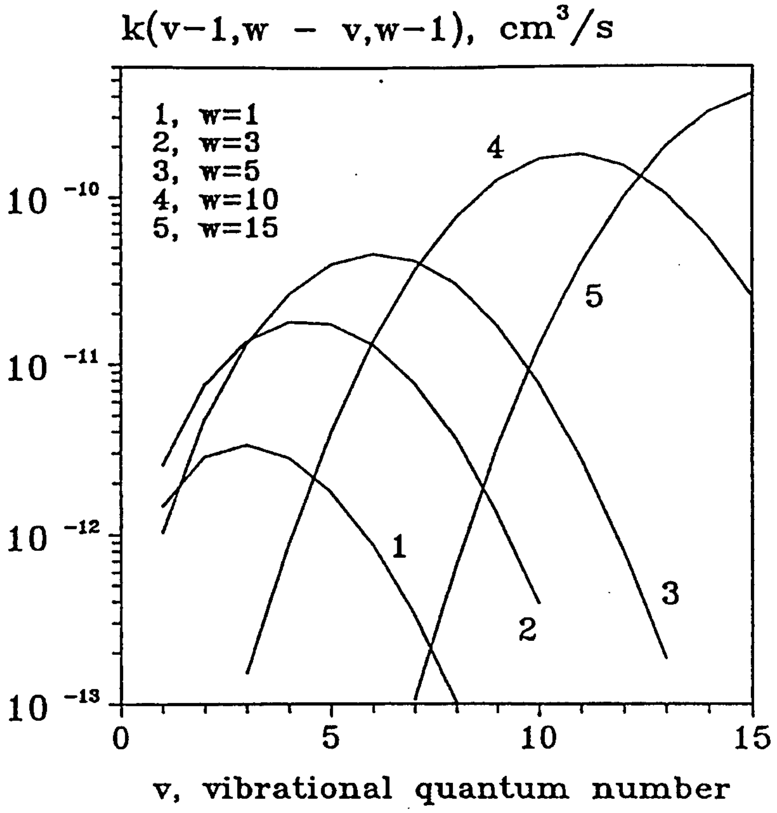

Figure 11. NO V-V rates inferred from comparison of the modeling calculations with the experiment

CHAPTER VI.

VIBRATIONAL ENERGY STORAGE IN HIGH-PRESSURE MIXTURES OF DIATOMIC MOLECULES

1. Introduction

Nonequilibrium vibrational kinetics of diatomic molecules has been a focus of attention for many years in gas discharge plasmas, molecular lasers, pollution control, upper atmosphere chemistry, and gas dynamic flows [1,2]. The rate of energy transfer between the vibrational molecular modes and the "external" modes of rotation and translation is, in particular, a determining process in many high enthalpy fluid environments (such as in supersonic nozzles and behind shock waves). Furthermore, the details of energy distribution among the quantum states within the vibrational modes is a key issue in non-thermal plasma chemical reactor design, in predicting radiation from supersonic nozzle expansions, and in the design of a variety of molecular gas lasers [3]. This energy distribution is primarily controlled by vibration-to-vibration (V-V) energy exchange processes [4,5],

$$AB(v) + CD(w) \rightarrow AB(v-1) + CD(w+1)\,, \tag{1}$$

which in a broad range of parameters are known to be much faster than vibration-to-translation (V-T) relaxation,

$$AB(v) + CD \rightarrow AB(v-1) + CD\,. \tag{2}$$

In Eqs. (1,2), AB and CD stand for diatomic molecules, v and w are vibrational quantum numbers. Near-resonance V-V exchange processes, such as $E_v(AB)-E_{v-1}(AB)\cong E_{w+1}(CD)-E_w(CD)$ in Eq. (1), are of particular importance, since they can sequentially populate very high vibrational levels of the molecules [4,5], and thereby precipitate nonequilibrium chemical reactions, electronic excitation with subsequent visible and UV radiation, and ionization.

Methods of sustaining strong vibrational disequilibrium in gases include (i) rapid expansion in a supersonic nozzle, (ii) excitation of molecular vibrations in electric discharges, and (iii) optical pumping by laser radiation absorption. The use of the first approach is difficult due to the short available test time, while the second approach is limited to fairly low pressures (P~1 atm) and low energy loading per molecule because of rapid development of discharge instabilities [6,7]. In contrast to this, steady state optically pumped plasmas can be sustained at high pressures (up to 20 atm in CO-Ar mixtures) [8]. The main problem with optical pumping, however, is that the use of efficient resonance absorption provides access only to a very few heteropolar molecules (such as CO and NO with a CO laser [9-14], or CO with a frequency doubled CO_2 laser [15]). On the other hand, the use of nonlinear absorption techniques, such as PUMP-DUMP [16], RELIEF [17], spontaneous Raman absorption [18], etc., allows only pulsed mode operation and makes energy addition to vibrational modes of homopolar molecules, such as N_2 and O_2, extremely inefficient.

These obstacles prevent development of new promising applications of vibrationally nonequilibrium environments, including sustaining stable large-volume ionization in high-pressure air and energy efficient high-yield mode-selective chemical synthesis.

The present work discusses a new method of vibrational excitation of high-pressure gases, including nitrogen and oxygen, by collision-dominated vibrational energy transfer of Eq. (1) from an infrared active species (carbon monoxide), optically pumped by resonance absorption of the CO laser radiation. This method combines the advantage of the use of an efficient gas laser with the capability of excitation of various species at high pressures, without using electron impact.

2. Experimental

2.1 Emission spectroscopy

Figure 1 shows a schematic of the experimental setup for the study of vibrational energy transfer in $CO/Ar/N_2/O_2$ mixtures. A carbon monoxide laser is used to irradiate a gas mixture, which is slowly flowing through the pyrex glass optical absorption cell shown. The residence time of the gases in the cell is about 1 sec. The liquid nitrogen cooled CO laser was designed in collaboration with the University of Bonn and fabricated at Ohio State. It produces a substantial fraction of its power output on the $v = 1 \rightarrow 0$ fundamental band component in the infrared. The laser can operate at more than 100 W continuous wave (c.w.) power. However, in the present experiment, the laser is typically operated at 15 W c.w. broadband power on the lowest ten fundamental bands, with up to ~0.3 W on the $v = 1 \rightarrow 0$ component. The output on the lowest bands (1→ 0 and 2→ 1) is necessary to start the absorption process in cold CO (initially at 300 K) in the cell. The quantum efficiency of the CO pump laser approaches 90%, with the overall efficiency about 40%, which makes is the most efficient gas laser available. The present use of CO laser pumped absorption cells to study the V-V process is a further development of a technique with a considerable literature [9-14].

The emission spectroscopy measurements reported here are made at CO partial pressure of 2 torr and total gas pressure of 100-130 torr. At these conditions, the gas mixture is optically thick for the CO laser radiation. A substantial portion of the laser power (up to 5 W) is absorbed over the absorption distance of L=12.5 cm. The Gaussian laser beam, which has a diameter of ~0.5 cm, does not have to be focused to provide substantial vibrational mode energy in the cell gases. However, in the present experiments it is focused to increase the power loading per CO molecule, providing an excitation region in the cell of ~1 mm diameter.

After the laser is turned on, the lower states of CO, $v \leq 10$, are populated by direct resonance absorption of the pump radiation in combination with the much more rapid redistribution of population by the intramode V-V exchange processes CO-CO (see Eq. (1)). These V-V processes then continue to populate the higher vibrational levels of CO above $v = 10$, which are not directly coupled to the laser radiation. At the same time, the intermode V-V exchange processes CO-N_2 and CO-O_2 also populate the low vibrational levels of nitrogen and oxygen molecules. In particular, rapid vibrational energy transfer from highly excited CO molecules to oxygen is facilitated by the near-resonance process

$$\mathrm{CO(v)} + \mathrm{O_2(0)} \rightarrow \mathrm{CO(v-1)} + \mathrm{O_2(1)}, \quad \mathrm{v} \sim 25 \tag{3}$$

If the vibrational energy storage per N_2 or O_2 molecule becomes sufficiently high, the high vibrational levels of these molecules will also be populated by the intramode V-V exchange N_2-N_2 and O_2-O_2. It is well known [19] that until vibrationally excited molecules start producing rapid V-T relaxers in chemical reactions (such as N and O atoms, CO_2, etc.), the overall rate of V-T relaxation in the gas mixture remains slow. Therefore, a substantial fraction of the energy added to the vibrational mode of CO by the laser remains stored in vibrational modes of N_2 and O_2.

When the laser is turned off, the vibrational levels are depopulated, again mainly by the V-V energy transfer, and the vibrational energy distribution approaches the Boltzmann distribution at the translational temperature. In the steady-state measurements reported in the present work, the laser remains on all the time, so that a complete steady state is reached. Note that the vibrational energy stored in the diatomic molecules is constantly converted into heat both in V-V and V-T processes. However, the large heat capacity of the gases (including the vibrational modes), as well as conductive and convective cooling of the gas flow, allow us to control the translational/rotational mode temperature in the cell. Even in steady-state conditions, when the average vibrational mode energy of the CO would correspond to a few thousand degrees Kelvin, the temperature does not rise above a few hundred degrees. Thus a strong disequipartition of energy can be maintained in the cell, characterized by very high vibrational mode energy and a low translational/rotational mode temperature. As discussed in Section 1, similar nonequilibrium conditions exist in a variety of rapid supersonic expansions, in glow plasma discharges, and in a number of other thermodynamic environments. The present setup allows us to study the energy transfer and kinetic processes in a closely controlled environment, without the complications of electron impact processes and instabilities, which occur in electric discharges, or the experimental difficulties of creating and controlling a supersonic flow.

As shown in Fig. 1, the population of the vibrational states of the CO in the cell is monitored by infrared emission spectroscopy. For this purpose, a Bruker Fourier transform (FT) IFS 66 spectrometer is used to record the spontaneous emission from the CO fundamental, first and second overtone bands through a window on the side of the cell. The emission spectra are recorded at both high spectral resolution of 0.25 cm^{-1} and low resolution of 8.0 cm^{-1}. The translational-rotational temperature of the cell gases is determined from the rotational structure of the R-branch of the CO fundamental band $1 \rightarrow 0$.

2.2. Raman spectroscopy

To measure vibrational populations of N_2 and O_2 molecules in optically pumped gas mixtures, spontaneous Raman spectroscopy is used. Laser Raman diagnostics were performed by combining the CO laser beam and a pulsed Nd:YAG Raman pump laser beam using a 90^0 CaF_2 dichroic mirror, which transmits the CO laser, while reflecting the Nd:YAG laser (see Fig. 2). Raman spectra were obtained using the second harmonic output of the Nd:YAG laser in combination with an Optical Multichannel Analyzer (OMA) detector. The Nd:YAG laser was focused coaxial to the CO pump laser and Raman scattering in a volume element approximately 0.100 mm in diameter x 2 mm long was captured at 90^0. A simple long wavelength pass (OG – 570) colored glass filter was used to attenuate the elastic scattering at 0.532 microns and transmit the Stokes shifted scattering, which was in the range 0.570 – 0.615 microns. The OMA consists of a 1/4 meter grating spectrometer with a micro-channel plate intensified CCD camera as the detector. The intensifier allowed a fast (~10 nsec) gate so that spontaneous emission from the optically pumped gas, which was much brighter than the detected Raman signal, could be minimized. The signal was integrated for time duration in the range 1-10 minutes. The resolution of the spectrometer was sufficient to resolve individual Q-branch vibrational bands but could not resolve any rotational fine structure. The wavelength coverage enabled the capture of approximately 15 vibrational bands simultaneously. Determining the complete N_2, O_2, and CO vibrational distributions required merging of 3 spectra, which were obtained sequentially with identical experimental conditions. More experimental detail can be found in our separate publication [20].

Note that inference of the vibrational level populations from Raman spectra requires knowledge of the Raman cross section dependence on the vibrational quantum number. For all data presented in this work, we assume that the Stokes scattering cross sections scale as v+1, which is rigorously true only for a harmonic potential [21]. The measurements are made in CO/N_2 and $CO/N_2/O_2$ mixtures at total gas pressures of P=400 torr up to 1 atm, with 2-5% fraction of CO and up to 16% of O_2 in the cell.

3. Kinetic Model and the V-V Rate Parametrization

To interpret the results of the measurements, we use a state-specific kinetic model of excitation and relaxation of optically pumped anharmonic oscillators in inhomogeneous media. It is based on the master equation model described in detail in [10]; a significant upgrade is the incorporation of laser power distribution profile and transport processes (diffusion and heat conduction) across the Gaussian laser beam, which become of crucial importance when the beam is focused. The model evaluates the time-dependent vibrational level populations in CO-N_2-O_2-Ar mixtures excited by a laser beam:

$$\frac{\partial n_{v,i}(r,t)}{\partial t} = \frac{1}{r}\frac{\partial}{\partial r}\left[rD_i \frac{\partial n_{v,i}(r,t)}{\partial r} \right] + VV_{v,i} + VT_{v,i} + SRD_{v,i} + VE_{v,i} + PL_{v,i}$$

$$\left.\frac{\partial n_{v,i}(r,t)}{\partial r}\right|_{r=0} = 0; \quad n_{v,i}(r,t)\big|_{r=\infty} = n_{v,i}(r,t)\big|_{t=0} = n_{v,i}(T_0) \tag{4}$$

$$v = 0, v_{\max,i}$$

$$\rho c_p \frac{\partial T(r,t)}{\partial t} = \frac{1}{r}\frac{\partial}{\partial r}\left[r\lambda \frac{\partial T(r,t)}{\partial r} \right] + HVR$$

$$\left.\frac{\partial T(r,t)}{\partial r}\right|_{r=0} = 0; \quad T(r,t)\big|_{r=\infty} = T(r,t)\big|_{t=0} = T_0 \tag{5}$$

In Eqs. (4,5), $n_{v,i}(r,t)$ is the population of vibrational level v of species i, $n_{v,i}(T_0)$ is the initial equilibrium population at T_0=300 K, $n_i=\Sigma n_{v,i}$ are the species concentrations, r is the distance from the beam axis, D_i and λ are the diffusion and heat transfer coefficients, respectively, ρ and c_p are density and specific heat of the gas mixture at constant pressure. The rest of the notation is the same as in [10]: VV, vibration-vibration term; VT, vibration-translation term; SRD, spontaneous radiative decay (infrared); VE, vibration-electronic coupling; PL, laser pumping; HVR, gas heating by vibrational relaxation. The explicit expressions for these terms are given in [10]. The line-of-sight averaged vibrational populations are calculated as follows [22],

$$n_{v,i}(t) = \int_0^\infty n_{v,i}(r,t)\,dr \tag{6}$$

Eq. (6) takes into account both the effect of the decrease of the radiating volume and the increase of the steradiancy toward the focal point of the FT spectrometer collection optics, which compensate each other. The V-V rates for CO-CO, the V-T rates for CO-Ar, and the vibration-to-electronic (V-E) energy transfer rates $CO(X^1\Sigma)+CO \rightarrow CO(A^1\Pi)+CO$, used in the present model, were inferred from previous time-resolved optical pumping experiments [9,23]. The V-V rate parametrizations for CO-N_2, N_2-N_2, O_2-O_2, and N_2-O_2 are based on the results of the close-coupled trajectory calculations by Billing et al. [24-27]. Since the V-V rates for CO-O_2 are not available, they are evaluated by replacing the vibrational quantum, ω_e, and anharmonicity, x_e, of N_2 for those of O_2 in the CO-N_2 rate parametrization, keeping all other parameters the same (see Eqs. (A5,A9) and Table A2 of the Appendix). The rationale for this assumption is that the near-resonance V-V exchange in both CO-N_2 and CO-O_2 collisions is primarily induced by the dipole-quadrupole interaction. The V-T rate parametrizations for CO-CO, N_2-N_2, and O_2-O_2 are also based on the results of calculations [24-27]; the remaining molecule-molecule V-T rates AB-M are considered to be independent of the collision partner M. Note that the V-T relaxation by molecules and by argon atoms is not expected to play an important part in the vibrational energy balance, because at the relatively low gas temperatures involved these V-T rates are very slow. The present version of the model does not incorporate V-T relaxation on reactive atoms such as N and O, because of the large uncertainty in prediction of chemical reaction rates of vibrationally excited molecules. The explicit analytic rate expressions used can be found in the Appendix.

The system of equations (4,5) for 40 vibrational levels of CO, N_2, and O_2 is solved using a standard solver for stiff partial differential equations, PDECOL [28]. In the calculations, a 21-point nonuniform grid, with most points located near the laser beam axis, is used. The laser line intensity distributions are given by the equation $I_l{\circledR}=I_{0l}\cdot[2/\pi R^2\cdot\exp(-2r^2/R^2)]$, where I_{0l} are the incident line intensities in W, and the parameter R=0.56 mm in the Gaussian intensity distribution across the focused laser beam is calculated by the code STRAHL developed at the University of Bonn [29]. The present code uses the spectroscopic data for the CO molecule [30] and accurate Einstein coefficients for spontaneous emission and absorption coefficients for the CO infrared bands [31] as inputs.

4. Results and Discussion

4.1. Emission Spectroscopy Results

Under the conditions described in Section 2, a highly nonequilibrium distribution of vibrational energy is created in the cell. Figure 3 shows the CO infrared emission from the CO-Ar mixture excited by the focused laser beam, as recorded by the FT spectrometer at a resolution of 0.25 cm^{-1}. The second overtone bands can be seen at the highest frequencies on the left

(ν>4300 cm^{-1}), the first overtone bands dominate at the lower frequencies (2250 cm^{-1}<ν<4300 cm^{-1}), and the high frequency tail of the R-branch of the v = 1→ 0 fundamental is the tall peak on the right. A long wavelength cut-off filter is used to prevent any more of the very intense fundamental band emission at frequencies ν<1950 cm^{-1} from entering the instrument, and swamping the overall signal. While this resolution is approximately 1/10 the rotational spacing of the CO molecule, there is a dense array of individual vibrational-rotational lines, due to the overlapping of the various band components.

The CO vibrational distribution functions (VDF) inferred from such high-resolution spectra using the standard technique [32], as well as theoretical line-of-sight averaged VDFs, are shown in Fig. 4 for two different gas mixtures, CO/Ar=2/100 and CO/N_2=2/100, at P=100 torr. The theoretical VDFs have been calculated using kinetic model discussed in Section 3. The measured translational-rotational temperatures for these two cases are T=600 K and 450 K, respectively. The distributions shown in Fig. 4 are the well-known "V-V pumped" distributions [4,5], maintained by the rapid redistribution of vibrational energy by the V-V processes, which pump energy into the higher vibrational levels. They are obviously extremely non-Boltzmann, and characterized by high population of the upper vibrational levels. Note that replacing argon with nitrogen in the cell somewhat reduces the measured CO vibrational level populations, since some vibrational energy is transferred from CO to N_2. This effect is somewhat less pronounced in the calculations (see Fig. 4), which suggests that the theoretical V-V rates for CO-N_2 [24] used in the present calculations are underestimated. Figure 4 also shows the calculated centerline CO and N_2 VDFs in the CO/N_2 mixture. One can see that carbon monoxide at the beam center is in extreme vibrational disequilibrium. Furthermore, modeling calculations suggest that nitrogen also becomes strongly V-V pumped by vibrational energy transfer from CO, as discussed in Section 3. Calculated radial distributions of the first level vibrational temperature T_v(CO),

$$T_v = \frac{\theta_1}{\ln[n_0 / n_1]}, \tag{7}$$

shown in Fig. 5, predict the centerline values of T_v(CO)=12,000 K in the CO/Ar mixture, and T_v(CO)=8500 K, $T_v(N_2)$=2400 K in the CO/N_2 mixture. In Eq. (7), θ_1 is the energy of the first vibrational level of a molecule, and n_0 and n_1 are the populations of vibrational levels v=0 and v=1, respectively. The first level vibrational temperature defined by Eq. (7) is used throughout the remainder of this chapter. For comparison, the apparent first level vibrational temperatures of CO inferred from the line-of-sight averaged VDFs of Fig. 4 are $T_v(CO)=3300$ K and 2700 K, respectively. Figure 6 plots the calculated CO distribution functions in the CO/Ar mixture at different distances from the laser beam axis. From Figs. 5,6, one can see that the optically pumped region is strongly nonuniform in the radial direction.

Figure 7 shows the experimental and the theoretical VDFs in CO/Ar/O_2 mixtures at different oxygen concentrations. One can see that the increase of O_2 partial pressure results in truncation of the CO VDF due to the V-V energy transfer from CO to O_2. However, even with 30 torr of O_2 in the cell, CO is still V-V pumped up to the level v~20. The model predictions do not fully reproduce the observed CO VDF fall-off at v>25 (see Fig. 7) unless the V-V rates for CO-O_2 at high vibrational levels (see Eq. (3)), varied in the calculations, considerably exceed the gas kinetic collision frequency. We believe this discrepancy to be due to (I) possible contribution of a fast nonadiabatic (i.e. reactive) channel of the V-V exchange between highly excited CO and O_2, and (ii) the effect of rapid V-T relaxation of CO by O atoms, both not incorporated into the model. An indirect evidence of these effects is the CO_2 infrared spectrum observed in CO/Ar/O_2 mixtures (see Fig. 8). CO_2 radiation, which could not be detected in CO/Ar and CO/N_2 mixtures, is most intense at oxygen partial pressures of 0.1-1.0 torr and becomes weaker as the O_2 concentration increases. CO_2 and oxygen atoms in the cell are likely to be produced in vibrationally stimulated chemical reaction $CO(v)+O_2(w)\rightarrow CO_2+O$. This scenario is consistent with the modeling calculations which predict strong vibrational excitation of diatomic species at the low O_2 partial pressures (see Fig. 9). For the conditions of Figs. 7,8, centerline first level vibrational temperatures are $T_v(CO)=13{,}000$ K, $T_v(O_2)=7000$ K and $T_v(CO)=9500$ K, $T_v(O_2)=3000$ K for 1 torr and 30 torr of O_2 in the cell, respectively.

4.2. Raman Spectroscopy Results

Spontaneous Raman spectroscopy allows access to vibrational levels of homopolar molecules and thereby provides powerful diagnostics of nonequilibrium gases. It also gives an opportunity for comparing predictions of modeling calculations discussed in Section 4.1 with the experimental data. In the experiments described in Section 3.2, Raman spectra of optically pumped CO, N_2, and O_2 are recorded in the pressure range P=400-760 torr. Figure 10 displays

Raman spectra of these species measured in a $CO/N_2/O_2$ mixture at P=740 torr, with CO and O_2 partial pressures of 40 torr and 30 torr, respectively. In these spectra, one can easily identify a few low vibrational levels of CO, N_2, and O_2. However, Raman vibrational spectra of CO in CO/N_2 mixtures also show multiple peaks corresponding to 38 first vibrational states of carbon monoxide, v=0-37 [20]. This makes the inference of vibrational populations of all these levels possible, provided that the Raman cross sections for highly vibrationally excited molecules are known with reasonable accuracy. As discussed in Section 3.2, Raman spectroscopy is essentially a point measurement. This means that if the focused Nd:YAG laser is aligned along the axis of the CO pump laser (see Fig. 2), the Raman spectra would provide vibrational level populations in the vicinity of the centerline of the excited region.

Figure 11 displays vibrational level populations of CO, N_2, and O_2 inferred from the Raman spectra such as shown in Fig. 10, at P=740 torr, with CO and O_2 partial pressures of 40 torr and 120 torr, respectively. Figure 12 shows vibrational level populations of CO and N_2 inferred from the Raman spectra of the optically pumped CO/N_2=3/100 mixture, at P=1 atm. At these conditions, the incident CO laser power of 10-13 W was about the same as in the experiments discussed in Section 4.1, while the gas pressure in the cell was much higher (~1 atm vs. 100 torr). Therefore vibrational energy loading per molecule in this second series of experiments is also much lower than in the first series. Indeed, the first level vibrational temperature of CO *near the centerline*, where vibrational disequilibirum is the strongest (T_v=2600-3000 K, see Figs. 11, 12), is in the same range as apparent values inferred from the *line-of-sight averaged* CO VDF in emission spectroscopy measurements (T_v=2700-3300 K, see Figs. 4,7). In addition, one can see that the calculated centerline vibrational temperature of CO at P=100 torr, $T_v(CO)$=8,500-12,000 K (see Figs. 3, 4) is much higher than its corresponding values calculated and measured at P=1 atm, $T_v(CO)$=2600-3900 K (see Fig. 11, 12). In other words, vibrational disequilibrium becomes weaker at higher pressures. However, even at P=1 atm it remains very strong. This is consistent with modeling calculations, also shown in Figs. 11, 12. Calculated centerline VDFs of the three diatomic species are in reasonable agreement with the data. Comparing the results of calculations in Figs. 11, 12, one can see that addition of oxygen to optically pumped gases results in depletion of the high vibrational levels of CO, as has been also observed in the emission spectroscopy experiments (see Fig. 7). From Fig. 11 one can see that the model somewhat overestimates the first level vibrational temperature of oxygen. We believe this to be an in indication of an additional energy sink from the vibrational mode of O_2, possibly due to V-T relaxation by O atoms.

The translational temperature in this series of experiments is evaluated from comparison of two Raman spectra of nitrogen, one with the CO laser on (e.g. see Fig. 10(a)), and the other with the laser turned off, i.e. in an equilibrium gas mixture at T_o=300 K. In the latter case, as expected, only the signal from v=0 is measured. Since the Raman signal intensity, I_v, is proportional to the product of the absolute population of a vibrational level, n_v, and the Raman cross section, $\sigma_v \sim (v+1)$, this allowed inference of the number density of N_2 molecules, as well as the translational temperature, on the centerline of the excited region,

$$\frac{T}{T_0} = \frac{n_{N_2}(T_0, non-excited)}{n_{N_2}(T, excited)} = \frac{n_0}{\sum_v n_v} = \frac{I_0}{\sum_v I_v/(v+1)} \tag{8}$$

Nitrogen spectra have been used for the temperature inference for two reasons, (I) in the present experiments it is the most abundant species (78-98% of the gas mixture), so that vibrationally-stimulated chemical reactions are least likely to affect its concentration, and (ii) it has the fewest number of vibrational levels excited. From Eq. (8), the centerline translational temperature of the optically pumped gases for the conditions of Figs. 10-12 is inferred to be T≅500 K. Additional experiments [20] demonstrate that the rotational structure of the S-branch Raman spectra can also be resolved, which also allows estimating the translational-rotational temperature of the optically pumped gas, T<600 K [20].

These experimental results confirm the predictions of modeling calculations (see Section 4.1) and demonstrate that strong vibrational disequilibrium can be sustained by a c.w. CO laser in relatively cold molecular gas mixtures at atmospheric pressure. Among the numerous implications of this major result is the possibility of sustaining a cold stable plasma in atmospheric pressure air (with CO used as an additive). Associative ionization of carbon monoxide in strongly vibrationally excited CO/N_2, CO/Ar/O_2, and CO/Ar/NO mixtures has already been demonstrated in our previous work [11,33,34]. The unconditional stability of these optically pumped plasmas is ensured by the absence of an external electric field and electron impact ionization. The present data (in particular, strong vibrational excitation of O_2), suggest that oxygen might also play an important role in vibrationally stimulated ionization kinetics. In addition, high concentrations of vibrationally excited molecules in optically pumped air plasmas might also affect the electron removal rates, i.e. recombination and attachment. Discussion of these issues is beyond the scope of the present work. Recent studies of rates and mechanisms of ionization, recombination, and electron attachment in optically pumped air plasmas, as well as their stability, are discussed in our separate publication [34].

Comparison of the experimental data with the modeling calculations provides insight into kinetics of vibrational energy transfer among diatomic species and energy transport in nonuniform optically pumped gases. However, the results suggest that the rates of V-V exchange for CO-N_2, and especially those for CO-O_2, are not known with sufficient accuracy. Further optical pumping experiments using complementary infrared and Raman diagnostics would allow inference of the rates of these key energy transfer processes.

6. Appendix

Notations:

T – translational temperature

ω_{ei} and x_{ei} – vibrational quantum and anharmonicity of the species *i*, respectively

v, w – vibrational quantum numbers

$P_{ij}^{v,v-1}$ – rate coefficient of V-T relaxation of the species *i* from level v to level v-1 by the species *j*, cm^3/sec

$\tau_{ij}P$ – vibrational relaxation time of the species *i* by the species *j* times pressure, atm·µsec

$Q_{ij}(v,w-1\rightarrow v-1,w)$ – rate coefficient of V-V exchange between the species *i* and *j*, cm^3/sec

Z - gas-kinetic collision frequency, cm^3/sec

V-T rate parametrization:

$$P_{ij}^{v,v-1} = P_{ij}(T)\frac{v}{1-x_{ei}v}F(\lambda_{ij}^{v,v-1}) \tag{A1}$$

$$F(\lambda) = \frac{1}{2}(3-e^{-2\lambda/3})e^{-2\lambda/3}\,,\quad \lambda_{ij}^{v,v-1} = 2^{-3/2}\sqrt{\frac{C_{ij}}{T}}\left|\Delta E_i\right|,\quad \Delta E = \omega_{ei}(1-2x_{ei}v) \tag{A2}$$

$$P_{ij}(T) = \frac{10^{-7}kT}{(\tau_{ij}P)F(\lambda_{ij}^{1,0})[1-\exp(-\omega_{ei}/T)]} \tag{A3}$$

$$\tau_{ij}P = \exp\left(A_{ij} + B_{ij}T^{-1/3} + C_{ij}T^{-2/3}\right) \text{ atm}\cdot\mu\text{sec} \tag{A4}$$

Table A1. Parameters used in the V-T rate expressions (Eqs. A1-A4)

Species	c_{ij}	A_{ij}	B_{ij}	C_{ij}
CO-Ar, N_2-Ar, O2-Ar	1.335e-3	10.38	0	0
CO-M	0.25	-15.23	280.5	-549.6
N_2-M	0.25	-12.54	258.9	-390.9
O_2-M	0.25	-14.0	205	-295

V-V rate parametrization:

$$\begin{gathered} Q_{ij}(v, w-1 \to v-1, w) = Z(S^{v,v-1}_{w-1,w} + L^{v,v-1}_{w-1,w})\, e^{-\Delta E/2T}, \\ \Delta E = \omega_{ei}(1 - 2x_{ei}v) - \omega_{ej}(1 - 2x_{ej}v) \end{gathered} \tag{A5}$$

$$S^{v,v-1}_{w-1,w} = S \cdot T \frac{v}{1 - x_{ei}v} \frac{w}{1 - x_{ej}w} F(\lambda^{v,v-1}_{w-1,w}) \tag{A6}$$

$$\mathrm{F}(\lambda) = \frac{1}{2}(3 - \mathrm{e}^{-2\lambda/3})\mathrm{e}^{-2\lambda/3}, \quad \lambda^{v,v-1}_{w-1,w} = 2^{-3/2}\sqrt{\frac{\mathrm{c}}{\mathrm{T}}}|\Delta \mathrm{E}| \tag{A7}$$

$$L^{v,v-1}_{w-1,w} = \frac{L}{T}\left(\frac{g^{v,v-1}}{g^{1,0}}\right)^2_i \left(\frac{g^{w-1,w}}{g^{1,0}}\right)^2_j \exp\left(-\frac{\Delta E^2}{bT}\right) \tag{A8}$$

$$\left(\frac{g^{v,v-1}}{g^{1,0}}\right)^2_i = \left(\frac{a+1}{a+3-2v}\right)^2 \frac{v(a+2-2v)(a+4-2v)}{a(a+3-v)}, \quad a = 1/x_{ei} \tag{A9}$$

Table A2. Parameters used in the V-V rate expressions (Eqs. A5-A9)

Species	S	L	c, K^{-1}	b, K
CO-CO	1.64e-6	1.614	0.456	40.36
N_2-N_2	1.0e-7	-	0.120	-
O_2-O_2	7.0e-8	-	0.185	-
CO-N_2	7.0e-8	0.03	0.185	87.67

N_2-O_2	1.0e-7	-	0.120	-
CO-O_2	7.0e-8	0.03	0.185	87.67

$Z=3\cdot 10^{-10}(T/300)^{1/2}$ cm^3/s

V-E rate $CO(X^1\Sigma)+M \rightarrow CO(A^1\Pi)+M$:

$k_{VE}=10^{-12}$ cm^3/s

References

1. "Nonequilibrium Vibrational Kinetics", ed. M. Capitelli, Springer, Berlin, 1986
2. C. Park, "Nonequilibrium Hypersonic Aerodynamics", Wiley, New York, 1990
3. J. W. Rich, S.O. Macheret, and I.V. Adamovich, "Aerothermodynamics of Vibrationally Nonequilibrium Gas", Experimental Thermal and Fluid Science, Vol. 13, 1996, p. 1
4. J. W. Rich, "Relaxation of Molecules Exchanging Vibrational Energy", in "Applied Atomic Collision Physics", Vol. 3, "Gas Lasers", ed. E.W. McDaniel and W.L. Nighan, Academic Press, New York, 1982, pp. 99-140
5. B.F. Gordiets, V.A. Osipov, and L.A. Shelepin, "Kinetic Processes in Gases and Molecular Lasers", Gordon and Breach, London, 1988
6. E.P. Velikhov, A.S. Kovalev, and A.T. Rakhimov, "Physical Phenomena in Gas Discharge Plasmas", Moscow, Nauka, 1987
7. Raizer, Y.P., "Gas Discharge Physics", Springer-Verlag, Berlin, 1991
8. J.W. Rich, R.C. Bergman, and M.J. Williams, "Measurement of Kinetic Rates for Carbon Monoxide Laser Systems", Final Contract Report AFOSR F49620-77-C-0020 (November 1979)
9. R.L. DeLeon and J.W. Rich, "Vibrational Energy Exchange Rates in Carbon Monoxide", Chemical Physics, Vol. 107, 1986, p. 283
10. C. Flament, T. George, K.A. Meister, J.C. Tufts, J.W. Rich, V.V. Subramaniam, J. P. Martin, B. Piar, and M.-Y. Perrin, "Nonequilibrium Vibrational Kinetics of Carbon Monoxide at High Translational Mode Temperatures", Chemical Physics, Vol. 163, 1992, p. 241
11. I. Adamovich, S. Saupe, M.J. Grassi, O. Shulz, S. Macheret, and J.W. Rich, "Vibrationally Stimulated Ionization of Carbon Monoxide in Optical Pumping Experiments", Chemical Physics, Vol. 173, 1993, p. 491
12. H.L. Wallaart, B. Piar, M.Y. Perrin, and J.P. Martin, "Transfer of Vibrational Energy to Electronic Excited States and Vibration Enhanced Carbon Production in optically pumped CO", Chemical Physics, Vol. 196, 1995, p. 149
13. H. Dunnwald, E. Siegel, W. Urban, J.W. Rich, G.F. Homicz, and M.J. Williams, "Anharmonic Vibration-Vibratino Pumping in Nitric Oxide by Resonant IR-Laser Irradiation", Chemical Physics, Vol. 94, 1985, p. 195

14. S. Saupe, I. Adamovich, M.J. Grassi, and J.W. Rich, "Vibrational and Electronic Excitation of Nitric Oxide in Optical Pumping Experiments", Chemical Physics, Vol. 174, 1993, p. 219
15. N.M. Gorshunov, private communication, 1990
16. Price, J.M., Mack, J.A., Rogaski, C.A., and Wodtke, A.M., "Vibrational-State-Specific Self-Relaxation Rate Constant Measurements of Highly Excited O_2(v=19-28)", Chemical Physics, Vol. 175, No. 1, 1993, p. 83
17. A. Noullez, G. Wallace, W. Lempert, R.B. Miles, and U. Frisch, "Transverse Velocity Increments in Turbulent Flow Using the RELIEF Technique," Journal of Fluid Mechanics, Vol. 339, p. 287, 1997.
18. N.G. Basov, E.M. Belenov, V.A. Isakov, E.P. Markin, A.N. Oraevskii, V.I. Romanenko, and N.B. Ferapontov, "Laser-Induced Chemical Reactions and Isotope Separation", Soviet Journal of Quantum Electronics, Vol. 2, p. 938, 1975
19. Billing, G.D., "Vibration-Vibration and Vibration-Translation Energy Transfer, Including Multiquantum Transitions in Atom-Diatom and Diatom-Diatom Collisions", Nonequilibrium Vibrational Kinetics, Springer-Verlag, Berlin, 1986, Chap. 4, pp. 85-111
20. W. Lee, I.V. Adamovich, and W.R. Lempert, "Optical Pumping Studies of Vibrational Energy Transfer in High-Pressure Diatomic Gases", submitted to Journal of Chemical Physics, May 2000
21. A. Eckbreth, "Laser Diagnostics for Combustion Temperature and Species", Gordon and Breach, Amsterdam , 1996
22. I.V. Adamovich, S.O. Macheret, and J.W. Rich, "Spatial Nonhomogeneity Effects in Nonequilibrium Vibrational Kinetics", Chemical Physics, vol. 182, 1994, p. 167
23. E. Ploenjes, P. Palm, A.P. Chernukho, I.V. Adamovich, and J.W. Rich, "Time-Resolved Fourier Transform Infrared Spectroscopy of Optically Pumped Carbon Monoxide", Chemical Physics, vol. 256, 2000, pp. 315-331
24. Cacciatore, M., Capitelli, M., and Billing, G.D., "Theoretical Semiclassical Investigation of the Vibrational Relaxation of CO Colliding with $^{14}N_2$", Chemical Physics, Vol. 89, No. 1, 1984, p. 17
25. Billing, G.D., and Fisher, E.R., "VV and VT Rate Coefficients in N_2 by a Quantum-Classical Model", Chemical Physics, Vol. 43, No.3, 1979, p. 395

26. Billing, G.D., and Kolesnick, R.E., "Vibrational Relaxation of Oxygen. State to State Rate Constants", Chemical Physics Letters, Vol. 200, No. 4, 1992, p. 382

27. Billing, G.D., "VV and VT Rates in N_2-O_2 Collisions", Chemical Physics, Vol. 179, No. 3, 1994, p. 463

28. N.K. Madsen and R.F. Sincovec, "Algorithm 540: PDECOL, General Collocation Software for Partial Differential Equations", ACM Transactions on Mathematical Software, Vol. 5, 1979, p. 326

29. A. Yariv and P. Yeh, "Optical Waves in Crystals: Propagation and Control of Laser Radiation", Wiley, New York, 1984; U. Sterr and W. Ertmer (Univ. Of Bonn, Germany), private communication

30. K.P. Huber and G. Herzberg, "Molecular Spectra and Molecular Structure", Vol. 4, "Constants of Diatomic Molecules", New York, Van Nostrand, 1979

31. C. Chackerian, Jr., R. Farrenq, G. Guelachvili, C. Rosetti, and W. Urban, Canadian Journal of Physics, Vol. 62, 1984, p. 1579

32. K.P. Horn and P.E. Oettinger, Journal of Chemical Physics, Vol. 54, 1971, p. 3040

33. I.V. Adamovich and J.W. Rich, “The Effect of Superelastic Electron-Molecules Collisions on the Vibrational Energy Distribution Function”, Journal of Physics D: Applied Physics, Vol. 30, 1997, p. 1741

34. E. Plönjes, P. Palm, I.V. Adamovich, and J. W. Rich, “Ionization Measurements in Optically Pumped Discharges”, accepted for publication in Journal of Physics D: Applied Physics, 2000

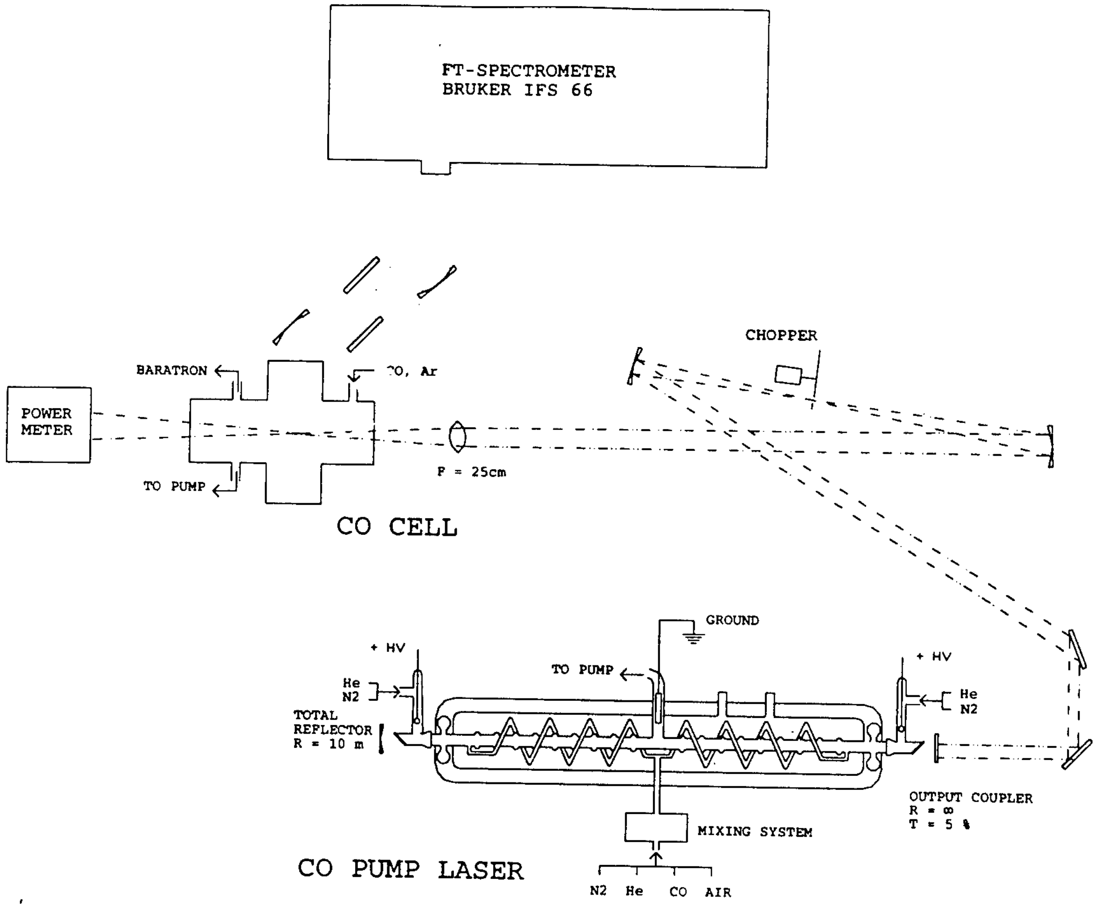
FT-SPECTROMETER
BRUKER IFS 66
CHOPPER
BARATRON
CO, Ar
POWER
METER
TO PUMP
F = 25cm
CO CELL
GROUND
+ HV
TO PUMP
+ HV
He
N2
He
N2
TOTAL
REFLECTOR
R = 10 m
OUTPUT COUPLER
R = ∞
T = 5 %
MIXING SYSTEM
CO PUMP LASER
N2
He
CO
AIR

Figure 1. Schematic of the experimental setup for emission spectroscopy

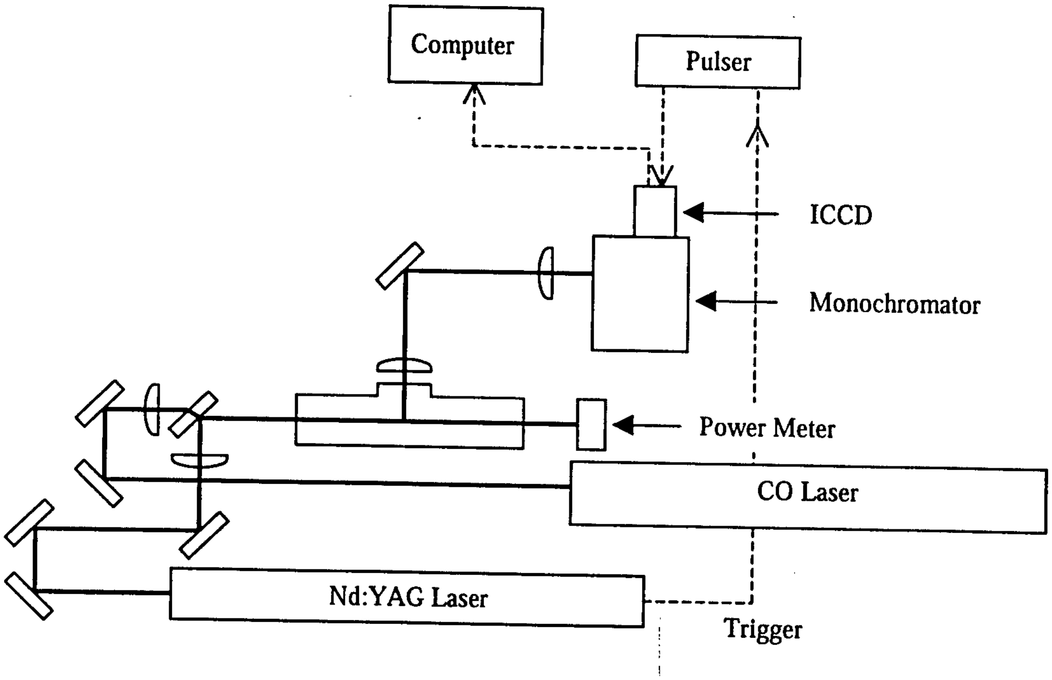
Computer
Pulser
ICCD
Monochromator
Power Meter
CO Laser
Nd:YAG Laser
Trigger

Figure 2. Schematic of the experimental setup for Raman spectroscopy

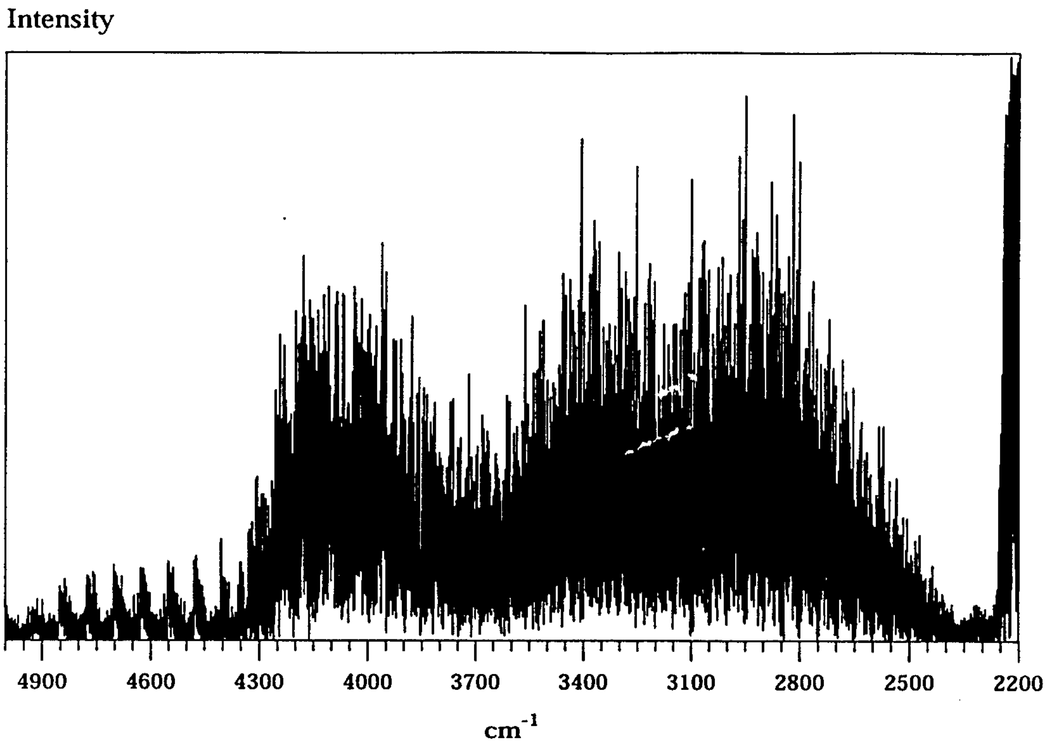

Figure 3. High-resolution (0.25 cm^{-1}) CO infrared spectrum. CO/Ar=2/100, P=100 torr

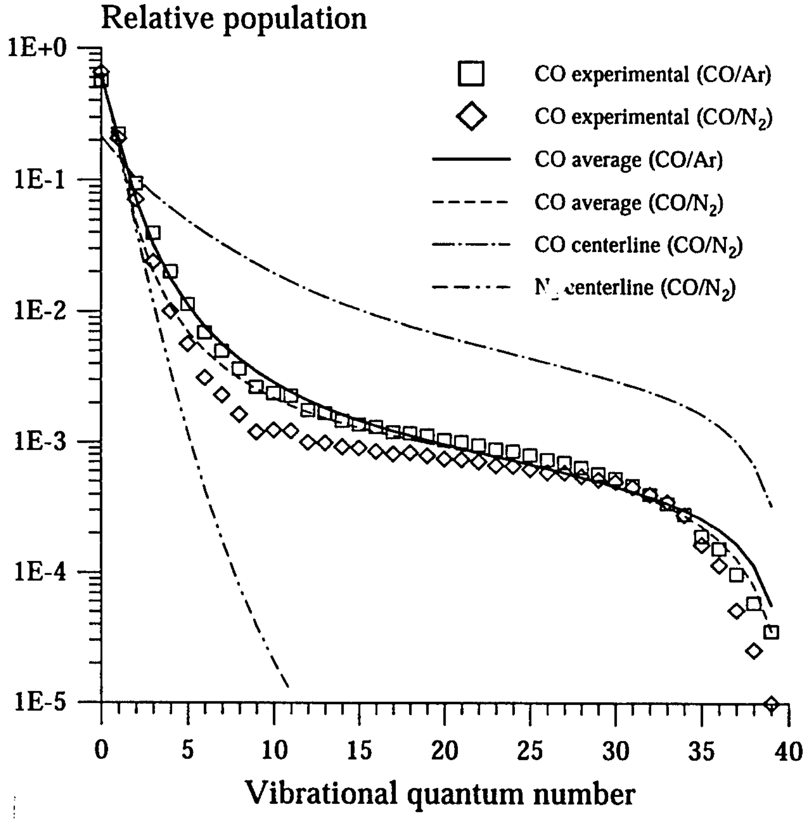

Figure 4. Experimental (CO) and theoretical (CO and N_2) distribution functions in CO/Ar=2/100 (T=600 K) and CO/N_2=2/100 (T=450 K) mixtures. P=100 torr, laser power is 15 W

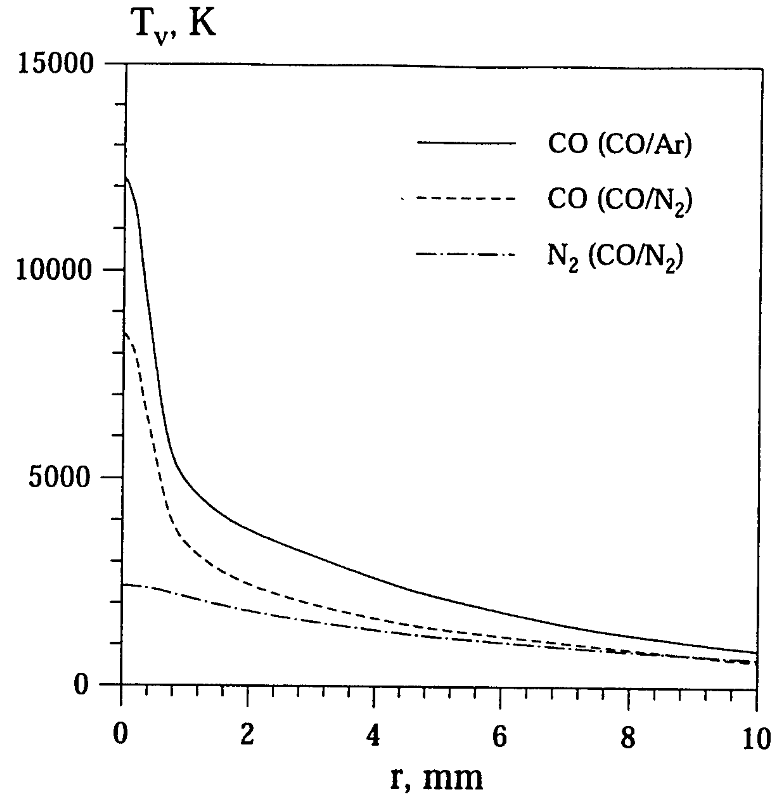

Figure 5. Calculated radial profiles of the first level vibrational temperatures of CO and N_2 in CO/Ar=2/100 and CO/N_2=2/100 mixtures. P=100 torr.

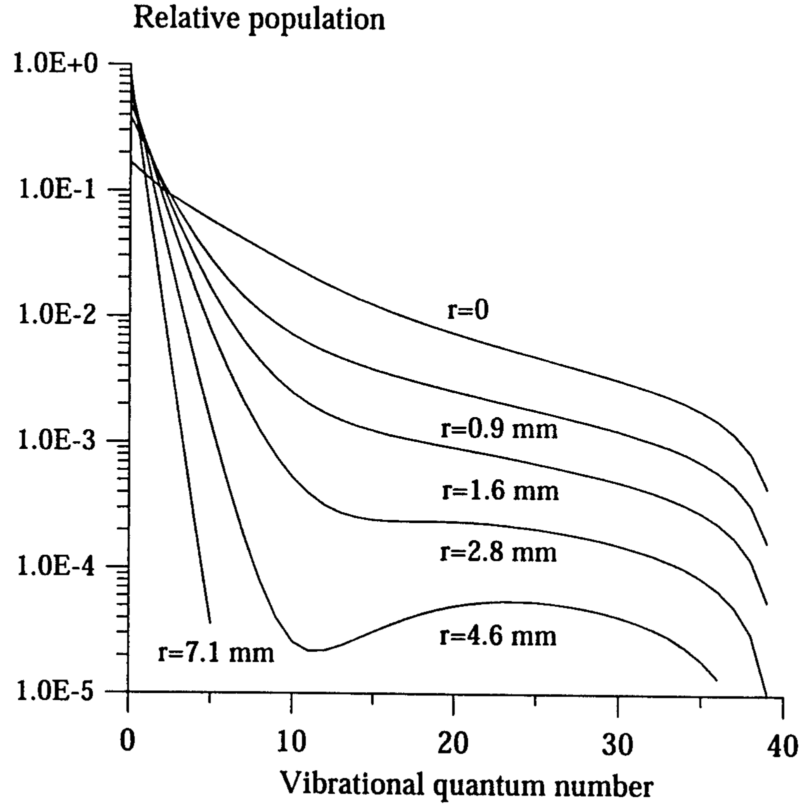

Figure 6. Calculated vibrational distribution functions in CO/Ar=2/100 mixture. P=100 torr.

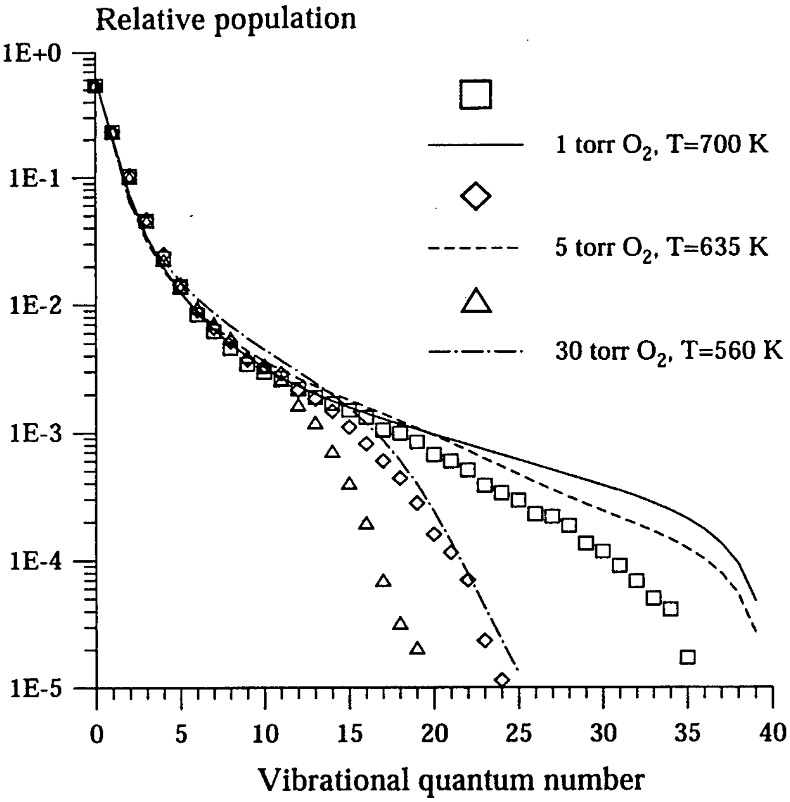

Figure 7. Experimental and theoretical CO distribution functions in CO/Ar/O_2 mixtures. P_{CO}=2 torr, P_{Ar}=100 torr, laser power is 15 W.

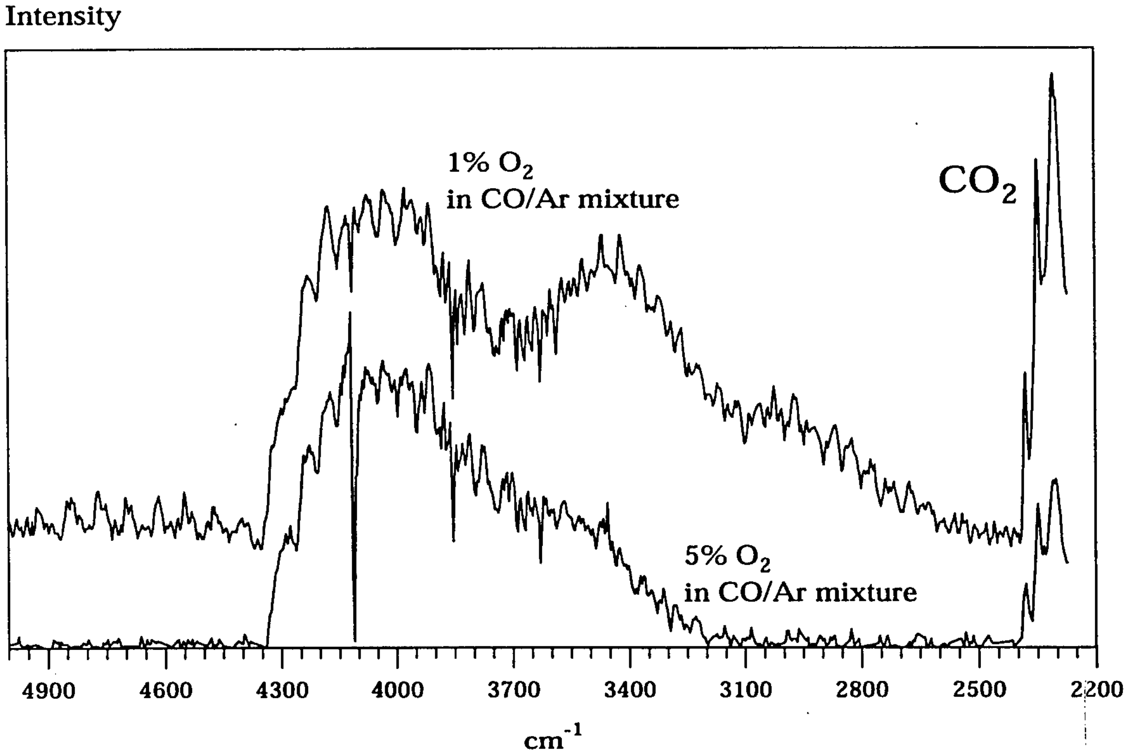

Figure 8. Low-resolution (8.0 cm^{-1}) CO infrared spectra for the conditions of Fig. 7

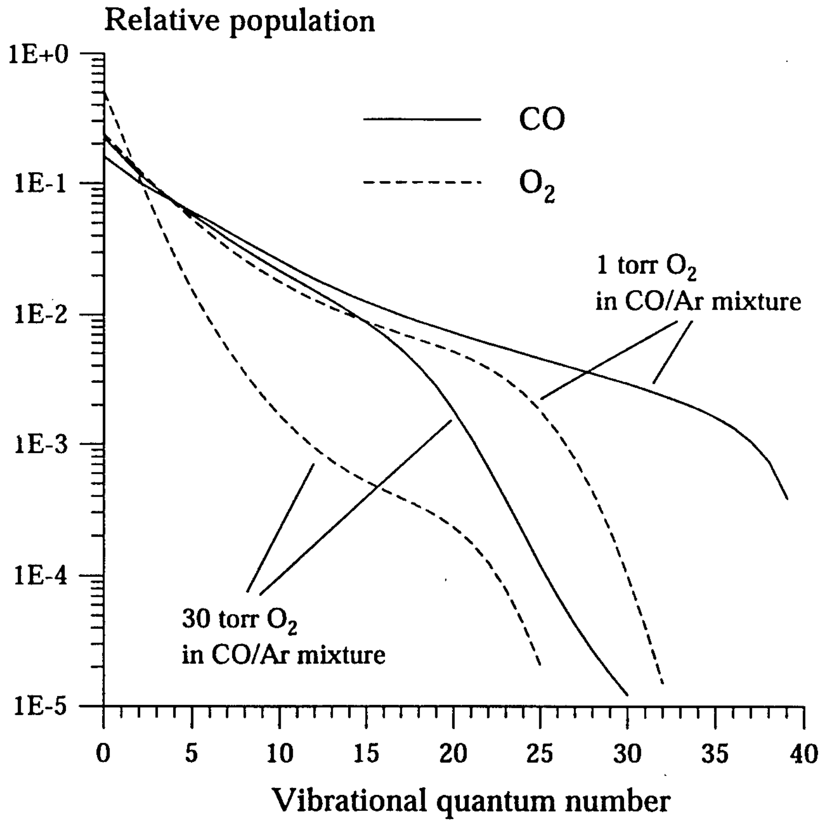

Figure 9. Calculated centerline vibrational distribution functions of CO and O_2 for the conditions of Fig. 7

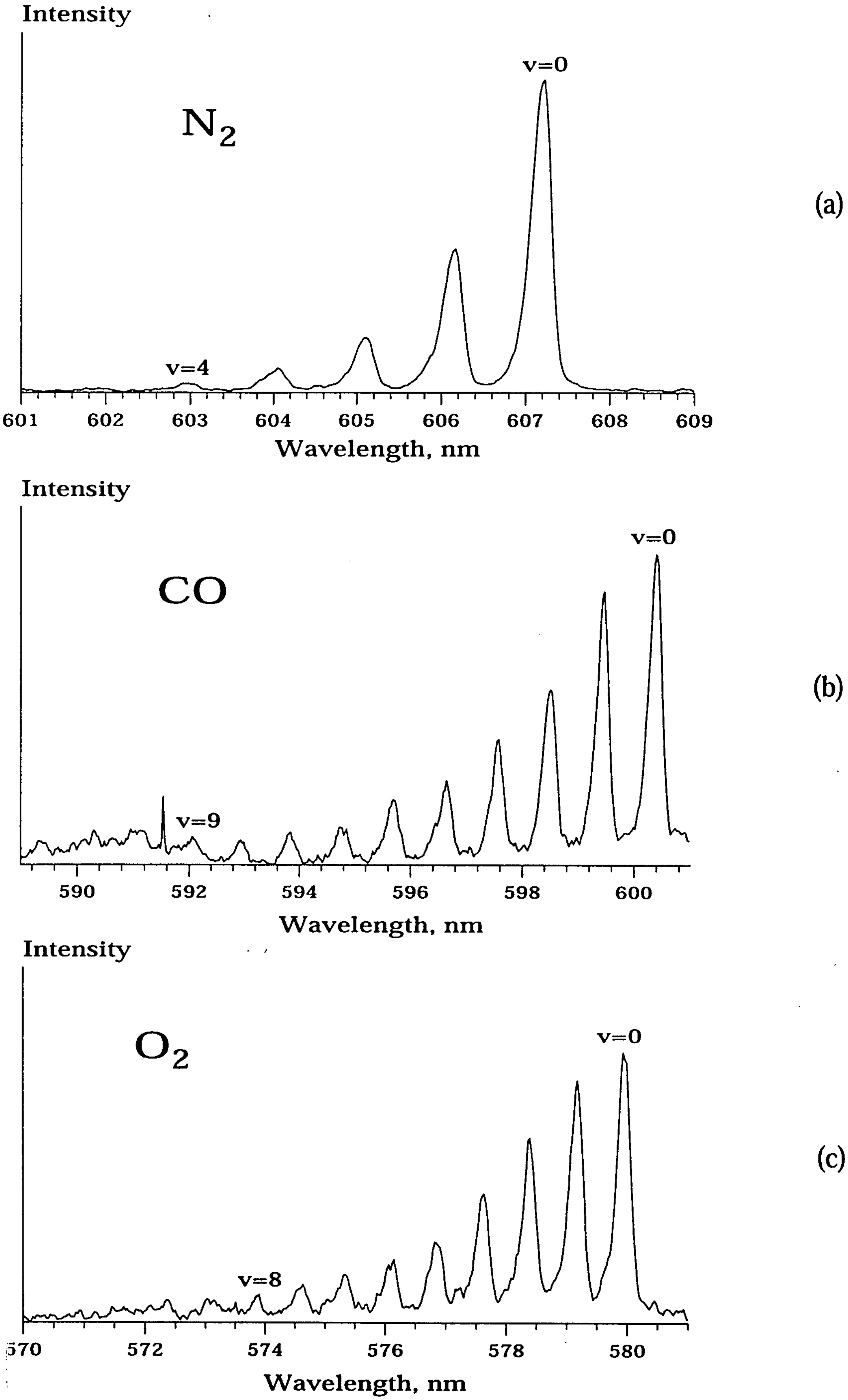

Figure 10. Raman spectra of N_2, CO, and O_2. $P(N_2)$=670 torr, P(CO)=40 torr, $P(O_2)$=30 torr

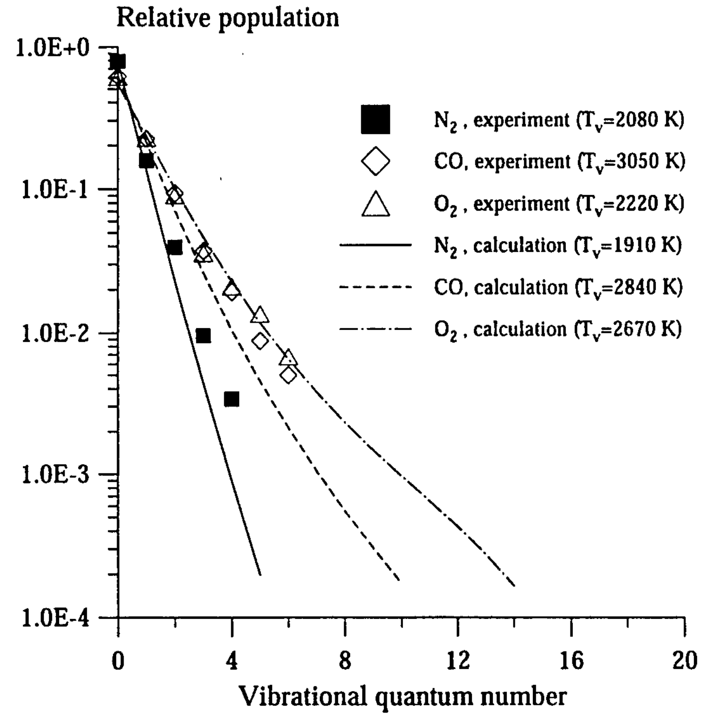

Figure 11. Experimental (symbols) and calculated (lines) centerline vibrational populations of N_2, CO, and O_2. $P(N_2)$=580 torr, P(CO)=40 torr, $P(O_2)$=120 torr

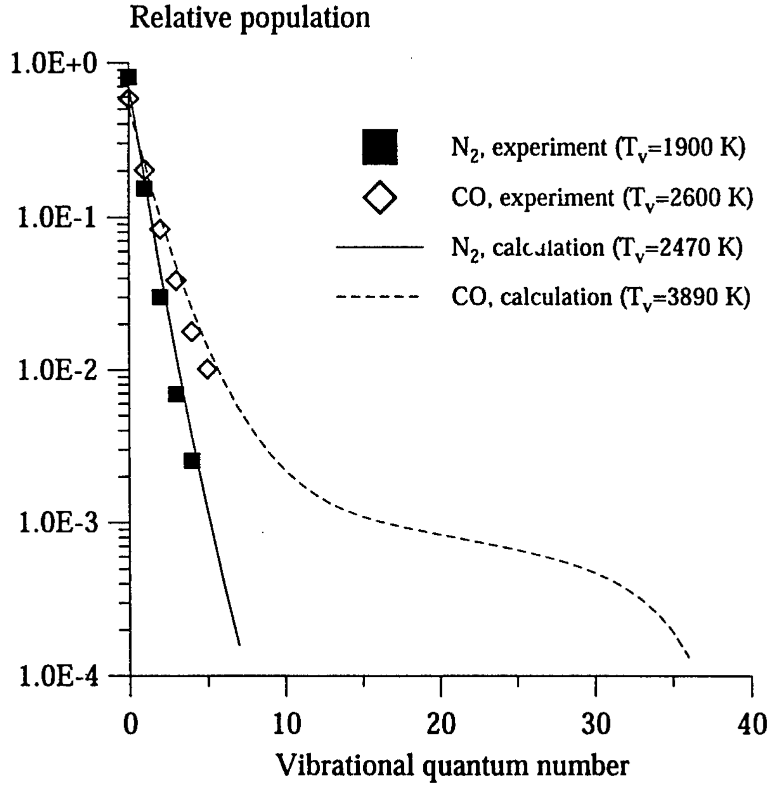

Figure 12. Experimental (symbols) and calculated (lines) centerline vibrational populations of CO and N_2. CO/N_2=3/100, P=1 atm

CHAPTER VII.

THE EFFECT OF SUPERELASTIC ELECTRON-MOLECULE COLLISIONS ON THE VIBRATIONAL ENERGY DISTRIBUTION FUNCTION

1. Introduction.

The vibrational energy transfer between diatomic molecules and low-energy electrons in electron-molecule collisions

$$AB(v)+e^{-}(\varepsilon)\leftrightarrow AB^{-}(v')\leftrightarrow AB(w)+e^{-}(\varepsilon+\Delta\varepsilon)\,, \tag{1}$$

has been rather extensively studied before (see [1-3] and references therein). In Eq. (1), AB is a diatomic molecule, e^- is an electron, AB^- is the intermediate negative ion, v, v', and w are vibrational quantum numbers, and ε is the electron energy. The results of the Boltzmann equation solution for the electron energy distribution function (EEDF) in N_2 and CO plasmas [1-3] have shown that these "superelastic" collisions strongly increase the number of electrons with higher energies. This effect also leads to a significant change in the electron energy balance and in the electron impact excitation rates. However, experimental measurements of the correlation between the molecular vibrational level populations and EEDF are still not available. To the best of our knowledge, the only direct evidence of such a correlation was obtained by measuring the CO vibrational distribution function (VDF) in a CO-Ar-He mixture optically pumped by a CO laser, with and without electrons present in the gas [4]. In this experiment, CO was vibrationally excited up to v~40 due to vibration-vibration (V-V) pumping [5], and the electrons in an optical cell containing the mixture were produced by the vibrationally-stimulated ionization process

$$\begin{gathered}CO(v)+CO(w)\rightarrow CO+CO^{+}+e\\ E_v+E_w\geq E_{ion}(CO)\end{gathered} \tag{2}$$

In Eq. (2), E_v is vibrational energy of the vth CO vibrational level, and $E_{ion}(CO)$ is the ionization potential of CO. The electrons were removed from the cell, if necessary, by means of a Thomson discharge between two plane electrodes placed in the cell. We emphasize that ionization by neither laser beam nor by electric field was observed (both the beam power density and the applied voltage were typically very low). As is well known, in a completely non-self-sustained Thomson discharge [6] the electron concentration between the electrodes can be dramatically reduced (up to several orders of magnitude) simply by increasing the discharge voltage (e.g. see Fig. 1, Ref. [4]). This effect allowed efficient control of the electron number density in the experiments [4]. It was observed that with the electrons present in the gas, relative populations of the low vibrational levels of CO ($v \leq 15$) are greater, while populations of the high levels are smaller, compared to their values in the "electron-free" environment (see Fig. 2). This quite noticeable effect was qualitatively explained by vibrational energy transfer by electrons from the high toward the low vibrational levels of CO.

The present work presents a detailed simulation of the process based on the numerical solution of master equation for the CO VDF coupled to the Boltzmann equation for EEDF.

2. Kinetic model.

The explicit form of master equation for the VDF and Boltzmann equation for the symmetric part of the EEDF used in the present calculations can be found in [7,8,3]. The kinetic model used takes into account CO vibrational excitation by resonance absorption of CO laser radiation, vibration-to-translation (V-T) relaxation in CO-Ar and in CO-CO collisions, vibration-to-vibration (V-V) exchange in CO-CO collisions, and collisional near-resonance vibration-to-electronic (V-E) energy transfer $CO(X^1\Sigma, v \cong 40)+M \rightarrow CO(A^1\Pi, v \cong 0)+M$. The rates of these processes were taken to be the same as in [7,8]. The collision integral in the Boltzmann equation incorporates elastic scattering of electrons on CO molecules and Ar atoms, inelastic processes of Eq. (1) for $0 \leq v,w \leq 40$, $|v-w| \leq 10$, as well as electronic excitation and ionization of CO and Ar. Elastic scattering cross-sections, vibrational excitation cross-sections $\sigma_{0\rightarrow w}(\varepsilon)$ of the process (1) for $0 \leq w \leq 10$, electronic excitation and ionization cross-sections of CO were taken to be the same as in [2]. Cross-sections for collision of electrons with Ar are taken from [9]. The vibrational cross-sections for other values of v and w were evaluated by two different methods, as has previously been done in [3]:

(i) Cross-section set I. From the semi-empirical theory by Chen [10], adjusted to fit the few available experimental cross-sections, $\sigma_{0\rightarrow w}(\varepsilon)$, (see [1,2,10] for more details).

(ii) Cross-section set II. Simple extrapolation of available experimental cross-sections to the higher vibrational levels with an energy correction:

$$\sigma_{v\to w}(\varepsilon)=\sigma_{0\to|w-v|}(\varepsilon+\delta E)\,,\delta E=E_{|w-v|}-(E_w-E_v) \qquad (3)$$

We realize that use of method [10] for the high vibrational quantum numbers, for which no experimental data are available, may well be inaccurate. For this reason we used the Set II cross-sections to estimate the influence of the cross-section model on the results. The effect of elastic collisions of vibrationally excited molecules with electrons (v=w in Eq. 1) on the total elastic scattering cross-section [1,2] is also incorporated.

3. Results and discussion.

The results of calculations for the experimental conditions of Ref. [4], P=100 torr, T=700 K, CO/Ar=3%/97% are presented in Figs. 3-6.

First, the calculations were carried out in the absence of the external electric field, so that superelastic collisions with the CO molecules (1) were assumed to be the only possible source of excitation of electrons that are produced in process (2). These are produced with fairly low energy, $\varepsilon<1$ eV. The electron concentration was found from the balance equation

$$q_{ion}=k_{ion}n_{CO}^2\sum_{E_v+E_w\geq E_{ion}}(f_vf_w)=\beta n_e^2, \qquad (4)$$

where k_{ion} is the rate constant of process (2), n_{CO} and n_e are concentrations of CO molecules and electrons, respectively, f_v is the relative population of vibrational level v, and $\beta\cong10^{-8}$ cm^3/s is the rate of dissociative recombination. The vibrational distribution function f_v has been measured in [4] (see Fig. 3). Ionization rate, $k_{ion}=(8\pm5)\cdot10^{-15}$ cm^3/s, inferred from the measurement of the Thomson discharge current-voltage characteristics, should be appropriately corrected for the CO laser beam width, which was overlooked in Ref. [4]:

$$I_s=eq_{ion}\frac{\pi d^2}{4}L \qquad (5)$$

In Eq. (5), I_s=6.6 μA is the Thomson discharge saturation current, $d\cong3$ mm and L=2 cm are the laser beam effective diameter and the electrode length in the beam direction, respectively. With this correction taken into account, $k_{ion}=(2.5\pm1.5)\cdot10^{-14}$ cm^3/s. From Eq. (4), the baseline case electron concentration was found to be $n_e=2\cdot10^{11}$ cm^{-3} (ionization fraction $n_e/n\sim10^{-7}$). Taking into account a substantial uncertainty in k_{ion} and β, this number was varied in the calculations.

Note that at these conditions ionization and recombination processes, not incorporated in the collision integral, can not significantly affect the electron energy distribution function since the frequency of the superelastic collisions is much greater than ionization and recombination frequency:

$$\sigma_{vib}v_{el}n_{CO} \sim 10^8\,s^{-1} >> \beta n_e \sim 10^3\,s^{-1} \qquad (6)$$

In Eq. (6), $\sigma_{vib}\sim10^{-15}$ cm^2 is the vibrational excitation cross-section and $v_{el}\sim10^7$ cm/s is the average electron velocity.

Figure 3 shows that the calculated CO VDF, agreeing very well with the experimental data for the "plateau" region (v>15), substantially overestimates the populations of the lower vibrational levels. This is the result of the line-of-sight integration, which differently affects the collected signal for the different regions of infrared spectrum, thereby perturbing the observed VDF, as was previously discussed in [11]. Note that the set of vibrational energy transfer rates used gives excellent agreement with the experimental VDFs obtained under spatially homogeneous conditions (see [11] and references therein). The EEDF, also shown in Fig. 3, is Boltzmann-like up to electron energy about ε=3 eV, where it sharply drops. This cut-off simply reflects the fact that the kinetic model does not incorporate any molecule-to-electron (superelastic) energy transfer process with an energy defect higher than 3 eV, and it may well be an artifact. For example, EEDF measurements in decaying nitrogen plasma [12] show a noticeable "bump" at $\varepsilon\sim5$ eV, which is rather close to the energy of the long-living metastable electronic state $N_2(A^3\Sigma_g^+)$, $\varepsilon\cong6.3$ eV. This effect was explained by energy transfer to electrons in superelastic process

$$N_2(A^3\Sigma_g^+) + e^-(\varepsilon) \rightarrow N_2(X^1\Sigma_g^+) + e^-(\varepsilon+\Delta\varepsilon)\,, \qquad (7)$$

which is consistent with the results of the Boltzmann equation kinetic modeling [3]. A similar process with participation of the metastable electronic state $CO(a^3\Pi)$, $\varepsilon \cong 5.5$ eV, observed in other optical pumping experiments [13], is quite possible. Unfortunately, lack of the kinetic rates of the V-E transfer that primarily populates the $a^3\Pi$ electronic state in the optical cell does not allow reliable determination of the $CO(a^3\Pi)$ concentration. However, the inclusion of such more energetic processes is unlikely to change the EEDF shape below $\varepsilon = 3$ eV. Finally, one can see from Fig. 3 that the EEDFs obtained with two different inelastic cross-sections sets are very close.

The calculated steady-state first level vibrational temperature is $T_V = 4100$ K, while the electron temperature turns out to be somewhat higher, $T_e = 5000\text{-}5000$ K, depending on the electron concentration.

The second series of calculations was made when a voltage, applied to the two plane electrodes in the cell, is such that the Thomson discharge current-voltage characteristic is saturated [4]. The experimental saturation voltage for the CO/Ar=3%/97% mixture at P=100 torr and interelectrode distance D=1 cm is $U_s \cong 480$ V [4]. The corresponding reduced electric field value is $E/N = 3.4 \cdot 10^{-16}$ $V \cdot cm^2$. At the saturation conditions, the steady-state electron concentration in the cell is determined by ionization rate in the process (2) and the electron removal rate by the field, with the collisional electron loss being negligible [4]:

$$n_{e\,max} \cong \left(\frac{q_{ion} \hat{\varepsilon}_0}{e \mu_e} \right)^{1/2}, \tag{8}$$

where q_{ion} is given by Eqs. (4,5) and μ_e is the electron mobility, $\mu_e \sim 10^3$ $cm^2/V/s$. One can see that $n_e \leq 4 \cdot 10^8$ cm^{-3}, which is much lower than n_e in the field-free environment (see also Fig. 1).

In these calculations, it was found that the VDF is almost completely unaffected by the electrons due to their very low concentration (ionization fraction $n_e/n \sim 10^{-10}$). We may therefore consider this regime electron-free. Figures 4 and 5 demonstrate both the experimental and the calculated ratio of relative populations of CO vibrational levels with and without electrons. One can see that the results of calculations correctly reflect the main tendency of overpopulating of the low levels (v<15) by the electrons and depopulating of the high levels. The qualitative explanation of this effect, previously given in [4], is that in the steady-state for the vibrational levels with the "local" vibrational temperature higher than T_e,

$$T_{vib}(v) = -\frac{\partial E_v}{\partial \ln f_v} > T_e \ , \qquad (9)$$

the process of vibrational energy transfer to the electrons is more probable that the reverse one. Obviously, the condition (9) is satisfied for the high vibrational levels in the plateau region of the VDF (see Fig. 3, the left-hand-side of Eq. (9) is just a reciprocal slope of the VDF). For the low levels, where the "local" vibrational temperature is close to the first level temperature, $T_{vib}(v) < T_e$, and the opposite is true, so that electrons supply energy to the vibrational mode.

Figures 4,5 show that the observed effect is proportional to the electron concentration, and the value $n_e=2\cdot10^{11}$ cm^{-3} gives the best agreement with experiment. This value is consistent with the electron number density inferred from the optical pumping experiment [4], and confirms that vibrationally-stimulated ionization is capable of producing rather large steady-state electron concentrations, with ionization fractions up to $n_e/n=10^{-7}$. This number is comparable with the ionization fraction of the glow discharge. From Fig. 5 one can see that the vibrational population ratio at the high vibrational levels is reproduced rather poorly, the results being quite close for both sets of cross-section used. This demonstrates inaccuracy of both approaches of the cross-section calculations at the high vibrational levels. Therefore incorporation of more advanced cross-section model , e.g. [14], should be considered.

Figure 6 compares the "no field" EEDF ($n_e=2\cdot10^{11}$ cm^{-3}) with the one at the saturation conditions ($n_e=4\cdot10^{8}$ cm^{-3}), when the electrons obtain most of their energy from the applied field. The applied voltage results in the dramatic increase of the number of high-energy electrons ($T_e\cong3.5$ eV), so that the calculated electron impact ionization rate becomes rather high, $k_{imp.ion.}\cong2\cdot10^{-13}$ cm^3/s. At these conditions, impact ionization frequency sharply rises and may become comparable with that of the vibrationally simulated ionization (2), $k_{imp.ion}\cdot n\cdot n_e/q_{ion}\sim0.2$-0.3, despite the very low ionization fraction. In a CO/Ar=3%/97% mixture, impact ionization resulted in a breakdown in the cell at $U\cong U_s$ [4].

4. Summary.

Interaction of highly vibrationally excited CO molecules with the low-energy electrons is studied using kinetic modeling. Comparison with experimental measurements in optically pumped CO [4] explains the observed effect of vibrational energy transfer by electrons from the high toward the low vibrational levels. The best agreement is obtained for the electron concentration in the cell $n_e=2\cdot10^{11}$ cm^{-3}, which is consistent with the previous measurements of the vibrationally stimulated ionization rate [4].

Reasonable agreement between the experimental data and the results of kinetic modeling calculations provides better insight into kinetics of energy exchange between vibrationally excited molecules and electrons. The present model might also be useful in studying $CO(a^3\Pi)$ kinetics. As a matter of fact, $CO(a^3\Pi)$ together with $CO(X^1\Sigma, v)$ has been considered as possible precursor of ionization [15]. Also, recent experiments on $CO(a^3\Pi)$ formation in the optically pumped cell [13] suggest that the V-E transition

$$CO(X^1\Sigma, v \cong 25) + CO \rightarrow CO(a^3\Pi, v \cong 0) + CO \qquad (10)$$

may require presence of some low-energy electrons, presumably incapable of direct impact excitation of the $a^3\Pi$ state. Therefore, it is conceivable that processes (1), (2), and (10) are closely related. For example, CO^- ion formation in vibrational excitation process (1), with electrons produced in the vibrationally-stimulated ionization (2), might be an intermediate stage for process (10).

The experimental setup, previously used in the optical pumping experiments [4,7] has a capability of creating strongly nonequilibrium, fully controlled environment, where vibrational temperature and electron concentration can be independently varied. Further time-resolved experiments using step-scan FT IR/Visible/UV spectrometer are expected to yield additional kinetic rate data, including vibrational excitation cross-sections (1) for the high vibrational levels, state-resolved rates of ionization (2), and $CO(a^3\Pi)$ production (10).

References

1. N.L. Aleksandrov, A.M. Konchakov, and E.E. Son, Sov. Journal of Plasma Physics, vol. 4, p. 663, 1978
2. N.L. Aleksandrov, A.M. Konchakov, and E.E. Son, Sov. Physics - Technical Physics, vol. 24, p. 664, 1979
3. N.A. Dyatko, I.V. Kochetov, and A.P. Napartovich, J. Physics D: Applied Physics, vol. 26, p. 418, 1991
4. I. Adamovich, S. Saupe, M.J. Grassi, O. Shulz, S. Macheret, and J.W. Rich, Chemical Physics, vol. 173, p. 491, 1993
5. C.E. Treanor, J.W. Rich, and R.G. Rehm, Journal of Chemical Physics, vol. 48, p. 1798, 1968
6. J.J. Thomson and G.P. Thomson, Conduction of Electricity through Gases, vol. 1, Cambridge Univ. Press, Cambridge, 1928
7. C. Flament, T. George, K.A. Meister, J.C. Tufts, J.W. Rich, V.V. Subramaniam, J.-P. Martin, B. Piar, and M.-Y. Perrin, Chemical Physics, vol. 163, p. 241, 1992
8. A. Chiroux de Roany, C. Flament, J.W. Rich, V.V. Subramaniam, and W.R. Warren, AIAA Journal, vol. 31, p. 119, 1993
9. Y. Itikawa, Atomic Data and Nuclear Data Tables, vol. 21, p. 69, 1978
10. J.C.Y. Chen, Journal of Chemical Physics, vol. 40, p. 3513, 1964
11. I.V. Adamovich, S.O. Macheret, and J.W. Rich, Chemical Physics, vol. 182, p.167, 1994
12. N.A. Gorbunov, N.A. Khromov, N.V. Kollokolov et al., Abstracts of Invited Talks and Contributed Papers, 10th ESCAMPIG (Orleans), vol. 14E, p. 159, 1990
13. O. Shulz, J.X. Lin, W. Urban, Ber. Bunsenges. Phys. Chem., vol. 99, p. 348, 1995
14. M. Zubek, C. Szmytkowski, Journal of Physics B, vol. 10, p. L27, 1977
15. G.M. Grigor'yan, Y.Z. Ionikh, I.V. Kochetov, and V.G. Pevgov, Journal of Physics D, vol. 25, p. 1064, 1992

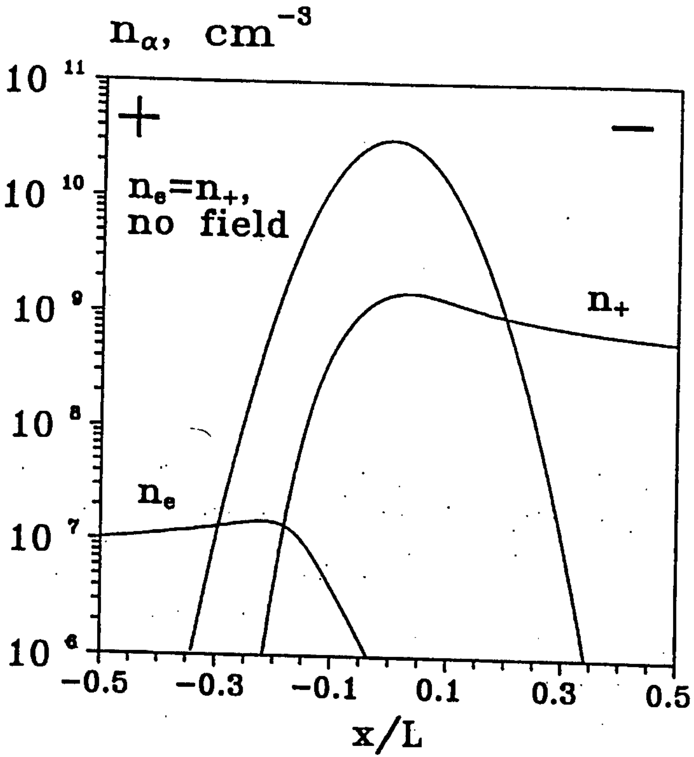

Figure 1. Theoretical electron and ion concentration distributions in Thomson discharge between two plane electrodes in a saturation regime [4]. External ionization occurs in a narrow region midway between the electrodes. Gaussian curve $n_e=n_+$ shows the distributions with no field applied.

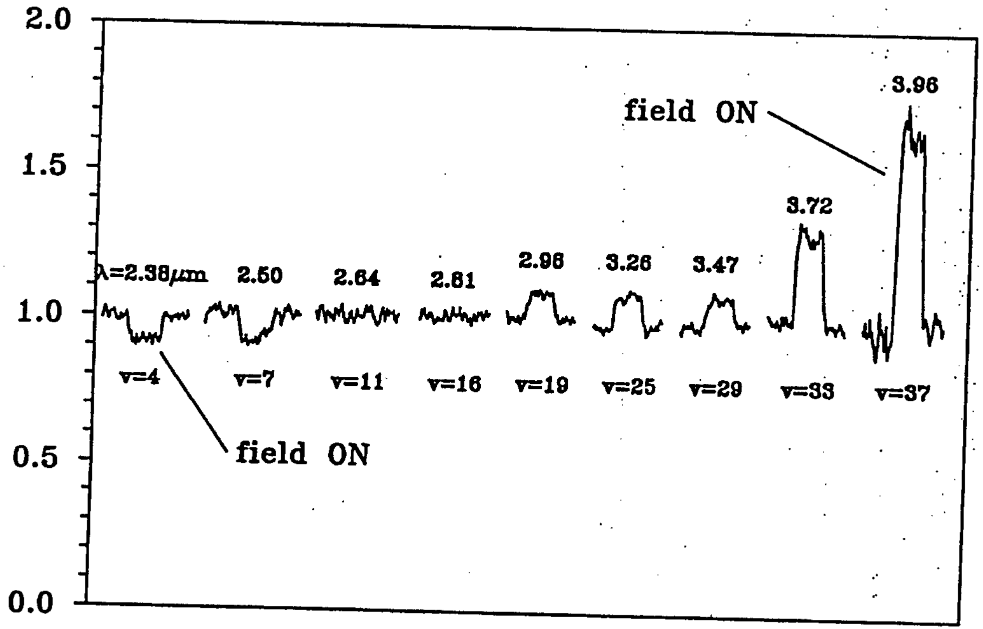

Figure 2. The effect of electron removal by means of Thomson discharge on the CO vibrational level populations [4]. "Field ON" means "no electrons" (see also Fig. 1).

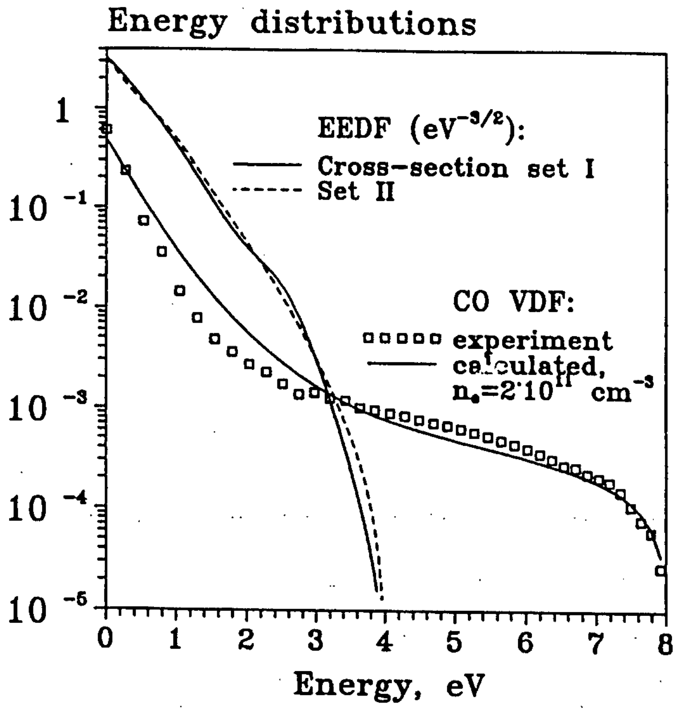

Figure 3. Experimental [4] and calculated CO VDF. Calculated EEDF for two inelastic cross-section sets. CO:Ar=3:97, P=100 torr, T=700 K, T_V=4100 K, T_e=5200 K, n_e=$2\cdot10^{11}$ cm^{-3}, no external electric field applied.

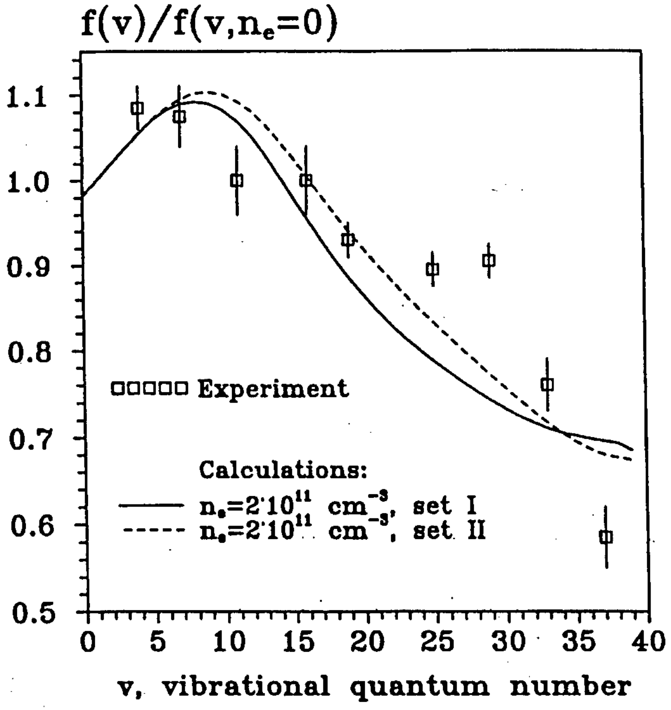

Figure 4. Experimental and calculated ratio of CO vibrational level populations with the electrons present (no field applied) and without electrons (saturation voltage applied) for two inelastic cross-section sets used. CO:Ar=3:97, P=100 torr, T=700 K.

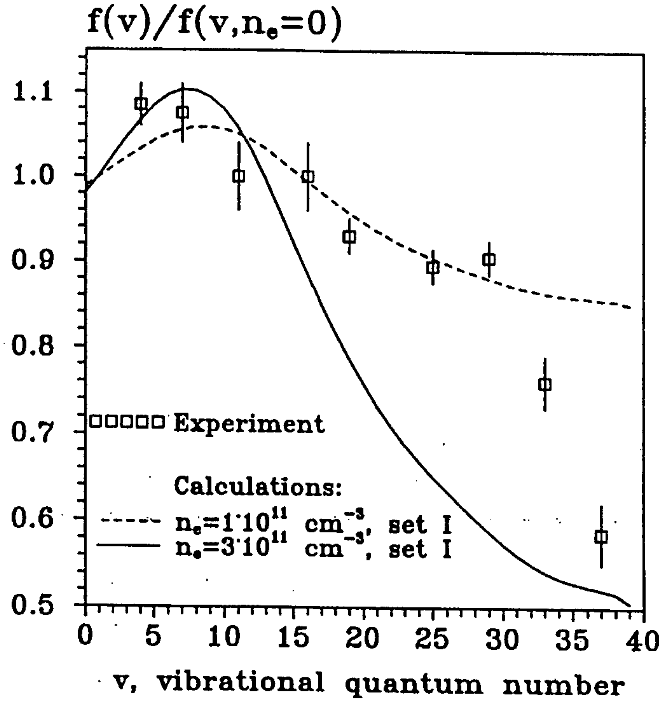

Figure 5. Experimental and calculated ratio of CO vibrational level populations with the electron present (no field applied) and without electrons (saturation voltage applied) for different electron concentrations. CO:Ar=3:97, P=100 torr, T=700 K.

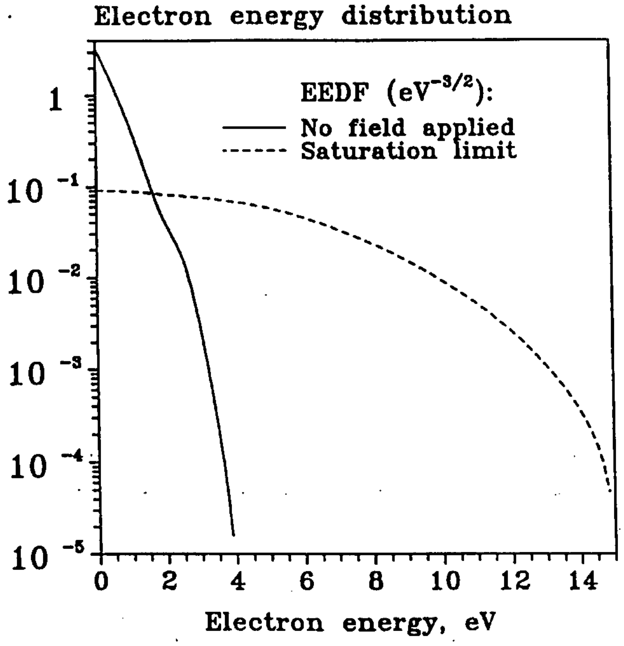

Figure 6. EEDF with no field applied ($n_e=2\cdot10^{11}$ cm^{-3}, T_e=5200 K) and in the saturation limit ($n_e=4\cdot10^{8}$ cm^{-3}, T_e=3.5 eV). CO:Ar=3:97, P=100 torr, T=700 K.

CHAPTER VIII.

IONIZATION MEASUREMENTS IN OPTICALLY PUMPED DISCHARGES

1. Introduction

Nonequilibrium optically pumped environments can be produced by resonance absorption of infrared laser radiation by molecules in the low vibrational quantum states, with subsequent vibration-to-vibration (V-V) pumping up to high vibrational levels [1],

$$\mathrm{AB(v) + AB(w) \rightarrow AB(v-1) + AB(w+1)} \tag{1}$$

In Eq. (1), AB stands for a diatomic molecule, and v and w are vibrational quantum numbers. This approach allows sustaining strong vibrational disequilibrium at high densities and a low power budget. Optical pumping by a CO laser has been previously achieved in gas phase carbon monoxide [2-7] at pressures of up to 20 atm [2], gas phase nitric oxide [8-9], liquid phase CO [10,11], and solid CO and NO matrices [12,13]. Recently, optical pumping has also been demonstrated in infrared inactive gases, such as nitrogen and air, at atmospheric pressure [14]. In this case, N_2 and O_2 molecules become vibrationally excited by near-resonance V-V energy transfer from CO,

$$\mathrm{CO(v) + N_2(w) \rightarrow CO(v-1) + N_2(w+1)} \tag{2}$$

$$\mathrm{CO(v) + O_2(w) \rightarrow CO(v-1) + O_2(w+1)} \tag{3}$$

In the experiments of Refs. [2-14], the CO laser power was fairly low, ranging from a few Watts to 200 W c.w.

Ionization in optically pumped gases is produced by an associative ionization mechanism, in collisions of two highly vibrationally excited molecules when the sum of their vibrational energies exceeds the ionization potential [15,6,16],

$$\begin{gathered}\mathrm{AB(v) + AB(w) \rightarrow (AB)_2^+ + e^-}\ ,\\ E_v + E_w > E_{ion}\end{gathered} \tag{4}$$

Ionization of carbon monoxide by this mechanism has been previously observed in CO-Ar gas mixtures optically pumped by resonance absorption of CO laser radiation [6,16]. The estimated steady-state electron density sustained by a 10 W CO laser in optically pumped CO/Ar/He plasmas with the high vibrational level populations of $n_{CO}(v{\sim}30){\sim}10^{15}$ cm^{-3} is $n_e{\sim}10^{10}$-10^{11} cm^{-3} [16].

It is remarkable that ionization mechanism of Eq. (4) appears to be unconditionally stable with respect to the heating instability [17]. In high-pressure electric discharge plasmas, this instability is produced by the positive feedback between the gas heating and the electron impact ionization rate. Therefore small electron density perturbations, producing excess Joule heat, result in a more rapid electron production and eventually lead to runaway ionization. Indeed, in optically pumped plasmas both the upper level populations and the electron production rate sharply drop with temperature because of the exponential rise of the vibration-translation (V-T) relaxation rates [18]. This creates a negative feedback between the gas heating and the ionization rate, which precludes the instability development. This effect shows a possibility of sustaining unconditionally stable, strongly nonequilibrium optically pumped plasmas in high-pressure environments. Such plasmas would have a decisive advantage over electric discharge sustained plasmas, which are difficult to control at high pressures. These plasmas would find numerous applications in high-yield mode-selective chemical synthesis and high-speed aerodynamics. In particular, recent results on anomalous shock wave propagation in nonequilibrium gas discharges (see [19,20] and references therein) suggest the possibility of wave drag reduction and supersonic flow control by plasmas. This provides a strong motivation for exploring the approaches to sustain stable optically pumped plasmas in atmospheric-pressure air.

The present work represents a first effort to study the effect of adding air species to optically pumped CO/Ar plasmas on the electron production and removal kinetics. The main objective is to investigate the role of additives, such as N_2, O_2, and NO, in the associative ionization process of Eq. (4) and to explore the effect of such additives on the electron removal rate in the plasma.

2. Experimental

To address the issues discussed in Section 1, ionization measurements using non-self-sustained DC and RF discharges have been conducted in optically pumped plasmas sustained by a CO laser. The use of the non-self-sustained discharges precludes electron impact ionization and thereby allows identification of the associative ionization mechanism of Eq. (4) [6,16].

The schematic of the experimental setup is shown in Fig. 1. A carbon monoxide laser is used to irradiate a gas mixture of CO and Ar, with additives such as N_2, NO, O_2, or air, which is slowly flowing through the pyrex glass optical absorption cell shown. The residence time of the gas mixture in the cell is about 1 sec. The liquid nitrogen cooled CO laser was designed in collaboration with the University of Bonn and fabricated at Ohio State. It produces a substantial fraction of its power output on the $v = 1 \rightarrow 0$ fundamental band component in the infrared. The laser can operate at more than 100 W continuous wave (c.w.) power. However, in the present experiment, the laser is typically operated at 20 W c.w. broadband power on the lowest ten vibrational bands, with up to ~0.3 W on the $v = 1 \rightarrow 0$ component. The output on the lowest bands ($1 \rightarrow 0$ and $2 \rightarrow 1$) is necessary to begin the absorption process in cold CO (initially at 300 K) in the cell. The Gaussian laser beam of ~6 mm diameter can be focused to a focal area of ~1 mm diameter to increase the power loading per CO molecule, providing an excitation region in the cell of ~2 mm diameter. The absorbed laser power is typically 5-6 W over the absorption length of 12.5 cm, which gives an absorbed power density of 10 W/cm^3 for the focused laser beam.

The lower vibrational states of CO, $v \leq 10$, are populated by direct resonance absorption of the pump radiation in combination with rapid redistribution of population by the V-V exchange processes. The V-V processes then continue to populate the higher vibrational levels above $v=10$, which are not directly coupled to the laser radiation (see Eq. (1)). The large heat capacity of the Ar diluent, as well as conductive and convective cooling of the gas flow, allow us to control the translational/rotational mode temperature in the cell. In steady-state conditions, when the average vibrational mode energy of the CO would correspond to a few thousand degrees Kelvin, the temperature never rises above a few hundred degrees. Thus a strong disequipartition of energy can be maintained in the cell, characterized by very high vibrational mode energy and a low translational/rotational mode temperature. As shown in Fig. 1, the population of the vibrational states of the CO in the cell is monitored by infrared emission spectroscopy. For this purpose, a Bruker Fourier transform IFS 66 spectrometer is used to record the spontaneous emission from the CO fundamental, first and second overtone bands through a window on the side of the cell.

Two 3 cm diameter brass plate electrodes are placed in the cell as shown in Fig. 2, so that the laser beam creates a cylindrical excited region between the electrodes. The probe electrodes, which are typically 8 to 12 mm apart, can be connected to a DC or to an RF power supply. A reversible polarity DC power supply (Thorn EMI GENCOM Inc., Model 3000R) produced voltage that could be varied between 0-3000 V. The current was measured with a Keithley 2001 multimeter, with a 1 MΩ resistor connected in series with the cell to protect the multimeter in case of breakdown. The RF voltage at a frequency of ν=10 MHz was produced by an HP function generator used as power supply without further amplification. Ionization of CO molecules in the cell occurs by an associative ionization mechanism (4). In both DC and RF experiments, the reduced electric field E/N was deliberately kept low to preclude electron impact ionization.

The electron production rate per unit volume of the plasma is determined from the saturation current of the DC Thomson discharge between the electrodes [6,16],

$$S \cong \frac{I_s}{e\pi d^2 D/4}, \tag{5}$$

where $d \cong 1.0$ and 0.2 cm are the diameters of the excited regions created by the unfocused and the focused beams, respectively, $D=3$ cm is the electrode diameter, and $\pi d^2 D/4$ is the volume of the excited region. The excited region diameter was estimated from the diameter of the visible blue glow of the C_2 Swan band radiation, strongly coupled with high vibrational levels of CO [6].

The electron density was inferred from the RF conduction current between the electrodes, I_C, and the applied RF voltage, U [21],

$$n_e \cong \frac{I_C}{e\mu_e U d}, \tag{6}$$

The conduction current was evaluated by measuring the voltage drops on a resistor R=50 Ohm connected in series with the discharge gap with the laser turned on and off, $U_{R,on}$ and $U_{R,off}$, using a 100 MHz HP54600B oscilloscope, $I_C=(U_{R,on}-U_{R,off})/R$. Note that Eqs. (5,6) are approximate since they do not account for the electrode edge effects, as well as the voltage drops across the sheaths in the RF discharge. Therefore they somewhat underestimate both the electron production rate and the electron density.

3. Results and Discussion

3.1. DC Thomson discharge measurements

Figure 3 shows vibrational population distribution functions (VDF) of carbon monoxide inferred from high-resolution (0.25 cm^{-1}) CO infrared emission spectra recorded by the FT spectrometer. Vibrational level populations are inferred from the spectra using a standard technique [22]. These measurements are made in a CO/Ar mixture at a total pressure of P=100 Torr, at different CO partial pressures in the cell. The translational/rotational temperatures at these conditions, inferred from the rotationally resolved R-branch of the $1\rightarrow0$ CO fundamental band with an accuracy of ±10 K, are also shown in Fig. 3. The distributions shown in these figures are the well-known "V-V pumped" distributions [23,24], maintained by the rapid redistribution of vibrational energy by the V-V processes, which pump energy into the higher vibrational levels. They are obviously extremely non-Boltzmann, and characterized by high population of the upper vibrational levels. Note that as the CO partial pressure increases, the high vibrational level populations v~35-40 drop, both because of the lower energy loading per CO molecule and because of the translational temperature rise.

Typical current voltage characteristics of the DC discharge, sustained by the unfocused and focused 10 W CO laser beams in a CO/Ar=3/100 mixture at P=100 Torr, are shown in Fig. 4. One can see that the discharge current reaches saturation at $U_s\cong300$ V, $I_s\cong2.5$ μA, when the laser is unfocused, and $U_s\cong600$ V, $I_s\cong7.0$ μA, when the laser is focused. In the saturation regime, the current continues to rise with the applied voltage because of the finite size of the electrodes that draw current from an increasingly larger region. As can also be seen from Fig. 4, at $U\cong1400$-1600 V, electron impact ionization starts contributing to the discharge current, which increases by about an order of magnitude, up to $I\cong100$ μA. In this region, the discharge is still non-self-sustained and extinguishes after the laser is turned off. Finally, at U≅2500-2700 V, breakdown occurs and the discharge collapses into an arc with a current of up to I~100-1000 μA. When the laser is off, breakdown and arcing also occur at U≅2500 V. Using I_s=2.5 μA and 7.0 μA for the two cases shown in Fig. 4, determined at the beginning of the saturation region, we obtain $S=8.0\cdot10^{12}$ 1/cm^3/s and $5.6\cdot10^{14}$ 1/cm^3/s for the unfocused and the focused laser beam, respectively.

Figure 5 shows current-voltage characteristics of the Thomson discharge measured in CO/Ar, CO/Ar/O_2, and CO/N_2 mixtures at P=100 torr and with a higher laser power of 20 W. One can see that both adding oxygen and replacing Ar with N_2 reduces the electron production rate, from $S=9.7\cdot10^{14}$ 1/cm^3/s (I_s=12 μA) in CO/Ar, to $S=5.2\cdot10^{14}$ and $2.0\cdot10^{14}$ 1/cm^3/s (I_s=6.5 and 2.5 μA) in CO/Ar/O_2, and $S=1.6\cdot10^{14}$ 1/cm^3/s (I_s=2.0 μA) in CO/N_2. The reduction of the ionization rate correlates with depletion of high vibrational level populations of CO by V-V energy transfer to N_2 and O_2 (see Fig. 6, 7), similar to what has been previously observed in CO/Ar/He mixtures [6]. Note that the inferred electron production rates S in CO/Ar/O_2=2/100/0.5 and in CO/N_2=2/100 are about the same, while the CO level populations in the presence of oxygen are much more strongly depleted (see Figs. 6, 7). This suggests that O_2 molecules, vibrationally excited by V-V energy transfer between CO and O_2 (3) may also contribute to associative ionization of Eq. (4). This is consistent with recent Raman spectroscopy measurements of the N_2 and O_2 vibrational populations in optically pumped CO/N_2/O_2 mixtures [14]. They show that although all three diatomic species (CO, N_2, and O_2) are at strong vibrational disequilibrium, the vibrational temperatures of CO and O_2 substantially exceed that of N_2.

Figure 8, which shows DC discharge saturation currents in CO/Ar/air and in CO/Ar/O_2 mixtures at P=100 torr, demonstrates that the current is primarily controlled by the oxygen content in the plasma. A similar plot for CO/Ar/NO mixtures at P=50 torr (see Fig. 9) actually shows an increase of the saturation current (i.e. increase of the electron production rate) at low NO concentrations, from I_s=23 μA ($S=1.8\cdot10^{15}$ 1/cm^3/s) without NO to a maximum I_s=44 μA ($S=3.4\cdot10^{15}$ 1/cm^3/s) at P_{NO}=0.2 torr. This occurs even though the high vibrational levels of CO are strongly depleted by nitric oxide (see Fig. 10). This unambiguously shows that NO molecules, which may also become vibrationally excited by V-V energy transfer between CO and NO,

$$CO(v) + NO(w) \rightarrow CO(v-1) + NO(w+1) \ , \tag{7}$$

play an important role in associative ionization kinetics.

Finally, from Figs. 8, 9 it is seen that small admixtures of O_2 and NO (less than 0.1 torr) result in a fairly weak change of the net electron production rate, within 50% from the baseline value measured without additives. The measured rate of electron production in CO/Ar at P=20-100 torr, $S=9.7\cdot10^{14}$ - $1.8\cdot10^{15}$ $1/cm^3/s$ is consistent with the ionization rate coefficient $k_{ion}=(1.1\text{-}1.8)\cdot10^{-13}$ cm^3/s, where k_{ion} is defined as

$$k_{ion} = \frac{S}{n_{CO}^2 \sum\limits_{E_v+E_w>E_{ion}} f_v f_v} \tag{8}$$

In Eq. (8), f_v and f_w are relative populations of the CO vibrational levels, inferred from the infrared spectra and plotted in Figs. 6,7,10. This value of k_{ion} exceeds the result of our previous study, $k_{ion}=2.5\cdot10^{-14}$ cm^3/s [16], by almost an order of magnitude. However, the present measurements of the CO vibrational level populations from the high-resolution CO FT spectra are far more accurate than the previous results [6] obtained using a low-resolution monochromator, and we recommend the new value of k_{ion} as more reliable.

In these experiments, it has been observed that when a DC voltage is applied to the electrodes, a dark deposit rapidly (within a few minutes) accumulates on the negative electrode in CO/Ar plasmas. The deposit quickly disappears when O_2 or NO are added to the cell gases. The deposit has the shape of a shadow image of the vibrationally excited region between the plates (see Fig. 11). No corresponding deposit is formed on the positive electrode, and there is only a small deposition anywhere in the cell except on the negatively biased electrode, even after several hours of operation. We conclude that the deposit is formed by positive ions moving toward the negative electrode in the electric field. The average positive ion mass was determined from the difference in the electrode weight before and after the experiment, $m=\Delta M/t/(I/e)\cong250$ amu [25]. These results indicate the presence of large ion clusters in the CO/Ar plasma, which are apparently destroyed by adding small amounts of O_2 and NO. Such clusters, having the general form $(CO)_2C_n$, n=1-15, have been previously observed in glow discharges in CO/Ar and CO/He mixtures [26]. In addition, a mass spectrum of the electrode deposit shows a number of peaks above 100 amu [25] (see Fig. 12). Odd peak numbers are most likely due to hydrogen (water vapor) impurities in the cell.

3.2. RF discharge measurements

In this series of measurements, a weak RF field with an RMS voltage $\langle U\rangle=3.5$ V at a frequency of $\nu=10$ MHz, produced by a function generator, was applied to the cell electrodes. The RF discharge RMS conduction current did not exceed $\langle I_C\rangle=500$ μA. Therefore, the maximum power coupled to the plasma by the RF field, $\langle U\rangle\langle I_C\rangle<2$ mW, was much smaller then the absorbed laser power, ~5W. This makes additional vibrational excitation by the RF field, with subsequent ionization by associative mechanism of Eq. (4), negligible. Figures 13, 14 show the RF discharge conduction current, $\langle I_C\rangle$, measured in the optically pumped $CO/Ar/O_2$ plasmas excited by a focused CO laser at the total pressure in the cell of P=100 torr and 20 torr, respectively.

At P=100 torr, in CO/Ar plasma with no oxygen additive no conduction current has been detected within the accuracy of the present experiment (see Fig. 13). The same result was obtained in a CO/N_2 plasma without oxygen added. We estimate a minimum detectable conduction current, $\langle I_C\rangle\sim\langle U_{R,on}-U_{R,off}\rangle/R$, to be about 1% of the displacement current $\langle I_D\rangle=\langle U_{R,off}\rangle/R=190$ μA, or $\langle I_C\rangle\sim2$ μA. From this, using Eq. (6), one obtains an upper bound of electron density at these conditions, $n_e<4\cdot10^9$ cm^{-3}. Adding small amounts of dry or room air to the CO/Ar mixture resulted in a dramatic conduction current rise up to $\langle I_C\rangle=110$ μA with 0.2 torr of dry air in the cell (see Fig. 13). This indicates the electron density increase by at least a factor of 50 compared with both CO/N_2 and CO/Ar plasmas without oxygen additive, up to $n_e=2\cdot10^{11}$ cm^{-3}. The results at P=20 torr are quite similar (see Fig. 14). The conduction current in CO/Ar and CO/N_2 mixtures is $\langle I_C\rangle=12\text{-}17$ μA, which gives an electron density of $n_e=(5\text{-}7)\cdot10^9$ cm^{-3}. However, with 0.2-0.5 torr of air or 0.1 torr of O_2 added to the CO/Ar mixture the conduction current increases by about a factor of 15, up to $\langle I_C\rangle=215$ μA, which gives an electron density of $n_e=0.9\cdot10^{11}$ cm^{-3}. We emphasize that the observed sharp electron density increase occurs despite the fact that the electron production rate S in $CO/Ar/O_2$ mixtures actually somewhat drops with the O_2 partial pressure (see Fig. 8). Since small admixtures of oxygen are unlikely to produce a noticeable change in electron mobility, this can only mean that the electron removal rate significantly decreases in the presence of small amounts of oxygen.

This result suggests a possible qualitative scenario of the apparent electron removal rate reduction in optically pumped CO/Ar/O_2 and CO/Ar/N_2 plasmas. Indeed, the deposit formation on the negative electrode due to the heavy ion current in the CO/Ar plasma without additives, and its absence in the plasmas doped with O_2 (see Section 3.1) indicate that the dominant positive ions in these two cases are quite different. Dimer ions, such as $(CO)_2^+$, are known to have a very high dissociative recombination rate, $\beta \sim 10^{-6}$ cm^3/s [21]. Presumably, the recombination rate for the heavy cluster ions, such as $(CO)_2C_n^+$, which are likely to be the dominant ions in the CO/Ar plasma without additives [26], might well be even higher. On the other hand, adding small amounts (tens of microtorr) of O_2 to a glow discharge CO/Ar plasma results in destruction of cluster ions and their replacement by monomer ions such as O_2^+ and CO^+ [26], which have a much slower recombination rates, $\beta \sim 10^{-6}$ cm^3/s [17]. However, this interpretation leaves open the question what role electron attachment to oxygen plays in these strongly nonequilibrium plasmas. Indeed, one would expect the electron density to be reduced in the presence of a strongly electronegative gas such as oxygen, while the present experiments demonstrate exactly the opposite behavior. Further studies of ion composition of optically pumped plasmas using ion mass-spectrometry, such as has been previously done in CO/Ar and CO/He glow discharges [26] are expected to provide new insight into this problem.

4. Summary

Kinetics of ionization and electron removal in optically pumped nonequilibrium plasmas sustained by a CO laser is studied using non-self-sustained DC and RF electric discharges. Experiments in optically pumped CO/Ar/N_2 mixtures doped with O_2 and NO demonstrated that associative ionization of CO by mechanism (4) generates free electrons at a rate up to $S=10^{15}$ 1/cm^3/s. The ionization rate coefficient, inferred from the CO vibrational populations measurements, is $k_{ion}=(1.1\text{-}1.8)\cdot 10^{-13}$ cm^3/s. It is shown that excited NO and possibly O_2 molecules also contribute to the vibrationally stimulated ionization process. In CO/Ar plasmas, applying a DC bias to the cell electrodes resulted in rapid accumulation of a deposit on the negative electrode due to a large cluster ion current. The average mass of an ion in this plasma, estimated by measuring the mass of the deposit, is m≅250 a.m.u., which is consistent with the mass-spectrometer analysis of the deposit. The deposit did not accumulate when small amounts of O_2 and NO were added to the CO/Ar plasma, which presumably indicates destruction of the cluster ions.

It is demonstrated that adding small amounts of O_2 to the optically pumped CO/Ar plasmas significantly increases the electron density, from $n_e=(4\text{-}7)\cdot10^9$ cm^{-3} to $n_e=(1\text{-}2)\cdot10^{11}$ cm^{-3}. This effect occurs at a nearly constant (within 50%) electron production rate, indicating substantial reduction in the overall electron removal rate. This reduction can be qualitatively interpreted as destruction of rapidly recombining cluster ions in the presence of the O_2 additive, and their replacement by monomer ions with a slower recombination rate. Further studies of ion composition in optically pumped plasmas are suggested.

References

1. C.E. Treanor, J.W. Rich, and R.G. Rehm, J. Chem. Phys., Vol. 48, 1968, p. 1798
2. J.W. Rich, R.C. Bergman, and M.J. Williams, Measurement of Kinetic Rates for Carbon Monoxide Laser Systems, Final Contract report AFOSR F49620-77-C-0020 (November 1979)
3. J.W. Rich and R.C. Bergman, Chem. Phys., Vol. 44, 1979, p. 53
4. R.L. DeLeon and J.W. Rich, Chem. Phys., vol. 107, 1986, p. 283
5. C. Flament, T. George, K.A. Meister, J.C. Tufts, J.W. Rich, V.V. Subramaniam, J.-P. Martin, B. Piar, and M.-Y. Perrin, Chem. Phys., vol. 163, 1992, p. 241
6. I. Adamovich, S. Saupe, M.J. Grassi, O. Schulz, S. Macheret, and J.W. Rich, Chem. Phys., vol. 173, 1993, p. 491
7. H.L. Wallaart, B. Piar, M.Y. Perrin, and J.P. Martin, Chem. Phys., Vol. 196, 1995, p. 149
8. H. Dünnwald, E. Siegel, W. Urban, J.W. Rich, G.F. Homicz, and M.J. Williams, Chem. Phys., Vol. 94, 1985, p. 195
9. S. Saupe, I. Adamovich, M.J. Grassi, and J.W. Rich, Chem. Phys., vol. 174, 1993, p. 219
10. D.S. Anex and G.E. Ewing, J. Phys. Chem., Vol. 90, p. 1604, 1986
11. R.S. Disselkamp and G.E. Ewing, J. Phys. Chem., Vol. 93, p. 6334, 1989
12. J.P. Galaup, J.Y. Harbec, R. Charneau, and H. Dubost, Chem. Phys. Lett., Vol. 120, 1985, p. 188
13. I. Hadj Bachir, R. Charneau, and H. Dubost, Chem. Phys., Vol. 177, 1993, p. 675
14. W. Lee, M. Chidley, R. Leiweke, I. Adamovich, and W.R. Lempert, "Determination of O_2 and N_2 Vibrational State Distributions in CO Laser-Sustained Plasmas", AIAA Paper 99-3723, AIAA 30th Plasmadynamics and Lasers Conference, Norfolk, VA, June 28 – July 1, 1999
15. L.S. Polak, P.A. Sergeev, and D.I. Slovetskii, Sov. High Temperature Physics, Vol. 15, 1977, p. 15
16. I.V. Adamovich and J.W. Rich, J. Physics D: Applied Physics, vol. 30, 1997, p. 1741
17. Raizer, Y.P., "Gas Discharge Physics", Springer-Verlag, Berlin, 1991
18. Billing, G.D., "Vibration-Vibration and Vibration-Translation Energy Transfer, Including Multiquantum Transitions in Atom-Diatom and Diatom-Diatom Collisions", Nonequilibrium Vibrational Kinetics, Springer-Verlag, Berlin, 1986, Chap. 4, pp. 85-111

19. Ganguly, B. N. , Bletzinger, P. and Garscadden, A., Physics Letters, Vol. 230, p. 218, 1997
20. H. Lowry, J. Blanks, C. Stepanek, M. Smith, L. Crosswy, P. Sherrouse, J. Felderman, and B. Wood, "Shock Structure of a Spherical Projectile in Weakly Ionized Air", AIAA Paper 99-0600, 37th Aerospace Sciences Meeting and Exhibit, Reno, NV, Jan. 11-14, 1999
21. R. Johnsen, "Recombination of Cluster Ions", in B.R. Rowe et al. (eds.), "Dissociative Recombination", Plenum, New York, 1993
22. K.P. Horn and P.E. Oettinger, J. Chem. Phys., vol. 54, 1971, p. 304
23. J. W. Rich, "Relaxation of Molecules Exchanging Vibrational Energy", in "Applied Atomic Collision Physics", vol. 3, "Gas Lasers", ed. E.W. McDaniel and W.L. Nighan, Academic Press, New York, 1982, pp. 99-140
24. B.F. Gordiets, V.A. Osipov, and L.A. Shelepin, "Kinetic Processes in Gases and Molecular Lasers", Gordon and Breach, London, 1988
25. E. Plönjes, I.V. Adamovich, V.V. Subramaniam, and J.W. Rich, "Isotope Separation in Optically Pumped Thomson Discharges", AIAA Paper 98-0993, 36th Aerospace Sciences Meeting & Exhibit, Reno, NV, January 12-15, 1998
26. Y. Kaufman, P. Avivi, F.Dothan, H. Keren, J. Malinowitz, J. Chem. Phys., Vol. 72, 1980, p. 2606

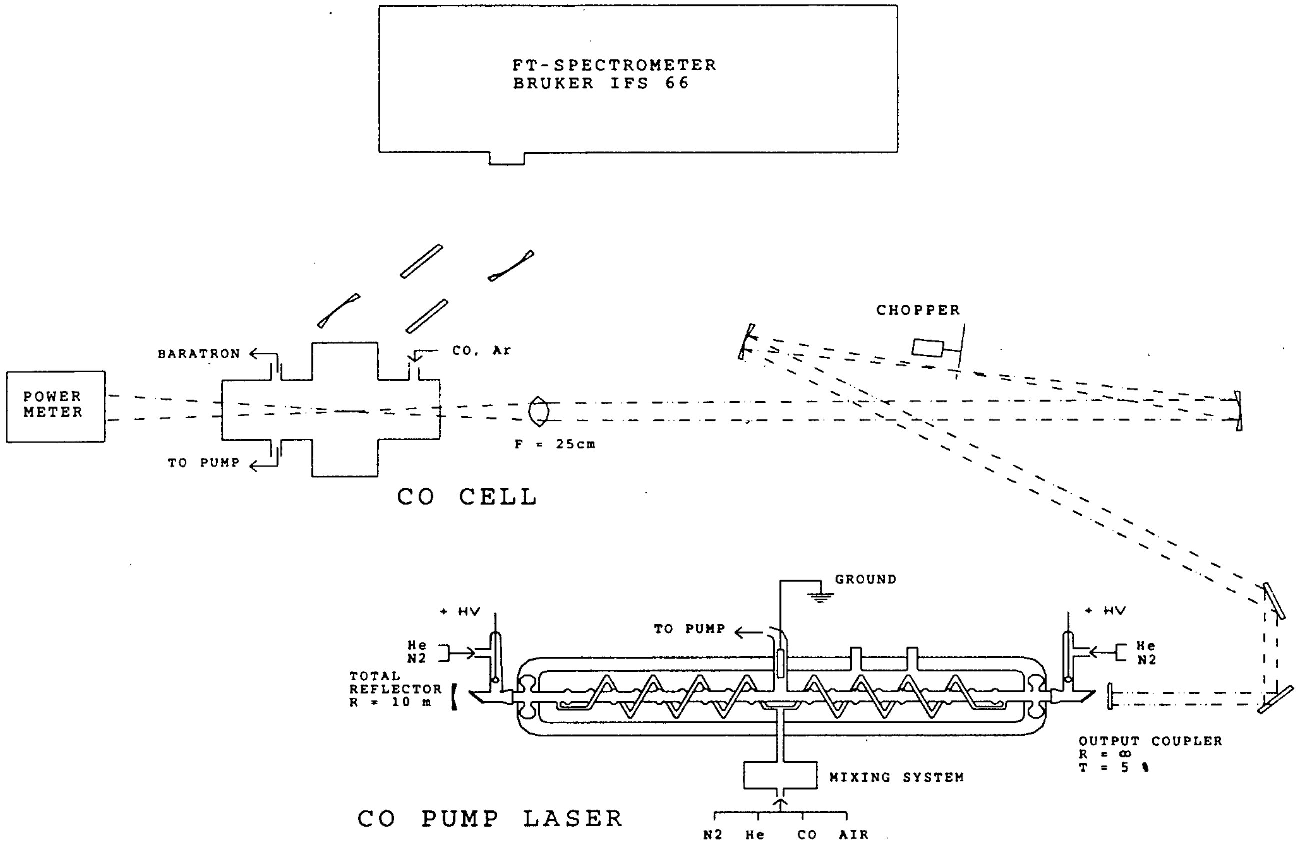
FT-SPECTROMETER
BRUKER IFS 66
CHOPPER
BARATRON
CO, Ar
POWER METER
F = 25cm
TO PUMP
CO CELL
GROUND
+ HV
TO PUMP
+ HV
He
N2
He
N2
TOTAL REFLECTOR
R = 10 m
OUTPUT COUPLER
R = ∞
T = 5 %
MIXING SYSTEM
CO PUMP LASER
N2
He
CO
AIR

Figure 1. Schematic of the experimental setup

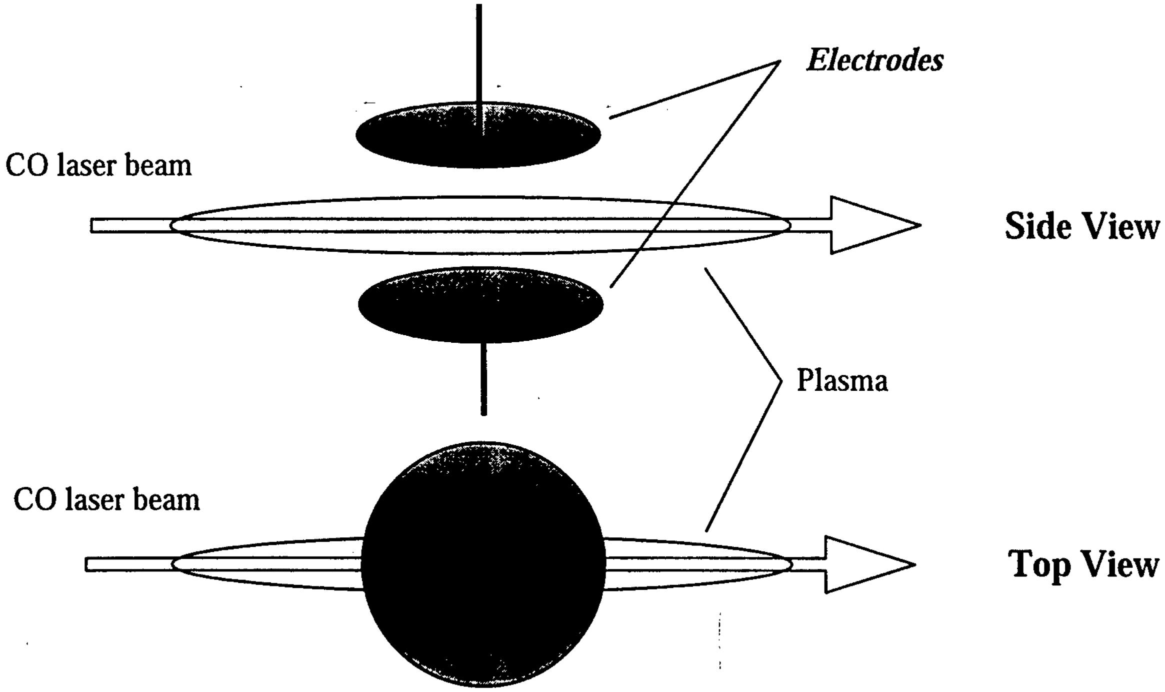
Electrodes
CO laser beam
Side View
Plasma
CO laser beam
Top View

Figure 2. Schematic of electrodes in the cell

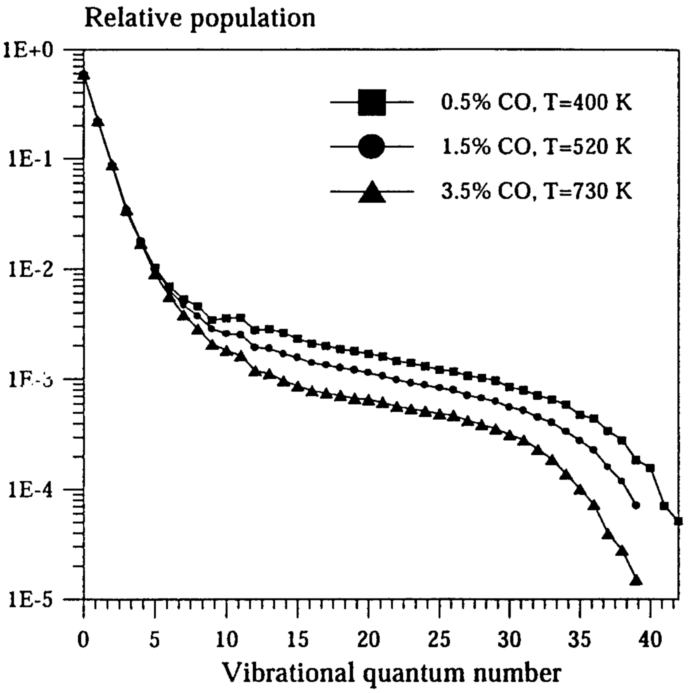

Figure 3. Vibrational distribution functions of CO in different CO/Ar mixtures. P=100 Torr, CO laser power is 10 W.

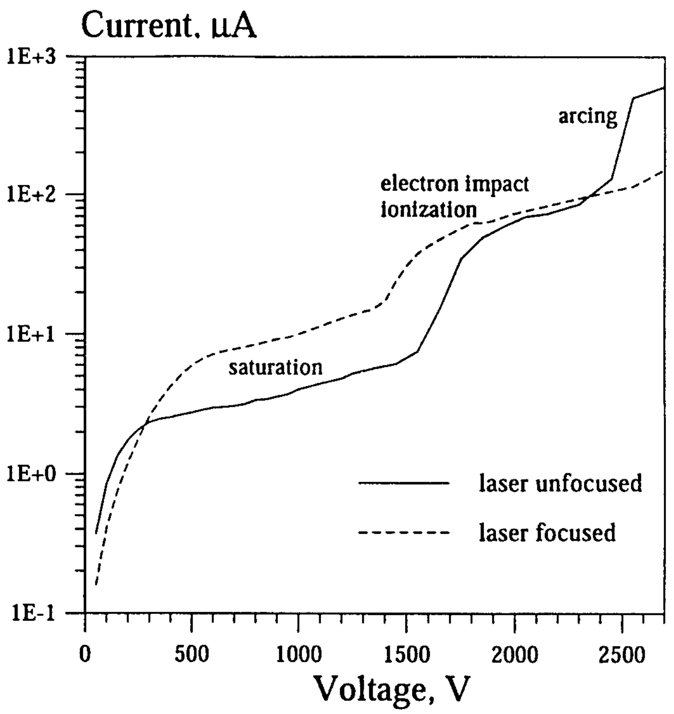

Figure 4. Current-voltage characteristics of the laser-sustained DC discharge. CO/Ar=3/100, P=100 Torr, CO laser power is 10 W.

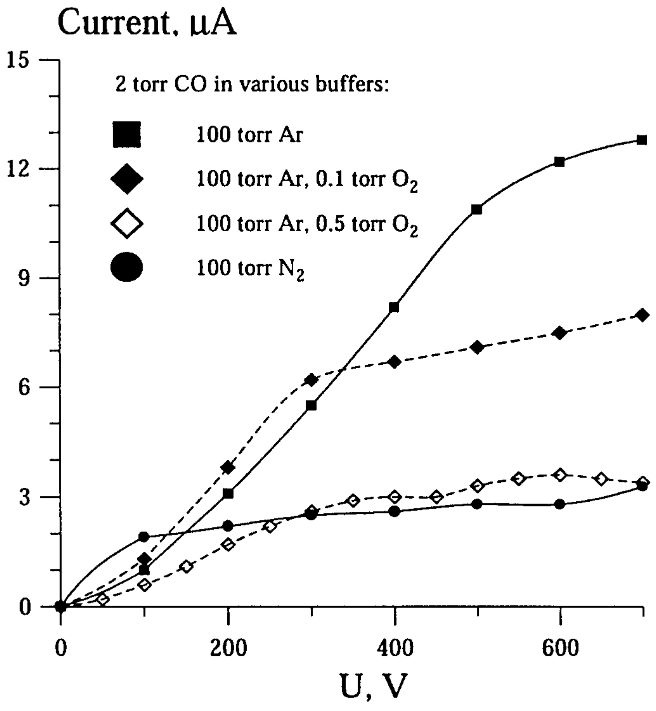

Figure 5. Current-voltage characteristics of the laser-sustained DC discharges. P_{CO}=2 torr, P=100 Torr, CO laser power is 20 W.

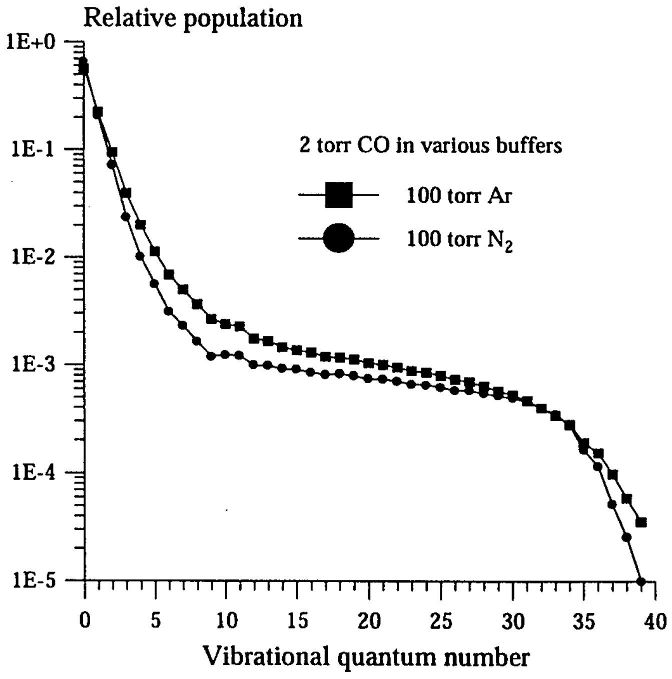

Figure 6. CO vibrational distribution function in CO/Ar (T=600 K) and CO/N$_2$ (T=450 K) mixtures

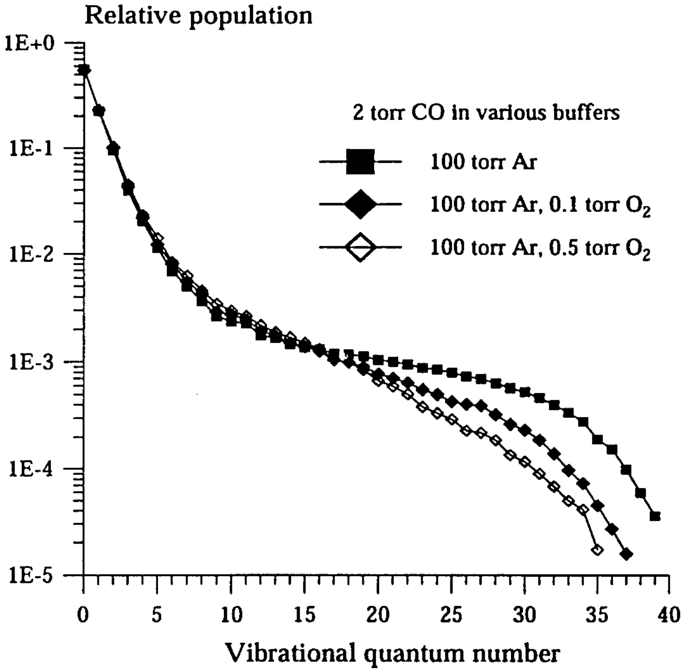

Figure 7. CO vibrational distribution function in CO/Ar/O_2 mixtures (T=600, 680, and 700 K for the O_2 partial pressures of 0, 0.1, and 0.5 torr, respectively)

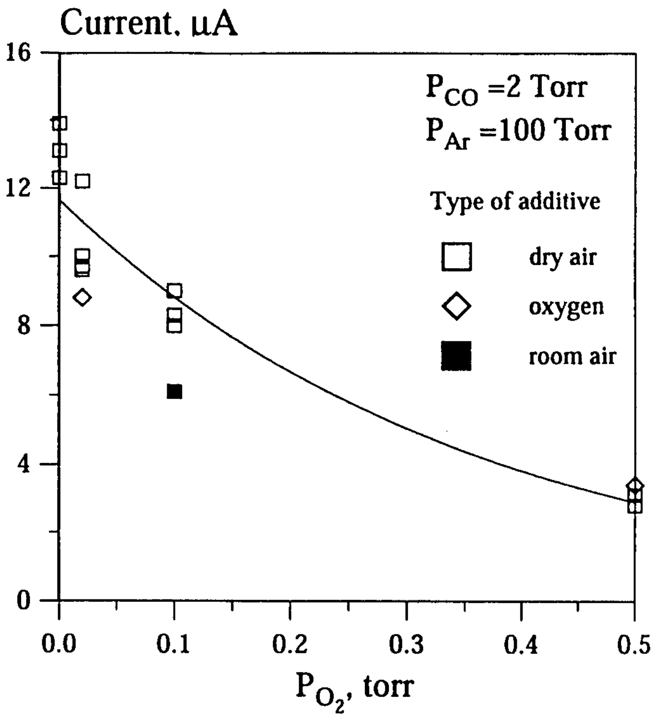

Figure 8. Thomson discharge saturation current in CO/Ar/air and CO/Ar/O_2 mixtures

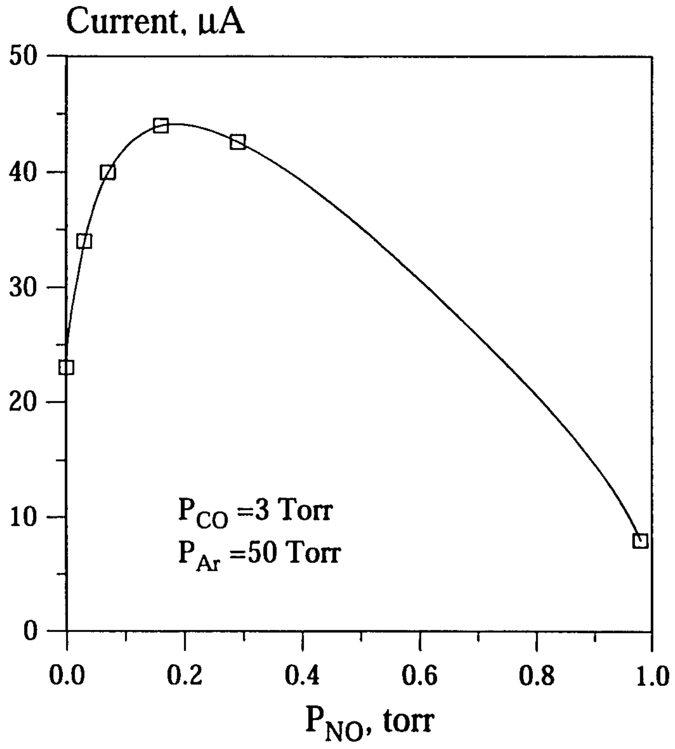

Figure 9. Thomson discharge saturation current in CO/Ar/NO mixtures

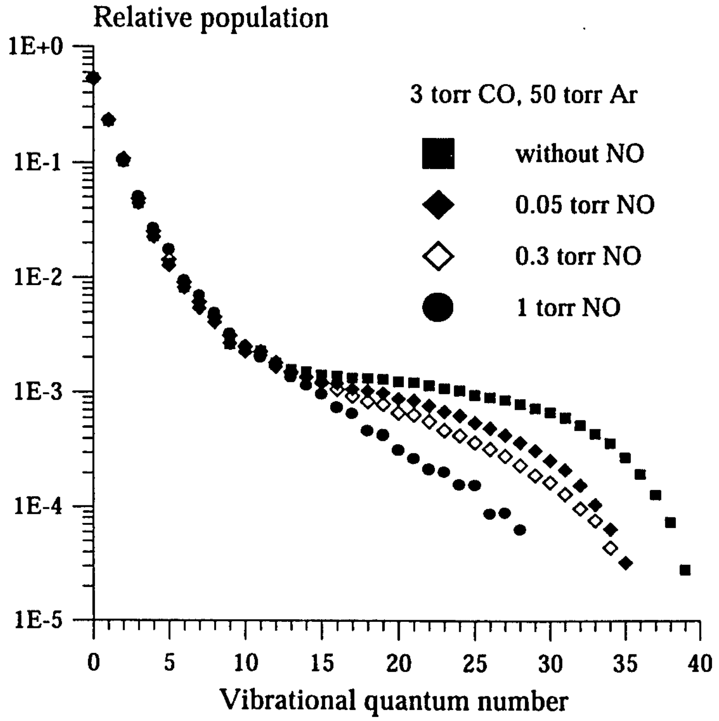

Figure 10. CO vibrational distribution function in CO/Ar/NO mixtures (T=710, 800, 780, and 770 K for the NO partial pressures of 0, 0.05, 0.3, and 1.0 torr, respectively)

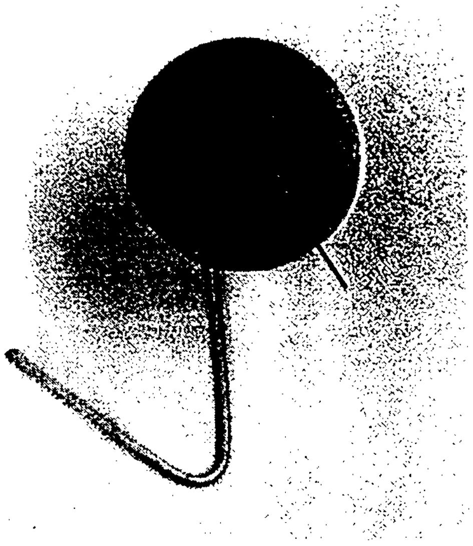

Figure 11. Photograph of a negative electrode with the deposit (shown with an arrow) accumulated during a 10 min run.

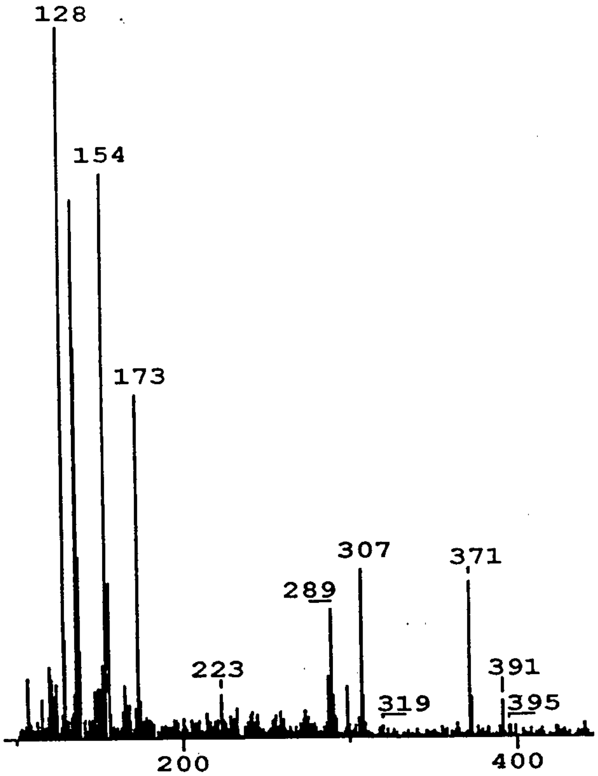

Figure 12. Mass-spectrum of the deposit shown in Fig. 11

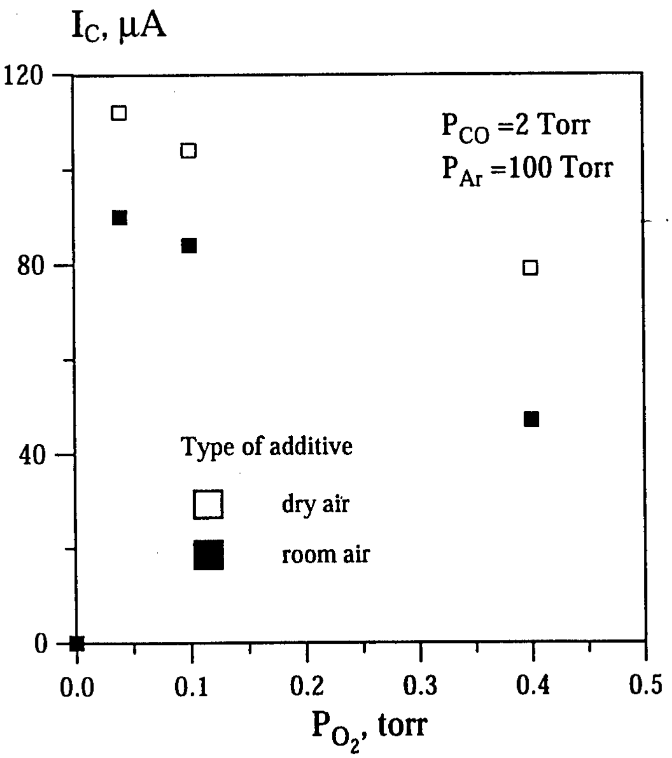

Figure 13. RF discharge conduction current in CO/Ar/O$_2$ mixtures at P=100 torr

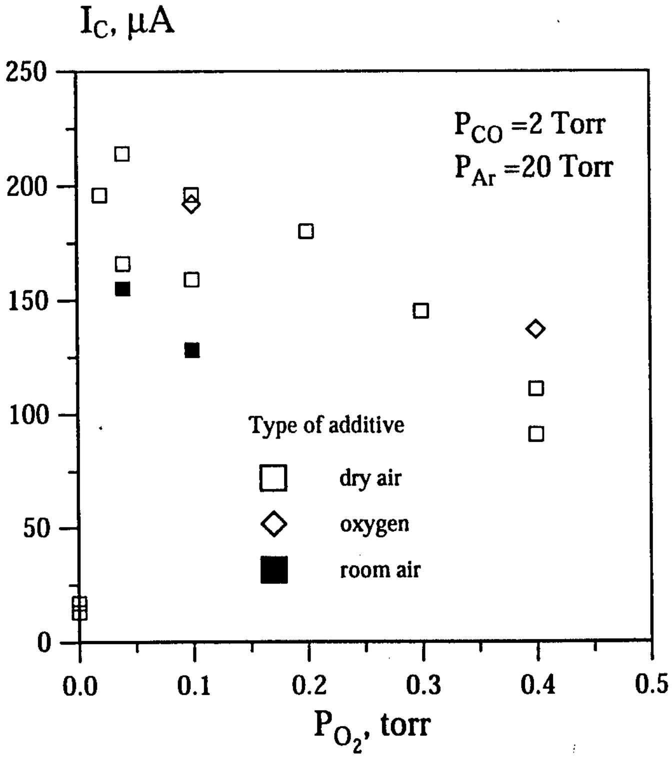

Figure 14. RF discharge conduction current in CO/Ar/O$_2$ mixtures at P=20 torr

CHAPTER IX.

THE EXISTENCE OF THE "BOTTLENECK" IN VIBRATIONAL RELAXATION OF DIATOMIC MOLECULES

1. Introduction.

The present work addresses the nature and the conditions of existence of the so-called "bottleneck" effect in the vibrational relaxation of diatomic molecules, first discussed in [1,2]. Theoretical calculations of vibrational energy transfer rates in high-temperature nitrogen at T=4000 K, based on the "generalized" SSH theory [1], predict a profound minimum in the rate of molecular relaxation as a function of vibrational quantum number v [2]. For example, Fig. 1 shows behavior of the second moment of vibrational transition rate coefficients M(v),

$$M(v)=\frac{1}{2}\sum_{w}(v-w)^2\cdot K(v,w)\,, \qquad (1)$$

where K(v,w) is the effective rate of the molecule relaxation from vibrational level v to level w [2]:

$$K(v,w)=\sum_{v',w'}f_{v'}\cdot k(v,v'\rightarrow w,w') \qquad (2)$$

In Eqs. (1,2), v, w, v′, and w′ are vibrational quantum numbers, $f_{v'}$ is the relative population of vibrational level v', and k(v,v'→w,w′) are individual transition rates, calculated in [1]. One can see a well-pronounced minimum in M(v) at vibrational energy that corresponds $v\cong25$. The transition moment M(v) given by Eq. (1) is interpreted as a diffusion coefficient in vibrational energy space [2]. Therefore, the predicted minimum ("bottleneck") at the intermediate vibrational energies (about one half of the molecular dissociation energy) would mean slowing down the vibrational quanta flow toward the high levels during the relaxation process. This would also substantially decrease the molecular dissociation rate for the conditions when dissociation preferentially occurs from the high vibrational quantum states. These effects have been observed in the master equation modeling of vibrational relaxation of N_2 at T=8000 K [1].

Recent experimental measurements of vibrational relaxation rates in oxygen at T=300 K [3-5] seemingly confirm that this effect does exist (see Fig. 2), at least at the low translational temperatures. However, extrapolation of this conclusion to high temperatures, based on the results of calculations [1], has no firm theoretical basis. First, in their calculations of vibration-translation (V-T) and vibration-vibration (V-V) rates, the authors of [1] applied first-order perturbation theory (SSH theory, [6]) to the high energy molecular collisions, and also to multi-quantum processes. However, it is well known that first order perturbation theory is not applicable to calculations of large transition probabilities, which can become comparable to unity at high collision energies. Also, it has been recently shown that multi-quantum vibrational energy transfer occurs not by a first-order mechanism [7], and one has to use an N-term wavefunction expansion to evaluate the probability of a process that transmits N vibrational quanta [8]. Finally, the intermolecular potential used in [1] is quite different from the potential obtained from ab initio calculations.

In the present work, we analyze the behavior of the vibrational energy diffusion coefficient and the conditions for the existence of the "bottleneck" effect over a large range of translational and vibrational temperatures. The state-specific vibrational energy transfer rate coefficients are calculated on the basis of non-perturbative forced harmonic oscillator analytic theory (FHO) [9-13,7], that gives an exact analytic solution of the Schrodinger equation instead of expanding the wavefunctions in a series. The intermolecular potentials used in the calculations fit ab initio potentials used in 3-D close-coupled semiclassical calculations [14-16]. The V-T and V-V rates predicted by the FHO theory are in very good agreement both with the results of these 3-D calculations for N_2-N_2, O_2-O_2, and N_2-O_2 and with available experimental data in oxygen [3-5] (e.g. see Refs. [12,7]).

2. Results and discussion.

Figures 2,3 show the transition moment $M(\varepsilon)$, similar to $M(v)$ given by Eq. (1),

$$M(\varepsilon_v) = \frac{1}{2}\sum_w \frac{(E_v - E_w)^2}{E_1^2} \cdot K(v,w) = \frac{1}{2}\sum_w (\varepsilon_v - \varepsilon_w)^2 \cdot K(v,w), \qquad (3)$$

calculated for N_2 and O_2 at different translational temperatures. In Eq. (3) and in Figs. 2,3, $E_v=\omega_e v[1-x_e(v+1)]$ is the energy of vibrational level v in K, and $\varepsilon_v=E_v/E_1$ is the dimensionless vibrational energy. One can see that, indeed, V-V exchange results in a dramatic increase in $M(\varepsilon)$ at low temperatures, in agreement with experimental data (see Fig. 2). However, at high translational temperatures such as $T/E_1\geq 1.5$ ($T\geq 3000$ K for O_2 and $T\geq 5000$ K for N_2) the effect becomes much smaller (compare with Fig. 1). One can see that the high-temperature V-V rates calculated for realistic intermolecular potentials are much smaller than obtained in Ref. [1].

Note that in the presence of V-V exchange the transition moment, given by Eqs. (1,3) cannot be interpreted simply as a diffusion coefficient in the vibrational energy space, as in the case when V-T relaxation dominates. In the high temperature limit, when $T/E_1>>1$, the master equation for the populations of vibrational levels of diatomic molecules,

$$\frac{1}{N}\frac{df_v}{dt}=\sum_{v',w,w'}k(w,w'\to v,v')f_w f_{w'}-\sum_{v',w,w'}k(v,v'\to w,w')f_v f_{v'}\,, \tag{4}$$

reduces to an integro-differential equation [17,18]

$$\frac{1}{N}\frac{\partial f(\varepsilon,t)}{\partial t}=\frac{\partial}{\partial\varepsilon}\left\{\begin{array}{l}\left[\dfrac{\partial f(\varepsilon)}{\partial\varepsilon}-f(\varepsilon)\dfrac{\partial\ln f_{eq}(\varepsilon)}{\partial\varepsilon}\right]\int d\varepsilon'\cdot f(\varepsilon')M_1(\varepsilon,\varepsilon')\\ -f(\varepsilon)\int d\varepsilon'\cdot M_2(\varepsilon,\varepsilon')\left[\dfrac{\partial f(\varepsilon')}{\partial\varepsilon'}-f(\varepsilon')\dfrac{\partial\ln f_{eq}(\varepsilon')}{\partial\varepsilon'}\right]\end{array}\right\}, \tag{5}$$

where

$$M_1(\varepsilon,\varepsilon')=\frac{1}{2}\sum_{w,w'}k(v,v'\to w,w')\cdot(\varepsilon_v-\varepsilon_w)^2 \tag{6}$$

and

$$M_2(\varepsilon,\varepsilon')=\frac{1}{2}\sum_{w,w'}k(v,v'\to w,w')\cdot\left|\varepsilon_v-\varepsilon_w\right|\cdot\left|\varepsilon_{v'}-\varepsilon_{w'}\right| \tag{7}$$

Equation (5) may be further reduced to a diffusion-type equation if one assumes that the V-V-T rate matrix k(v,v'→w,w') can be presented as two separate matrices, V-T mode rates $k_{VT}(v \to w)$ and V-V mode rates $k_{VV}(v,v' \to v+\Delta v, v'-\Delta v)$:

$$\frac{1}{N}\frac{\partial f(\varepsilon,t)}{\partial t} \cong \frac{\partial}{\partial \varepsilon}\left\{\left[D_{VT}(\varepsilon) - D_{VV}(\varepsilon,t)\right]\left[\frac{\partial f(\varepsilon)}{\partial \varepsilon} - f(\varepsilon)\frac{\partial \ln f_{eq}(\varepsilon)}{\partial \varepsilon}\right]\right\}, \qquad (8)$$

where

$$D_{VT}(\varepsilon) \cong \frac{1}{2}\sum_{\Delta v} k_{VT}(v \to v+\Delta v)\cdot(\varepsilon_v - \varepsilon_{v+\Delta v})^2 = Z\frac{\left\langle(\Delta\varepsilon)^2\right\rangle}{2} \qquad (9)$$

and

$$\begin{aligned} D_{VV}(\varepsilon,t) &\cong \frac{1}{2}\sum_{\Delta v, v'} f_{v'}\cdot k_{VV}(v,v' \to v+\Delta v, v'-\Delta v)\cdot\left|\varepsilon_v - \varepsilon_{v+\Delta v}\right|\cdot\left(\left|\varepsilon_{v'} - \varepsilon_{v'-\Delta v}\right| - \left|\varepsilon_v - \varepsilon_{v+\Delta v}\right|\right) \\ &= Z\frac{\left\langle\left|\Delta\varepsilon\right|\cdot\left(\left|\Delta\varepsilon'\right| - \left|\Delta\varepsilon\right|\right)\right\rangle}{2} \end{aligned} \qquad (10)$$

In Eqs. (9,10), Z is the gas-kinetic collision frequency. In the absence of the V-V exchange, $D_{VV}=0$ and Eq. (8) becomes the well-known Fokker-Planck diffusion equation [19]. Both Eq.(5) and Eq. (8) are valid only if

$$\left(\frac{E_1}{T}\right)^2\left\langle(\Delta\varepsilon)^2\right\rangle \ll 1, \qquad (11)$$

and also if $T/E_1 \gg 1$, $\langle\Delta\varepsilon\rangle/\varepsilon \ll 1$.

From Eqs. (9,10) one can see that (i) the overall diffusion coefficient $D=D_{VT}-D_{VV}$ may change sign depending on the vibrational distribution function $f(\varepsilon)$ (i.e. on time) and on vibrational energy ε, and (ii) $|D(\varepsilon,t)|=|D_{VV}(\varepsilon)-D_{VT}(\varepsilon,t)|<M(\varepsilon)$. Therefore the effect of V-V

exchange on the diffusion flux is even less than one might assume from Figs. 2,3. Figs. 4,5 demonstrates that if $T/E_1 \geq 1.5$-2.0, the contribution of the V-V processes to the overall diffusion coefficient D does not exceed 10% and dramatically decreases with temperature. In other words, at the high temperatures vibration-vibration exchange between the molecules of the same species can be neglected.

The effect of the V-V exchange at low temperatures, when $T/E_1<1$, is certainly much more pronounced, especially at high vibrational temperatures (see Figs. 4,5). Although the diffusion equation (8) is not applicable at these conditions, it can nevertheless qualitatively predict the time evolution of the distribution function. For example, the behavior of the overall diffusion coefficient $D=D_{VT}-D_{VV}$ at T=1000K, T_v=5000 K, shown in Fig. 5, predicts depopulation of the low and the high vibrational levels of O_2, and overpopulation of the middle levels, where $D<0$, during the relaxation process at $T_v>T$. This is a well-known result of vibrational kinetics of anharmonic oscillators. The diffusion theory of vibrational relaxation at the low translational temperatures, when $T/E_1<<1$, is based on a different form of the Fokker-Planck equation, and has been developed in the 70's (e.g. see [20,21] and references therein). It also shows remarkably good agreement with the "exact" master equation calculations.

To verify the applicability of the diffusion approximation (8) at very high temperatures, when $T/E_1>>1$, we considered the problem of vibrational relaxation behind a shock wave using two different approaches: (i) "exact" master equation (4), and (ii) diffusion equation (8) with the diffusion coefficient given by Eqs. (9,10). In both cases, the same V-T and V-V rates have been used. To account for the molecular dissociation that is assumed to occur from the high vibrational levels, the equivalent constraints of total absorption have been imposed:

$$f(v = v_{diss}) = 0 \qquad \text{and} \qquad f(\varepsilon = \varepsilon_{diss}) = 0 \tag{12}$$

A Boltzmann distribution with vibrational temperature $T_v=E_1$ was assumed at t=0.

The results of the calculations for oxygen at the constant translational temperatures T=4000 K and T=8000 K are shown in Figs. 6,7. One can see that at T=4000 K the diffusion approximation is applicable except for the high vibrational levels near the dissociation limit. At T=8000 K the two approaches give different results even at much lower energies, especially for $t/\tau_{VT}<<1$ (τ_{VT} is the Landau-Teller vibrational relaxation time). In both cases, the high vibrational level populations given by the master equation quickly get to equilibrium with translational temperature T, so that the boundary condition (12) has almost no effect on the distribution function. The criterion of Eq. (11) which limits the applicability of the diffusion approximation, is satisfied in both cases, excluding high vibrational energies $\varepsilon \cong \varepsilon_{diss}$ (see Fig. 8). However, Fig. 9 demonstrates that the reason for the difference between the two model predictions at the high temperature is multi-quantum relaxation. One can see that the products of the V-T relaxation of oxygen initially at the vibrational level $v=20$ spread much wider over the vibrational energy axis as the temperature increases, so that $\langle\Delta\varepsilon\rangle/\varepsilon \sim 1$. This makes the high-temperature ($T/E_1>>1$) relaxation in air an essentially non-local process, the diffusion approximation therefore being inapplicable over the broad range of vibrational energies. We note, however, that the difference between the two approaches (master equation vs. diffusion approximation) almost ceases to exist at $t/\tau_{VT} \geq 1$, the distribution function becoming Boltzmann-like, except for the high energies within $\delta\varepsilon \sim T/E_1$ from the dissociation limit.

Figure 7 looks very similar to the results of master equation modeling of the high-temperature relaxation using the FHO model and the first-order rate model (SSH theory, single-quantum processes only) [13,22]. The latter also strongly underestimates the populations of the high vibrational levels during the relaxation at $t/\tau_{VT} \leq 1$, despite predicting much greater V-T rates than given by the FHO model. We conclude that the failure of the first-order models to adequately describe the distribution function at conditions of extreme vibrational disequilibrium is mainly due to their neglect of multi-quantum relaxation, not just because they predict the single-quantum rates incorrectly. Finally, Figs. 6,7 show that the use of diffusion approximation for modeling of relaxation and dissociation at the high vibrational levels such as $\varepsilon_v \geq \varepsilon_{diss}-T/E_1$, is not justified, as also pointed out in [2].

As expected, in the present calculations only a small difference has been found between the distribution function $f_v(t)$ formed by the V-T relaxation only, and the one controlled by both V-T and V-V exchange. No bottleneck effect that would create a bimodal vibrational distribution [1,2] has been observed.

These results can be also applied to interpretation of the thermal dissociation data ($T_v=T$) at not very high temperatures $T/E_1 \sim 1\text{-}3$, when dissociation preferentially occurs from the high vibrational levels [22]. At these conditions, the dissociation is controlled by the rate of activation of the high vibrational levels such as $\varepsilon_v \cong \varepsilon_{diss}$. It is well-known that the rate of the thermal molecular dissociation is greater when the collision partner is another molecule, rather than an atom. For example, the ratio $k_{diss}(O_2\text{-}O_2)/k_{diss}(O_2\text{-}Ar)$ changes from 30-40 at T=3500 K to 5-10 at T=7000 K [19]. The fact that V-V exchange has almost no contribution in the molecular activation at the high temperatures shows that it can not be responsible for the dissociation rate increase in diatom-diatom collisions. Also, calculations of the activation rate,

$$k_{act}(T) = \sum_{v} k_{VT}(v \to v_{diss}) \cdot f_v(T)\,, \tag{13}$$

for O_2-O_2 and O_2-Ar collisions give rather close results (within a factor of 2-3 in this temperature region), which shows that the slightly different collision reduced masses and intermolecular potentials also do not explain the observed effect. The activation rate of Eq. (13) can be interpreted as the rate of dissociation for the total absorption condition (12). This suggests that the rotational energy of the collision partner, disregarded in the FHO vibrational energy transfer model, must play an important role in the molecular activation at the high vibrational levels. A qualitative estimate of the role of rotations predicts about an order of magnitude increase in the diatom-diatom dissociation rate [19]. More theoretical effort is needed to obtain a better insight into this problem.

References

1. S.P. Sharma, W. Huo, and C. Park, AIAA Paper 88-2714, 1988
2. C. Park, "Nonequilibrium Hypersonic Aerodynamics", Wiley, New York, 1990, Chaps. 2,3
3. J.M. Price, J.A. Mack, C.A. Rogaski, and A.M. Wodtke, Chemical Physics, v. 175, p. 83, 1993
4. H. Park and T.G. Slanger, Journal of Chemical Physics, v. 100, p. 287, 1994
5. M. Klatt, I.W.M. Smith, R.P. Tuckett, and G.N. Ward, Chemical Physics Letters, v. 224, p. 253, 1994
6. R.N. Schwartz, Z.I. Slawsky, and K.F. Herzfeld, Journal of Chemical Physics, v. 22, p. 767, 1954
7. I.V. Adamovich, S.O. Macheret, J.W. Rich, and C.E. Treanor, AIAA Paper 95-2060, 1995
8. D. Rapp amd T. Kassal, Chemical Reviews, v. 69, p. 61, 1969
9. E.H. Kerner, Canadian Journal of Physics, v. 36, p. 371, 1958

10. C.E. Treanor, Journal of Chemical Physics, v. 43, p. 532, 1965
11. A. Zelechow, D. Rapp, and T.E. Sharp, Journal of Chemical Physics, v. 49, p. 286, 1968
12. I.V. Adamovich, S.O. Macheret, J.W. Rich, and C.E. Treanor, AIAA Journal, v. 33, p. 1064, 1995
13. I.V. Adamovich, S.O. Macheret, J.W. Rich, and C.E. Treanor, AIAA Journal, v. 33, p. 1070, 1995
14. G.D. Billing and E.R. Fisher, Chemical Physics, v. 43, p. 395, 1979
15. G.D. Billing and R.E. Kolesnick, Chemical Physics Letters, v. 200, p. 382, 1979, 1992
16. G.D. Billing, Chemical Physics, v. 179, p. 463, 1994
17. V.M. Volokhov, M.N. Safaryan, and O.V. Skrebkov, Soviet Theoretical and Experimental Chemistry, vol. 18, p. 456, 1978
18. O.V. Skrebkov, Chemical Physics, v. 191, p. 87, 1995
19. E.E. Nikitin, “Theory of Elementary Atomic and Molecular Processes in Gases”, Clarendon Press, Oxford, 1974, Chaps. 6,7
20. B.F. Gordiets, A.I. Osipov, and L.I. Shelepin, “Kinetic Processes in Gases and Molecular Lasers”, Gordon and Breach, London, 1988, Chap. 4
21. B.F. Gordiets and S.A. Zhdanok, “Analytical Theory of Vibrational Relaxation of Anharmonic Oscillators”, Chap. 3 in “Nonequilibrium Vibrational Kinetics”, ed. M. Capitelli, pp. 47-83, Springer, Berlin, 1986
22. S.O. Macheret and J.W. Rich, Chemical Physics, vol. 174, p.25, 1993

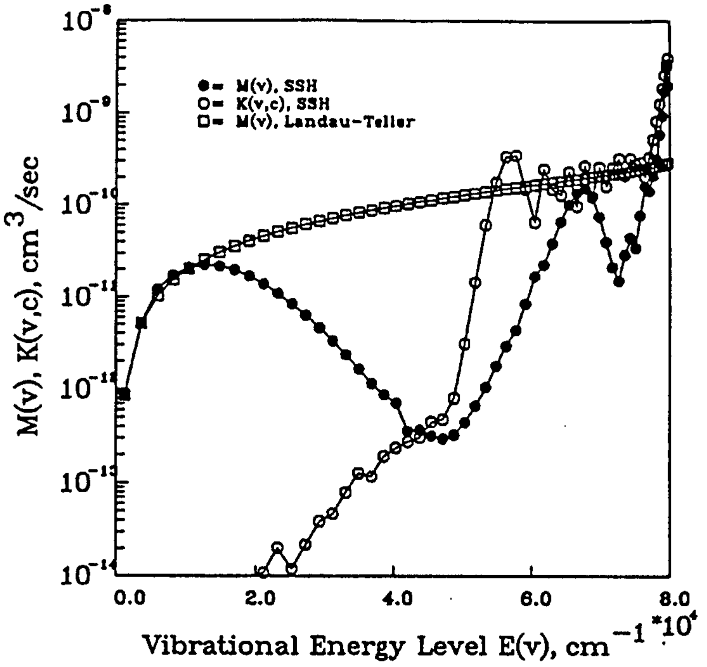

Figure 1. Transition moment of Eq. (1) M(v), based on the transition rates, calculated in Ref. [1], for nitrogen at T=4000 K. Open circles show the rate of dissociation. Taken from Ref. [2].

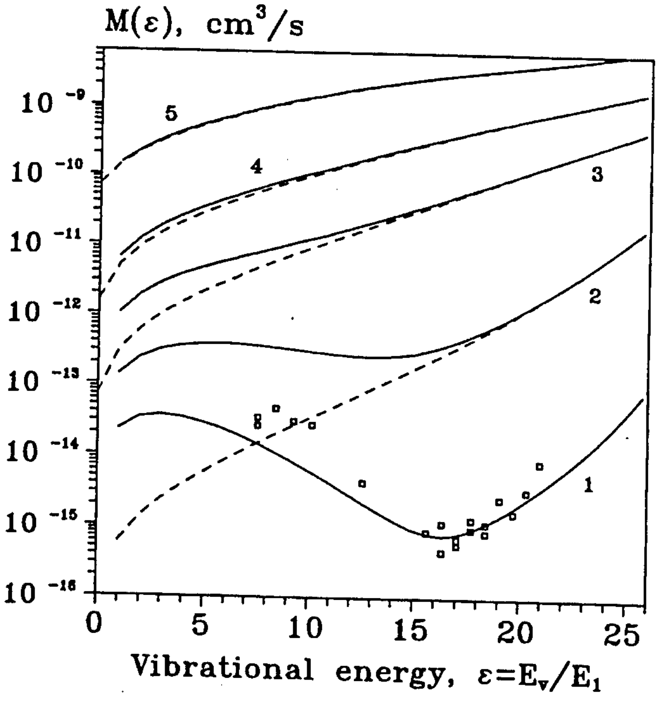

Figure 2. Transition moment of Eq. (3) M(ε), based on the FHO relaxation rates for O_2 [7] at T_v=300 K. Solid line, both V-T and V-V processes are considered; dashed line, V-T processes only; symbols, experimental data at T=300 K [3-5].
1, T=300 K; 2, T=1000 K; 3, T=3000 K: 4, T=5000 K; 5, T=10000 K.

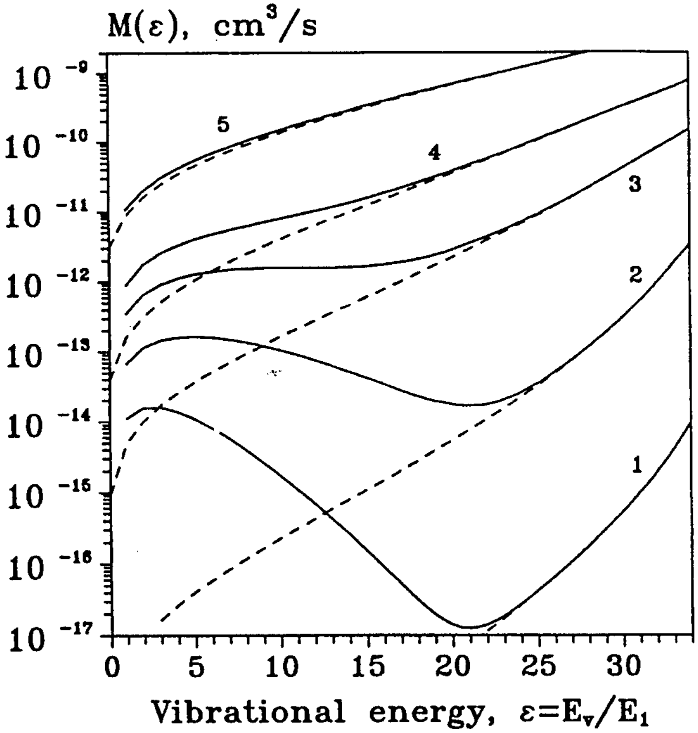

Figure 3. Transition moment of Eq. (3) M(ε), based on the FHO relaxation rates for N_2 [7] at T_v=300 K. Solid line, both V-T and V-V processes are considered; dashed line, V-T processes only. 1, T=300 K; 2, T=1000 K; 3, T=3000 K; 4, T=5000 K; 5, T=10000 K.

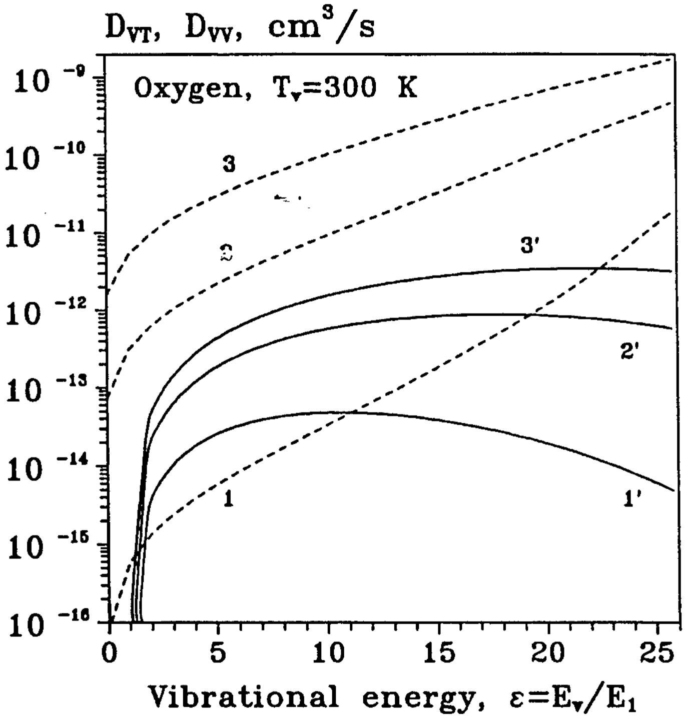

Figure 4. Vibrational energy diffusion coefficients due to V-T (dashed lines) and V-V (solid lines) processes. Oxygen at T_v=300 K. 1,1' - T=1000 K; 2,2' - T=3000 K; 3,3' - T=5000 K.

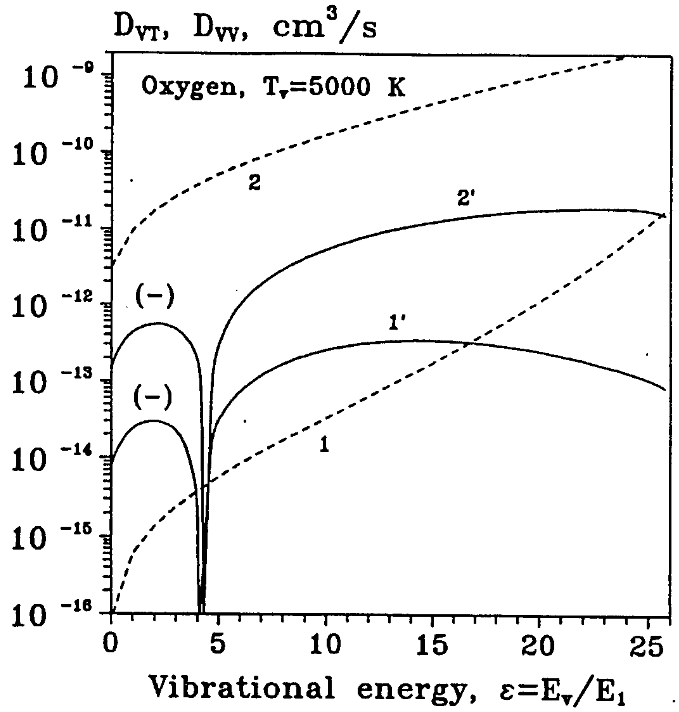

Figure 5. Vibrational energy diffusion coefficients due to V-T (dashed lines) and V-V (solid lines) processes. Oxygen at T_V=5000 K. 1,1' - T=1000 K; 2,2' - T=5000 K. Symbol (-) shows the region where D_{VV} becomes negative.

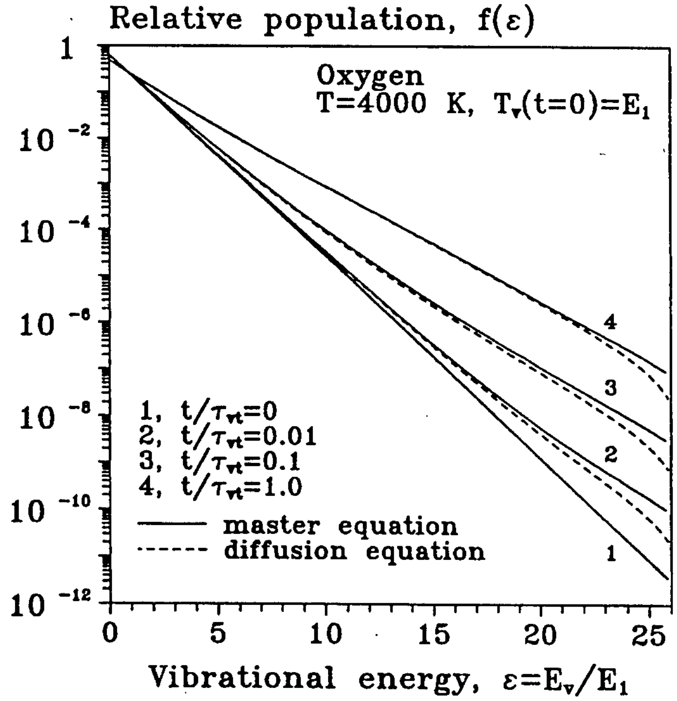

Figure 6. Vibrational distribution function of oxygen during the relaxation at constant temperature T=4000 K.

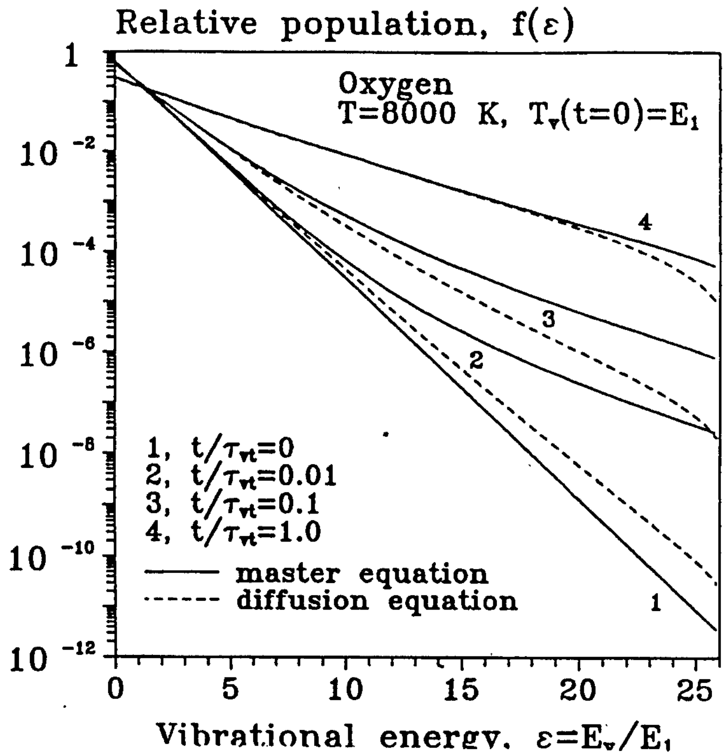

Figure 7. Vibrational distribution function of oxygen during the relaxation at constant temperature T=8000 K.

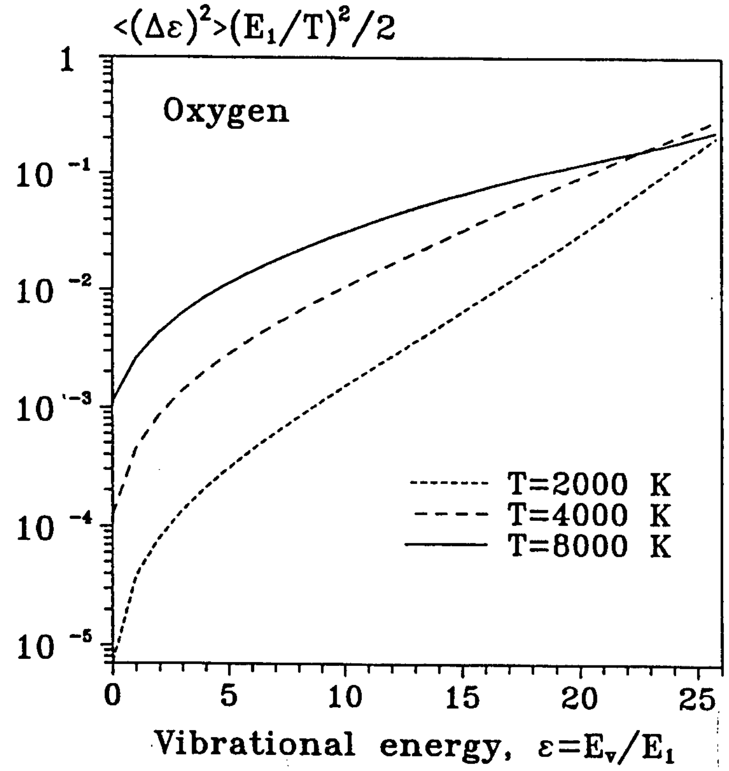

Figure 8. Normalized vibrational energy diffusion coefficient D_{VT} in oxygen.

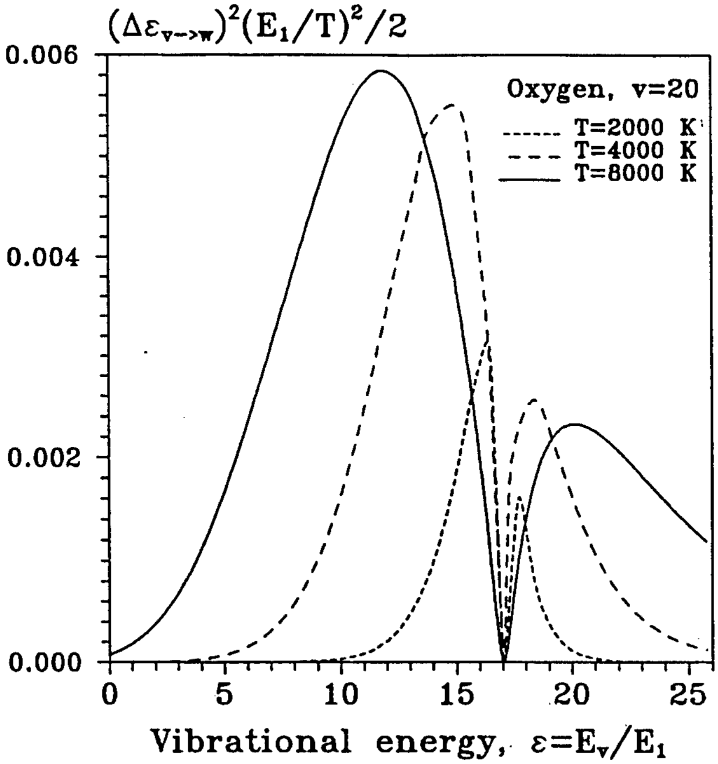

Figure 9. Distribution of the V-T relaxation products of O_2(v=20) at different translational temperatures.

CHAPTER X.

KINETICS OF NO FORMATION BEHIND STRONG SHOCK WAVES

Nomenclature

S = observed in-band infrared radiation, W/cm^2 sr
L = optical path-length, cm
n_{NO} = number density of NO molecules, cm^{-3}
T = translational temperature, K
AB(v) = molecule AB in vibrational level v
k_i = chemical reaction rate for reaction i, cm^3/molecule s
E_v = energy of the vth vibrational level, K
$F(E_v)$ = threshold translational energy for dissociation from level v, K
E_a = reaction activation energy, K
α = mass ratio factor
β = energy fraction that goes into vibration in reverse reaction
W = an energy parameter, Eq. (16), K
s = a parameter in Park model
τ_{inc}(NO) = observed incubation time (laboratory time) for NO production, μs
τ_{VT}(NO) = vibrational relexation time at observed conditions (laboratory time), μs

Subscripts
i = initial
f = final
st = stagnation point
max = maximum value

1. Introduction

The contribution of vibrational energy to the dissociation process in diatomic molecules is significant in many gas environments, such as high-enthalpy gas-dynamic flows, molecular gas discharges, plasma chemical reactors and upper-atmosphere chemistry. In shock-wave flows it has been the subject of many investigations, particularly under conditions of low density, where non-equilibrium conditions exist for an appreciable portion of the flow. It remains the goal of hypersonic flow simulation to develop programs which contain the proper physics of this interaction, while retaining tractable numerical complexities.

The most important approximation made in computing non-equilibrium flows[1] is the assumption that each degree of freedom of a molecule retains a Boltzmann-like distribution during chemical reaction processes. This assumption permits great simplifications in the formulation of the gas-dynamic equations. For the translational and rotational degrees this assumption is valid over a wide range of flow conditions, since these degrees exchange energy readily in molecular collisions. However, for the vibrational degree. many collisions are required to transfer a single quantum of energy, and the vibrational distribution can easily become non-Boltzmann during relaxation processes.

The extent of this variation, and the effect it has on observed chemical reaction rates, depends on the values of the state-to-state vibrational transition probabilities. These rates have recently been calculated for nitrogen and oxygen.[2,3] They can be used in master equation shock-wave calculations, along with a rational vibration-chemistry coupling scheme,[4-6] to calculate vibrational energy distributions and chemical reaction rates behind shocks. It is the purpose of the present work to present such calculations and compare them with experimental results and with calculations which assume a Boltzmann distribution. Section 2 contains a brief description of the experiment that was used for comparison. Section 3 describes the modeling that was employed, and Section 4 presents the results of the calculations and comparisons. A Summary is provided in Section 5.

2. Experimental

The experimental results that were used for comparison with the present calculations are described in detail in Refs. 7 and 8. For completeness a brief summary of the experiment and previous analysis is presented here.

The time-history of infrared radiation behind a normal shock was measured using a pressure-driven shock tube with a 3-inch (7.62 cm) inside diameter. The driver section of the shock tube is 5 feet long, and was operated at pressures of up to 4000 psi (260 atm) of hydrogen. The routine double-diaphragm technique provided excellent run-to-run reproducibility in wave speed (~1%) and radiation records. Initial test gas pressures were measured to better than 1% with an MKS Baratron unit. Scientific grade (99.999%) O_2 and N_2 were used throughout, and were premixed in three different proportions for the experiments. Ultraviolet radiation measurements were also taken during the experiments. The principal elements of the shock-tube experiment are shown in Fig. 1, taken from Ref. 7.

An InSb detector was used in the radiometer to measure the NO infrared radiation behind the shock wave. It was found that even though the long-wave roll-off of the detector response clips one wing of the NO band, the high detectivity resulted in an excellent signal-to-noise ratio,[8] better than that obtained in earlier experiments with HgCdTe.[7] The combined filter-detector bandpass function, between 5-5.5 μm was determined by separate bench experiments. A standard blackbody source through a scanning monochromator was calibrated and then used to establish the wavelength dependence of the radiometer. System calibration was achieved by means of a chopped, standard blackbody which completely filled the field of view and whose intensity spanned the range of those for the test gases. The system was linear over this range.

As described in Ref. 2, Appendix D, the observed in-band infrared radiation is related to the NO concentration and the gas translational temperature through the relation

$$S = 1.29 \cdot 10^{-20} \cdot L \cdot n_{NO}\left[1 - 3.21 \cdot 10^{-4}(T - 3000)\right] \quad W / cm^2 \cdot sr \tag{1}$$

with n_{NO} in cm^{-3}, L in cm and T in degrees Kelvin. For these experiments, L, the shock-tube diameter, had the value of 7.62 cm. This equation is consistent with the equilibrium values of NO radiation measured in the shock tube and with the known band strength of the molecule. It was used to relate the measurements of non-equilibrium radiation to the non-equilibrium NO molecular density.

The optical system used in the experiment was designed to produce a sharp definition of the region behind the shock wave contributing to the radiation received by the detector at any given time, and to avoid reflections that would provide spurious signals. As illustrated in Fig. 2, taken from Ref. 8, the physical apertures, (the InSb detector and a razor-blade slit) are both external to the shock tube, and each provides a 3 mm image on a shock tube window. The external placement precludes any reflections from the apertures. With shock speeds of 3 to 4 mm/μs, this results in a temporal resolution of 1 μs in the data.

Analysis of the data[9] determined an optimum set of rate coefficients chosen from available measured values. These rates are also used in the present work.

3. Kinetic Modeling

To simulate the kinetics of NO formation behind normal shock waves, we have used nonequilibrium-flow master-equation modeling, herein called "Model II". The kinetic model incorporates (i) the equations of one-dimensional gas dynamics for nonequilibrium reacting real gases;[10] (ii) chemical kinetics equations for reacting species N, N_2, O, O_2, NO; and (iii) master equations for populations of vibrational levels of each diatomic species. The chemistry-vibration coupling terms are incorporated into both the chemical kinetics equations and the master equation, while the effects of relaxation and chemical reactions are taken into account in the energy and motion equations. Thus, the system of equations used is completely self-consistent. The explicit form of equations (ii) and (iii) can be found in an earlier publication.[11]

It is assumed that the gas mixture components participate in the following dissociation reactions

$$N_2(v) + M \leftrightarrows N + N + M \tag{2}$$

$$O_2(v) + M \leftrightarrows O + O + M \tag{3}$$

$$NO(v) + M \leftrightarrows N + O + M \tag{4}$$

and in Zel'dovich mechanism reactions

$$N_2(v) + O \leftrightarrows NO + N \tag{5}$$

$$O_2 + N \leftrightarrows NO(v) + O \tag{6}$$

In Eqs. (2-4), M stands for a collision partner, and v is the vibrational quantum number. The notation AB(v) in a reaction equation shows that the effect of vibrational excitation of molecule AB on the rate of an endoergic reaction is taken into account. The rates of reactions (2-6) in thermal equilibrium are taken the same as in Ref. 11, where they were incorporated from:[12,13]

$$k_1 = 8.0 \cdot 10^{-7} \cdot T^{-0.5} \cdot \exp(-113{,}200 / T), \qquad M = N_2 \tag{7}$$

$$k_2 = 5.4 \cdot 10^{-5} \cdot T^{-1.0} \cdot \exp(-59{,}380 / T), \qquad M = O_2 \tag{8}$$

$$k_3 = 6.6 \cdot 10^{-4} \cdot T^{-1.5} \cdot \exp(-75{,}490 / T), \qquad \text{for any } M \tag{9}$$

$$k_4 = 3.0 \cdot 10^{-10} \cdot \exp(-38{,}016 / T) \tag{10}$$

$$k_5 = 2.2 \cdot 10^{-14} \cdot T \cdot \exp(-3{,}565 / T) \tag{11}$$

The rates of N_2 dissociation on other collision partners are $15 \cdot k_1$ for M=N, and $0.4 \cdot k_1$ for M = O, O_2, NO; the rates of O_2 dissociation are $2.8 \cdot k_2$ for M=O, and $0.22 \cdot k_2$ for M = N, N_2, NO (see Ref. 11). All the rates of Eqs. (7-11) are given in cm^3/molecule·s.

The rates of nonequilibrium dissociation and bimolecular reactions (2-6) are evaluated according to the classical impulsive model by Macheret-Fridman-Rich (MFR).[4-6] According to this model, the state-specific rate is given by the equation

$$k(v \rightarrow, T) = A(T) \cdot \exp(-F(E_v) / T), \tag{12}$$

where E_v is the energy of a vibrational level v, $F(E_v)$ is the threshold translational energy, and A(T) is a factor obtained from normalization on the thermal reaction rate. The threshold energy (or "threshold curve"), determined for reactions of dissociation[5] and for bimolecular reactions,[4] is also a function of the reaction activation energy and masses of collision partners. For example, for the endoergic exchange reaction

$$AB(v) + C \rightarrow A + BC \tag{13}$$

one has[4]

$$F(E_v) = \begin{cases} W + \dfrac{1}{1-\alpha}\left[(E_a - W)^{1/2} - (\alpha E_v)^{1/2}\right]^2, & \text{if } E_v \le \dfrac{E_a - W}{\alpha} \\ W, & \text{if } E_v > \dfrac{E_a - W}{\alpha} \end{cases} \tag{14}$$

In Eq. (14), E_a is the reaction activation energy,

$$\alpha = \frac{m_B(m_A + m_B + m_C)}{(m_A + m_B)(m_B + m_C)}, \tag{15}$$

and W can be found from the relation

$$\beta = \alpha \cdot (1 - W / E_a), \tag{16}$$

where β is the energy fraction that goes into vibrations in the reverse exoergic reaction. For reaction (5), this parameter is measured to be β=0.25.[14] One can see from Eq. (14) that $F(E_v) \geq E_a - E_v$, which is also true for dissociation.[5]

The rates for vibration-translation (V-T)

$$AB(i) + M \leftrightarrows AB(f) + M \quad , \tag{17}$$

and vibration-vibration (V-V)

$$AB(i_1) + CD(i_2) \leftrightarrows AB(f_1) + CD(f_2) \tag{18}$$

processes, used in the master equation, are evaluated according to the non-perturbative semiclassical analytic model of the forced harmonic oscillator (FHO).[2,3] The FHO model rates were shown to agree very well with the results of the state-of-the-art close-coupled calculations[15-17] and recent experiments.[18-20] The model is applicable up to very high temperatures, high vibrational quantum numbers, and also for multiquantum transitions. Separate cross-sections for vibrational energy transfer from oxygen and nitrogen atom collisions have not been taken into account. Under conditions of appreciable dissociation, these reactions have been shown[21] to have an effect on the vibrational distribution of N_2.

To compare the present master equation model with kinetic models commonly used in nonequilibrium hypersonic aerodynamics calculations, we also ran a code based on simplified vibrational and chemical kinetics.[9] It incorporates one equation for the vibrational energy of each diatomic species (the VDF is therefore assumed to be Boltzmann with vibrational temperature T_v). The rates of nonequilibrium chemical reactions (forward reactions (2-5)) are calculated according to the Park model,[1]

$$k(T,T_v) = k_{eq}(T^s \cdot T_v^{1-s}), \quad s = 0.7, \tag{19}$$

where k_{eq} is the equilibrium rate constant at $T=T_v$, given by Eqs. (7-11). This model will be called "Model I" throughout the remainder of the present work, while the master equation model will be referred to as "Model II".

Model I has been previously validated by comparing the predicted and the experimental[8] NO radiation profiles behind the shock for shock velocities u_s=3-4 km/s, showing good overall agreement.[9] However, Model I is based on experimental relaxation data, available only for not too high temperatures, and on the empirical nonequilibrium reaction rate model of Eq. (19). Therefore, it has no predictive capability for modeling of gas flows behind strong shocks at u_s>4 km/s. On the other hand, Model II, that incorporates validated nonperturbative relaxation rate models and nonempirical impulsive rate models of nonequilibrium chemical reactions, can be used up to high temperatures. Note, however, that the use of parameter β=0.25, measured at T~300K,[14] at high temperatures needs to be validated by comparing the rate of Eqs. (12) and (14) and the results of trajectory calculations, where available.

In the normal shock calculations, the initial conditions for the translational temperature, pressure, density and gas velocity immediately behind the shock are given by the Rankine-Hugoniot normal shock relations. The initial vibrational energy distribution function (VDF) for each of diatomic species is a Boltzmann distribution with the vibrational temperature assumed to be equal to the gas temperature before the shock. The initial concentrations of N, O, and NO are taken to be negligibly small, except for the bow shock calculation at a 100 km altitude, where oxygen in the incoming flow was assumed to be partially photodissociated.

The systems of equations is solved using the standard routine LSODE, the efficient integrator of stiff ordinary differential equations.[22]

4. Results and Discussion

To validate the use of Model II with kinetic rates described in the previous Section for very strong shocks (u_s=7-9 km/s), we first compared its predictions with experiments at lower shock velocities, u_s=3-4 km/s.[8] To obtain the NO IR signal intensity from the calculated concentration of nitric oxide, we used the results of IR spectral analysis, calibrated on the equilibrium NO radiation, measured in the experiment (see Ref. 11 for details). The absolute intensity of the IR signal, S/L, in W/cm·sr is calculated from Eq. (1).

Figures 3 and 4 show typical experimental time-dependent IR signals behind the shock, for the low (u_s=3.06 km/s) and the high (u_s=3.85 km/s) shock velocities, respectively. In both cases the conditions before the shock are T_0=300 K, P_0=2.25 torr (which corresponds to a 40 km altitude), giving the conditions behind the shock T_1=4900K, P_1=210 torr and T_1=7400K, P_1=320 torr, respectively. Also shown in Figs. 3 and 4 are results of calculations by Model I and Model II. One can see that in both cases the predictions of the two models agree well with the experiment.

At the low shock velocity u_s~3 km/s one can clearly see that NO radiation is delayed by an incubation time τ_{inc}(NO) (see Fig. 3). The incubation time, plotted in Fig. 5 against the nitrogen fraction in the mixture, reaches τ_{inc}(NO)~20 μs at u_s=2.97 km/s in an N_2-O_2=95%/5% mixture. At these temperatures (T=4-5 kK for $u_s \approx 3$ km/s), the nitrogen vibrational relaxation time $\tau_{VT}(N_2)$~30 μs is much longer than both the vibrational relaxation time of O_2, $\tau_{VT}(O_2)\sim1$ μs and the O_2 dissociation incubation time, $\tau_{inc}(O_2)\sim1$ μs. This proves that the bottleneck for the NO production at a shock velocity of $u_s\sim3$ km/s is reaction (5) due to vibration-chemistry coupling, rather than due to oxygen dissociation. The same effect, although not seen in the experiments at higher shock velocities due to the limited time resolution of about 1 μs, has been observed in all normal shock calculations for u_s=3-4 km/s. At the high shock velocities, $u_s\sim4$ km/s, there exists the well-known overshoot in radiation intensity before the reverse reactions (5,6) take over and the NO concentration reaches equilibrium (see Fig. 4).

Calculations made for 16 experimental conditions (u_s=3-4 km/s) in three N_2-O_2 mixtures (95%/5%, 78%/22%, and 60%/40%) all show good agreement between experimental and calculated radiation signals. For example, Figs. 6 and 7 show the experimental and calculated radiation rise time (time to signal half-maximum), as functions of shock velocity, for two different N_2-O_2 mixtures. Also, the results of calculations did not reveal any substantial difference between the predictions of Model I and Model II, which were quite close for all considered experimental conditions. This is expected for two reasons. First, nonequilibrium rates of dissociation and of bimolecular reactions (2-6) by the Macheret-Fridman-Rich model can be approximated fairly well by the Park formula (Eq. (19)), except for the case of extreme disequilibrium $T_v/T<0.1$ (see Ref. 22 for dissociation reactions (2,3) and Fig. 8 for reaction (5)). Second, for the temperatures T<8 kK, the effect of multi-quantum relaxation on the vibrational energy distribution function (VDF) of N_2 and O_2 is not very dramatic, so that the VDF, calculated by the state-to-state kinetic model (Model II), is Boltzmann-like. A considerable deviation from a Boltzmann distribution occurs only at $T_v/T<<1$ for the high vibrational levels, when their populations are very low. Finally, since at these temperatures most of the NO behind the normal shock is produced at $T_v(O_2)/T>T_v(N_2)/T>0.4$, both models should give close results, as they actually do.

To compare the predictions of Model I and Model II at very high shock velocities, we ran the normal shock code for air at u_s=9 km/s, T_0=220 K, P_0=40 mtorr (these conditions correspond to a 70 km altitude). We note that in this case the first-order vibrational relaxation model used in Model I and based on the low-temperature experimental data, has no predictive capability and may be not applicable at all. Indeed, Fig. 9 shows that the vibrational temperature of nitrogen, predicted by Model I, is several times higher than the temperature of the first vibrational level,

$$T_v^{N_2} = \frac{\omega_e(1-2x_e)}{\ln(f_0 / f_1)}, \tag{20}$$

as given by Model II. In Eq. (20), f_0 and f_1 are relative populations of vibrational levels v=0 and v=1, respectively. Figure 10 compares the VDFs calculated by the two models, showing that the Model II VDF is strongly non-Boltzmann and that the relative populations of high vibrational levels, predicted by Model II, are generally lower. One might expect the NO production rate given by Model II to be also lower than given by Model I. However, one can see from Fig. 9 that the predictions of NO production by the two models are again very close.

The reasons for this behavior are as follows. First, molecular dissociation at these high temperatures (T>20 kK in the region of the most intensive NO production x<0.05 cm) is very rapid. The dissociation rates in this region only weakly depend on the vibrational temperature, while the rates for N_2 and O_2 dissociation become comparable (see Ref. 22). Dissociation therefore becomes the major source of both N and O atoms, so that the Zel'dovich mechanism reactions (5) and (6) are no longer coupled in a chain. Under these conditions, NO is produced mainly in the second Zel'dovich reaction (6), which has very low activation energy and therefore is not vibrationally stimulated. Second, at these high temperatures the rate of another NO-producing reaction, the vibrationally induced reaction (5), also weakly depends on the vibrational temperature or on the VDF (see Fig. 8). Obviously, when the gas temperature is comparable to the reaction activation energy ($E_a \approx 38$ kK for reaction (5)), a considerable part of all N_2 molecules can react with O atoms regardless of how much vibrational energy they have. Thus, NO production behind strong shocks is very weakly coupled to the vibrational energy of the gas.

A considerable difference between the two model predictions does occur in the first stage of relaxation when $T_v/T \ll 1$. The Model II NO production rate in this region exceeds the prediction of Model I by as much as an order of magnitude (not seen in Fig. 9 because the rates are small). This effect is due to the unphysical behavior of the Park model chemical reaction rates (19), incorporated in Model I, at $T_v/T \to 0$, when they tend to zero (see Ref. 23 and Fig. 8). However, this effect is strongly overshadowed by the much greater amount of NO produced in the less nonequilibrium stage (at higher T_v/T ratio), where the prediction of both models are getting much closer.

The effect of the reaction rate behavior at extreme vibrational disequilibrium (when $T_v/T<<1$), first studied by Boyd et al.,[23] may be very dramatic for low density bow shocks, where there is no clearly defined shock wave. To separately estimate the sensitivity of the NO production rate to the chemical reaction and vibrational relaxation rate models, we used the results of the DSMC bow shock flow field calculations.[23] In the following calculations, the gas velocity, temperature, and pressure along the stagnation streamline (see Figs. 11 and 12) were used as input data for the overlay modeling of vibrational relaxation and chemical reactions in the gas flow on this streamline. This uncoupled approach assumes that the resulting variations in N, O, and NO mole fractions are quite small and do not substantially perturb the flowfield. It is also assumed that the use of the FHO model, rather than the more simplified vibrational relaxation model incorporated in the DSMC calculations,[23] would not change the flowfield since both models predict very close vibrational relaxation times τ_{VT}.[10]

The input flowfield data and the results of the calculations for air at the two altitudes of 88 and 100 km are shown in Figs. 11 and 12, respectively. One can see that in both cases there exists a region of extreme vibrational disequilibrium, $T_v/T<0.1$, while the stagnation point temperature is much less than the maximum gas temperature behind the shock, $T_{st}/T_{max}\sim0.1$. In these calculations, we used four different kinetic models: (i) Model II; (ii) Model I (both described in the Section 3); (iii) Model I with $s=0.5$ instead of $s=0.7$ in Eq. (19); and (iv) Model I with the Macheret-Fridman-Rich (MFR) reaction rates instead of the Park rates of Eq. (19).

At an 88 km altitude ($u_s=5$ km/s, see Fig. 11), the use of the MFR reaction rate model leads to a one and a two orders of magnitude increase in NO concentration, compared to the Park model (19) with $s=0.7$ and $s=0.5$, respectively. This result is in qualitative agreement with the 3-D DSMC calculations of Boyd et al.,[23] who use the MFR model for dissociation reactions only, and predict an order of magnitude increase compared to the Park model with $s=0.5$. The much faster NO production, predicted by the MFR model, compared to the Park model, occurs due to two equally important factors.

First is the greater rate of oxygen dissociation at $T_v/T \rightarrow 0$, discussed in Ref. 23 and resulting in the earlier triggering of the Zel'dovich mechanism chain reactions (5) and (6), so that they occur at a higher translational temperature. Second is the higher rate of the key NO production reaction (5) in the region of extreme disequilibrium (see Fig. 8). One can also see that the NO production rate is only weakly sensitive (within a factor of two) to the vibrational relaxation model (curves "MFR" and "FHO+MFR" in Fig. 11). This happens because the calculated vibrational temperature is so low that chemical reactions (2-6) proceed mainly from the ground vibrational level.

The main difference of NO production kinetics at a 100 km altitude (u_s=8 km/s) is that there is already enough photodissociated oxygen in the incoming flow (~4% of the mixture).[23] Thus, delayed oxygen dissociation is no longer a trigger for the Zel'dovich mechanism reactions. Calculations at this altitude, shown in Fig. 12, therefore demonstrate only the effect of the variation of the reaction (5) nonequilibrium rate. One can see that the predictions of all models are closer than at an 88 km altitude, giving about an order of magnitude difference between the Park, s=0.5 model and the MFR model. The predicted NO concentrations in the vicinity of the stagnation point are very close for all models. NO production here is compensated by its decomposition in the reverse reaction (5,6), so that NO mole fraction reaches a quasi-equilibrium value and is not rate-sensitive. We note that the overlay approximation in the stagnation point region is no longer valid, since NO model fraction here reaches several percent. Finally, the effect of the vibrational kinetics rate model on NO concentration is again negligibly small, due to the very low vibrational temperature in the region of the most intensive NO production.

5. Summary

In the present work, we have analyzed nitric oxide production kinetics behind strong normal and bow shocks. The nonempirical self-consistent state-to-state kinetic model, described here (Model II), was validated by comparison with shock tube experiments, for the shock velocities u_s=3-4 km/s. The results of the calculations illustrate, however, that a simplified kinetic model (Model I) and the Model II predict very close NO production rates behind normal shocks up to very high shock velocities u_s=9 km/s. This justifies the use of Model I in normal shock calculations.

NO production kinetics behind bow shocks is simulated by an overlay modeling of the gas flow along the stagnation streamline, with the results of the DSMC flowfield calculations[23] used as inputs. The results of the overlay calculations support the idea of Boyd et al.[23] that correct modeling of vibration-dissociation coupling in extreme vibrational disequilibrium is one of the most crucial points in prediction of NO radiation behind the low density bow shocks. Our data also show that taking into account the vibrational coupling in bimolecular reaction (5,6) is equally important. Satisfactory agreement obtained in Ref. 23 between the DSMC calculations and the flight data allows suggesting the Macheret-Fridman-Rich dissociation and bimolecular reaction rate model for the use in hypersonic aerodynamics calculations. On the other hand, these results demonstrate that the NO production rate is only weakly affected by the vibrational relaxation rate model. We also note that a reliable prediction of the NO ultraviolet radiation behind shocks requires additional studies of mechanisms of electronically excited NO formation, which are far from being understood at this time.

References

1. Park, C., *Nonequilibrium Hypersonic Aerodynamics,* Wiley, New York, 1990, Chap.3.
2. Adamovich, I.V., Macheret, S.O., Rich, J.W., and Treanor, C.E., "Vibrational Relaxation and Dissociation Behind Shock Waves. Part 1: Kinetic Rate Models", *AIAA Journal,* Vol.33, No. 6, 1995, pp. 1064-1069.
3. Adamovich, I.V., Macheret, S.O., Rich, J.W., and Treanor, C.E., "Nonperturbative Analytic Theory of V-T and V-V Rates in Diatomic Gases, Including Multi-Quantum Transitions", AIAA Paper 95-2060, June 1995.
4. Macheret, S.O., Fridman, A.A., and El'kin, A.A, "Rates Constants of Exchange Reactions in Nonequilibrium Conditions: Classical Model", *Khimicheskaya Fizika (Soviet Chemical Physics),* Vol. 9, No. 2, 1990, pp. 174-179.
5. Macheret, S.O., and Rich, J.W, "Nonequilibrium Dissociation Rates Behind Strong Shock Waves", *Chemical Physics,* Vol. 174, No.1, 1993, pp. 25-43.

6. Macheret, S.O., Fridman, A.A, Adamovich, I.V., Rich, J.W., and Treanor, C.E, "Mechanisms of Nonequilibrium Dissociation of Diatomic Molecules", AIAA Paper 94-1984, June 1994.

7. Wurster, W.H., Treanor, C.E., and Williams, M.J., "Kinetics of UV Production Behind Shock Waves in Air", AIAA Paper 90-1666, June 1990.

8. Wurster, W.H., Treanor, C.E., and Williams, M.J. "Non-equilibrium Radiation from Shock-Heated Air", Final Report. U.S. Army Research Office, Contract No. DAAL03-88K-0174, July 1991, Calspan UB Research Center, Buffalo, NY.

9. Treanor, C.E., and Williams, M.J., "Kinetics of Nitric Oxide Formation Behind 3 to 4 km/s Shock Waves", Final Report. U.S. Army Research Office, Contract No. DAAL03- 92K-0003, February 1993, Calspan UB Research Center, Buffalo, NY.

10. Clark, J.F., and McChesney, M., *Dynamics of Real Gases,* Butterworths, London, 1976, Chap. 2.

11. Adamovich, I.V., Macheret, S.O., Rich, J.W., and Treanor, C.E., "Vibrational Relaxation and Dissociation Behind Shock Waves. Part 2: Master Equation Modeling", *AIAA Journal,* Vol.33, No. 6, 1995, pp. 1070-1075.

12. Camac, M., Feinberg, R., and Teare, J.D., "The Production of Nitric Oxide in Shock-Heated Air", Avco Research Report 245, December 1966.

13. Monat, J.P., Hanson, R.K., and Kruger, C.H., "Shock Tube Determination of the Rate Coefficients for the Reaction $N_2+O \rightarrow NO+N$", Proceedings of the 17th International Symposium on Combustion", 1978, pp. 543-548.

14. Black, G., Sharpless, R.L., and Slanger, T.G., "Measurements of Vibrationally Excited Molecules by Raman Scattering. I. The yield of Vibrationally Excited Nitrogen in the Reaction $N+NO \rightarrow N_2+O$", *Journal of Chemical Physics,* Vol. 58, No. 11, 1973, pp. 4792-4797.

15. Billing, G.D., and Fisher, E.R., "VV and VT Rate Coefficients in N_2 by a Quantum-Classical Model", *Chemical Physics,* Vol. 43, No. 3, 1979, pp. 395-401.

16. Billing, G.D., and Kolesnick, E.R., "Vibrational Relaxation of Oxygen. State to State Rate Constants", *Chemical Physics Letters,* Vol. 200, No. 4, 1992, pp. 382-386.

17. Billing, G.D., "VV and VT Rates in N_2-O_2 Collisions", *Chemical Physics,* Vol. 179, No.3, 1994, pp. 463-467.

18. Price, J.M., Mack, J.A., Rogaski, C.A., and Wodtke, A.M., "Vibrational-State-Specific Self-Relaxation Rate Constant. Measurements of Highly Vibrationally Excited O_2 (v=19-28)", *Chemical Physics,* Vol. 175, No. 1, 1993, pp. 83-98.

19. Park, H., and Slanger, T.G., "O_2(X,v=8-22) 300 K Quenching Rate Coefficients for O_2 and N_2, and O_2(X) Vibrational Distribution from 248 nm O_3 Photodissociation", *Journal of Chemical Physics,* Vol. 100, No. 1, 1994, pp. 287-300.

20. Klatt, M., Smith, I.W.M., Tuckett, R.P., and Ward, G.N., "State-Specific Rate Constants for the Relaxation of $O_2(X^3\Sigma_g^-)$ from Vibrational Levels v=8 to 11 by collisions with NO_2 and O_2", *Chemical Physics Letters,* Vol. 224, No. 2, 1994, pp. 253-259.

21. Armenise, I., Capitelli, M., Celiberto, R., Colonna, G., Gorse, C., Lagana, A. "The Effect of $N+N_2$ Collisions on the Non-equilibrium Vibrational Distributions of Nitrogen under Reentry Conditions", Chemical Physics Letters, Vol. 227, pp. 157-163, 1994.

22. Hindmarsh, A.C., "ODE Solvers for Use With the Metod of Lives", UCRL-85293. Preprint, Lawrence Livermore Laboratory, March 1981.

23. Boyd, I.D., Candler, G.V., and Levin, D.A., "Dissociation Modeling in Low Density Hypersonic Flows of Air", *Physics of Fluids,* Vol.7, No. 7, 1995, pp. 1757-1763.

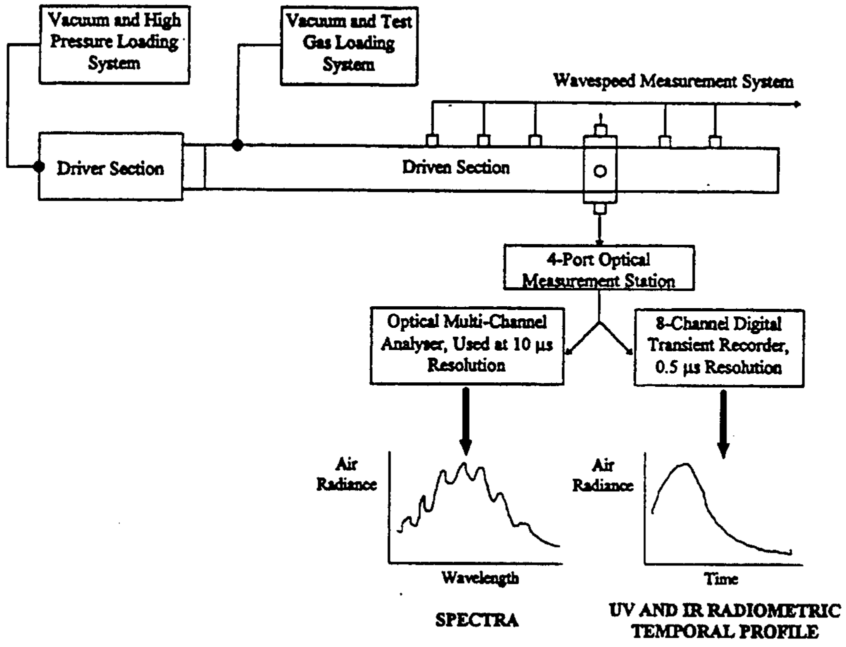
Vacuum and High Pressure Loading System
Vacuum and Test Gas Loading System
Wavespeed Measurement System
Driver Section
Driven Section
4-Port Optical Measurement Station
Optical Multi-Channel Analyser, Used at 10 μs Resolution
8-Channel Digital Transient Recorder, 0.5 μs Resolution
Air Radiance
Wavelength
SPECTRA
Air Radiance
Time
UV AND IR RADIOMETRIC TEMPORAL PROFILE

Figure 1. Principal elements of the shock tube radiation experiment

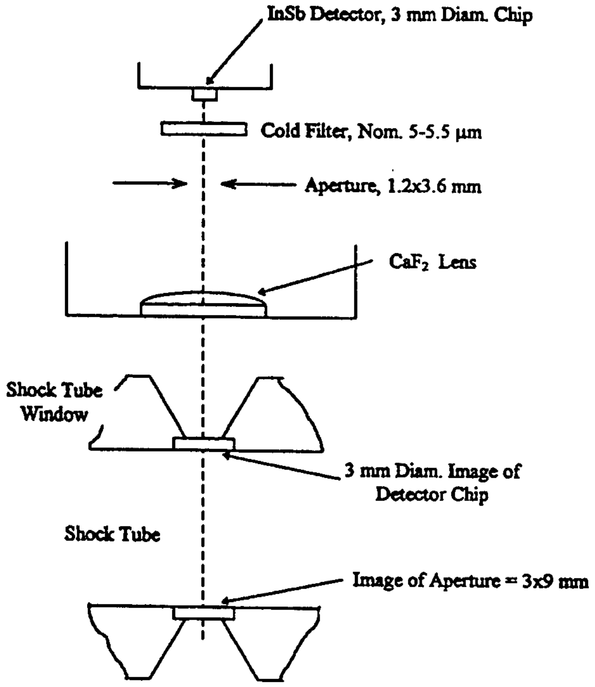
InSb Detector, 3 mm Diam. Chip
Cold Filter, Nom. 5-5.5 μm
Aperture, 1.2x3.6 mm
CaF₂ Lens
Shock Tube Window
3 mm Diam. Image of Detector Chip
Shock Tube
Image of Aperture = 3x9 mm

Figure 2. Major elements of the IR radiometer - shock tube system. The beam in the shock tube is wedge-shaped, optimized for axial resolution at 3 mm, and for throughput by a 9-mm width across the tube at the lower window.

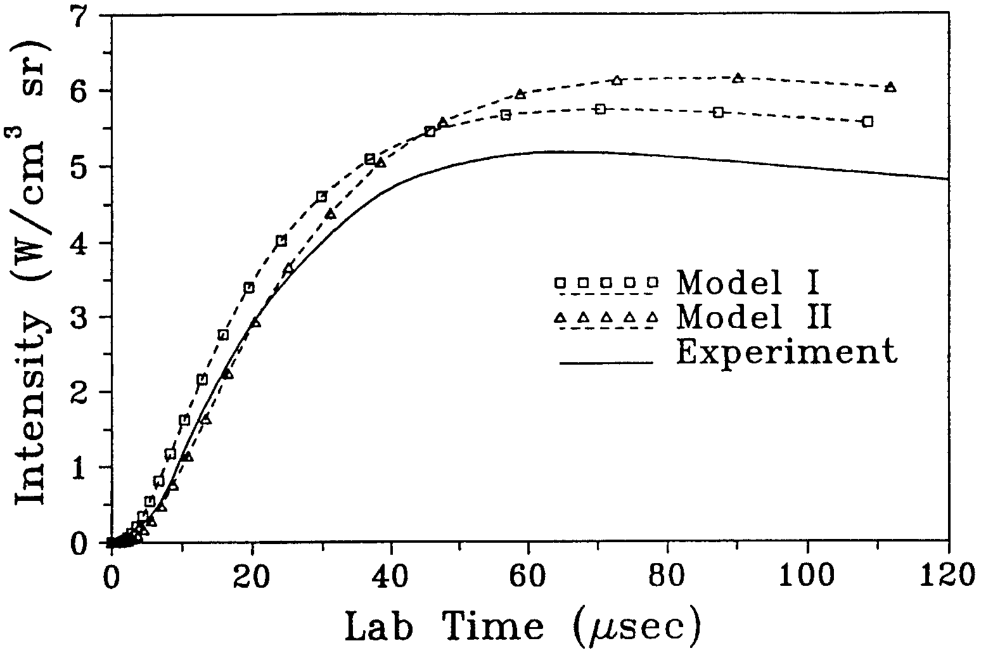

Figure 3. Experimental and calculated NO infrared radiation profiles behind the normal shock. N_2:O_2=60:40, u_s=3.06 km/s, P_0=2.25 torr

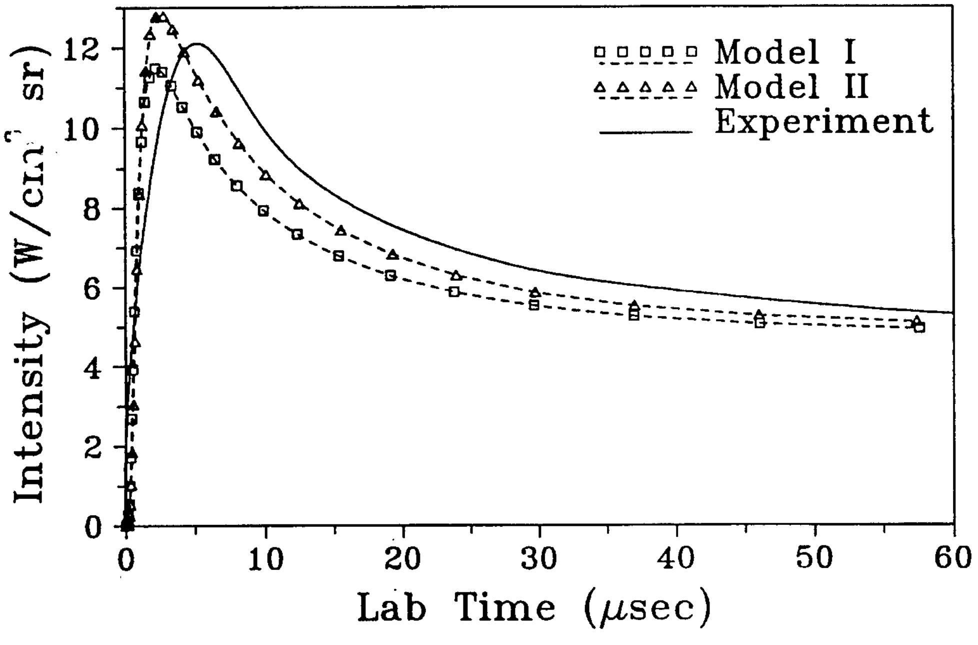

Figure 4. Experimental and calculated NO infrared radiation profiles behind the normal shock. N_2:O_2=77.7:22.3, u_s=3.85 km/s, P_0=2.25 torr

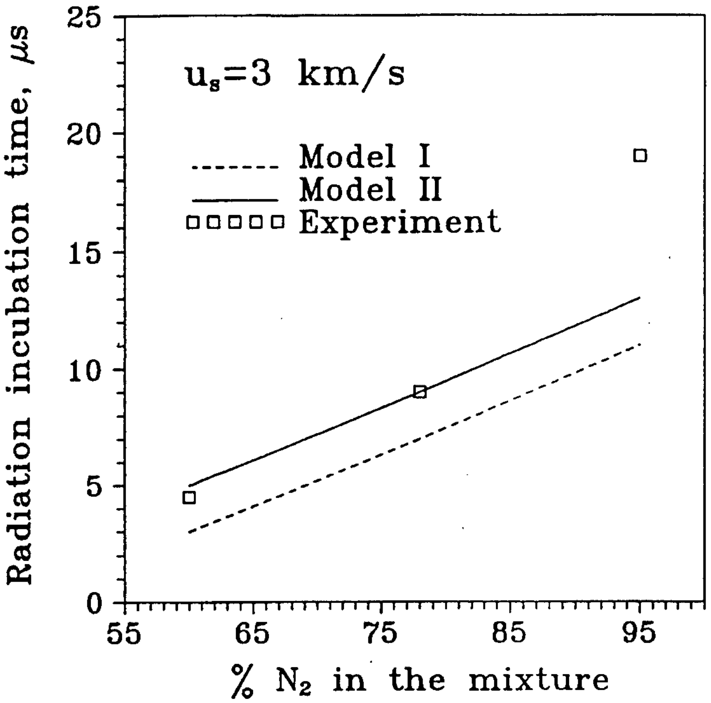

Figure 5. Experimental and calculated NO IR radiation incubation time at u_s= 3 km/s as a function of the nitrogen mole fraction in the mixture

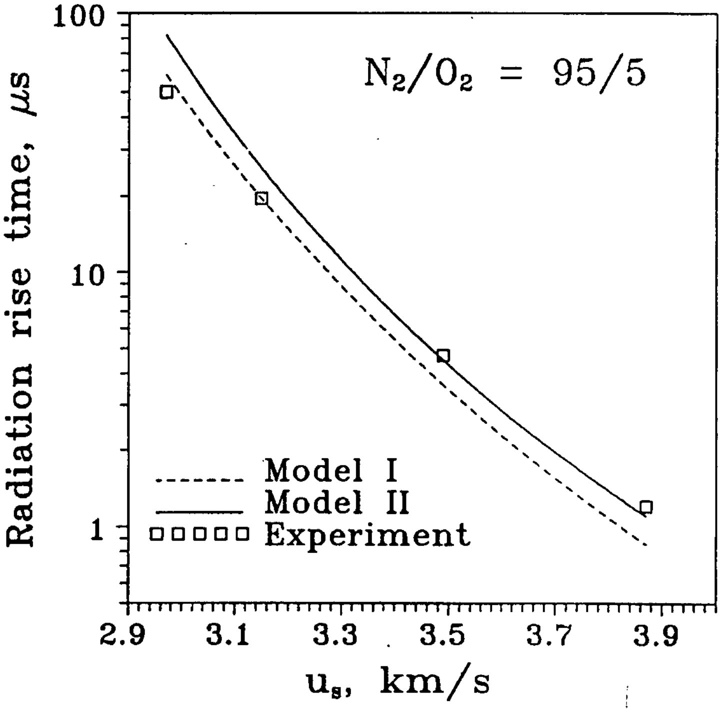

Figure 6. NO IR radiation rise time (time to the half-maximum) as a function of the shock velocity. N_2:O_2=95:5

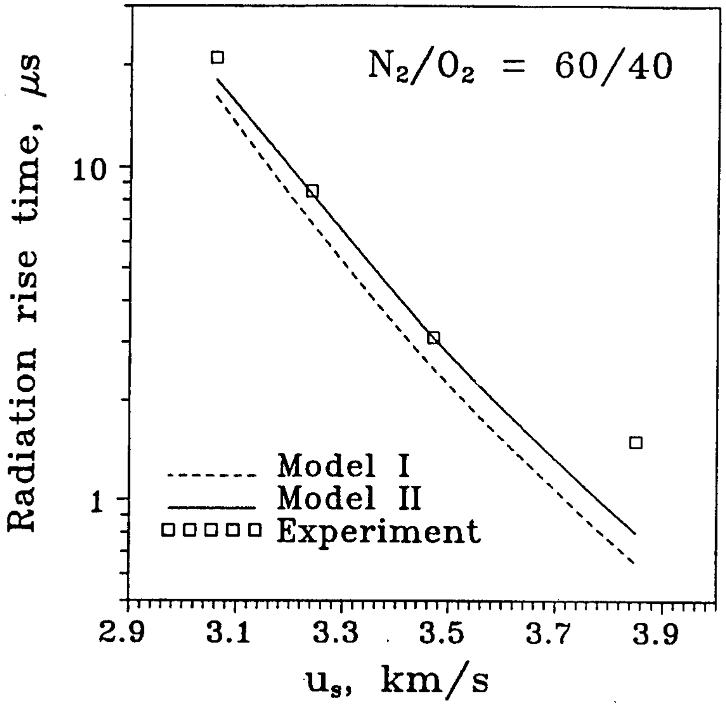

Figure 7. NO IR radiation rise time (time to the half-maximum) as a function of the shock velocity. $N_2:O_2=60:40$

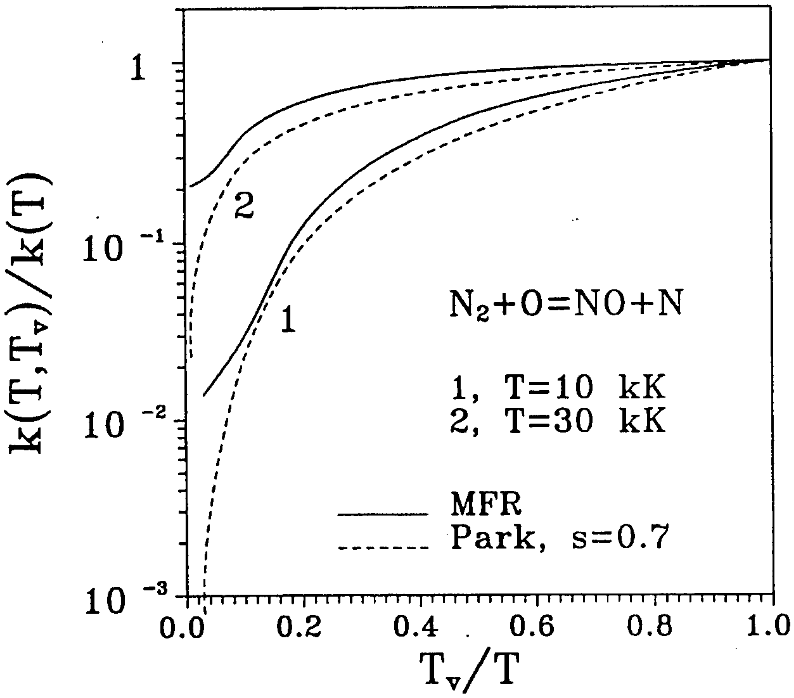

Figure 8. Nonequilibrium rate of reaction (5) according to the Macheret-Fridman-Rich and the Park models

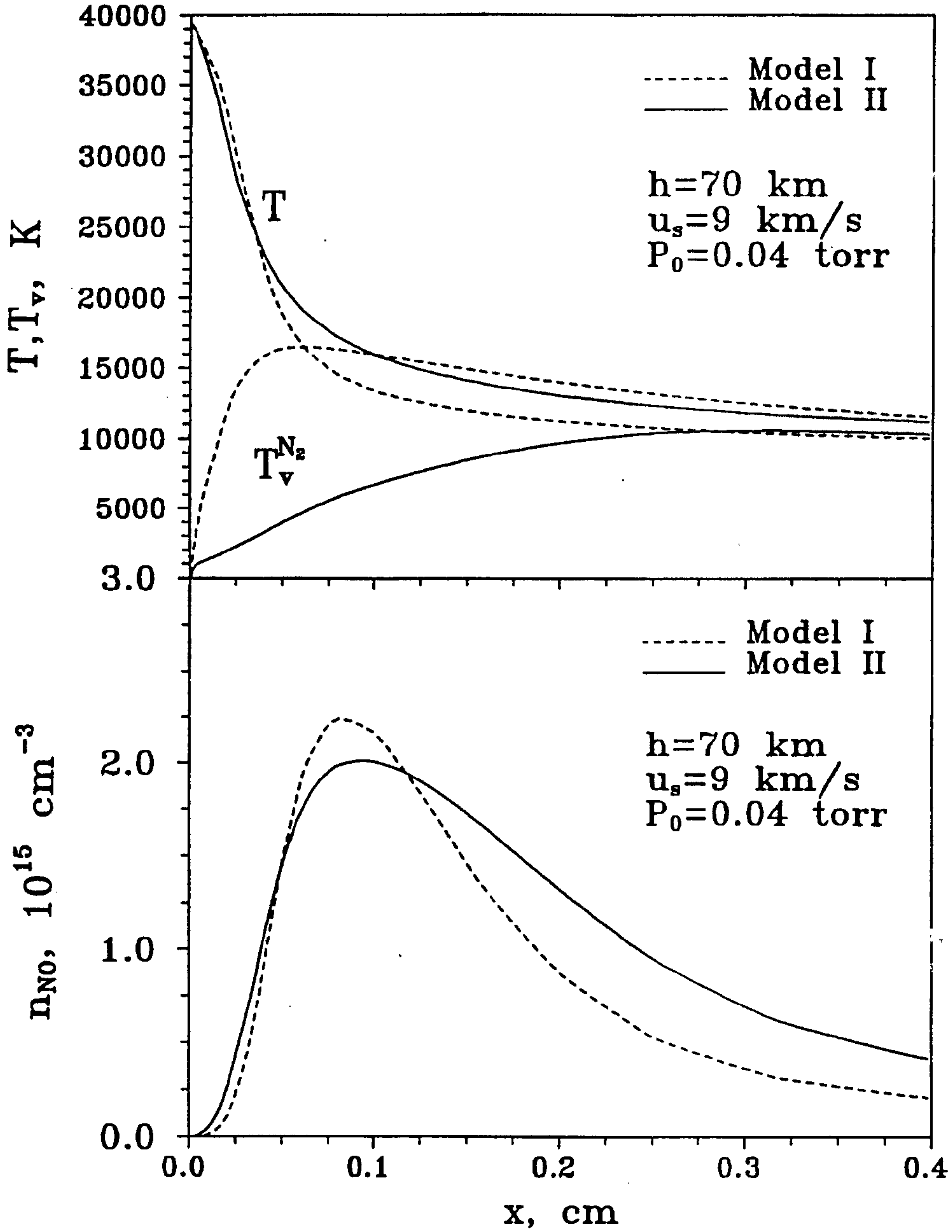

Figure 9. Vibrational relaxation and NO production behind a strong normal shock. h=70 km, u_s=9 km/s, P_0=40 mtorr

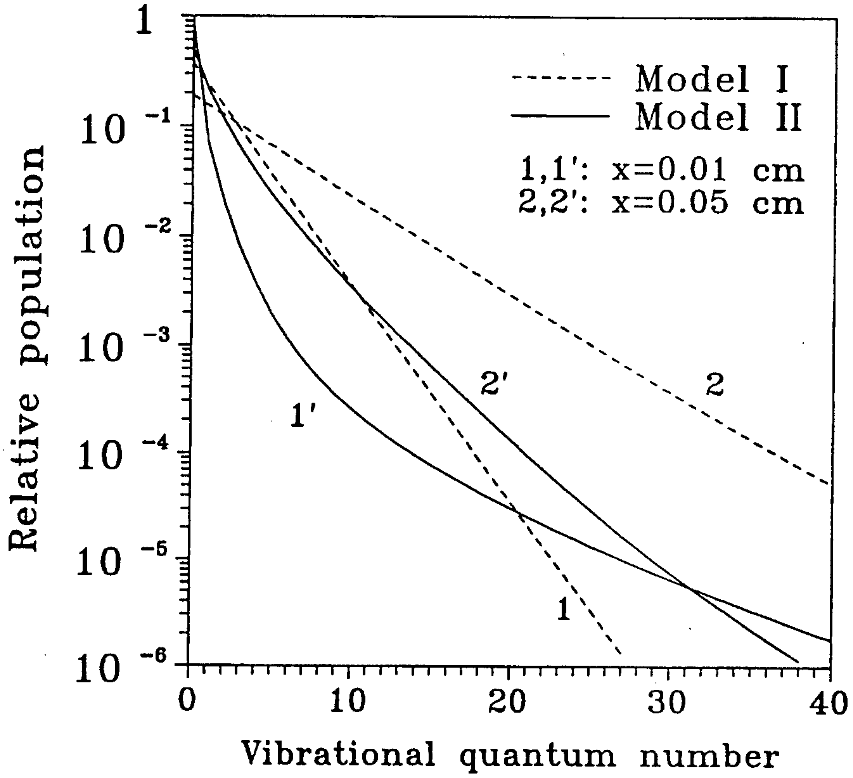

Figure 10. Vibrational distribution function of N_2, calculated by Model I and Model II for the conditions of Fig. 9

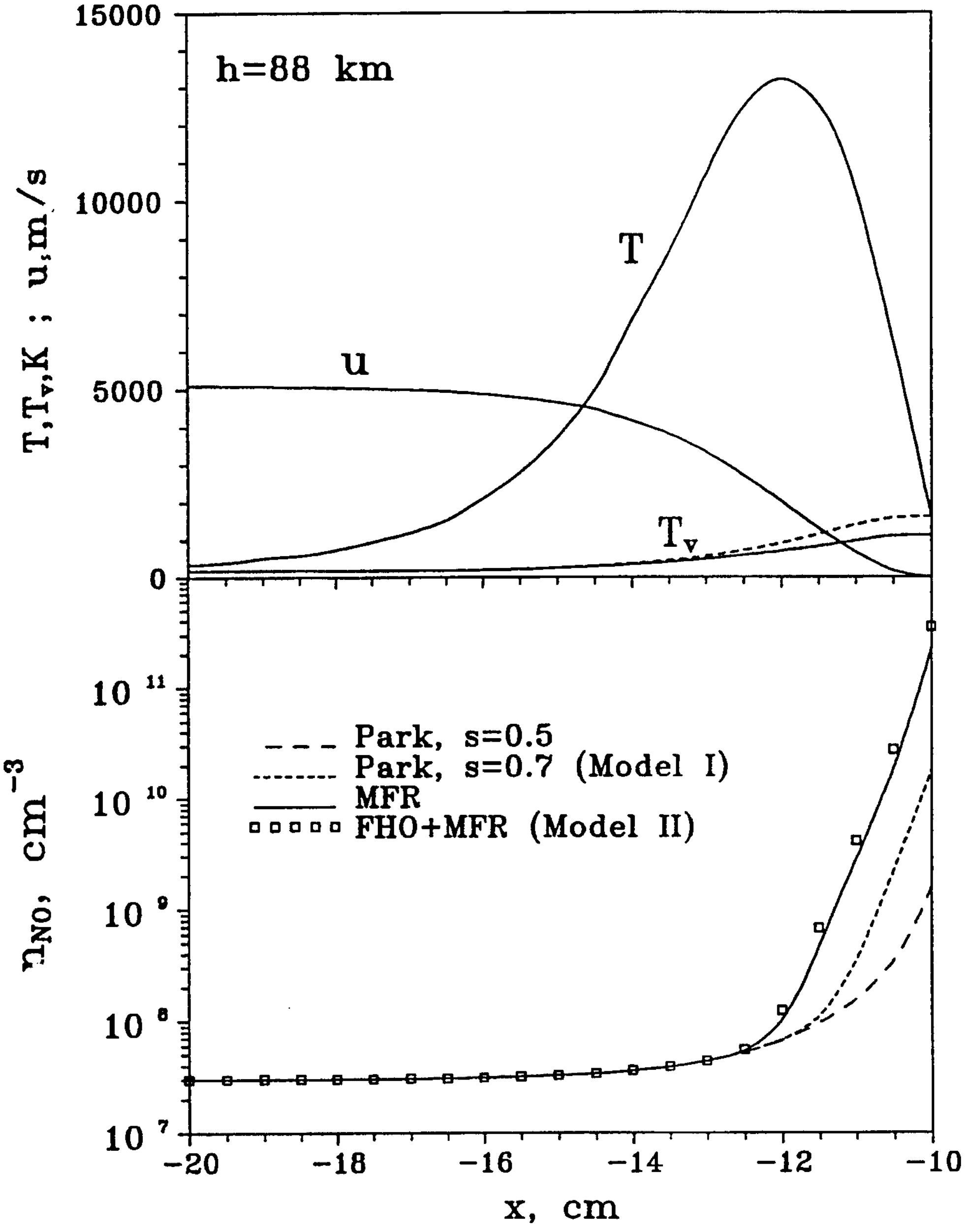

Figure 11. The DSMC flowfield data (upper part), and the NO concentration (lower part) on the stagnation streamline. h=88 km, u_s= 5 km/s, P_0=1.9 mtorr. The two curves for $T_v^{N_2}$ in the upper part are predicted by Model I (dashed curve) and Model II (solid curve)

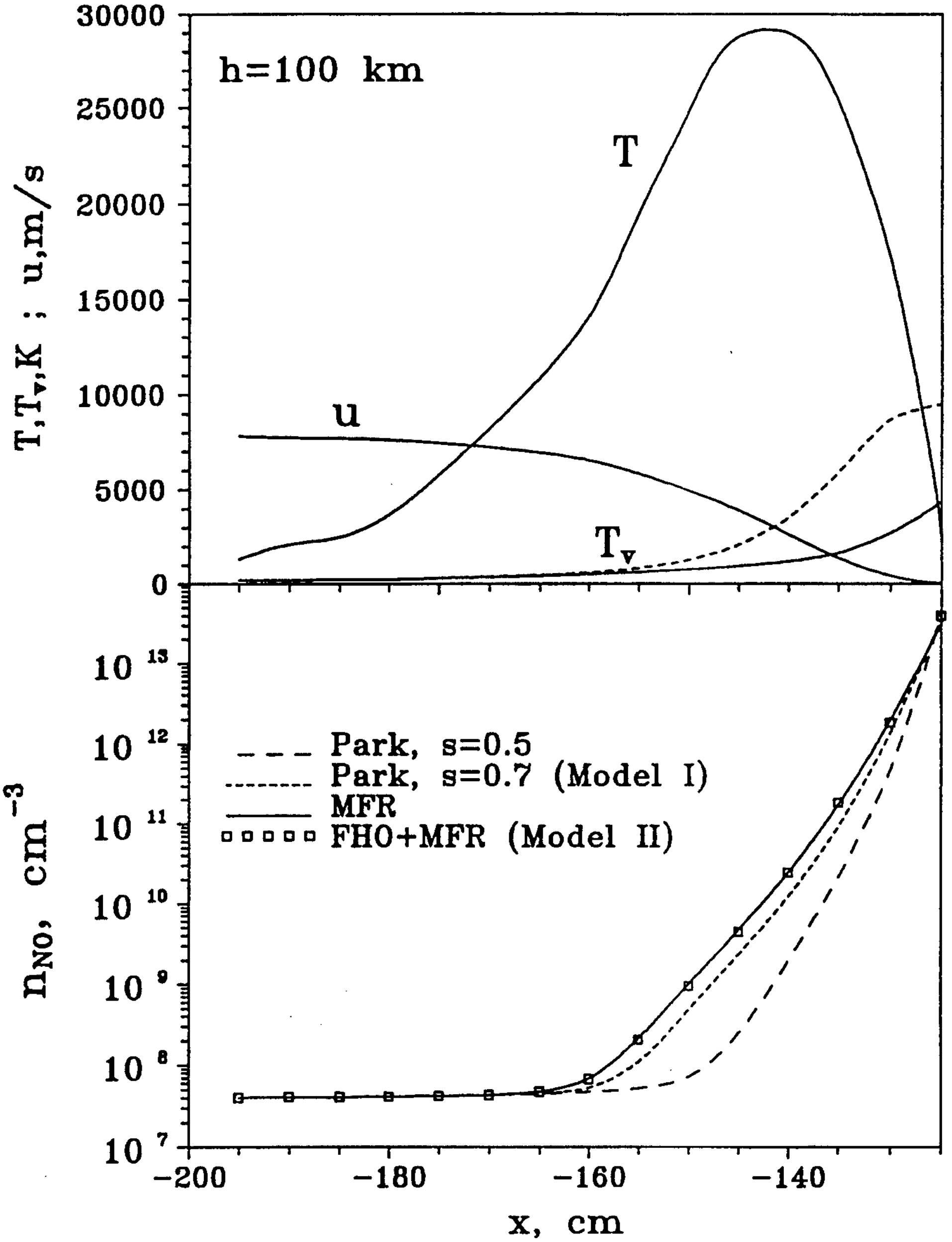

Figure 12. The DSMC flowfield data (upper part), and the NO concentration (lower part) on the stagnation streamline. h=100 km, u_s= 8 km/s, P_0=1.6 mtorr. The two curves for $T_v^{N_2}$ in the upper part are predicted by Model I (dashed curve) and Model II (solid curve)

CHAPTER XI.

FEASIBILITY STUDY OF MHD ACCELERATION OF UNSEEDED AND SEEDED AIR FLOWS

Nomenclature

B - magnetic field, T

B_i - rotational constant of the diatomic species, eV

c_f - skin friction coefficient

c_h - heat transfer coefficient

c_p^f - frozen specific heat at constant pressure, J/kg/K

D - electron beam load, eV/mol/s

E - electric field, V/m

ΔE_{beam} - absorbed electron beam power, W

$E_{vib,i}(T)$ - equilibrium vibrational energy of the species, J/kg

$E_{vib,i}(x)$ - nonequilibrium vibrational energy of the species, J/kg

e - electron charge, C

F - channel cross-section, m^2

$f_i(v)=n_i(v)/n_i$ - relative population of vibrational level v of ith species (vibrational distribution function)

G - mass flowrate, kg/s

G_i^0 - Gibbs free energy of the species at standard pressure, J/kg

g_i - g-factors, efficiencies of electron beam initiated processes, mol/eV

h_i - specific enthalpy of the species, J/kg

h - enthalpy of the mixture, J/kg

$H=h+u^2/2$ - total enthalpy, J/kg

j - current density, A/m^2

j_{beam} - electron beam current density, A/m^2

l - electron beam penetration length, m

L - MHD channel length, m

k - Boltzmann constant, J/K

k_{ion} - rate of ionization, cm^3/s

k_{rec} - rate of electron recombination, cm^3/s

k_{att} - rate of electron attachment, cm^3/s

$k_{ij}(v \to w)$ - vibration-translation rates, cm^3/s

$k_{ij}(v,v' \to w,w')$ - vibration-vibration rates, cm^3/s

$k_{ej}(v \to w)$ - electron-vibration (e-V) rates, cm^3/s

$k(v \to ,T)$, $k(\to v,T)$ - state-specific chemical reaction rates, cm^3/s

M_f - frozen Mach number

δM_f - correction to the frozen Mach number due to vibrational specific heat

m_e - electron mass, kg

m_p - proton mass, kg

$n_i(v)$ - absolute population of vibrational level v of ith species, mol/m^3

n_i - number density of the species, mol/m^3

N - total number density, mol/m^3

P - pressure, Pa

P_0 - standard pressure (1 atm)

Pr - Prandtl number

$Q_{tr,i}$ - electron transport cross-section for i^{th} species, m^2

$Q_{rot,i}$ - rotational excitation cross-section, m^2

$Q_{vib,i}$ - vibrational excitation cross-section, m^2

$Q_{el,i}$ - electronic excitation cross-section, m^2

$Q_{ion,i}$ - ionization cross-section, m^2

R_0 - universal gas constant, J/kmol/K

r - channel half-width, m

Re_d - Reynolds number based on the channel width

Re_x - Reynolds number based on the axial coordinate

S - entropy, J/kg/K

T - heavy species translational temperature, K

$T_{v,i}$ - species vibrational temperatures, K

T_e - electron temperature, K

$T_{ref}=300$ K - reference temperature

u - gas velocity, m/s

$x_{e,i}$ - anharmonicity of ith diatomic species

x - axial coordinate, m

y - transverse coordinate, m
z - magnetic field direction

β - Hall parameter
$\gamma = c_p^f / c_v^f$ - frozen specific heat ratio
δ - boundary layer thickness, m
ε - plasma (secondary) electron energy, eV
ε_{beam} - beam electron energy, eV
μ_i - species molecular weight, kg/kmol
μ - mixture molecular weight, kg/kmol
$\nu_0 = (e/m_e)B$ - plasma frequency, s^{-1}
$\langle \nu \rangle$ - electron-heavy species collision frequency, s^{-1}
ρ - gas density, kg/m^3
σ - electric conductivity, mhos/m
$\phi_i = (n_i/n)$ - species mole fractions
ϕ_e - ionization fraction
$\xi_i = (n_i/n) \cdot (\mu_i/\mu)$ - species mass fractions
$\omega_{e,i}$ - vibrational quantum of diatomic species, K
Ω - instability increment, s^{-1}

1. Introduction

The MARIAH program is a NASA-sponsored program the objective of which is to investigate the applicability of MHD as a driver for hypersonic test facilities. The focus of this program is to demonstrate the feasibility of such drivers in the context of high speed combustion test facilities, such as might be suitable for testing advanced hypersonic airbreathing engine concepts. Previous papers have reported on the concept [1] and the basic requirements for such a facility [2].

In this work we report on an analysis of MHD accelerators which was conducted as a part of the MARIAH program for the purpose of investigating the performance limits of such devices. This analysis is based on a one-dimensional simulation of the entire flow train, starting at the plenum, passing through the nozzle and MHD accelerator, and continuing through the secondary expansion duct up to the inlet of the test section. Several issues have been investigated using this model, such as (a) the question of pressures needed in the heater or plenum region, (b) whether electron beam addition can be utilized to enhance the unseeded flow conductivity in the MHD duct, (c) the question of seeded vs. unseeded flows, and (d) issues relating to basic thermodynamic limits of such drivers. These issues are discussed and reported on in some depth in the following sections.

There are several basic requirements which have been used to define the testing scenario and the performance objectives of the present study. These have been discussed in previous papers [1-3]. Since they largely define the operating scenario for the MHD flow train, these requirements are summarized below:

(a) The hypothetical test facility should be a "test and evaluation" facility in the sense that test duration of the order of tens of seconds to minutes can be obtained.

(b) The facility should be capable of testing advanced engine modules at near full scale. An area cross section for the test section of 80 square feet has been adopted as a working number.

(c) The facility should be capable of simulating true total enthalpy and thermodynamic conditions. For engine testing, this implies that the Mach numbers, total enthalpies, and entropies should match those seen behind the bow shock of the hypersonic aircraft. The facility should be capable of matching post bow shock conditions corresponding to the 2000 lb/ft^2 free stream dynamic pressures trajectory.

(d) The facility should provide an air stream chemistry corresponding approximately to the post-bow shock regime of the aircraft; i.e. - having minimal dissociation, vibrational non-equilibrium and contaminants.

(e) The facility should be a true "test and evaluation" facility. This implies high testing throughput, high reliability and lifetimes for critical components, and versatility of the MHD accelerator across a wide range of pressures and Mach numbers.

Analytical studies similar to the present one have been conducted in the past by several researchers [4-6]. The present study is unique in that the flow model incorporates several novel features, namely (a) the inclusion of a Boltzmann equation solver for the electron distribution function, (b) the ability to simulate the addition of electron beam energy directed into the MHD channel, (c) the ability to simulate both chemical kinetics and vibrational nonequilibrium, and (d) the ability to correctly account for all important ionization processes. These capabilities permitted us to systematically explore both the nonequilibrium and the equilibrium flow regimes across a wide spectrum of control parameters. Details of the kinetic model are given in Section 2.

The computer code developed on the basis of the kinetic model was run across a rather large set of control parameters, including variation of seed fraction and type, electron beam energy, plenum pressures and temperatures, and nozzle geometry (see Section 3). The overall objective of the study was to demonstrate whether or not it was possible to place points on the total enthalpy versus entropy diagram corresponding to the post-bow shock, 2000 lb/ft^2 flight trajectory. This has been adopted as the limiting operating envelope for the hypothetical test facility. The major conclusions are given in Section 4.

2. Kinetic modeling

2.1. Kinetic equations

To simulate the gas dynamics and kinetics of both alkali-seeded and unseeded air flows in supersonic nozzles and MHD channels, we have used quasi-one-dimensional nonequilibrium flow kinetic modeling. The model incorporates the following equation groups:

(i) the equations of one-dimensional magnetogasdynamics for nonequilibrium reacting ionized real gases [7,8]

$$\frac{dT}{dx}=\frac{u^2}{c_p^f[1-M_f^2(1-\delta M_f)]}\cdot\left\{\frac{1}{F}\frac{dF}{dx}+\frac{1}{\mu}\frac{d\mu}{dx}-\frac{\gamma M_f{}^2-1}{u^2}\frac{dQ}{dx}+\frac{\gamma M_f{}^2}{u^2}\left[\frac{j_yB_z}{\rho}-\frac{c_fu^2}{r}\right]\right\} \qquad (1)$$

$$\frac{du}{dx}=\frac{1}{u}\left\{\left[\sum_J\xi_J\frac{dE_{vib,J}(T)}{dT}-c_p^f\right]\frac{dT}{dx}+\frac{d\Phi}{dx}\right\} \qquad (2)$$

$$\rho uF=G \qquad (3)$$

$$\frac{P}{\rho}=\frac{R_0T}{\mu}, \qquad (4)$$

where

$$M_f^2=\frac{u^2\mu}{\gamma_fR_0T}, \qquad \delta M_f=\frac{\gamma M_f^2-1}{c_p^fM_f^2}\sum_j\xi_j\frac{dE_{vib,j}(T)}{dT}, \qquad (5)$$

$$E_{vib,j}=\frac{R_0}{\mu_j}\sum_v f_j(v)\left\{\omega_{e,j}v[1-x_{e,j}(v+1)]\right\}, \qquad (6)$$

$$\frac{d\Phi}{dx}=\frac{j_xE_x+j_yE_y}{\rho u}+\frac{eDN}{\rho u}-\frac{2c_h\sum_i \xi_i h_i}{r}-\frac{j_y\left(\frac{k}{e}\sum_{\substack{\text{electrons}\\ \text{ions}}}\frac{\xi_i h_i}{c_{pi}}+\Delta U_e\right)}{\rho u r}-\frac{d\Phi_{\text{chem,vib}}}{dx} \tag{7}$$

In Eq. (1), the terms in the right-hand-side describe gas temperature variation due to nozzle cross-section change, change of molecular weight of the mixture, translational mode energy addition dΦ/dx, push force and wall friction work. Eq. (6) gives the energy stored in vibrational mode of diatomic species such as N_2, O_2, and NO. The terms in the right-hand-side of Eq. (7) describe electric field and electron beam power input (D is the e-beam load per molecule in eV/mol/s), wall heat losses due to heat transfer, enthalpy transfer by the current, and electrode voltage drop ΔU_e, and enthalpy storage in chemical reaction products and vibrational energy mode. The last term in Eq. (7) can be written in the following form:

$$\frac{d\Phi_{\text{chem,vib}}}{dx}=\sum_i h_i(T)\frac{d\xi_i}{dx}+\sum_j\left\{\left[E_{\text{vib},j}(x)-E_{\text{vib},j}(T)\right]\frac{d\xi_i}{dx}+\xi_j\frac{dE_{\text{vib},j}(x)}{dx}\right\} \tag{8}$$

Note that Eq. (8) requires knowledge of both equilibrium and nonequilibrium values of diatomic species vibrational energy, $E_{\text{vib},j}(T)$ and $E_{\text{vib},j}(x)$, respectively. Both of these energies are calculated using Eq. (6), where the equilibrium vibrational distribution function $f_j(v,T)$ is the Boltzmann distribution with temperature T, and the nonequilibrium vibrational level populations $f_j(v,x)$ are given by the master equation (see below). In Eqs. (2,5,7,8), the sum over index *i* is evaluated for all reacting species and the sum over index *j* is taken only for three diatomic species, N_2, O_2, and NO.

(ii) chemical and ionization kinetics equations for a number of reacting species (including electrons, ions, and electronically excited metastable species)

$$\frac{d\xi_i}{dx}=\frac{\rho}{u}\mu_i\sum_j(b_{ij}-a_{ij})W_j, \tag{9}$$

where the sum is taken for all chemical reactions, a_{ij} and b_{ij} are stoichiometric coefficients of ith species in j^{th} chemical reaction

$$\sum_i a_{ij} A_i \leftrightarrows \sum_i b_{ij} A_i \quad , \tag{10}$$

and W_j is the rate of jth chemical reaction per unit stoichiometric coefficient:

$$W_j = \rho^{\sum_i a_{ij} - 2} \left\{ \vec{k}_j \cdot \prod_i \left(\frac{\xi_i}{\mu_i} \right)^{a_{ij}} - \left(\frac{P\mu}{P_0} \right)^{\sum_i (b_{ij} - a_{ij})} \overleftarrow{k}_j \cdot \prod_i \left(\frac{\xi_i}{\mu_i} \right)^{b_{ij}} \right\} \tag{11}$$

In Eqs. (10,11), the sums and the products are taken for all reacting species. In Eq. (11), P_0=1 atm is a standard pressure. For bimolecular reaction $A_1+A_2 \leftrightarrow A_3+A_4$ the expression for W_j is particularly simple:

$$W_j = \vec{k}_j \cdot \frac{\xi_1}{\mu_1} \frac{\xi_2}{\mu_2} - \overleftarrow{k}_j \cdot \frac{\xi_3}{\mu_3} \frac{\xi_4}{\mu_4} \tag{12}$$

For chemical reactions at vibrational equilibrium the reverse reaction rates in Eqs. (11,12) are determined from thermochemical equilibrium,

$$\overleftarrow{k}_j(T) = \vec{k}_j(T) \cdot \exp\left(- \frac{\sum\limits_{\text{products}} b_{ij} G_i^0(T) - \sum\limits_{\text{reactants}} a_{ij} G_i^0(T)}{R_0 T} \right), \tag{13}$$

where $G_i^0(T)$ are the molar Gibbs free energies of species evaluated at a standard pressure P_0=1 atm.

For vibrationally stimulated reactions, such as nonequilibrium dissociation of diatomic molecules

$$AB(v) + M \leftrightarrows A + B + M \tag{14}$$

and bimolecular exchange reactions

$$AB(v) + C \leftrightarrows A + BC \tag{15}$$

the forward rates at vibrational disequilibrium are determined as follows:

$$\vec{k} = \sum_{v} k(v \rightarrow, T) f(v) , \tag{16}$$

where $k(v \rightarrow, T)$ are state-resolved reaction rates (see Section 2.2) and $f(v)$ is nonequilibrium relative population of vibrationally excited diatomic species, given by the master equation. In Eqs. (13-15), AB stands for diatomic molecule, C for atom, M for an collision partner, and v is vibrational quantum number.

For nonequilibrium plasma electron impact processes (ionization, attachment, electronic excitation) the kinetic rates are determined by integration of the cross-sections over the electron energy distribution function (EEDF). For example, for ionization

$$k_{ion} = \frac{2e}{m_e} \int_{E_{ion}}^{\infty} Q_{ion}(\varepsilon) \varepsilon^{1/2} f(\varepsilon) d\varepsilon , \tag{17}$$

where $f(\varepsilon)$ is the EEDF as a function of electron energy, determined by the Boltzmann equation (see below), Q_{ion} is the cross-section of ionization, and E_{ion} is the ionization potential.

For the high-energy electron beam initiated reactions, the reaction rates are as follows:

$$W_{j,beam} = \frac{g_j D}{\rho} \frac{\xi_l}{\mu_l} , \tag{18}$$

where D is the e-beam load, and g_j (g-factors) are the beam reaction efficiencies in mol/eV.

(iii) master equation for populations of vibrational levels of three diatomic species N_2, O_2, and NO [9]

$$\begin{aligned}\frac{df_i(v)}{dx} &= \frac{\rho}{\mu u}\sum_j\left\{\phi_i\sum_w\left[k_{ij}(w\to v)f_i(w)-k_{ij}(v\to w)f_i(v)\right]\right\}\\ &+\frac{\rho}{\mu u}\sum_j\left\{\phi_i\sum_{v',w,w'}\left[k_{ij}(w,w'\to v,v')f_i(w)f_j(w')-k_{ij}(v,v'\to w,w')f_i(v)f_j(v')\right]\right\}\\ &+\frac{\rho}{\mu u}\phi_{el}\sum_w\left[k_{ej}(w\to v)f_i(w)-k_{ej}(v\to w)f_i(v)\right]+\left(\frac{df_i(v)}{dx}\right)_{chem}\end{aligned}\tag{19}$$

In Eq. (19), the terms in the right-hand-side describe the change of vibrational distribution function $f_i(v)$ of a diatomic species due to vibration-translation (V-T), vibration-vibration (V-V), and electron-vibration (e-V) energy transfer processes, and chemical reactions, respectively. Note that Eq. (19) also takes into account multi-quantum vibrational energy transfer processes. The chemical reaction term in Eq. (19) can be written as follows:

$$\begin{aligned}\left(\frac{df_{AB}(v)}{dx}\right)_{chem} &= \frac{\rho}{u}\left[\frac{P\mu}{P_0}\cdot k(\to v,T)\frac{\xi_A}{\mu_A}\frac{\xi_B}{\mu_B}\frac{\xi_M}{\mu_M}\frac{\mu_{AB}}{\xi_{AB}}-k(v\to,T)\frac{\xi_M}{\mu_M}f_{AB}(v)\right]\\ &+\frac{\rho}{u}\left[k(\to v,T)\frac{\xi_A}{\mu_A}\frac{\xi_{BC}}{\mu_{BC}}\frac{\mu_{AB}}{\xi_{AB}}-k(v\to,T)\frac{\xi_C}{\mu_C}f_{AB}(v)\right]-\frac{f_i(v)}{\xi_i}\frac{d\xi_i}{dx}\end{aligned}\tag{20}$$

where the first two terms in the right-hand-side describe vibrationally-stimulated dissociation and exchange reactions of Eqs. (14,15), respectively. The direct and the reverse state-resolved rates in Eq. (18) are related by the detailed balance equation

$$\frac{k(v\to,T)f_{AB}(v,T)}{k(\to v,T)}=\frac{\vec{k}(T)}{\overleftarrow{k}(T)},\tag{21}$$

where the relation between the overall direct and reverse thermal rates is given by Eq. (13). Note that in Eq. (21) $f_{AB}(v,T)$ is the equilibrium relative population of vibrational level v of molecule AB.

The vibrational "temperatures" of the diatomic species are determined as follows:

$$T_{v,i}=\frac{\omega_{e,i}(1-2x_{e,i})}{\ln[f_i(0)/f_i(1)]}\tag{22}$$

(iv) Boltzmann equation for symmetric part of electron energy distribution function f(ε) (EEDF) in crossed electric and magnetic fields [10,11]

$$\begin{aligned}
&\frac{1}{3}\frac{E_x^2+(E_y-uB_z)^2}{N^2}N\frac{d}{d\varepsilon}\left(\frac{\nu(\varepsilon)^2}{\nu(\varepsilon)^2+\nu_0^2}\frac{\varepsilon}{Q_{tr}(\varepsilon)}\frac{df(\varepsilon)}{d\varepsilon}\right)\\
&+N\frac{d}{d\varepsilon}\left\{\left[f(\varepsilon)+\frac{kT}{e}\frac{df(\varepsilon)}{d\varepsilon}\right]\sum_i\phi_i\left[\frac{m_p}{m_p\mu_i}\varepsilon^2Q_{tr,i}(\varepsilon)+B_i\varepsilon Q_{rot,i}(\varepsilon)\right]\right\}\\
&+N\phi_{N_2}\sum_{0\le v,w\le 8}f_{N_2}(v)\left[Q_{vib,N_2}^{v\to w}(\varepsilon+\Delta E_{v,w})(\varepsilon+\Delta E_{v,w})f(\varepsilon+\Delta E_{v,w})-Q_{vib,N_2}^{v\to w}(\varepsilon)\varepsilon f(\varepsilon)\right]\\
&+N\phi_{O_2}\sum_{0\le w\le 3}f_{O_2}(0)\left[Q_{vib,O_2}^{0\to w}(\varepsilon+\Delta E_{0,w})(\varepsilon+\Delta E_{0,w})f(\varepsilon+\Delta E_{0,w})-Q_{vib,O_2}^{0\to w}(\varepsilon)\varepsilon f(\varepsilon)\right]\\
&+N\sum_{i,k}\phi_i\left\{Q_{i,k}^{el}(\varepsilon+\Delta E_{i,k})(\varepsilon+\Delta E_{i,k})f(\varepsilon+\Delta E_{i,k})-Q_{i,k}^{el}(\varepsilon)\varepsilon f(\varepsilon)\right\}\\
&+\frac{2\pi}{3}n_e\frac{q^4}{e^2}\ln\Lambda\left[I_1(\varepsilon)\frac{df(\varepsilon)}{d\varepsilon}+I_2(\varepsilon)f(\varepsilon)\right]+S(\varepsilon)=0
\end{aligned} \tag{23}$$

In Eq. (23), the separate terms describe the EEDF change due to applied fields, momentum transfer and rotational excitation, vibrational excitation, electronic excitation (excitation of the kth electronic level of the ith species), electron-electron collisions, and ionization by the e-beam electrons. Also in Eq. (23)

$$\nu(\varepsilon)=N\cdot\left(\frac{2e}{m_e}\right)^{1/2}\varepsilon^{1/2}Q_{tr}(\varepsilon) \tag{24}$$

is the momentum transfer frequency,

$$\nu_0=\frac{e}{m_e}B, \tag{25}$$

$$\Lambda=\frac{r_d}{r_0}=\left(\frac{kT_e}{4\pi n_e e^2}\right)^{1/2}\frac{3kT_e}{2q^2} \tag{26}$$

is the ratio of the Debye length to the classical closest approach distance, and

$$I_1(\varepsilon) = \int_0^\varepsilon x^{3/2} f(x)dx + 2\varepsilon^{3/2} \int_0^\varepsilon f(x)dx$$
$$I_2(\varepsilon) = 3\int_0^\varepsilon x^{1/2} f(x)dx \tag{27}$$

In the present study we are interested only in the low-energy part of the EEDF (ε<20-30 eV), which is independent of the electron beam energy if ε_{beam}>>E_{ion} [12,13]. Therefore Eq. (23) does not incorporate the detailed model of ionization by an e-beam that uses the double differential cross-section of ionization $Q_{ion}(\varepsilon_p,\varepsilon)$ as a function of primary and secondary electron energies [12,13]. Instead, a simplified approach is used, with the source term $S(\varepsilon)$ in Eq. (23) expressed in terms of the g-factor for the beam ionization g_{ion} (ionization efficiency) and the secondary electron energy ε:

$$S(\varepsilon) = \frac{const}{(\varepsilon + E_{ion})^{3/2}}, \qquad \int S(\varepsilon)d\varepsilon = g_{ion}D \tag{28}$$

The g-factors are also known to be independent of the beam energy if ε_{beam}>>E_{ion} [13].

The electron "temperature" is determined by the following relation

$$T_e = -\left.\frac{f(\varepsilon)}{df(\varepsilon)/d\varepsilon}\right|_{\varepsilon=0} \tag{29}$$

Note that Eq. (23) also takes into account superelastic processes (electron heating in collisions with vibrationally excited N_2 molecules):

$$N_2(v) + e(\varepsilon) \rightarrow N_2(w < v) + e(\varepsilon + \Delta E_{v,w}), \tag{30}$$

where $\Delta E_{v,w}$ is the vibrational energy defect. These processes are well-known to strongly affect the electron temperature in gas flows at strong vibrational disequilibrium [14,15].

(v) generalized Ohm's law [8]:

$$
\begin{aligned}
j_x &= \frac{\sigma}{1+\beta^2}\left[E_x - \beta(E_y - uB_z)\right] \\
j_y &= \frac{\sigma}{1+\beta^2}\left[(E_y - uB_z) + \beta E_x\right],
\end{aligned}
\tag{31}
$$

where

$$\sigma = \frac{e^2 n_e}{m_e \langle \nu \rangle} \tag{32}$$

is the plasma electric conductivity and

$$\beta = \frac{\nu_0}{\langle \nu \rangle} = \frac{eB}{m_e \langle \nu \rangle} \tag{33}$$

is the Hall parameter. In Eqs. (32,33),

$$\langle \nu \rangle = N\left(\frac{2e}{m_e}\right)^{1/2} \int_0^\infty Q_{tr}(\varepsilon)\varepsilon^{1/2} f(\varepsilon)\, d\varepsilon \tag{34}$$

is the electron-heavy species collision frequency [10].

As one can see, the effects of vibrational relaxation and chemical reactions are accounted for in the energy and motion equations (1,2). The chemistry-vibration coupling terms are incorporated into both the chemical kinetics equations (9) and the master equation (19). Rates of electron impact processes used in kinetic equations (9,19) (vibrational and electronic excitation, ionization, attachment etc.), as well as electric conductivity are calculated based on the EEDF calculated by the Boltzmann equation (23). The latter takes into account superelastic processes, which couple vibrational and electron mode energies. Therefore, the system of equations solved is self-consistent.

In this quasi-1-D approach, the applied electric and magnetic fields are given as functions of the axial coordinate: $E_x(x)$, $E_y(x)$, and $B_z(x)$. Time and space derivatives in the Boltzmann equation are omitted, since they become important only in extremely fast oscillating fields and in sheath areas, so that the Boltzmann equation becomes a simple second-order differential equation with electron energy as an independent variable, solved by standard iteration method [11]. The rest of differential equations are first-order equations solved by a widely used stiff ODE system solver LSODE [16].

2.2. Rates and cross-sections

The list of the neutral species chemical reactions (32 reactions for 12 species N, N_2, O, O_2, NO, O_3, NO_2, N_2O, NO_3, N_2O_4, N_2O_5, N_3), as well as the reaction rates at thermal equilibrium are taken from the Russian AVOGADRO database [17], where the most reliable available data have been recommended in a wide temperature range. The vibration-chemistry coupling is modeled using the Macheret-Fridman-Rich nonequilibrium rate model [18,19], and the state-specific reaction rates $k(v\rightarrow,T)$ for the reactions

$$\begin{array}{l} N_2(v)+M \leftrightarrows N+N+M \\ O_2(v)+M \leftrightarrows O+O+M \\ NO(v)+M \leftrightarrows N+O+M \\ N_2(v)+O \leftrightarrows NO+N \\ NO(v)+O \leftrightarrows O_2+N \end{array} , \tag{35}$$

used in chemical and vibrational kinetics equations (9,19) are the same as in our previous paper [20].

The list of ion-molecular reactions, including ionization, recombination, ion conversion, attachment and detachment processes (more than 300 reactions for 13 species e^-, N^+, N_2^+, O^+, O_2^+, NO^+, O^-, O_2^-, N_2O^+, NO_2^-, Na^+, K^+, Cs^+) as well as most of the reaction rates were taken from the review [21] and [22-25]. The rates of electron impact ionization and electron attachment to the following species: N_2, O_2, NO, Na, K, Cs are calculated by the Boltzmann equation solver using the experimental cross-sections of these processes as functions of electron energy [26-29]. The latter group of processes describes kinetics of nonequilibrium ionization and attachment of the plasma electrons in the presence of external electric and magnetic fields.

Note that thermochemical data both for neutral and charged species are incorporated into the code, so that the rates of reverse processes are evaluated from detailed balance (e.g. see Eq. (13)). Therefore the kinetic model correctly predicts the chemical composition of alkali-seeded air, including electron and ion concentrations, in thermodynamic equilibrium (with no fields applied). Thermochemical parameters such as enthalpies, entropies, and specific heats of the species in the temperature range 300-6000 K are taken from [30,31].

The rates of electronic excitation and dissociation of N_2 and O_2 by the plasma electrons, with the production of metastable species $N_2(A^3\Sigma_u^+)$, $N(^2D)$, $N(^2P)$, $O_2(a^1\Delta_g)$, $O_2(b^1\Sigma_g^+)$, $O(^1D)$, $O(^1S)$ are also calculated by the Boltzmann solver using the experimental cross-sections [26,27]. Metastable species collisional quenching and chemical reaction rates are taken from the review [21].

The rates of vibrational excitation of N_2 ad O_2 by plasma electrons are evaluated by the Boltzmann solver using the experimental cross-sections $Q_{vib}^{0\rightarrow v}$ [26,27]. The detailed cross-section matrix for nitrogen, $Q_{vib}^{v\rightarrow w}$, $0\leq v,w\leq 8$, needed for modeling of superelastic processes (27), is calculated using the semi-empirical method [32]. The rates of vibration-translation (V-T) and vibration-vibration (V-V) rates for N_2 and O_2, including multiquantum processes, are taken the same as in [20] where they have been evaluated using the forced harmonic oscillator (FHO) rate model [33]. These rates show good agreement with the recent experiments and state-of-the-art close-coupled calculations in a wide temperature range [33]. The V-T rates for N_2-Na, N_2-K, and N_2-Cs are taken from [34]. As shown in [35], these rates are consistent with the Na-seeded nitrogen vibrational relaxation measurements behind shock waves.

The experimental electron transport cross-sections for N_2, O_2, NO, Na, K, and Cs necessary for the plasma electric conductivity calculations, are taken from [26-28,36].

In these calculations, we considered the use of a high energy electron beam as a possible efficient way to sustain nonequilibrium ionization in the supersonic flow. It is well known that up to 50% of the relativistic e-beam power goes into electron impact ionization [21]. This external ionization method has been previously extensively used to sustain a discharge in supersonic flows in gas dynamic lasers [37]. The e-beam power fractions going into ionization, dissociation, and electronic excitation of N_2 and O_2 in air (g-factors) are taken from the review [21]. The experimental secondary electron energy distribution in N_2 and O_2 for the beam energies 50-2000 eV are taken from [26,27] and extrapolated toward the higher energies [12].

Note that in the present study we do not address the high-power e-beam engineering issues (beam entering the high-pressure flow, focusing, X-ray radiation etc.). Our primary interest is the e-beam initiated kinetics.

Wall heat transfer coefficient c_h and skin friction coefficient c_f, as well as the boundary layer thickness δ are estimated based on the results of turbulent compressible boundary layer theory [38]:

$$c_f \cong \frac{0.059}{Re_x^{0.2}} \frac{1}{1+Pr^{1/3}(\gamma-1)M_f^2/2}, \quad 5\cdot 10^5 \le Re \le 10^7 \tag{36}$$

$$c_h = \frac{1}{2} c_f / Pr^{2/3}, \quad 5\cdot 10^5 \le Re \le 10^7 \tag{37}$$

$$\frac{\delta(x)}{r} = \frac{0.37}{Re_x^{0.2}} \frac{x}{r}, \quad 5\cdot 10^5 \le Re \le 10^7 \tag{38}$$

Heat fluxes to the electrode surfaces (see Eq. (7)) are estimated based on the experimental heat transfer measurements in MHD accelerators [39] (see section 2.3).

2.3. Code validation

Various parts of the kinetic model used in the present work have been previously validated in modeling calculations. First, V-T and V-V rates, neutral species chemical kinetic rates and vibration-chemistry coupling in high temperature air were validated in modeling of NO production in N_2-O_2 mixtures behind shock waves, which showed good agreement with time-resolved shock tube measurements [20]. Second, electron swarm parameters (drift velocity, magnetic drift velocity, diffusion coefficient, ionization and attachment coefficients) for N_2, O_2, and air, predicted by the Boltzmann equation solver are in very good agreement with available experimental data [10,40].

We have also carried out two series of validation calculations for the entire model. The results of the first series were compared with the experimental data (somewhat scarce), obtained on the GE unseeded air MHD accelerator [41,42]. In these experiments, air was heated up to T_0=9500 K at a pressure P_0=550 atm behind the reflected shock and then expanded through a supersonic MHD channel (channel length L=30 cm, area ratio F_2/F_1=2.0, magnetic field B=4.2 T). The experimentally determined test area impact pressure in the MHD-augmented flow was about 1.5-2 times higher than in the isentropic flow in the same channel. Fig. 1 shows calculated axial profiles of the gas temperature and velocity in the channel for both MHD-augmented and isentropic flow, as well as velocity profile obtained from the GE group 1-D equilibrium flow model [41]. The good agreement between these two models, both predicting about 15% velocity increase, is due to the fact that at the high temperature T≅6800 K and pressure P=10-30 atm the flow in the channel is very close to the local thermodynamic equilibrium. The effective reduced electric field that determines the electron energy in crossed electric and magnetic fields, was also quite low,

$$\left(\frac{E}{N}\right)_{\text{eff}} = \frac{1}{N}\left[\frac{E_x^2 + (E_y - uB_z)^2}{1+\beta^2}\right]^{1/2} \leq 10^{-17}\ \text{V}\cdot\text{cm}^2, \tag{39}$$

so the electron temperature was very close to the gas temperature throughout the channel. The electric conductivity calculated by the present model is also in good agreement with the value measured in the channel, σ=110 mhos/m. Fig. 2 shows the axial pressure profile, as well as distributions of nitric oxide and atom mole fractions, as well as ionization fraction. One can see that the flow quality in the test area is poor: the atom fractions remain frozen and reach 10% for N atoms and 30% for O atoms. In other words, oxygen is almost completely dissociated. Another disadvantage of this reflected shock tunnel MHD accelerator is an extremely short test time (about 1 ms in these experiments). The calculated total flow power increase for these experiments is about 25%, from 20 to about 25 MW, which corresponds to a total enthalpy increase from 24 to 30 MJ/kg.

The second series of calculations was made for the AEDC continuous mode MHD accelerator running on potassium-seeded (at 1.5%) nitrogen (Accelerator B of Ref. [39]). In these experiments, nitrogen was heated by an arc heater up to a temperature of about T_0=6000 K at a pressure P_0=3.3 atm and expanded through an MHD channel (channel length L=77 cm, area ratio F_2/F_1=2.1, magnetic field B=1.5 T). Figure 3 shows the temperature and the flow velocity distributions along the channel. Figure 4 presents gas temperature and velocity at the channel exit as functions of the accelerator power. One can see that experimental and calculated data are in good agreement, temperature and pressure in the MHD-augmented flow being up to 30-50% higher than in the isentropic flow. Nonequilibrium effects in the channel (N_2 vibrational disequilibrium) and chemical dissociation are both insignificant. The gas temperature in the channel T~3000-4000 K is not high enough to stimulate substantial thermal dissociation of nitrogen, while fast N_2 V-T relaxation on K atoms and quite slow expansion prevented freezing of nitrogen vibrations. Again, the effective reduced electric field was low, $(E/N)_{eff} \cong 10^{-17}$ V·cm^2, so that $T_e \cong T$ in the channel. The experiments also show that the boundary layers in the channel overlap [39], so that one has a fully developed channel flow. Indeed, the estimate of Eq. (34) gives the ratio of the boundary layer thickness to the channel halfwidth $\delta/r \cong 1$ already at $x/L=0.5$ ($Re_x=6\cdot10^5$). This results in significant power loss due to heat transfer and wall friction. Experiments [39] and present calculations show that in the fully powered accelerator (at maximum power loading of 375 kW) as much as 30% of the initial flow power of 640 kW is lost in heat transfer. Both measured and calculated total enthalpy increase for the fully powered accelerator is about 25%, from 7.6 to 9.5 MJ/kg.

In both series of calculations, the agreement with the experiments is quite good. We note, however, that additional model validation is desirable, in particular for MHD flows where the flow is far from thermal and ionization equilibrium.

3. Results and discussion

We applied the kinetic model described and validated in Section 2 for modeling of both alkali-seeded and unseeded air flows in MHD accelerators, in a wide range of plenum conditions and for various nozzle geometries. The main objective was to determine the feasibility and efficiency of using the MHD technology for the high Mach number energy addition wind tunnel. All subsequent calculations are made for the nozzle throat cross-section area $F_{throat}=4$ cm^2 and ideal Faraday accelerator ($E_x=\beta\cdot(E_y-uB_z)$, $j_x=0$ throughout the channel) with the magnetic field in the channel $B_z=10$ T. The secondary expansion duct was assumed to be 2 m long, with the exit area of 9 m^2.

3.1. Unseeded flows

The first series of runs was made for the $N_2:O_2=78:22$ air for the plenum temperatures $T_0=3000-6000$ K, and plenum pressures $P_0=10-1000$ atm. The MHD channel length was L=30 cm, with the entrance cross-section area $F_1=8$ cm^2, and the area ratio $F_2/F_1=2$ (geometry similar to the MHD channel used in [41,42]). In all calculated cases, the Mach number at the MHD channel entrance was M=2, and the channel entrance pressure was about 10% of the plenum pressure (1, 10, and 100 atm, respectively). Constant loading parameter $K=E_y/uB_z=2$ was assumed. Ionization in the MHD channel was sustained by a relativistic e-beam. The e-beam loading per molecule D was in the range 0.0-1.0 keV/mol/s and was assumed to be constant.

Figures 5,6 summarize the obtained results. Fig. 5 shows the total enthalpy of the flow H as a function of the flow entropy S, for the beam load D=1.0 keV/mol/s . The exceptions are Runs #6 and #3 for which the beam load was taken to be D=0.3 and 0.1 keV/mol/s, respectively, to avoid thermal instability. One can see that the total enthalpy increase is very small unless the plenum pressure is low. Note that all runs with D=0 did not show any enthalpy increase, since the thermal ionization of air at these plenum temperatures is too small. Fig. 6 gives the ratio of the total enthalpy increase ΔH to the initial enthalpy H_0 and also the ratio of the absorbed e-beam power to the enthalpy increase $\Delta E_{beam}/\Delta H$ (beam efficiency) for $T_0=3000$ K. As one can see, only for the plenum pressure of $P_0=10$ atm (channel pressure $\leq$ 1atm) does the nonequilibrium ionization sustained by the e-beam provide substantial flow power increase at reasonable efficiency ($\Delta H/H_0=0.5$-2 and $\Delta E_{beam}/\Delta H=0.03$-0.05). At higher plenum pressures the power increase does not exceed 10-20% of the initial flow power ($\Delta H/H_0<0.2$), and it is mainly due to the e-beam stimulated gas heating in recombination processes ($\Delta E_{beam}/\Delta H=0.6$-1.0). The reason is that at the high number densities the recombination and electron attachment rates are so fast that the ionization fraction sustained by the beam in the MHD channel becomes far too low to produce a noticeable Lorentz force. For example, for the same beam load of 0.3 keV/mol/s, the ionization fraction in the channel is $\sim 10^{-5}$ at the channel pressure of 1 atm, $\sim 10^{-6}$ at 10 atm, and $\sim 10^{-7}$ at 100 atm. Since the total power addition in the full-scale high pressure wind tunnel facility has to be $\Delta H \sim 1$ GW, and at the high channel pressure conditions $\Delta E_{beam}/\Delta H \sim 1$, this would require the use of about a 1 GW e-beam (in a very inefficient way). Let us emphasize that the low efficiency of this method at high pressures is primarily due to the high rate of electron loss (recombination and attachment), which is independent of the particular method of nonequilibrium ionization. Since the high-energy e-beam is one of the most efficient ionization sources available (see Section 2.2), the use of any other method of external ionization in the high pressure MHD channels (P>1 atm) is also not feasible.

The only conceivable way of efficient use of e-beams (or any other ionization source) in high plenum pressure flows appears to be expanding the flow down to the low pressures prior to creating nonequilibrium ionization. We considered the feasibility of this mode of operation in the second series of calculations, made for T_0=3000-6000 K, P_0= 1000 atm, and the beam load D=1 keV/mol/s. The MHD channel length was again L=30 cm, with the entrance cross-section area $F_1=170\ cm^2$, the area ratio $F_2/F_1=2.35$ and K=2=const. The channel entrance Mach number now was M=5, and the channel pressure was about 1 atm. The results shown in Fig. 7 demonstrate a considerable total enthalpy rise (up to 70%) and reasonable beam efficiency (5-10%) for the high plenum and channel temperatures. Higher temperature in the channel leads to (i) partial compensation of electron attachment by thermal detachment from the negative ions, and (ii) slower recombination rate at the lower number density.

It is easy to see that the slope of the H(S) curves on the Molier charts (Figs. 4,6) is

$$\tan\theta = \frac{dH}{dS} = \frac{dQ_{total}}{dQ_{thermal}} T = \frac{j\cdot E}{j\cdot E - u\cdot(j\times B)} T = \frac{\sigma K(K-1)u^2B_z^2}{\sigma(K-1)^2u^2B_z^2} T = \frac{K}{K-1} T, \tag{40}$$

where dQ_{total} and $dQ_{thermal}$ are differentials of the total power added to the flow and of the power going into internal degrees of freedom, respectively (in Eq. (40) we neglect gas heating by the beam). Therefore, the flow entropy rise ΔS for the given total enthalpy increase ΔH is determined by the average temperature at which the energy is added to the flow T_{avg}, and by the loading parameter K>1. MHD accelerators sustained by external ionization have an obvious disadvantage compared to the traditional seeded-flow accelerators since the flow expansion prior to the MHD channel needed to reduce the pressure also results in the low channel entrance temperature. For the three cases show in Fig. 7, T_{avg}= 1300, 2400, and 4400 K, with the steepest slope dH/dS corresponding to the highest value of T_{avg}. Reducing the loading parameter would not increase tan(θ) since it would reduce the total power added to the flow, proportional to K(K-1) (see Eq. (40)), and inhibit the Joule heating, which would result in further reduction of T_{avg}.

The third series of calculations for the full-scale accelerator was made for T_0=5000 K, P_0= 1000 atm, mass flowrate G=17.4 kg/s, and beam loads 0.0-2.0 keV/mol/s. The MHD channel length now was L=140 cm, with the entrance cross-section area $F_1=200\ cm^2$, and the area ratio $F_2/F_1=1.65$ (channel entrance Mach number M=5, channel pressure P=1-2 atm). To prevent the large-scale thermal instability (see Section 3.3) leading to excessive gas heating in the channel and increasing chemical dissociation, the loading parameter at high temperatures was reduced :

$$\begin{aligned} &K = 1.5\,, \quad T < 2500\ \mathrm{K} \\ &K = 1.0 + 0.5 \cdot (T/2500)\,, \quad T \geq 2500\ \mathrm{K} \end{aligned} \tag{41}$$

The results of calculations are shown in Figs. 8-11. Fig. 8 presents the obtained H(S) curves, plotted together with the target values for transatmospheric vehicle (TAV) trajectory ("flight envelope"). One can see that although the total enthalpy of the flow increases 1.5-2.5 times, the flow entropy is considerably larger than the target values. The main reason for that, as discussed above, is the low MHD channel entrance temperature (see Fig. 9 and Eq. (40)). Therefore, while the calculated Mach numbers in the MHD-augmented flow are close to the target values, conditions, the flow pressure is more than an order of magnitude lower than the pressure behind the bow shock (see Table 1).

Table 1. Unseeded air MHD accelerator performance.

Left and central sub-columns - target values for P_{dyn}=2000 and 1000 lb/ft^2, respectively, right sub-column - present calculations.

Case #	H, MJ/kg			S/R			u, km/s			M		
1	7.2	7.0	*6.9*	27.9	28.6	*28.9*	3.76	3.64	*3.60*	9.4	9.0	*8.9*
2	11.6	11.0	*11.4*	28.7	29.3	*32.1*	4.78	4.58	*4.60*	10.9	10.4	*10.4*
3	13.6	14.6	*14.5*	29.0	29.9	*33.5*	5.16	5.31	*5.15*	11.4	11.3	*10.9*
4	15.8	16.9	*17.2*	29.3	30.2	*34.8*	5.58	5.71	*5.49*	11.8	11.8	*10.9*

Case #	P, mbar			y_O, %	y_{NO}, %	$T_v(N_2)$	D_{beam}, keV/mol/s	ΔE_{beam}, MW	ΔH, MW
1	41.1	21.4	*12.8*	*0.4*	*7.0*	*1574*	*0.0*	*0.0*	*0*
2	35.7	18.5	*2.0*	*1.5*	*6.2*	*2776*	*0.3*	*6.5*	*77*
3	34.4	17.2	*1.3*	*5.6*	*6.2*	*2857*	*1.0*	*21*	*130*
4	33.1	16.1	*1.3*	*14.7*	*6.2*	*2455*	*2.0*	*41*	*176*

Note that raising the beam load increases recombination losses (the ratio $\Delta E_{beam}/\Delta H$, see table 1). In particular, this makes greater the average loading parameter K_{avg} defined as the ratio of the total power going into internal degrees of freedom to the total power into kinetic energy. For this reason the slope dH/dS actually decreases with the beam load despite the fact the T_{avg} becomes higher (see Figs. 8,9).

The calculated transverse current density in the channel did not exceed j_y=10 A/cm^2. Both Joule heating and e-beam electron impact induce chemical reactions in the channel, first of all, dissociation of oxygen, raising O atom fraction in the test section (see Fig. 10). Note that at the same time the exit NO concentration changes very weakly (see Fig. 10, Table 1). This type of behavior simply reflects the dependence of equilibrium concentration of these species on temperature at $P \cong 1$ atm at the channel exit, which was verified by comparing the results with the equilibrium chemical composition data. Higher-than-equilibrium O and NO exit fractions at D_{beam}=0 (see Table 1) are due to their considerable initial concentrations in high-temperature plenum. Fig. 11 also shows that the flow becomes close to the vibrational equilibrium toward the end of the channel. However, one can see from Table 1 and Figs. 10-11 that the flow in the test section is far from being at equilibrium, both molecular vibrations and chemical composition being frozen in the rapid expansion which occurs at low pressure and temperature. This effect can be somewhat reduced (i) if the energy is added at the high pressure (which in this case is not feasible), so that the relaxation in the secondary expansion becomes faster, or (ii) slower expansion is used.

Finally, Table 1 shows that one would need a tens of Megawatt ionization source to operate the full scale facility at the channel pressure of about 1 atm. The beam efficiency can be improved by further reducing the channel pressure, but this would lead to even greater flow entropy rise because of the lower channel entrance temperature, according to Eq. (40). The electron beam load D can be simply related to the beam current density j_{beam} and the energy of the beam electrons ε_{beam} that determines the penetration length,

$$l \approx 0.5 \cdot \frac{(\varepsilon_{beam}/300)^{1.35}}{(\rho/1.2)}, \qquad (42)$$

where l is in m, ε_{beam} is in keV, and ρ is in kg/m^3 [21]. For the conditions of Table 1, keeping in mind that $l \cong 2r \cong 0.2$ m, and the absorbed beam power $\Delta E_{beam} = eDN \cdot (Ll^2) \cong j_{beam}\, \varepsilon_{beam} \cdot (Ll)$, one has $\varepsilon_{beam} \sim 30$ keV, and for D=1 keV/mol/s

$$j_{beam} \cong \frac{eDNl}{\varepsilon_{beam}} \cong 0.3\,\mathrm{A/cm^2}. \tag{43}$$

3.2. Seeded flows

The first series of runs was made for potassium-seeded (at 1%) air for the plenum temperatures T_0=3000-6000 K, and pressures P_0=10-1000 atm. The MHD channel length was L=30 cm, with the entrance cross-section area F_1=8 cm^2, and the area ratio F_2/F_1=2-25. Again, in all calculated cases, the channel entrance Mach number was M=2, and the channel entrance pressure was about 10% of the plenum pressure. Some of the results are shown in Fig. 12. All runs for T_0=3000 K did not show any flow acceleration due to MHD augmentation, since the thermal electric conductivity of the mixture was too low (see Fig. 12). Calculations for T_0=4500 K demonstrated noticeable total enthalpy rise ΔH only for the plenum pressures of P_0=100 atm and lower (see Fig. 12). One can see that ΔH also increases with the channel area ratio, which results in the lower channel pressure. This is understandable since the term describing the flow acceleration in the motion equation is inversely proportional to the gas density (see Eqs. (1,2)),

$$\frac{du}{dt} \sim \frac{j_y B_z}{\rho} \sim \frac{\sigma(T)\, u B_z^2 (K-1)}{\rho}, \tag{44}$$

where σ(T) is proportional to the ionization fraction $\phi_e = n_e/N$ (see Eqs. (32,34)). Thus, to produce the same acceleration at the higher pressure, higher ionization fraction (and therefore higher plenum temperature) is needed. Finally, substantial acceleration for P_0=1000 atm was obtained only at the highest plenum temperature considered, T_0=6000 K, also for the large area ratio F_2/F_1=9-25 (see Fig. 12). One can see that the seeded MHD accelerator for the wind tunnel, which requires plenum pressures of the order of thousand atmospheres (see Table 1), should also operate at high plenum temperatures of $T_0 \sim 6000$ K. This limit can be somewhat lowered if a seed with lower ionization potential (e.g. cesium) is used. Large operating area ratios F_2/F_1~25 are also preferable.

The second series of runs was carried out for the full-scale cesium-seeded (at 0.5%) air accelerator for plenum conditions T_0=5000 K, P_0= 1000 atm (mass flowrate G=17.4 kg/s). The MHD channel length was L=140 cm, with the entrance cross-section area F_1=8 cm^2, and the area ratio F_2/F_1=36 (channel entrance Mach number M=2, entrance pressure P=120 atm). The loading parameter was again limited to prevent the developing of the thermal instability (see Section 3.3) and the current density becoming too high,

$$K = 1.0 + \frac{j_{y\max}}{\sigma u B_z} \tag{45}$$

The calculated H(S) curves are shown in Fig. 13 for different values of j_{ymax}, plotted together with the target TAV trajectory data. One can see that at these conditions the total enthalpy can be increased up to 5 times, if the maximum current density does not exceed j_{ymax}=100 A/cm^2, while the flow entropy rise is considerably less than for the unseeded flows discussed in Section 3.1 (see Fig. 8). Although the flow entropy is still somewhat greater than the target value (see Fig. 13), the seeded accelerator performance is clearly much better. NO and O fractions in the test section are much less than in the unseeded accelerator at comparable total enthalpy (see Tables 1,2). Also, the calculated flow pressure is now only 1.5-4 times less than the pressure behind the bow shock (see Table 2).

Table 2. Cs-seeded air MHD accelerator performance.

Left and central sub-columns - target values for P_{dyn}=2000 and 1000 lb/ft^2, respectively, right sub-column - present calculations.

Case #	H, MJ/kg			S/R			u, km/s			M		
1	7.2	7.0	*6.7*	27.9	28.6	*28.3*	3.76	3.64	*3.53*	9.4	9.0	*9.1*
2	13.6	14.6	*14.1*	29.0	29.9	*30.8*	5.16	5.31	*5.14*	11.4	11.3	*11.5*
3	18.4	19.4	*19.7*	29.6	30.4	*31.4*	6.02	6.14	*6.07*	12.3	12.2	*12.3*

4	24.8	25.7	*25.2*	30.2	31.0	*31.9*	6.99	7.07	*6.88*	13.1	13.0	*13.1*
5	33.2	33.8	*33.9*	30.9	31.6	*32.5*	8.08	8.12	*7.98*	13.9	13.8	*13.7*

Case #	P, mbar			y_{Cs}, %	y_O, %	y_{NO}, %	$T_v(N_2)$	j_{ymax}, A/cm^2
1	41.1	21.4	*14.5*	*0.5*	*0.01*	*4.5*	*1992*	*0*
2	34.4	17.2	*3.9*	*0.5*	*0.6*	*4.3*	*2630*	*30*
3	32.1	16.1	*5.4*	*0.5*	*1.6*	*4.1*	*2829*	*50*
4	30.4	15.3	*6.3*	*0.5*	*2.9*	*4.2*	*2944*	*70*
5	29.1	14.7	*9.6*	*0.5*	*5.1*	*4.9*	*3078*	*100*

The latter result is in agreement with the criterion of Eq. (40). First, the average channel temperature in the seeded MHD accelerator is generally higher than in the e-beam controlled channel, even though it is being controlled to reduce chemical dissociation (see Figs. 8,14). Second, the average loading parameter in these runs is considerably lower ($K_{avg} \cong 1.1$-1.3 vs. $K_{avg} \cong 1.6$-1.8 for the unseeded runs), so greater part of the input power goes directly into the flow kinetic energy and does not contribute to the entropy rise. One can see from Fig. 14 that the efficiency of the first half of the channel is less than that of the second (du/dx is lower) due to the higher gas density near the channel entrance (see Eq. (44)). The flow in the channel is very close to the thermochemical equilibrium (e.g. see Fig. 16), which is also confirmed by the equilibrium chemical composition calculations. However, freezing of molecular vibrations (despite the fast V-T relaxation of N_2 on Cs and oxygen atoms) and of chemical composition of the mixture in the test area is still well-pronounced (see Figs. 15,16).

The boundary layer growth in the channel is quite significant. The estimate of Eq. (38) gives $\delta/r \sim 0.25$ at $x/L=1$ ($Re_x=10^7$). The calculated heat transfer losses, although quite large, did not exceed 15% of the initial flow power. However, the calculated local wall heat fluxes in the channel reach 10-20 kW/cm^2 for $j_{ymax}=100$ A/cm^2, which may severely limit the operation time.

3.3. Flow stability

Calculated effective reduced electric field values (see Eq. (39)) are quite low for all calculated regimes, typically $(E/N)_{eff} \leq 0.5 \cdot 10^{-16}$ V$\cdot$cm^2 for unseeded flows and $(E/N)_{eff} \leq 1.0 \cdot 10^{-}$

^{17} V·cm^2 for the alkali-seeded flows. Analysis of the results shows that in both cases nonequilibrium ionization by the slow plasma electrons is negligibly small. For this reason, thermal instability [37] and breakdown due to the field-stimulated nonequilibrium ionization in the core flow are extremely unlikely. However, thermal instability due to the Joule heating might still develop. Using the linear stability analysis [37], one can obtain expression for the large-scale instability increment:

$$\Omega = \frac{K-1}{K}\frac{\gamma-1}{\gamma}\frac{j_y E_y}{P}\left(\frac{\delta \ln n_e}{\delta \ln T}+\frac{1}{2}\right)-\frac{2u}{L} \quad (46)$$

The last term in Eq. (46) is the reciprocal characteristic time of gas cooling. In high-pressure flows, where the convective cooling is dominant, it is simply proportional to the channel residence time L/u. Combining Eq. (46) with the expression for the quasi-steady-state electron density,

$$S_{beam} = k_{rec} n_e^2 + k_{att} n_e N^2 \quad (47)$$

for the e-beam-sustained discharge (note that S_{beam} [1/cm^3/s]~N and k_{rec}~$T^{-0.5}$) , or with the Saha equation

$$n_e = \mathrm{const} \cdot n_{seed}^{1/2} \cdot T^{3/4} \cdot \exp(-E_{ion}/2T) \quad (48)$$

for the thermal ionization, one obtains the thresholds of the large-scale thermal instability. For the MHD channel with external ionization by an e-beam one has

$$j_y \le a \frac{K}{K-1}\frac{\gamma}{\gamma-1}\frac{P}{E_y}\frac{u}{L}, \quad (49)$$

where a=8 and a=4/3 for the recombination and attachment controlled discharges, respectively. The first regime is realized only at high ionization fractions ϕ_e~10^{-4} and higher, when $k_{rec}n_e >> k_{att}N^2$ in Eq. (47) (in air, k_{rec}~10^{-8} cm^3/s, k_{att}~10^{-30} cm^6/s^2), or high temperatures T≥3000

K, when thermal detachment from the negative ions compensate electron attachment. For the channel with equilibrium ionization one has

$$j_y \le \frac{1}{\frac{3}{8}+\frac{E_{ion}}{4T}} \frac{K}{K-1} \frac{\gamma}{\gamma-1} \frac{P}{E_y} \frac{u}{L} \tag{50}$$

One can see that the equilibrium flow is less stable than the flow controlled by the external ionization: for $E_{ion}/T \sim 10\text{-}15$, typical for the seeded MHD flows, one has $(3/8+E_{ion}/4T)^{-1} \cong 0.2\text{-}0.4$. The criteria of Eqs. (49,50), applied to the full-scale accelerators simulated in Sections 3.1 ($K \cong 1.6\text{-}1.8$), and 3.2 ($K \cong 1.1\text{-}1.3$), predict stable flow at $j_y \le 8\text{-}10$ A/cm^2 and $j_y \le 40\text{-}100$ A/cm^2, respectively, depending on the loading parameter K. One can see that in both cases the channels operate on the verge of stability, which was actually observed in the calculations. This was the primary reason for the limiting of the loading parameter for both accelerators (see Eqs. (41,45)). The criteria (49,50), used for the estimate of the flow stability in experimental MHD accelerators [39,41] predict stable core flow at $j_y \le 120$ A/cm^2 for the unseeded GE accelerator and at $j_y \le 15$ A/cm^2 for the K-seeded AEDC accelerator. In these experiments, where the stable core flow was indeed observed, the current densities did not exceed 20 A/cm^2 and 15 A/cm^2, respectively.

Note that this one-dimensional core flow stability analysis cannot be applied to the boundary layer, and it also does not account for the spoke instability that occurs in the nonuniform flows with large Hall parameters [43].

The possibility of arcing in the boundary layer appears to be very high, for two reasons. First, electric field in the sheath regions near the electrodes is much higher than in the core flow due to the voltage drop across the sheath [37], which leads to the electron heating by the field and may result in a breakdown and arc formation between the adjacent electrodes. Second, core flow Faraday mode conditions $E_x=\beta\cdot(E_y-uB_z)$, $j_x=0$, assumed in these calculations, will no longer hold in the boundary layer, which would result in the Hall current j_x flowing between the adjacent electrodes. This current can be very large because of the high recovery temperature in the boundary layer and high scalar electric conductivity σ (in fact, the seed could be completely ionized). Both these effects would short circuit the segmented electrodes along each wall, so in the worst possible case that the accelerator would run in a continuous electrode mode $E_x=0$, $\sigma_{eff}=\sigma/(1+\beta^2)$ (see Eqs. (31)). The effective electric conductivity in the full-scale accelerator calculations, where β_{max}~5-10 would therefore be reduced by 1-2 orders of magnitude, making the accelerator performance much worse. These simple arguments are consistent with the experimental observations made on the GE unseeded MHD accelerator [41], where the diffuse discharge in the core flow and arcing between each pair of electrodes on the same wall was observed in the high pressure MHD channel at P=10-30 atm, $(E/N)_{eff} \sim 10^{-17}$ V·cm^2. Severe electrode erosion due to arcing was also found.

The spoke instability results from increasingly small flow nonuniformities at the higher values of the Hall parameter β (the threshold nonuniformity scale is $\Delta\sigma/\sigma \sim 1/\beta^2$), for example near the segmented electrodes. It can be analyzed using a two-dimensional linear stability model that must incorporate electric field perturbations and Maxwell equations [43].

The quasi-1-D approach used in the present study, where the electric and magnetic field axial profiles are assumed given (see Section 2.1), does not allow determining whether these distributions are consistent with the boundary layer effects or whether they can be operated at the stable conditions. At the same time, we believe that these issues are of utmost importance for the MHD channel performance. A time-dependent 2-D model, where the coupled flow equations, chemical kinetics equations, Maxwell equations for the fields distributions, and Boltzmann equation are solved, is required to address this problem, which is beyond the scope of the present work.

3.4. Comparison with the thermal energy addition methods

If all the energy added to the flow goes into internal degrees of freedom by pure heating, Eq. (40) simplifies:

$$\tan\theta = \frac{dH}{dS} = T, \tag{51}$$

We estimate the average energy addition temperature for this pure heating, assuming the initial and the final flow conditions are the same as in Case #5 of Table 2 (ΔH=27.2 MJ/kg, ΔS=1.18 kJ/kg/K, see Table 2). Eq. (51) gives $T_{avg} \cong 23000$ K, while the average temperature for the MHD energy addition process is just about 3000 K (see Fig. 14). This remarkable difference is due to the fact that most of the field power in the MHD channel goes directly into the flow kinetic energy ($K_{avg}\cong 1.2$ for Case #5). Let us also estimate T_{avg} for pure heating from plenum conditions T_0=2000 K, P_0=10000 atm to the conditions of Case #5, assuming that caloric equation of state [30,31] is still valid at these pressures. One obtains ΔH=31.9 MJ/kg, ΔS=3.15 kJ/kg/K, giving $T_{avg}\cong 10000$ K ($T_{avg}\cong 8000$ K for T_0=1000 K). For the more modest conditions of Case #2 $T_{avg}\cong 4500$ and 3800 K for T_0=2000 and 1000 K, respectively. Note that the gas temperature prior to energy addition is considerably lower than T_{avg}. This means that any attempt of reaching the test section Mach number higher than M~11-12 by means of thermal energy addition to the high pressure air flow would require heating the gas to prohibitively high temperatures, thereby inducing considerable chemical contamination of the flow.

4. Conclusions

The results of the modeling calculations based on the quasi-one-dimensional kinetic model described and validated in Section 2 allow making the following conclusions:

(i) the use of high-energy electron beams (or any other external ionization source) to sustain nonequilibrium ionization in high-pressure MHD channels is not feasible due to the fast electron loss in recombination and attachment processes. In the high plenum pressure (P_0~1000 atm) flows, e-beams can be efficiently applied to create nonequilibrium ionization only after the flow is expanded to the low pressures $P\leq 1$ atm.

(ii) in the latter mode of operation, nonequilibrium ionization sustained by an e-beam allows considerable increase of the total enthalpy of the flow (1.5-2.5 times, M~11 in the test section) due to MHD augmentation. However, in this case the static pressures in the test section are more than an order of magnitude lower than required by the TAV flight envelope.

(iii) the test section flow quality is rather poor and gets steadily worse with the increase of the total enthalpy due to both e-beam initiated dissociation and thermal chemical reactions.

(iv) the high plenum pressure (P_0~1000 atm) alkali-seeded flows, which also require high plenum temperatures ($T_0\geq$5000-6000 K), look more promising for the wind tunnel application. Calculations for Cs-seeded flows predict up to 5 times total enthalpy increase (test section Mach number M~14). Predicted test section static pressures are also closer to the reference values (although they are still 1.5-4 times lower). The calculated oxygen atom and NO concentrations in the test section are considerably lower than for the unseeded flows.

(v) these predicted test section flow parameters can be obtained in a flow stable with respect to large-scale thermal instability.

(vi) simple thermodynamic analysis shows the advantage of adding energy to the flow by means of a body force over the purely thermal energy addition.

A two-dimensional time-dependent kinetic model including Maxwell equations is necessary to study the sheath and boundary layer effects, as well as to get a better insight into the flow stability.

References

1. G. Simmons, G.L. Nelson, R. Hiers, and A. Western, "An Unseeded Air MHD Accelerator Concept for High Mach Number Hypersonic Propulsion", AIAA Paper 89-2535, 25th Joint Propulsion Conference, July 1989, Monterey, CA.
2. G.L. Nelson and G. Simmons, "Augmentation of Hypersonic Propulsion facilities Using MHD", AIAA Paper 95-1937, 26th Plasmadynamics and Lasers Conference, June 1995, San Diego, CA
3. G.A. Simmons, G.L. Nelson, and Y.M. Lee, " Feasibility Study of a Nonequilibrium MHD Accelerator Concept for Hypersonic Propulsion Ground Testing", AIAA Paper 95-2720, 31st Joint Propulsion Conference and Exhibit, July 1995, San Diego, CA.
4. J. Lineberry and J. Chapman, "MHD Accelerators for Hypersonic Applications", AIAA Paper 91-0384, 29th AIAA Aerospace Sciences Meeting, January 1995, Reno, NV
5. R.A. Crawford, J.N. Chapman, and R.P. Rhodes, "Potential Application of Magnetohydrodynamic Acceleration for Hypersonic Environment Testing", Report AEDC-TR-90-6, August 1990.
6. G.A. Simmons, G.L. Nelson, and Y.M. Lee, "Analysis of an Unseeded, Nonequilibrium MHD Accelerator Concept for Hypersonic Propulsion Ground Testing Applications", AIAA Paper 92-3994, 17th AIAA Aerospace Ground Testing Conference, July 1992, Nashville, TN
7. J.F. Clark and M. McChesney, "Dynamics of Real Gases", Butterworths, London Boston, 1976
8. G.W. Sutton and A. Sherman, "Engineering Magnetohydrodynamics", McGraw-Hill, New York, 1965

9. B.F. Gordiets and S. Zhdanok, "Analytical Theory of Vibrational Kinetics of Anharmonic Oscillators", in "Nonequilibrium Vibrational Kinetics", ed. by M. Capitelli, Springer, Berlin, 1986, pp. 47-83

10. L.G.H. Huxley and R.W. Crompton, "The Diffusion and Drift of Electrons in Gases", Wiley, New York, 1974

11. N.A. Dyatko, I.V. Kochetov, and A.P. Napartovich, J. Phys. D.: Appl. Phys., vol. 26, 1993, p. 418

12. D.R. Suhre, J.T. Verdeyen, J. Appl. Phys., vol. 47, 1976, p.4484

13. V.P. Konovalov, E.E. Son, Sov. Physics: Technical Physics, vol. 50, 1980, p.300

14. N.L. Aleksandrov, A.M. Konchakov, and E.E. Son, Sov. J. Plasma Phys., vol. 4, 1978, p.663

15. N.L. Aleksandrov, A.M. Konchakov, and E.E. Son, Sov. Physics: Technical Physics, vol. 49, 1979, p.1200

16. http://www.netlib.org/odepack/index.html

17. O.E. Krivonosova, S.A. Losev, V.P. Nalivaiko, Yu.K. Mukoseev, and O.P. Shatalov, "Recommended Data on Rates of Chemical Reactions between Molecules Consisting of N and O atoms", in Khimiya Plazmy (Plasma Chemistry), ed. by B.M. Smirnov, vol. 14, Moscow, Nauka, 1987, pp. 3-31

18. S.O. Macheret, A.A. Fridman, A.A. Elkin, Sov. Chem. Phys., vol.9, 1990, p. 174

19. S.O. Macheret, J.W. Rich, Chem. Phys., vol. 174, 1993, p. 25

20. C.E. Treanor, I.V. Adamovich, M.J. Williams, and J.W. Rich, J. Thermophys. Heat Trans., vol. 10, 1996, p. 193

21. H. Matzing, "Chemical Kinetics of Flue Gas Cleaning by Irradiation with Electrons", Adv. in Chem. Phys., vol.80, pp. 315-403

22. T.A. Cool and E.E. Zukoski, Phys. Fluids, vol.9, 1966, p.780

23. A.F. Ashton and A.N. Hayhurst, Combustion and Flame, vol.21, 1973, p.69

24. R.E. Olson, J. Chem. Phys., vol.56, 1972, p.2979

25. D.G. Torr, "The Photochemistry of Upper Atmosphere", in "The Photochemistry of Atmospheres", ed. by J.S. Levine, Academic Press, New York, 1985, Chap.5

26. Y. Itikawa, M. Hayashi, A. Ichimura et. al., J. Phys. Chem. Ref. Data, vol.16, 1986, p.985

27. Y. Itikawa, M. Hayashi, A. Ichimura et. al., J. Phys. Chem. Ref. Data, vol.18, 1989, p.23

28. B. Mojarrabi, R.J. Gulley, A.G. Middleton et. al., J. Phys. B: At. Mol. Opt. Physics, vol. 28, 1995, p.487 and references therein.
29. M.A. Lennon, K.L. Bell, H.B. Gilbody et. al., J. Phys. Chem. Ref. Data , vol.17, 1988, p.1988
30. V.P. Glushko (ed.) "Thermodynamic Properties of Individual Substances", Moscow, Nauka, 1976
31. "JANAF Thermochemical Tables", J. Phys. Chem. Ref. Data, vol.14, Suppl.1, 1985
32. J.C.Y. Chen, J. Chem. Phys., vol.40, 1964, p.3507
33. I.V. Adamovich, S.O. Macheret, J.W. Rich, and C.E. Treanor, AIAA Paper 95-2060
34. E. Fisher and G. Smith, Chem. Phys. Lett., vol.13, 1972, p.448
35. A.V. Eremin, A.A. Kulikovsky, and I.M. Naboko, Chem. Phys. Lett., vol.45, 1976, p.351
36. J. Perel, P. Englander, and B. Bederson, Phys. Rev., vol. 128, 1962, p.1148
37. Yu. P. Raizer, "Gas Discharge Physics", Springer, Berlin, 1991, Chap.14
38. H. Schlichting, "Boundary Layer Theory", McGraw-Hill, New York, 1960, Chap.21
39. L.E. Rittenhouse, J.C. Pigott, J.M. Whoric, and D.R. Wilson, "Theoretical and Experimental Results with a Linear Magnetohydrodynamic Accelerator Operated in the Hall Current Neutralized Mode", AEDC-TR-67-150, November 1967
40. J.W. Gallagher, E.C. Beaty, J. Dutton, and L.C. Pitchford, J. Phys.Chem. Ref. Data, vol.12, 1983, p. 109
41. "Feasibility Study of a High Density Shock Tunnel Augmented by a Magneto-hydrodynamic Accelerator", AEDC-TR-65-225, October 1965
42. C.J. Harris, C.H. Marston, and W.R. Warren, AIAA Journal, vol. 13, 1975, p. 229
43. R.J. Rosa, "Magnetohydrodynamic Energy Conversion", McGraw-Hill, New York, 1968

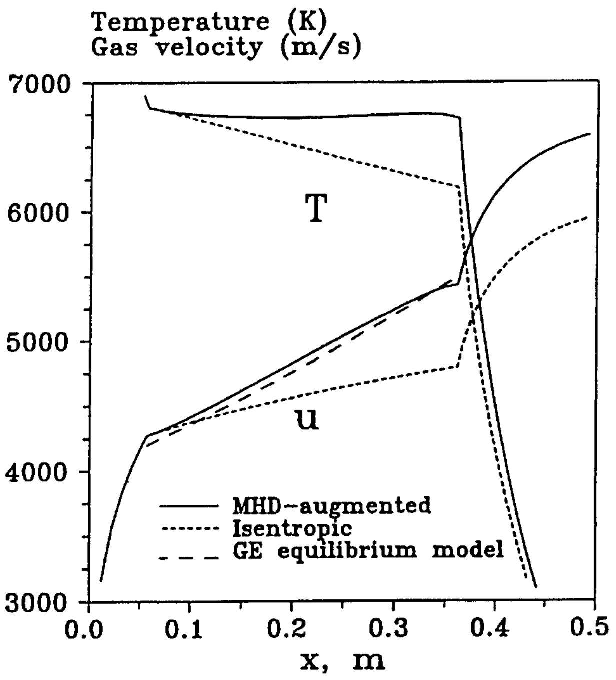

Figure 1. Axial temperature and velocity profiles for the GE reflected shock unseeded air accelerator.

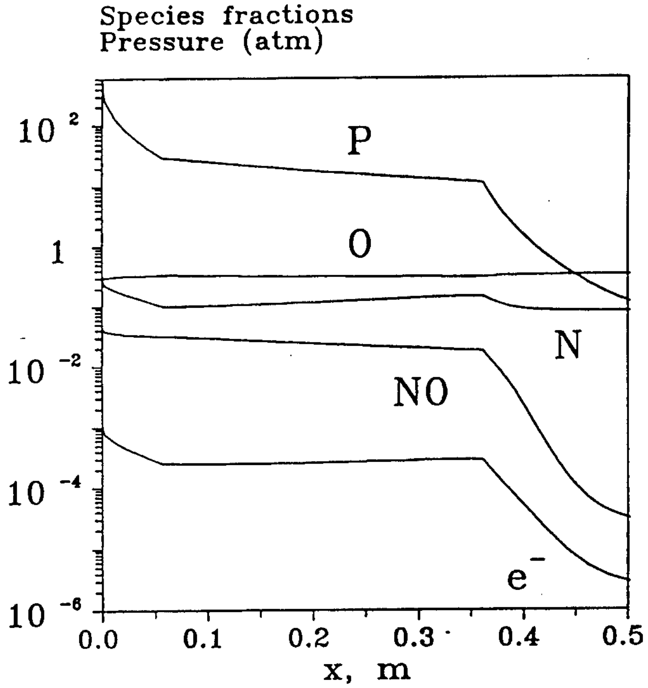

Figure 2. Axial profiles of pressure and species mole fractions for the GE accelerator.

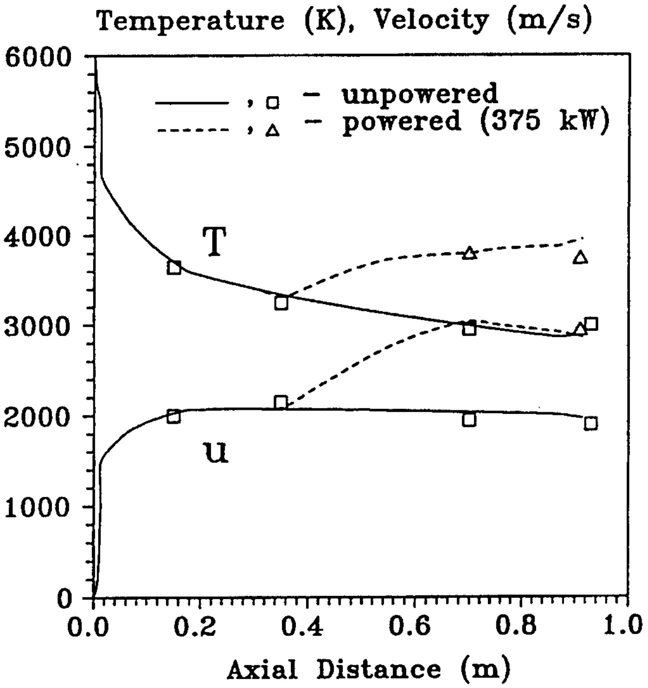

Figure 3. Experimental and calculated temperature and velocity axial profiles for the AEDC potassium-seeded accelerator.

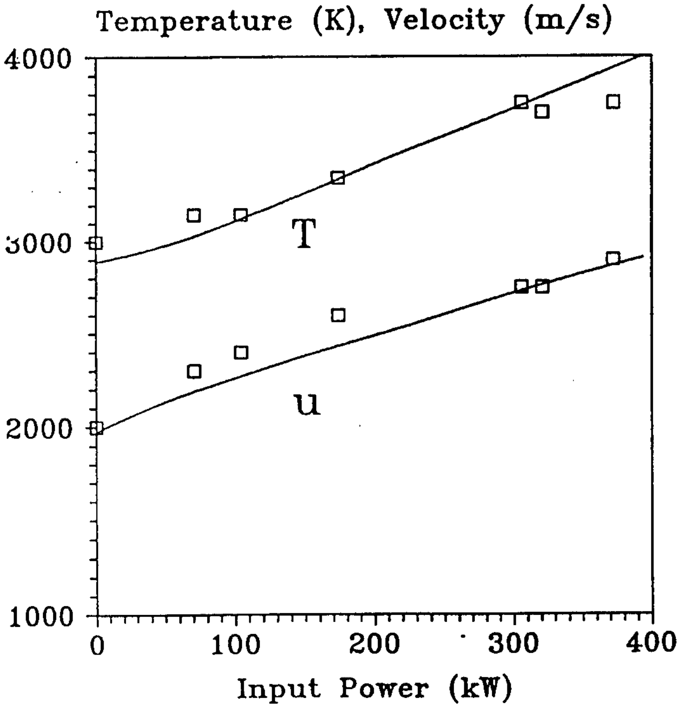

Figure 4. Experimental and calculated exit temperature and velocity for the AEDC potassium-seeded accelerator.

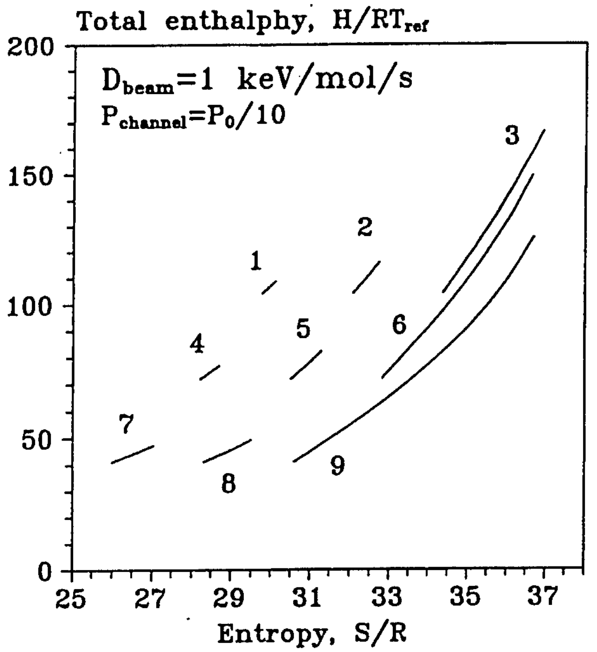

Figure 5. Total enthalpy vs. entropy diagram for the MHD-augmented unseeded air flows, ionized by a high-energy e-beam (D_{beam}=1 keV/mol/s): 1- T_0=6000 K, P_0=1000 atm; 2- T_0=6000 K, P_0=100 atm; 3- T_0=6000 K, P_0=10 atm; 4- T_0=4500 K, P_0=1000 atm; 5- T_0=4500 K, P_0=100 atm; 6- T_0=4500 K, P_0=10 atm, D_{beam}=0.3; 7- T_0=3000 K, P_0=1000 atm; 8- T_0=3000 K, P_0=100 atm; 9- T_0=3000 K, P_0=10 atm, D_{beam}=0.1

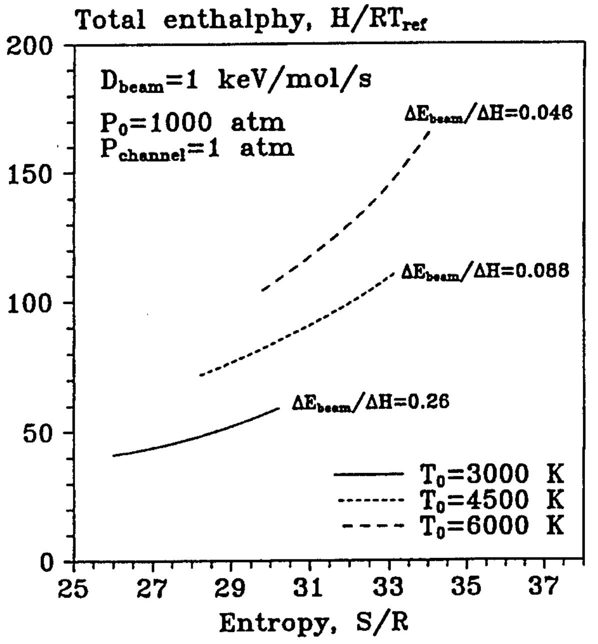

Figure 7. Total enthalpy vs. entropy diagram for the high plenum pressure (P_0=1000 atm) MHD-augmented unseeded air flows, ionized by a high-energy e-beam (D_{beam}=1 keV/mol/s). The flow is expanded to P~1 atm before entering the MHD channel.

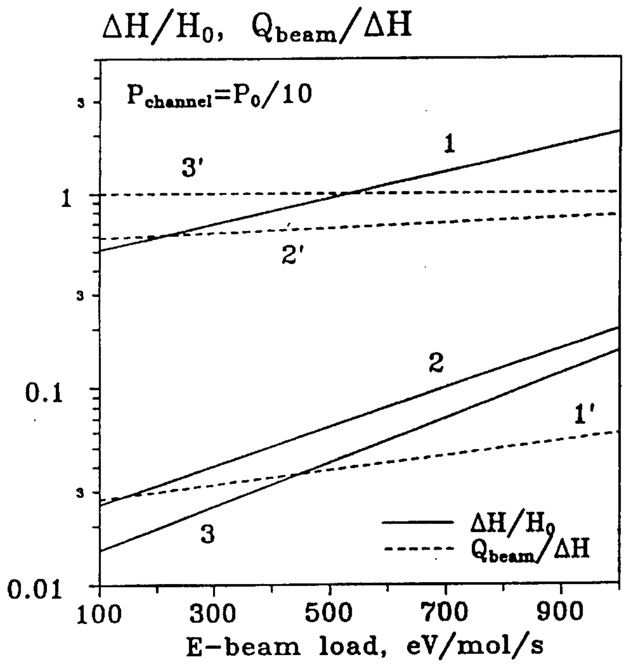

Figure 6. Total enthalpy increase $\Delta H/H_0$ and beam efficiency $\Delta E_{beam}/\Delta H$ for the MHD-augmented unseeded air flows at T_0=3000 K: 1,1'- P_0=10 atm, 2,2'- P_0=100 atm, 3,3'- P_0=1000 atm.

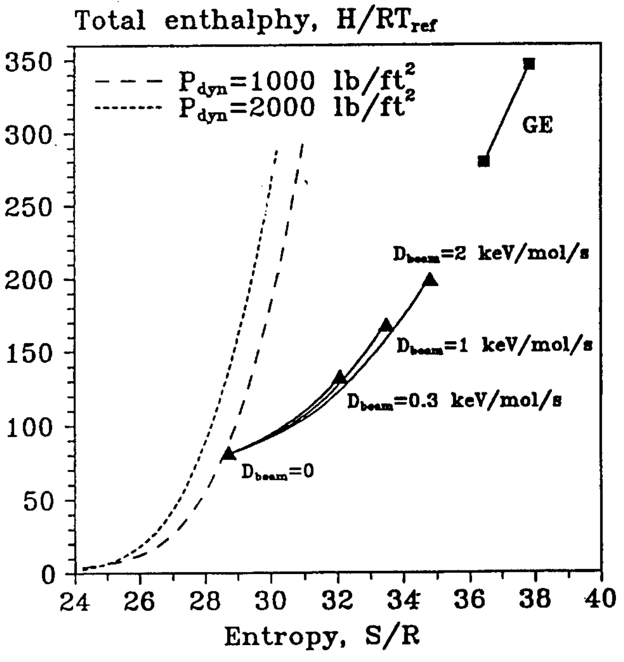

Figure 8. Total enthalpy vs. entropy diagram for the full-scale unseeded air MHD accelerator with external ionization by an e-beam. P_0=1000 atm, T_0=5000 K, L=140 cm, F_2/F_1=1.65. Dashed lines - TAV flight envelope. Also shown H(S) for the GE reflected shock unseeded air accelerator.

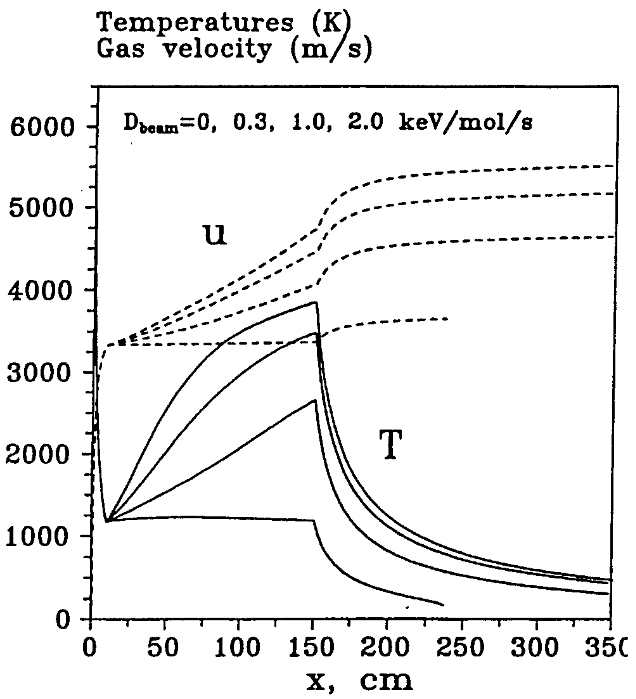

Figure 9. Axial temperature and velocity profiles for the accelerator of Fig. 8 for different beam loads.

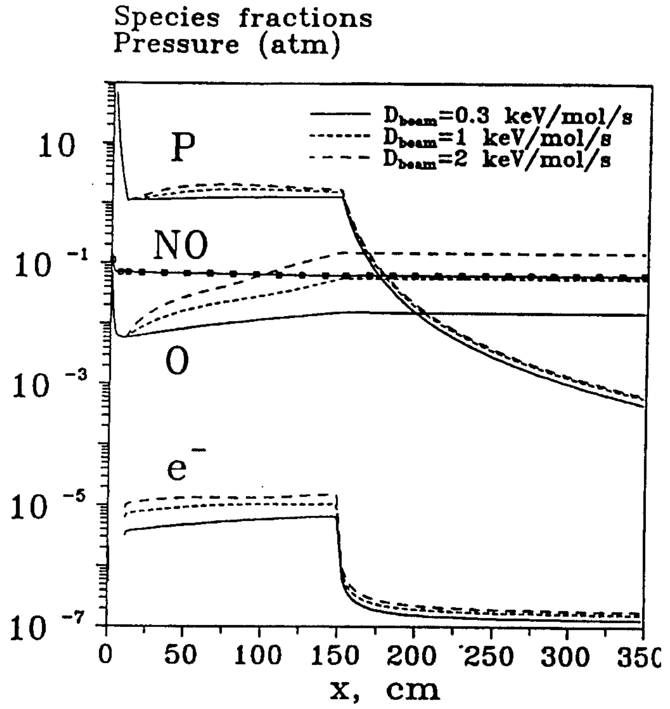

Figure 10. Axial profiles of pressure and species mole fractions for the accelerator of Fig. 8 for different beam loads.

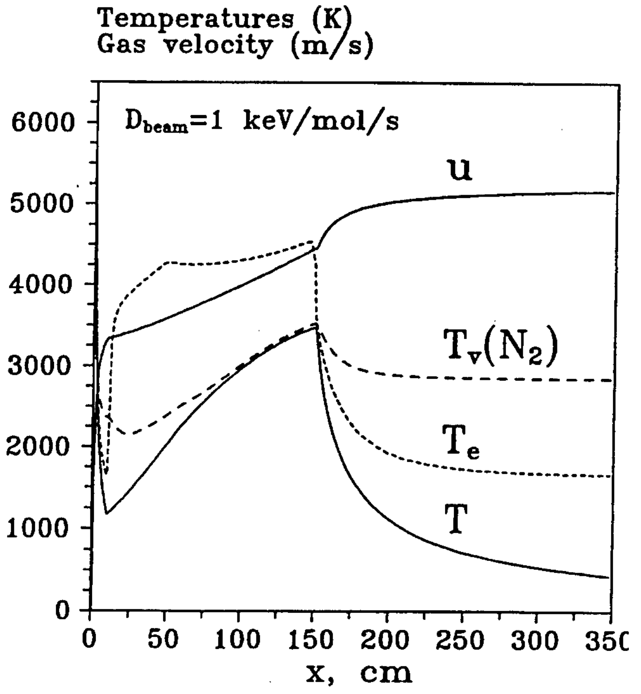

Figure 11. Axial profiles of the translational temperature, vibrational temperature of nitrogen, and electron temperature for the accelerator of Fig. 8 for D_{beam}=1 keV/mol/s.

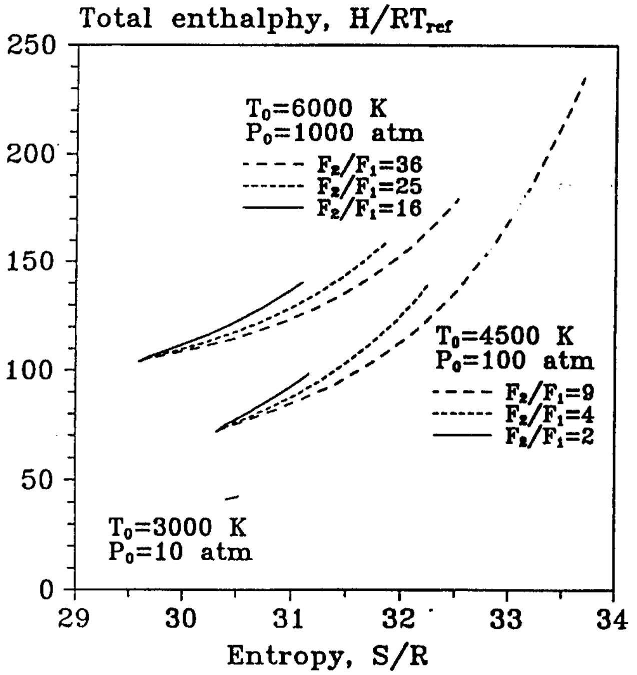

Figure 12. Total enthalpy vs. entropy diagram for the MHD-augmented K-seeded (at 1%) air flows.

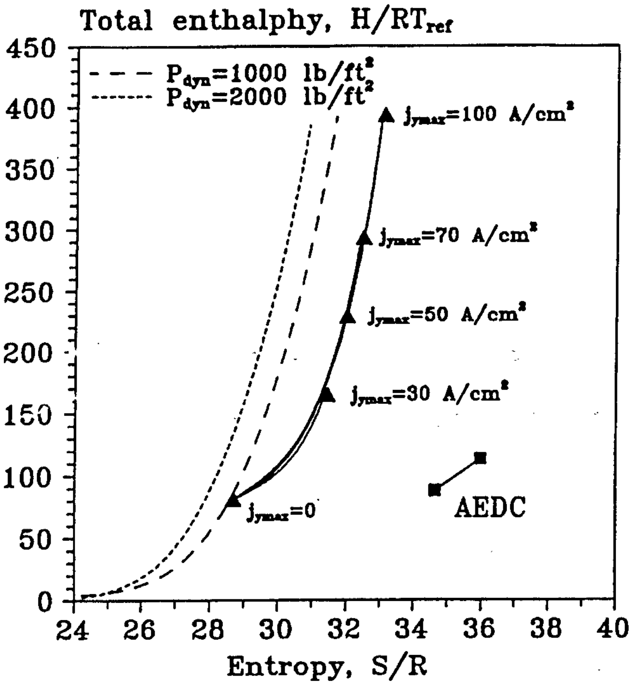

Figure 13. Total enthalpy vs. entropy diagram for the full-scale Cs-seeded (at 0.5%) air MHD. P_0=1000 atm, T_0=5000 K, L=140 cm, F_2/F_1=1.65. Dashed lines - TAV flight envelope. Also shown H(S) for the AEDC K-seeded (at 1.5%) accelerator.

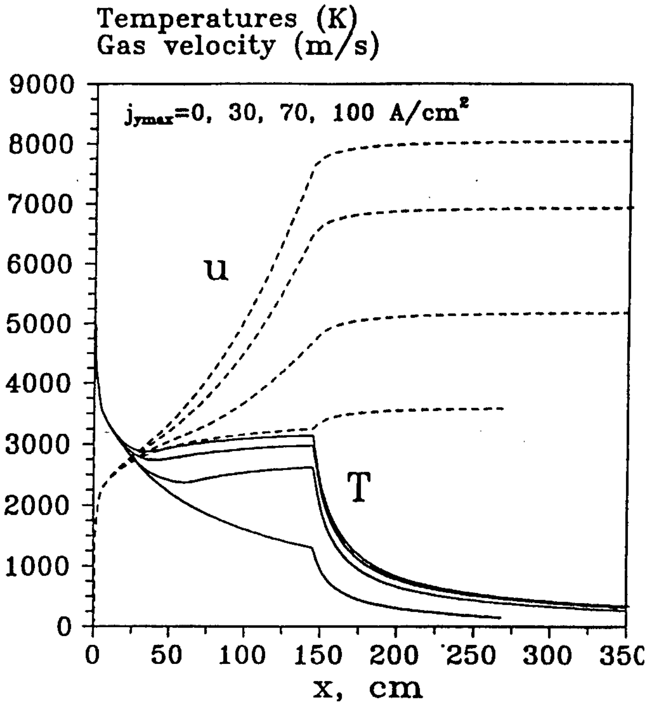

Figure 14. Axial temperature and velocity profiles for the accelerator of Fig. 13 for different maximum current densities.

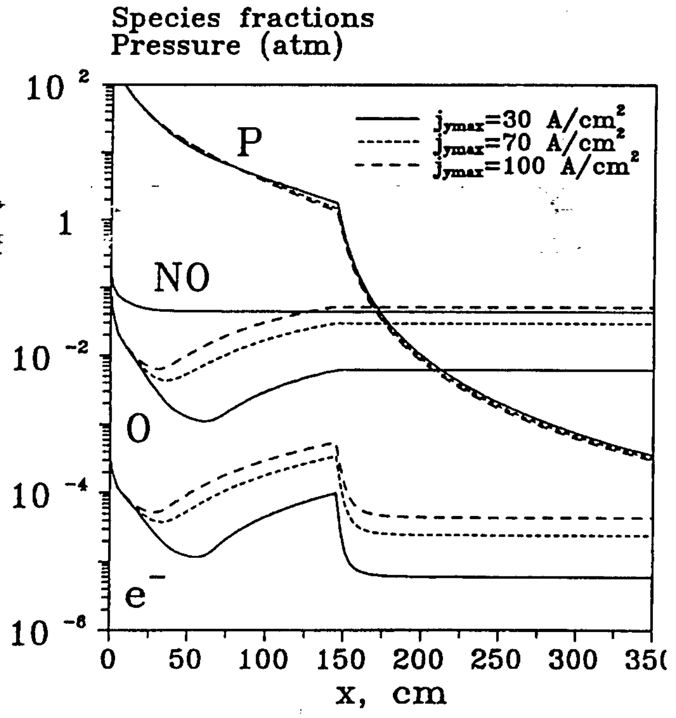

Figure 15. Axial profiles of pressure and species mole fractions for the accelerator of Fig. 13 for different maximum current densities.

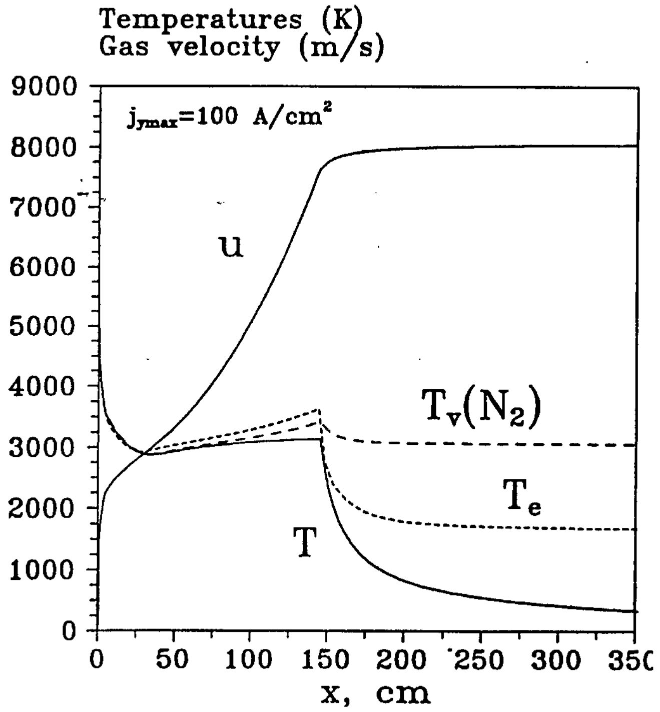

Figure 16. Axial profiles of the translational temperature, vibrational temperature of nitrogen, and electron temperature for the accelerator of Fig. 13 for j_{ymax}=100 A/cm^2.